Dynamic modelling of hydrogen storage at atmospheric pressure

D.H. van Bolhuis

Delft University of Technology

TU Delft

Dynamic modelling of hydrogen storage at atmospheric pressure

by

D.H. van Bolhuis

Student Name	Student Number
van Bolhuis D.H.	4694678

Supervisor: Prof. Dr. Ir. Vlugt T.J.H.
Supervisor: Dr. Ir. Rahbari A.
Faculty: Faculty of Mechanical Engineering, Delft

TU Delft

Preface

After obtaining my bachelor's degree in Mechanical Engineering from Tu Delft in 2022, this concludes the final chapter of my studies. In front of you lays my Master's thesis entitled: Dynamic modelling of hydrogen storage at atmospheric pressure.

The last eight months have been a journey I will never forget. I want to thank my supervisors, Dr. Ir. Ahmadreza Rahbari and Prof. Dr. Ir. Thijs Vlugt, for their guidance. Their help was an essential factor in my success. I would also like to thank XINTC as a company for the opportunity it gave me. I wish my colleagues the best and the company a bright future. At last, I would like to thank all those who supported me during this project, particularly Ir. L.S. Cras, whose invaluable assistance has significantly refined my coding skills. I'm looking forward to what life brings me next. My love goes to my family and all those I hold dear.

D.H. van Bolhuis
Delft, June 2024

Abstract

Due to greenhouse gas emissions, global warming has severe environmental consequences. To tackle this issue, XINTC produces green hydrogen using alkaline electrolysis to replace fossil fuels. Green hydrogen's primary challenge is its dependence on intermittent energy sources for electrolysis. Hydrogen storage is necessary for the hydrogen economy to meet production and demand peaks. This work focused on hydrogen storage using double membrane gas holders storing hydrogen at atmospheric pressure, a novel hydrogen storage method. The main goal of the storage is to avoid power cycling the downstream hydrogen compressor.

Energy and mass balances are calculated considering molecule permeation through the membranes and water condensation. Weather conditions are also taken into account. To regulate the pressure in the storage, a control system consisting of PID controllers connected to pressure relief valves was designed.

The model shows the behaviour as a response to changing weather conditions. It has been proven that the water in the system will condense and, at certain points, even freeze. A drain is necessary to evacuate the water forming in the system. The control system manages the system accordingly, opening the valves to the desired amounts at the desired moments.

It was also proven that one should not have to worry about forming a combustible hydrogen-oxygen mixture. If the storage is filled at 10% of its maximum value, it takes more than 500 days to reach that value.

The permeation of nitrogen through the membrane is a bigger issue. If the storage is filled to 10% of its maximum value, the maximum concentration of 300 PPM is exceeded within three days at a standstill. Thus, the storage will have to be drained long before safety issues arise.

The model is fully modular, meaning that it can be run for all locations around the world. It can easily compare storage behaviour and performance.

The outcome of this research has led to a better understanding of the behaviour of hydrogen storage in membrane gas holders. The model developed can be used to effectively manage hydrogen storage, reducing any hydrogen losses and maximising storage efficiency.

Contents

List of Figures

List of Tables

Nomenclature

Abbreviations

Abbreviation	Definition
BoP	Balance of plant
CO_2	Carbon dioxide
GHG	Greenhouse gas
H_2	Hydrogen
HE	Hydrogen embrittlement
HEE	Hydrogen environment embrittlemnent
HRE	Hydrogen reaction embrittlement
IHE	Internal hydrogen embrittlement
L.H.S.	Left hand side
M.S.	Maxwell-Stefan
N_2	Nitrogen
O_2	Oxygen
PPM	Part per million
TMY	Typical Meteorological Year
...	

Symbols

Symbol	Definition	Unit
A	Area	[m^2]
c	Molar concentration	[mol/m^3]
c_p	Specific heat at constant pressure	[J/ (mol K)]
c_v	Specific heat at constant volume	[J/ (mol K)]
d	Diameter	[m]
$Đ_i$	Unimpeded self-diffusivity	[m^2/s]
$Đ_{i,j}$	Maxwell-Stefan diffusivity	[m^2/s]
$F_{i,j}$	view factor	[-]
g	Acceleration due to gravity	[m/s^2]
$G(h)$	Global solar irradiance on the horizontal plane	[W/m^2]
Gr	Grashof number	[-]
h	Specific enthalpy	[J/mol]
h_c	Heat transfer coefficient	[W/(m^2 K)]
J	molar flux	[mol/ (m^2 s)]
k	Thermal conductivity	[W/(m62 K)]
$k_{i,j}$	mass transfer coefficient	[m/s]
k_b	Boltzmann constant	[J/K]
K_t	Clearness index	[-]
L_c	Characteristic length	[m]
m	Mass	[kg]
M	Molar mass	[kg/mol]
N	number of mols	[mol]
N_A	Avogrado constant	[1/mol]
$\dot{N}$	mol flow	[mol/s]

Symbol	Definition	Unit
Nu	Nusselt number	[-]
p	Partial pressure	[Pa]
P	Pressure	[Pa]
P_{sat}	Saturation pressure	[Pa]
Pr	Prandtl number	[-]
P_V	Partial vapour pressure in the air	[Pa]
$\dot{Q}$	Energy exchanged through heat transfer	[W]
R	Gas constant	[J / (mol K)]
Ra	Rayleigh number	[-]
Re	Reynolds number	[-]
RH	Relative humidity	[%]
T	Temperature	[K]
u	Velocity	[m/s]
V	Volume	[m^3]
v	molar volume	[m^3/mol]
$\dot{W}$	Thenrodynamic work	[W]
x	mol fraction	[-]
z	membrane thickness	[m]
α	Thermal diffusivity	[m^2/s]
β	Volume expansion coefficient	[1/K]
ϵ	Emmisivity	[-]
ρ	Density	[kg/m^3]
ζ	Maxwell-Stefan friction coefficient	[(N s)/(mol m)]
ψ	Total potential	[J/mol]
τ	time constant	[s]
μ	Dynamic viscosity	[(N s)/m^3]
ν	Kinematic viscosity	[m^2 /s]
σ	Stefan-Boltzmann constant	[W/(m^2K^4)]

1 Introduction

According to the Intergovernmental Panel on Climate Change, human activities have led to the global warming warming of the earth. The average global surface temperature of the earth from 2011-2020 was 1.09 °C higher than in 1850-1900 [1]. The increase in global temperature is known to have a severe environmental impact, leading to the disappearance of animal species, decreased agricultural yield, more extreme weather conditions, and human migration accompanied by conflicts [2].

With the Paris Agreement of 2015, an important step has been taken towards climate neutrality. To reach climate neutrality, global emissions of greenhouse gasses (GHG) must be reduced. Although not all emissions come from the usage of fossil fuels, they represent a significant part. Therefore, our usage of fossil fuels must be decreased. Nevertheless, accomplishing this is not straightforward since fossil fuels are our primary energy source. Hydrogen is seen as a solution to this problem. It is considered an important clean energy source because it can generate energy without emissions [3]. It can be used in fuel cells to produce electricity or be burned to provide heat. It is thus logical that the demand for hydrogen is increasing. In this context, the role of XINTC becomes prominent. XINTC is a Dutch original equipment manufacturer of highly modular alkaline electrolysers operating at atmospheric pressure. Electrolysers are used to produce hydrogen from water. The equipment produced by XINTC is innovative due to the possibility of capacity expansion. All components of the electrolyser and the balance of plant (BoP) are standardised and modular, allowing for easy scale-up or -down as extra modules can be added according to wish. Furthermore, each electrolyser stack can be turned on or off to respond to intermittent energy production by sustainable energy solutions.

Green energy sources such as solar or wind energy produce electricity in peaks, given their dependency on weather conditions. At times of low solar irradiance and weak winds, their energy production is low, while at times of high solar irradiance and strong winds, their energy production is high. XINTC's system already addresses the issue of an intermittent energy source, as the stacks can be turned on or off to respond to the power production, but there's still another problem to overcome. There are not only peaks in green energy production but also peaks in energy demand. These peaks will lead to times when the hydrogen production exceeds the hydrogen demand and vice versa. The proposed solution is the storage of excess hydrogen produced during energy peaks, which offers the possibility of distribution when required.

This thesis will focus on hydrogen storage directly applied to XINTC's system. The company plans on using double membrane gasholders as the medium for short-term hydrogen storage. This work aims to build a complete model for this type of storage. The model will used as a management tool to predict behaviour and thus conclude if it fits the company's needs. In the system designed by XINTC, the hydrogen is stored after production. It contains traces of water and oxygen. These traces will be removed post-storage. The storage is connected to downstream cleaning and a liquid-ring compressor. The compressor requires a constant feed of hydrogen to work. Furthermore, it is important to reduce the power cycling of the compressor as much as possible to extend the compressor's lifetime. The storage will thus mostly be a buffer. It will accommodate the intermittently produced hydrogen and, once full, will direct a constant hydrogen flow to the compressor.

This usage is uncommon for a double membrane gasholder, normally used to store biogas [4]. The storage of hydrogen in a double membrane gasholder is a novelty. The storage of hydrogen brings

complications regarding safety [5]. Therefore, analysing storage behaviour is critical. The behaviour of the double membrane gasholder is barely touched upon in the literature. This will thus be the focus of this work. By modelling the storage behaviour, a tool will be built capable of predicting the pressure, temperature and composition of the gas in the storage. This, combined with a control system regarding the storage pressures, will simulate storage behaviour. The tool will include condensation and permeation of the molecules through the membranes, two phenomena not considered in previous works.

The first step in this process is to conduct extensive research to determine the critical parameters when considering hydrogen storage at atmospheric pressure in this type of storage. This will be done in the literature review, chapter 2. The problem and system will be specifically described from these findings, chapter 3. Then, the derivation of the model will described. This has been separated into several parts: the derivation of the differential equations describing storage behaviour, chapter 4, the derivation of the heat transfer equations, chapter 5, the collection and pre-processing of input data for the model chapter 6 and at last the description of the control system used to monitor the storage chapter 7. The results will then follow, chapter 8, and at last, this work will be concluded, chapter 9. The conclusion will also contain recommendations to improve the model.

2

Literature study

2.1. Fundamentals of Hydrogen

Hydrogen is the simplest chemical element. The ordinary isotope of hydrogen, H, is known as protium with an atomic weight of 1 u (1 proton and 1 electron) [5, 6]. A stable isotope, deuterium D and an unstable isotope, tritium T, also exist with respectively atomic weight of 2 u (1 proton and neutron, 1 electron) and atomic weight of 3 u (1 proton and two neutrons, 1 electron) [6, 7]. Due to the single electron in the atom, all the isotopes of hydrogen react together to form covalent molecules like H_2, D_2, and T_2.

The hydrogen molecule exists in 2 forms: ortho- and para-hydrogen [5]. The difference between the two forms is the orientation of the nuclear spin, see Figure 2.1. Para-hydrogen has anti-parallel nuclear spin while ortho-hydrogen has parallel nuclear spin [5, 7]. At ambient conditions, there is three times as much ortho-hydrogen (75%) as para-hydrogen (25%). This is called 'normal' hydrogen. Para-hydrogen has a lower energy content than ortho-hydrogen [7]. This means that ortho-hydrogen transformation in para-hydrogen is exothermic, 1.063 kJ/mol of heat is released. The enthalpy of evaporation of hydrogen is equal to 0.902 kJ/mol. Thus, the transformation of one mol of ortho-hydrogen releases enough heat to evaporate one mol of hydrogen. This is an important aspect when considering liquified hydrogen.

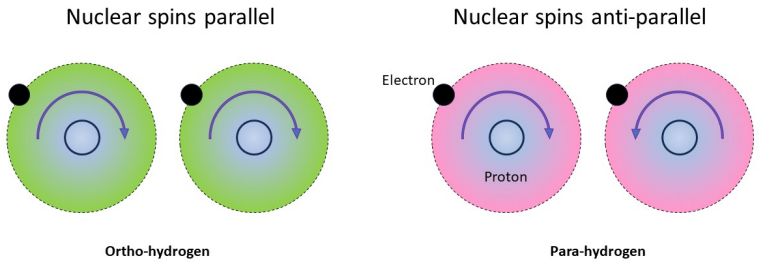

Figure 2.1: Spin direction of the two electrons in ortho- and para-hydrogen, reproduced from [7]

2.1.1. Thermophysical properties of hydrogen

Hydrogen is a gas at standard conditions. Hydrogen is liquefied at 20.2 K at atmospheric pressure and solidifies at 14 K. As seen in the phase diagram, Figure 2.2, the boiling point of hydrogen increases when pressure is applied. The maximum boiling point is reached at its critical point at a temperature and pressure of 33 K and 13 MPa, respectively.

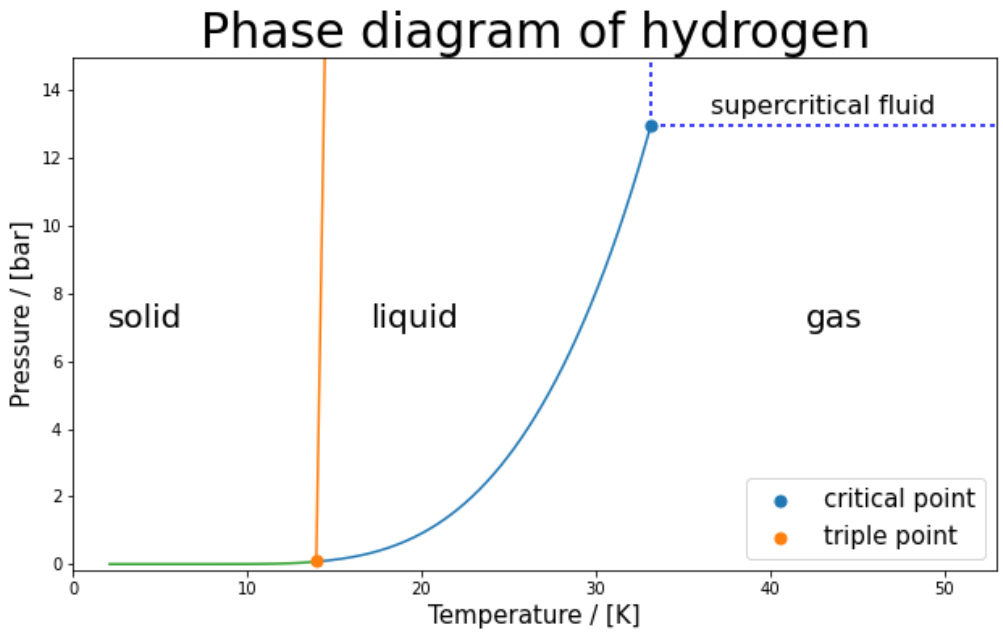

Figure 2.2: Phase diagram of hydrogen, data from Refprop [8]

The density of hydrogen is minimal; at atmospheric pressure and 298 K, the density of hydrogen is only 0.0824 kg/m^3 [9]. In comparison, this is about 7% of the density of air [5]. Its density increases to around 70.8 kg/m^3 when liquefied and to around 70.6 kg/m^3 when solidified [5–7, 10]. The density of most gases can be approximated with high accuracy using the ideal gas law. This is not the case for hydrogen, although the predictions are accurate below 100 atm [5, 7]. The deviation from the ideal gas behaviour is visualised in Figure 2.3. The deviation from ideal behaviour becomes more significant with increasing pressure and decreasing temperature. Thus, hydrogen does not behave as an ideal gas at high pressures. One could modify the ideal gas law by adding a compressibility factor to the equation, Equation 2.1 to compensate for the deviation from the ideal gas law.

$$PV = nRT * Z \tag{2.1}$$

Here, P is the pressure in Pascals, V is the volume in m^3, n is the number of moles, R is the ideal gas constant, 8.3145 J/K mol, and T is the absolute temperature in Kelvin. Z is the compressibility factor, dimensionless and equal to 1 for an ideal gas. The compressibility factor is temperature, pressure and substance dependent. There are also more suitable equations of states, such as the GERG 2008, which predict the behaviour accurately at extreme conditions [11, 12].

Hydrogen has the highest gravimetric energy density, energy content per unit of mass, of all known substances [5, 7, 9]. On the other hand, its volumetric energy density is low due to its extremely low density [7, 13, 14]. For example, its volumetric energy density at ambient conditions is 0.01 MJ/L, while at the same conditions, methane and gasoline contain 0.04 MJ/L and 32 MJ/L, respectively [9]. This means that a more extensive storage facility is needed if the same amount of energy is to be stored in the form of pure hydrogen compared to methane or gasoline. This problem is often overcome by increasing the density by liquefying or compressing the hydrogen before storage.

2.1.2. Physicochemical properties of hydrogen related with its storage

Hydrogen is an odourless, colourless and flammable gas [13]. Carelessness when dealing with hydrogen can lead to disasters. For example, on May 6, 1937, the LZ129 Hindenburg zeppelin filled with hydrogen burst into fire, causing the death of 35 individuals [15]. Hence, handling hydrogen carefully and thoroughly assessing its flammability limits is crucial. Hydrogen does not combust on its own. Only when it is mixed with oxygen is there a risk of combustion. At ambient conditions, the flammability limits of hydrogen in air mixture are 4-75.6% [16, 17] and the explosive limits are 15-59% [5]. Only 4% of

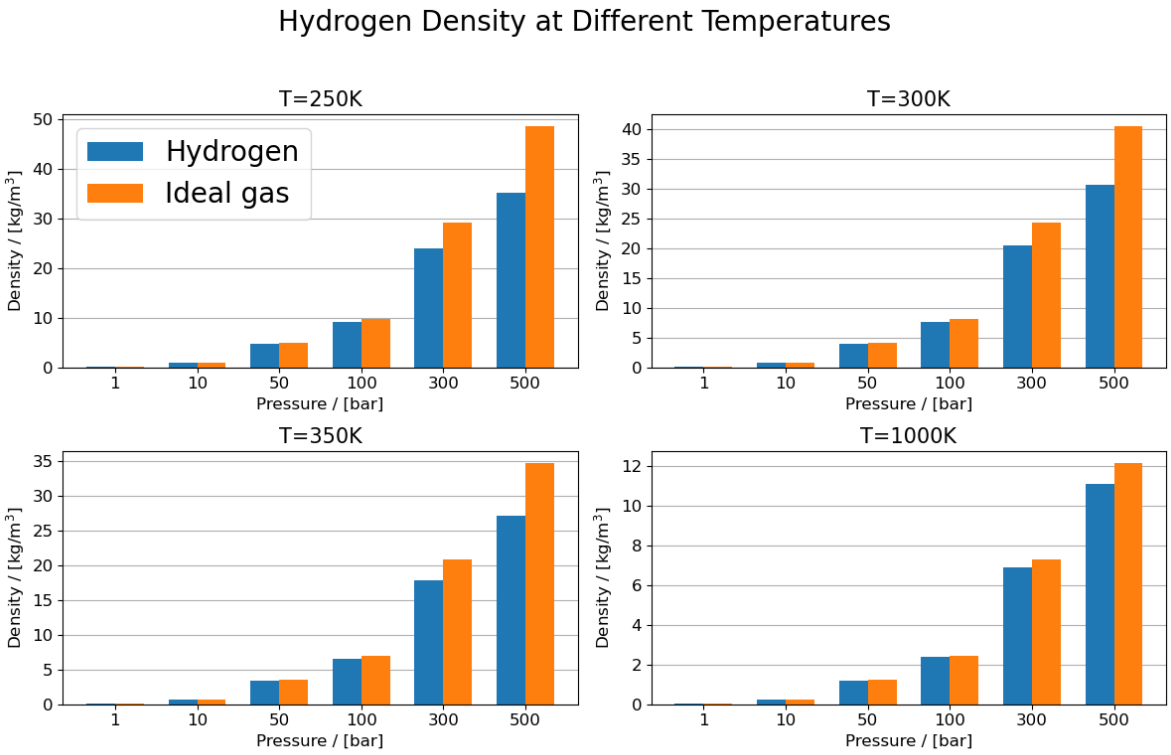

Figure 2.3: Density of hydrogen at 250 K, 300 K, 350 K and 1000 K at different pressures compared to ideal gas law prediction, data from Refprop [8]

oxygen is necessary to form a combustible mixture with pure hydrogen [17]. Flammability and explosive limits depend on pressure and temperature [5, 16]. It is evident that for safety reasons, the stored hydrogen should never be within the flammability range.

The auto-ignition temperature of hydrogen is 585°C, meaning that at temperatures of or above 585°C, a mixture of hydrogen and oxygen within flammability limits will initiate self-sustained combustion without the need for an ignition source [5]. Operating at these temperatures thus brings considerable risk.

Furthermore, a hydrogen fuel mixture has low ignition energy, the minimum energy required to initiate combustion. This ignition energy, 0.017 mJ [18], is nearly an order of magnitude lower than the ignition energy for conventional fuels [5]. Due to this, there is a possibility for ignition by a simple electrostatic discharge [18].

2.1.3. Hydrogen embrittlement

A hydrogen environment can significantly reduce the ductility of high-strength metals, such as steel [19, 20]. This phenomenon is called hydrogen embrittlement (HE). The effect of HE is the failure of a material below its designed strength and stress [19, 20]. Conventionally, HE is divided into three categories: internal hydrogen embrittlement (IHE), hydrogen reaction embrittlement (HRE) and hydrogen environment embrittlement (HEE) [20]. IHE is caused by the hydrogen in the metal, which is introduced during fabrication or prior processing. HRE is due to high pressures resulting from the chemical reaction of hydrogen in the metal. The hydrogen in a carbon-metal can form methane, leading to the decarbonisation of the metal and reducing strength. This is also called a ”strong hydrogen attack”. HEE is caused by hydrogen permeating or diffusing in an initially free material. HEE only occurs in hydrogen-containing atmospheres. Hydrogen molecules are adsorbed on the material’s surface and then dissociate into hydrogen atoms, which can enter the material. Hydrogen inside the material can accumulate in internal defects, leading to high pressures exceeding the material’s ultimate tensile strength, causing blisters.

A coating can be applied to protect materials from HE. This coating has a low H_2 permeability, meaning less hydrogen is in contact with the material surface.

2.1.4. The impact of hydrogen on the climate

Although hydrogen is a promising solution for the world's energy problems, it is also an indirect greenhouse gas, which contributes to global warming by forming other molecules. Its warming impact is widely overlooked and underestimated [21]. When H_2 is released into the atmosphere, there are two options: around 75% of the hydrogen is removed by soils and bacterial uptake, thus posing no harm to the climate. The leftover 25% is oxidised by hydroxyl radical (HO), a molecule present in the Earth's atmosphere [21]. The oxidation of hydrogen leads to global warming in different ways; see Figure 2.4.

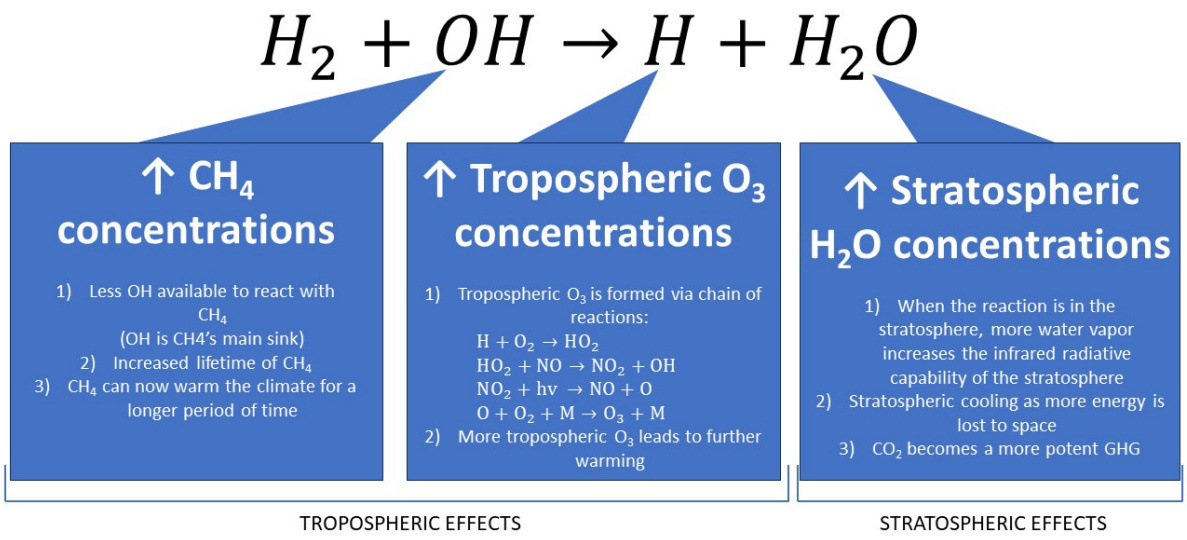

Figure 2.4: Effects of hydrogen oxidation on atmospheric greenhouse gas concentrations and warming, reproduced from [21]

First of all, the oxidation of H_2 in the atmosphere utilises precious hydroxyl radical, which usually reacts with gasses such as methane [21]. This prolongs the lifetime of methane in the atmosphere, increasing its global warming potential. Methane is a greenhouse gas responsible for about 30% of the current rise in Earth's temperature [1]. Furthermore, the atomic hydrogen produced during the oxidation reaction leads to a sequence of reactions, visible in Figure 2.4, resulting in the production of tropospheric ozone [21]. Tropospheric ozone is the third most important anthropogenic greenhouse gas after carbon dioxide and methane [22]. It absorbs infrared radiation, decreasing the radiation leaving Earth to space and warming the atmosphere. If the reaction happens in the stratosphere, the produced water vapour increases its radiative capability, leading to a temperature decrease [21]. The cooling of the stratosphere causes subsequent increases in CO_2 to have a larger heat-trapping effect. Overall, the global warming potential of hydrogen over 100 years was estimated at 11.6 [23].

2.1.5. Hydrogen grades

In both hydrogen production and hydrogen usage, the purity of the hydrogen is an essential factor. The purity of hydrogen is often indicated by a grade. The grade is expressed as a capital N followed by a two-digit decimal number. The first digit indicates the number of nines of purity. For example, grade 4.0 indicates a purity of 99.99%. The second digit indicates the number following the last nine. A grade of 4.6 would thus indicate a purity of 99.996% [24].

2.1.6. Hydrogen production by XINTC

XINTC produces hydrogen at grade 2.5 using an alkaline electrolyser. The hydrogen stream leaves the electrolyser at atmospheric pressure while containing a few impurities. The impurities in the stream leaving XINTC's electrolyser are O_2 and H_2O. Upon distribution, the hydrogen is compressed to 13 bar. The hydrogen will be stored at atmospheric pressure after production. It will serve as a buffer before the

cleaning process, which contains a liquid ring compressor that requires a constant hydrogen feed. The cleaning process removes the undesired O_2 and H_2O from the hydrogen. It is not capable of removing N_2. According to the International Organization for Standardization, the maximum contamination of N_2 in hydrogen produced for fuel cell utilisation is 300 PPM [25].

2.2. Hydrogen storage: state of the art

There are a vast number of options for hydrogen storage. These options have been categorised using a system developed by Andersson & Grönkvist [26]. They ordered the different storage options in terms of the nature of the interaction between the hydrogen and the storage vessel. The categorisation can be seen in Figure 2.5.

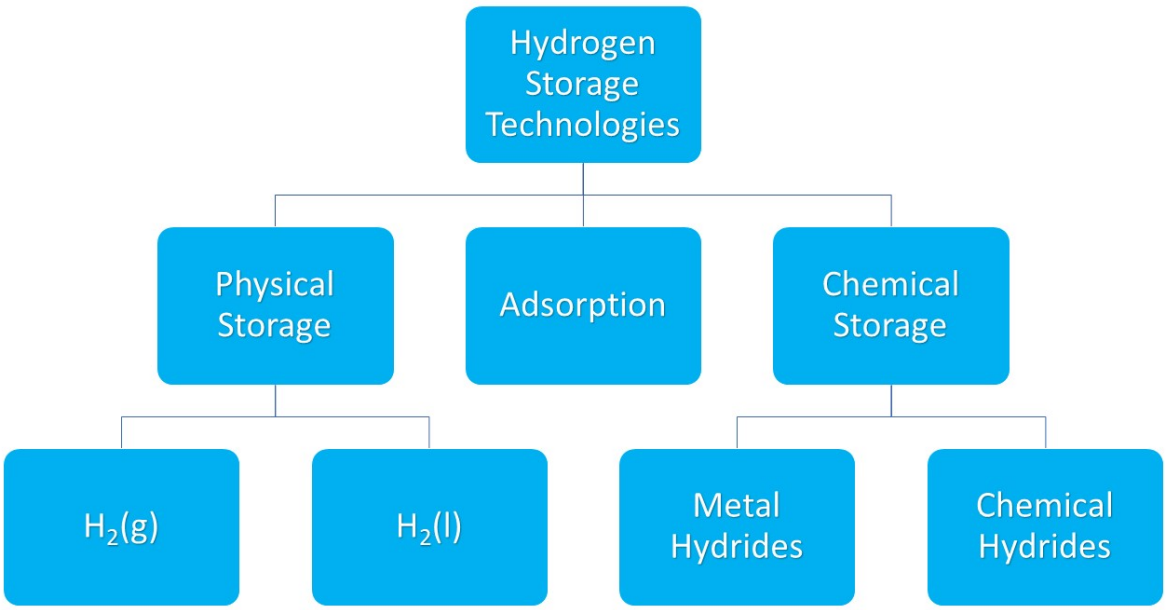

Figure 2.5: Categorization of hydrogen storage technologies. The H_2 sored in physical from can either be in the gas (g) or liquid (l) phase. Reproduced from [26]

There are three main categories. The first category, physical storage, represents the storage of pure hydrogen in molecular form without any significant physical or chemical bonding. Adsorption, the second category, is hydrogen adsorption onto a material by van der Waals bonds. The last category, chemical storage, represents the chemical bonding of the hydrogen atom and can be subdivided into two more categories: metal hydrides and chemical hydrides.

2.2.1. Physical storage

Pure hydrogen can either be stored in the gas or liquid phase. Storing hydrogen in the solid phase does not make sense as it requires a lower temperature than the liquid phase while having a lower volumetric energy density. Both the hydrogen storage in the gas and the liquid phase are implemented on a significant scale [2, 5, 26, 27].

2.2.1.1. Compressed hydrogen gas

High-pressure gas cylinders are the most common storage system for hydrogen [2, 6, 9, 10]. Commercial hydrogen vehicles such as the Toyota Mirai or the Honda Clarity rely on pressure vessels for onboard hydrogen storage [2]. This is because this technique high rates of H_2 filling and release [9, 10, 27]. Furthermore, no energy is required for the release. On the downside, compressing H_2 requires a substantial amount of energy, resulting in considerable losses, about 15% of its lower heating value if compressed to 700 bar [3, 7, 9, 10, 13, 27, 28]. Spheres have the largest volume per area of all shapes but due to manufacturing difficulties and impracticality, H_2 is stored in cylindrical containers [9, 10, 28].

The ideal vessel material is inexpensive, lightweight, and can withstand high pressures. It should also be HE proof, meaning it is H_2 diffusion resistant [9, 10]. There are five different types of vessels for compressed H_2 storage [5, 10, 26]. The first vessel, type 1, is made of metallic components, usually steel or aluminium. It is the most affordable option. Their maximum operating pressure is 30 bar [10]. Due to the high pressures, the walls must be thick, resulting in a heavy vessel. This leads to a low net hydrogen gravimetric energy density of about 1% [3, 9, 10, 29, 30]. Type 2 vessels are 30-40% lighter than type 1 vessels. The metallic wall is wrapped with fibre resin composite on the cylindrical part. This comes at the expense of a 50% cost increase [9, 10]. Type 3 vessels consist of carbon fibre composite materials lined with metal. The vessels are strong and lightweight but have a drawback: low thermal conductivity. This can pose problems as hydrogen compression produces heat, which will escape slowly. They store hydrogen at 450 bar but can handle pressures up to 700 bar [9, 10]. Type 4 vessels are similar to type 3 vessels. The main difference is the liner, which is polymeric and not a metal. The vessel is made entirely of composite material and stores hydrogen up to 700 bar [9, 10]. Type 5 vessels are not yet commercially available. The vessel is a modification to a type 4 vessel with reinforcing space-filling skeletons. They have higher strength and are thus designed to store hydrogen at higher volumetric and gravimetric densities [9, 10].

2.2.1.2. Liquid hydrogen

As discussed in subsection 2.1.1, hydrogen has a much higher density and thus volumetric energy density when liquefied [10, 13, 27, 29]. This is the main advantage as the storage vessel is reduced to an acceptable volume. Furthermore, the storage is performed at low pressures, so thin and cheap storage tanks can be used [10]. However, the main disadvantage is the low boiling point of hydrogen. First of all, the cost of liquefaction of hydrogen is about 30-40% of its net heating value [2, 3, 5, 9, 10, 13, 29]. Secondly, the vessel must be well isolated to prevent boil-off due to heat entering from the surroundings [2, 5, 13, 27, 29]. The insulation of the vessel will increase its weight and thus reduce the gravimetric energy density of the storage unit. An ortho-to para-hydrogen conversion is also necessary before storage to prevent boil-off [7, 29].

2.2.1.3. Cold/Cryo compression

This technique combines high-pressure hydrogen in the gas phase with liquid hydrogen [2, 29]. The hydrogen is stored at cryogenic temperatures and a pressure of 250-350 bar [9]. This increases the density of the hydrogen and reduces the boil-off losses [7, 29]. This technique requires the usage of type 3 vessels and increased energy input.

2.2.2. Adsorption

This technique, also called physisorption of hydrogen, stores hydrogen reversibly and physically in the absorbed form [7, 9]. The hydrogen is absorbed on the surface of solids following van der Waals interaction or dispersive forces [7]. The adsorbed hydrogen can quickly be loaded and unloaded. The enthalpy of adsorption/desorption is only 1-10 kJ/mol, meaning the heat transfer problems are easily managed [2]. Furthermore, there are no losses due to the formation of byproducts. Adsorption happens at the surface of a material; hence, a high surface area is an essential factor [30]. Suitable materials for hydrogen adsorption are microporous carbon structures, metal-organic frameworks, and zeolites [9, 28, 30]. At room temperature, the capacity of physical absorbents is low. The storage capacity increases with decreasing temperature and increasing pressure; cryogenic temperatures and high pressures up to 100 bar are necessary [2, 7, 26]. Boil-off losses, as discussed in subsubsection 2.2.1.2, also occur when hydrogen is adsorbed at cryogenic temperatures.

2.2.3. Chemical storage

The chemical storage chapter is divided into two sub-chapters: metal hydrides and chemical hydrides.

2.2.3.1. Metal hydrides

This technique uses metallic alloys acting like sponges absorbing gaseous hydrogen [5]. Hydrogen is absorbed into the solid metal at high pressures, releasing heat, while the hydrogen is released by applying heat to the metal and by reducing the pressure [30]. The hydrogen molecules are first absorbed on the surface of the metal before being dissociated into strongly chemisorbed individual hydrogen atoms [9, 29]. This bond is much stronger than the van der Waals interaction used for hydrogen adsorption.

The chemisorption of the hydrogen may lead to an expansion of the metal lattice of 20-30% [9]. Metal hydrides have a high hydrogen density per volume, higher than the volumetric hydrogen density of liquid hydrogen [9, 10, 29] while also storing the hydrogen at moderate temperatures and pressures. Moreover, the loading and unloading of the metal hydrides can be repeated infinitely without loss of storage capacity if no impurities are present [5, 9]. However, metal hydrides also have drawbacks. The kinetics of the hydrogen release are low, while the hydrogen release temperature is high [2, 28]. Also, undesirable gases can be formed during the release.

2.2.3.2. Chemical hydrides

Chemical hydrides are hydrogen-deficient organic elements [10]. They can be dehydrogenated and hydrogenated and are thus a form of hydrogen storage [7]. Their main advantage is that they are generally liquids at normal conditions [26]. This simplifies their transport and storage as well as heat and mass transfer. Some suggested chemical hydrides are bulk chemicals such as methanol, ammonia, and formic acid [26]. Their utility goes beyond storage. The vast experience with these chemicals is advantageous because the required equipment for production, handling, and transport is already in place [10]. The main advantages are the high volumetric energy density of the hydrogenated hydrides and their properties at ambient conditions, leading to efficient transportation over long distances. The main disadvantage is the necessary energy input needed for hydrogenation and dehydrogenation.

2.3. Double membrane gas-holder

Double membrane gasholders are a type of low-pressure gas storage structure, most commonly used for the storage of biogas [4]. Two variants of the double membrane gasholder exist: the independent double membrane gasholder and the double membrane gasholder placed on top of digesters [31]. The latter is also known as a tank rim-mounted double membrane gasholder. While conventional gasholders are made of steel, the double membrane gasholder is made of polymers, increasing its overall performance [31]. The main advantages of double membrane gasholders are due to the foldability of the membrane material. The gasholder is easily transported and can handle pressures smaller than 1 atm [31]. Traditional steel gasholders could collapse under such circumstances.

Additionally, the primary material of the membrane is made of fluoride which is an excellent protection against natural aging. It offers protection against ultraviolet rays, microorganisms and severe weather conditions [31–34]. Combined with good corrosion resistance, this allows for a long lifespan of the gasholder. On the other, the main disadvantages of the double membrane gasholder are the fact that it needs a power supply and the fact that the gas is not stored at high pressures, meaning that in most use cases, an extra pressurisation step is required after storage [31].

The double membrane gasholder is a relatively simple structure; see Figure 2.6. It consists of a membrane body composed of two membranes and supplementary parts. The membranes delimit two compartments; the compartment underneath the inner membrane stores the gas, while the compartment formed between the inner and outer membrane is filled with air [33]. The air compartment regulates the pressure in the gas compartment and helps support the outer membrane to overcome pressures due to snow or wind [31]. Both membranes are free to move. Thus, when the volume of stored gas increases, the volume of the air compartment decreases and vice versa. When the stored gas reaches its maximum volume, all excess gas is vented through a pressure relief valve. This avoids overpressures in the gas compartment, which can damage the inner membrane. The air compressor and air relief valve are used to adjust the pressure in the gas compartment and to maintain the rigidity of the outer membrane. A double membrane gasholder typically operates at about 1 kPa above atmospheric pressure to extend its lifetime, as this pressure range aligns with the mechanical properties of the gas holder materials [31]. Therefore, the double membrane gasholder needs a pressure control system. Although pressures up to 5 kPa are possible. The minimum required pressure is 0.2 kPa; below this pressure, the outer membrane claps in the wind [33]. Additional membranes may be added to the double membrane gasholder, creating additional compartments. Such storage systems are called multi-membrane gasholders. They operate similarly and under similar circumstances as the double membrane gasholder [35].

2.3.1. Modelling of a double membrane gasholder

Multiple studies by different authors have been conducted to increase the storage efficiency of the double membrane gasholder. All studies are though directed towards using a double membrane gasholder

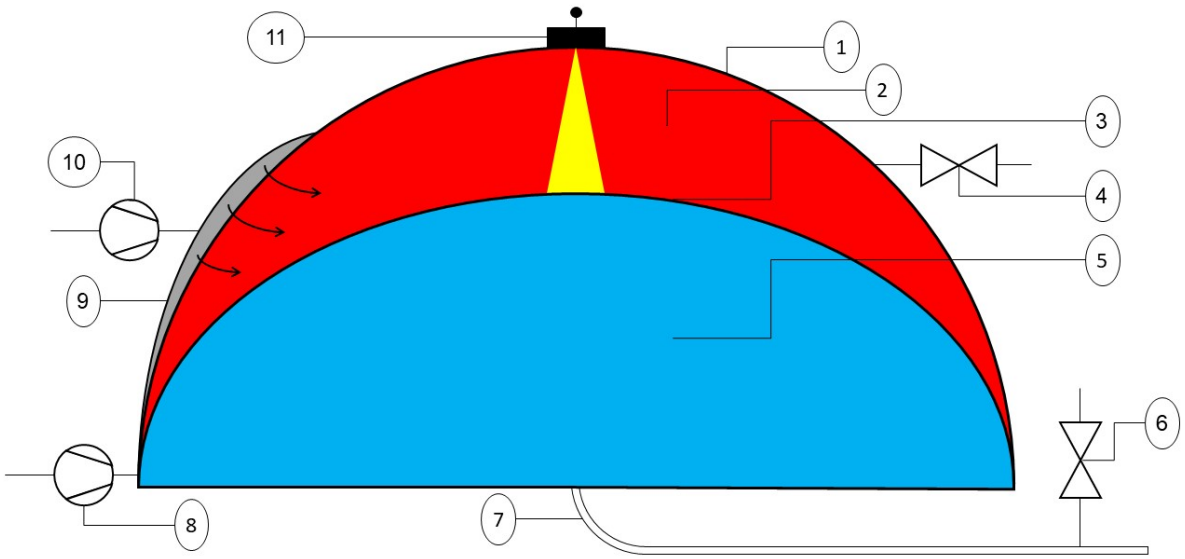

Figure 2.6: Schematic diagram of the composition of a double membrane gasholder, reproduced from [31] 1- Outer membrane 2- Air chamber 3- Inner membrane 4- Air relief valve 5- Gas chamber 6- Gas relief valve 7- Gas drainage pipe 8- Compressor gas inlet 9- Air supply passage 10- Compressor air inlet 11- Ultrasonic probe

in combination with anaerobic digestion. Kube [33] focuses on designing the pressure regulation system of a single double membrane gasholder and managing a whole system of interconnected storages. He elaborates on determining the pressure gradient between storages in different scenarios. Ahmadi et al. [35] set up an anaerobic digester's flexible and configuration-dependent heat model framework. Each part of the gasholder was associated with an energy balance including convection, conduction, radiation and longwave infrared heat losses. The same was done by Avila-Lopez et al. [36]. At last, Yuki-Junoir et al. [4] set up an anaerobic digester's mass and energy balances, including a double membrane gasholder, creating a numerical tool for dynamic simulation. This permitted the simulation of the storage behaviour during inflation, full load and deflation operation states.

As mentioned earlier, none of the studies aim to use the double membrane gasholder as a hydrogen storage method. Furthermore, although multiple energy balances have been set up, none seemed complete. The boundary work, done by the expansion or compression of the different compartments, has not been included in any of the studies. If the volume variations are significant enough, the work term can influence the outcome of the energy balance. Moreover, the condensation term of the water present in the compartments was also never mentioned. Again, adding this term could lead to a different outcome of the energy balance. Finally, none of the works have considered the permeation of various molecules through the membranes due to a difference in the chemical potential of the molecules in different compartments.

2.3.2. Membrane gas separation

A membrane for gas separation is an interphase between two gasses. It acts as a selective barrier, regulating the transport of gases among gas mixtures [37, 38]. The feed flows over the membrane. Part of the gas permeates through the membrane. This is called the permeate. Another gas can sweep the permeated gas, although this is not necessary. The fraction of the gas mixture that does not pass through the membrane is called the retentate [38]. Figure 2.7 shows a schematic representation of a membrane.

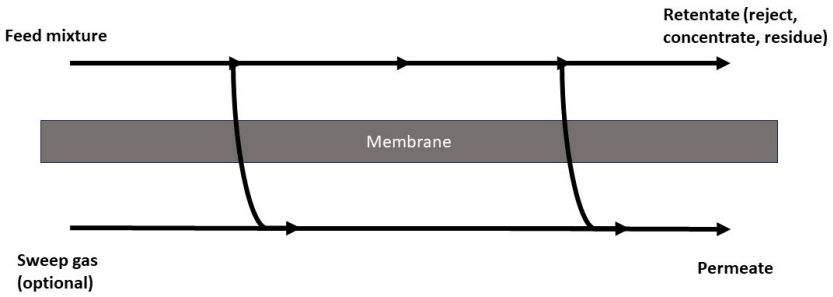

Figure 2.7: Schematic representation of a membrane

Gas separation membranes are used to separate gasses from a gas mixture when the particle diameter is several Ångström (Å, 10^{-10}m) while the difference in particle sizes is minimal. There are multiple mechanisms for gas permeation; see Figure 2.8. The mechanism depends on the type of membrane (porous vs dense) and, if present, the size of the pores in the membrane. When the pores of a porous membrane range from 0.1-10 μm, gasses permeate the membrane via convective flow; no separation occurs [39]. For pores smaller than 0.1 μm, the pore diameter is as large or smaller than the mean free path of the gas molecules. Knudsen diffusion is the governing diffusion mechanism. The transport rate of a gas is inversely proportional to the square root of its molecular weight [39, 40], meaning low molecular weight gasses diffuse faster than heavier ones. At last, when the pores of the membrane are extremely small (5-20 Å), the permeation mechanism is achieved by molecular sieving. This kind of transport includes both diffusion in the gas phase and surface diffusion, the diffusion of an absorbed species on the surface of the pores [39, 41]. The pores are small enough so large molecules cannot pass through the membrane, and thus, separation occurs [37, 40].

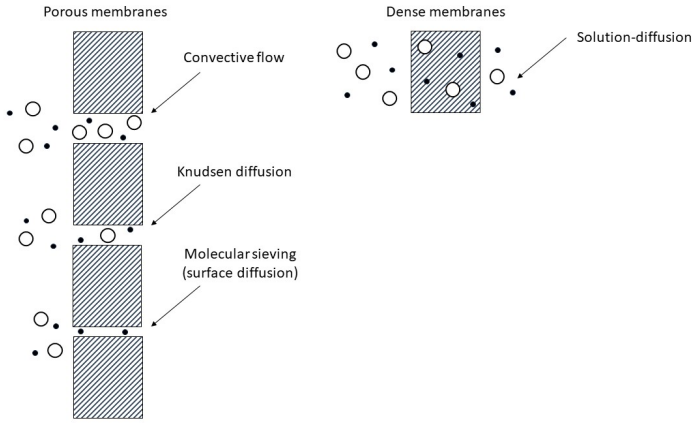

Figure 2.8: Mechanisms for the permeation of gasses through porous and dense gas separation membranes, reproduced from [39]

For a dense membrane, molecules can't pass directly between the polymer chains in contrast to a porous membrane [37]. The separation through dense membranes happens through the solution diffusion mechanism [39, 41–43]. There are three steps in the solution diffusion model, Figure 2.9. First, the molecules are absorbed at the boundary between the feed and the membrane. Then, the activated diffusion through the membrane follows. The diffusion depends on the polymer's free volume [41, 44]. The molecules' desorption or evaporation on the membrane's other side is the last step [37, 40, 45]. The driving force behind the solution diffusion mechanism is the difference in chemical potential between the feed and the permeate [40, 42]. Molecules will diffuse from a high chemical potential region to a low chemical potential region. The solution diffusion model assumes that the fluids on both sides of the membrane are in equilibrium with the interface of the membrane material [42]. Therefore, the chemical potential gradient must be continuous throughout the membrane. Furthermore, the model assumes that the pressure inside the membrane is uniform and that the concentration gradient across

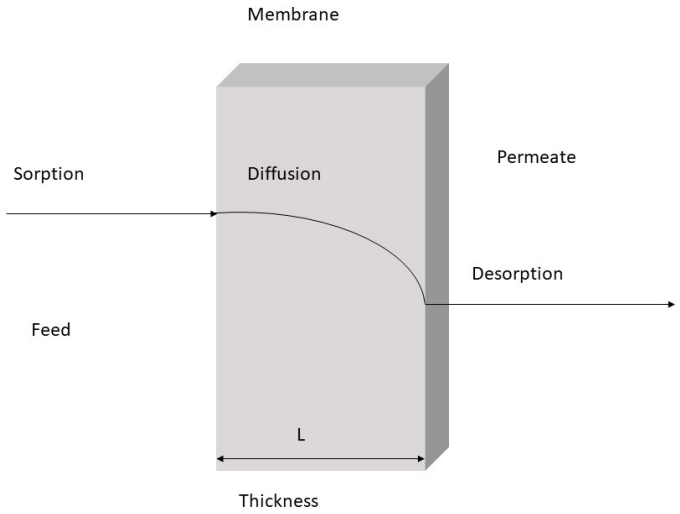

Figure 2.9: Solution diffusion mechanism, reproduced from [40]

the membrane represents the chemical potential gradient [40, 42].

Using the above assumptions, the permeated gas through the solution diffusion mechanism can be quantitatively measured using Fick's first law of diffusion and rewritten into Equation 2.2 [42, 43, 46]. The derivation can be found in Baker [42].

$$J_{\mathrm{i}} = P_{\mathrm{i}} \frac{p_{\mathrm{i_f}} - p_{\mathrm{i_p}}}{\delta} \tag{2.2}$$

Here J_i is the flux of the gas i [cm^3 (STP) of component i/(cm^2 s)], which represents the volume of gas transported through the membrane per area of membrane per second. While p_i is the partial pressure of component i [cmHg], the f and p subscript represent the feed and permeate side of the membrane. Here, cmHg is a pressure unit called centimetres of mercury. It represents the pressure pushing down due to the gravity of any volume of liquid mercury, which is 1cm high at 0 °C. While P_i is the permeability coefficient [cm^3 (STP) cm/(cm^2 s cmHg)]. In literature, its unit is commonly Barrer. The SI unit for permeability is mol (STP) m/(m^2 s Pa). The conversion of the three units can be found below.

$$1\ \text{Barrer} = 10^{-10} \frac{\text{cm}^3\ (\text{STP})\ \text{cm}}{\text{cm}^2\ \text{s cmHg}} = 3.348 \times 10^{-16} \frac{\text{mol}\ (\text{STP})\ \text{m}}{\text{m}^2\ \text{s Pa}}$$

The permeability coefficient of a membrane can be expressed as the product of the solubility coefficient (mol (STP)/ (m^3 Pa)) and the diffusion coefficient (m^2/s), Equation 2.3 [42, 43].

$$P_{\mathrm{i}} = D_{\mathrm{i}} S_{\mathrm{i}} \tag{2.3}$$

The membrane's selectivity is used as a metric to measure the separation performance of a membrane between gas A and gas B [39, 42, 43]. It is defined as the ratio of the permeability coefficient of gas A over gas B, Equation 2.4.

$$\alpha_{\mathrm{A/B}} = \frac{P_{\mathrm{A}}}{P_{\mathrm{B}}} = \frac{D_{\mathrm{A}}}{D_{\mathrm{B}}} \frac{S_{\mathrm{A}}}{S_{\mathrm{B}}} \tag{2.4}$$

The diffusivity ratio is the selectivity towards mobility, reflecting the different sizes of the two molecules [39]. The solubility ratio reflects the relative condensability of the two gases. If the mobility selectivity ratio is dominant, the membrane favours the passage of small molecules. In contrast, when the solubility term is dominant, the membrane favours the passages of large and more condensable molecules [39].

2.3.3. Influence of external factors on the permeation properties of membranes

The temperature of the polymer membrane greatly influences the magnitude of the mobility selectivity term. The difference in solubility coefficient (S_i) is far less marked [47]. If a polymer is below its glass transition temperature (T_g), it is considered as 'glassy', and the polymer is rigid [39]. With increasing temperature, the flexibility and mobility of the polymer chains increase, increasing the free volume in the polymer and thus the mobility selectivity term [41]. The polymer takes a flexible 'rubbery' state above its glass transition temperature [39]. It is thus clear that the transport parameters of a membrane are temperature-dependent [43]. This is also seen in the fact that permeability, diffusivity and solubility are typically all described by Arrhenius- van 't Hoff equations in case the polymer does not undergo a phase transition [41, 43, 47, 48]. Pressure can also influence permeation properties. However, as long as the pressure variations stay in a reasonable range (about 10 atm), the permeability of gases in rubbery or glassy polymers is unaffected [41]. This is far above the operating range of a double-membrane gasholder; see section 2.3. The presence of water in a gaseous mixture leads to increasing permeability in some hydrophilic polymers [44, 48]. A hydrophilic polymer will take up some condensated water, causing swelling. This will increase the free volume of the polymer. A hydrophobic polymer is naturally water-repellent and is thus not affected.

2.3.4. Permeability of hydrogen in polymers

There is a lot of interest in the permeability of hydrogen through polymers. Mainly because specific polymers, such as PVC, are considered future materials for hydrogen transport [44, 49]. The requirements for hydrogen transportation are similar to those for hydrogen storage: minimise leakage and degradation. Both Kane [44] and Hermkens & Jansma [49] found no mechanism for the degradation of polymers in the presence of hydrogen unless some other reaction catalyst, such as heat, humidity, or radiation source is present. In the tables below, some data on hydrogen permeability through polymers is presented; more data can be found in Kane [44], San Marchi [50] and Tanaka et al. [51].

Table 2.1: Hydrogen permeability for some common plastics, reproduced from [50].

Material	Temperature (K)	Permeability 10^9 / [$\frac{\text{mol·H}_2}{\text{m·s·MPa}}$]
LDPE	298	3.3
PP	293	13.8
PS	298	7.58
PMMA	308	1.24
PVC	298	0.58
PTFE	298	3.3
PVF	308	0.18

Table 2.2: Relationships for the temperature dependence of hydrogen transport properties for some common polymers, reproduced from [50].

Material	Temperature range (K)	Pre exponential factor P_0 10^3 / [$\frac{\text{mol·H}_2}{\text{m·s·MPa}}$]	Activation energy of permeation / [$\frac{\text{kJ}}{\text{mol}}$]
PP	298 - 343	99.9	38.5
PVC	298 - 353	0.651	34.5
PTFE	293 - 403	0.0185	21.4
Poly(butadiene)	298 - 323	0.959	27.6
Neoprene	288 - 323	3.93	33.9

2.3.5. Experimental determination of the permeability coefficient

Several techniques are available to determine the permeability coefficient of a gas in a polymeric material. All methods clamp the membrane in a module, ensuring the only possible fluid flow is through the membrane. The most straightforward approach is static permeation with pure penetrants [48].

Here, the feed consists of a pure gas at high pressure, which permeates through the membrane to a low-pressure chamber filled with the same gas. The flux is determined by keeping the chamber at a constant volume and measuring the increasing pressure or by holding the chamber at a constant pressure and determining the volume increase [48]. Keeping the pressure constant provides a stable flux through the membrane. However, it may seem contradictory to let the pressure at the permeate side increase as this will lead to an unsteady flow. Still, if the pressure variations are negligible with respect to the pressure difference over the membrane, pseudo-steady state conditions can be reached. Another static method considers equal pressure but different concentrations at the feed and permeate side. An initial concentration gradient over the membrane is set. Permeability can be calculated by determining the concentration at the permeate side over time [48]. Again, the measurements proceed in an intrinsic non-steady mode as the concentration gradient varies over time. Nevertheless, pseudo-steady state conditions can be reached if the concentration at the permeate side remains sufficiently small enough to neglect the effect on the driving force reduction. There are also multiple dynamic permeation techniques available. These techniques employ a sweeping gas at the permeate side. The permeability follows from the mass balance and concentrations of the sweep gas [48]. The composition of the permeate stream is usually determined by mass spectrometry or gas chromatography [48]. Specific sensors may also be used if the permeability of a particular penetrant must be determined.

3

Goal & System description

The literature review aimed to determine the critical parameters related to hydrogen storage and the import aspects of membrane gasholders. The first important finding is that at standard conditions, the ideal gas law can be used to predict the behaviour of hydrogen.

The literature study found that hydrogen is a difficult substance to store due to its properties. The first is its very low volumetric energy density; hydrogen is a gas under most conditions. This leads to difficulties in storing large amounts of hydrogen in pure form. Current forms of storage are either under extremely high pressure or at extremely low temperatures or use chemical interactions between hydrogen and another substance. Storage of pure hydrogen at atmospheric conditions is an unconventional way of storage. The last was also affirmed in section 2.3. Here, it was found that membrane gasholders are usually used to store biogas. Using them to store hydrogen can be considered a novelty.

The research on modelling membrane gasholders has focused chiefly on the thermal management of biogas storage. None of the studied papers mentioned the permeation of molecules through the polymer membranes. The permeation of hydrogen or other gases through the membranes of the gasholder can significantly impact the storage's safety. It was found in subsection 2.1.2 that the flammability range of hydrogen is extensive. The permeation of hydrogen to the air compartment or oxygen to the hydrogen gas compartment can lead to a flammable or explosive mixture. Therefore, the permeation through the membranes has to be studied. The driving force for permeation is a difference in chemical potential between the fluids on either side of the membrane. This can be translated into a difference in the partial pressure of each substance. Consequently, the pressure and composition of each compartment must be known at every instance to construct a complete model.

The study into permeation through polymer membranes also showed that hydrogen does not lead to the degradation of the membranes. The hydrogen embrittlement phenomenon discussed in subsection 2.1.3 can thus be disregarded.

This research will focus on extending prior research by modelling a double membrane gasholder for hydrogen storage. This is an innovation; gasholders operate around atmospheric pressure, an unconventional storage pressure for gaseous hydrogen. Furthermore, gasholders are not commonly used to store hydrogen but natural gas. The main function of the storage is to serve as a buffer for the downstream compressor station. The electrolyser system is directly coupled to a solar park, leading to intermittent hydrogen production. The compressor has a constant inlet debit. It is turned on when the storage reaches its maximum capacity and turned off when fully drained. This mode of operation minimises the power cycling of the compressor. The main goal of this work is to ensure that the envisioned storage, a double membrane gasholder, is a suitable option for integrating into this process. The main research question is: "Does the design and operation of double membrane gasholders meet the requirements for efficient and reliable hydrogen storage under dynamic storage conditions?". This question will be answered by building a model in Python. This will be a 0-D model. This tool should be able to predict the behaviour of the storage as a reaction to weather circumstances and the intermittent production and demand of hydrogen. By enabling the tool for different weather input data, it can be used for various locations to facilitate informed decision-making regarding the storage facility. The tool will contain the appropriate mass and energy balances for the components of the gasholder. The mass balances, taken around the air/gas compartments, will consider all matter entering and exiting

each compartment, including the fluxes due to the membrane permeation. The energy balances will be taken for the compartments and the membranes. They will include energy transfer due to mass transport, thermodynamic work and heat transfer (conduction, convection and radiation). These balances provide a comprehensive understanding of the system dynamics, allowing for informed decision-making in system design and operation. The permeation through the membranes is an important factor to consider regarding the purity and safety of the storage. Due to the amount of considered gasses, multicomponent diffusion will be considered. Maxwell-Stefan diffusion is used to describe the permeation of molecules through the membranes. The outcoming results will indicate for which time interval the hydrogen can be stored before the purity of the hydrogen is compromised due to the permeation of other types of molecules. This will ultimately lead to the correct and optimised management of the produced hydrogen by XINTC for direct use or storage.

3.1. System description

The model will be built around a single gasholder. It is based on Figure 2.6, but a few simplifications have been made. First, only the air and gas chambers were considered, and the storage floor was assumed to be made out of concrete. The additional volume of the air supply passage or the gas drainage pipe has been neglected. Therefore, the volume of the gasholder is the sum of the air and gas compartments. It has also been assumed the outer membrane is rigid. This means that the total volume of the storage is constant, proving a relation between the volume of the components. Although, when fully blown up, the compartments are semi-ellipsoidal in reality, they are seen as hemispherical here to facilitate volume and area calculations. At last, possible folds in the membrane have been neglected. It has been assumed that the full surface area of the membrane is in contact with the gas compartments. The above assumptions facilitate the modelling of the gasholder but possibly make the results deviate from reality.

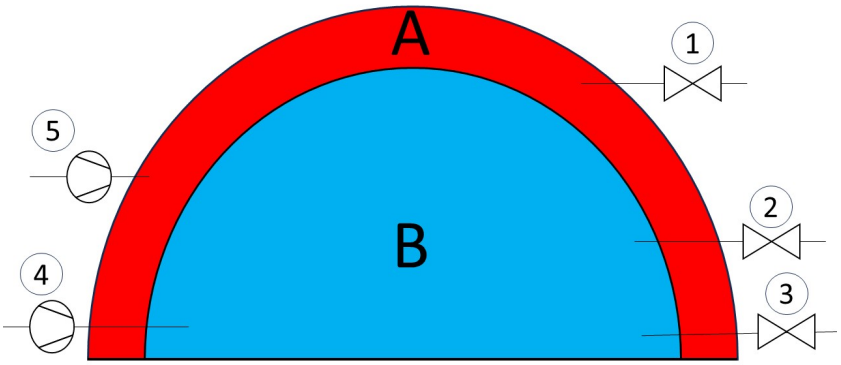

Figure 3.1: Simplification of the double membrane gasholder. 1- Air relief valve 2- Hydrogen relief valve 3- Hydrogen outlet valve 4- Hydrogen compressor 5- Air compressor A- Air compartment B- hydrogen compartment

From now on, the air and hydrogen compartments will often be called compartments A and B, respectively; see Figure 3.1. The company provided the storage capacity of the gasholder: 400 m^3. This is also the maximum volume of compartment B. This leads to a radius of around 5.76 m of compartment B and an inner membrane area of around 208 m^2. Compartment A has been assumed to have a radius of 5.9 m, leading to a maximum volume of around 430 m^3 and an outer membrane area of 218 m^2.

Furthermore, it has been assumed that the minimum volume of compartment B is 5% of its maximum volume or 20 m^3. The company provided the thickness of the membranes: 0.8 mm and 1.1 mm for the inner and outer membranes, respectively. The maximum allowed pressure in compartment A was assumed to be 141325 Pa, while a slightly higher pressure is allowed in compartment B: 151325 Pa.

4

Derivation of the differential equations describing the gasholder system

4.1. Mass Balance

The mass balances are taken around the control volumes delimited by the gas compartments A and B; see Figure 4.1a and Figure 4.1b. Due to condensation, two phases may form in the control volumes: gas and liquid. The mass balances are written for every molecule considered in the system. The general mass balances can be rewritten considering every molecule.

$$\frac{dN^{\mathrm{A}}}{dt} = \sum_{i=1}^{\mathrm{N}} \frac{dN_i^{\mathrm{A}}}{dt} \tag{4.1}$$

$$\frac{dN^{\mathrm{B}}}{dt} = \sum_{i=1}^{\mathrm{N}} \frac{dN_i^{\mathrm{B}}}{dt} \tag{4.2}$$

Here, N indicates the number of moles in the system, while the superscripts indicate the control volume considered. The subscript i indicates the considered molecule. Due to condensation, two phases may form in the control volumes: gas and liquid. It is assumed that the mol flows through the different valves and the membranes consist solely of gas, meaning the liquid phase does not permeate through the membranes. In reality, the condensed water could form suspended water droplets in the gas and thus be pulled along by the gas. It is very difficult to assess the amount of water being dragged

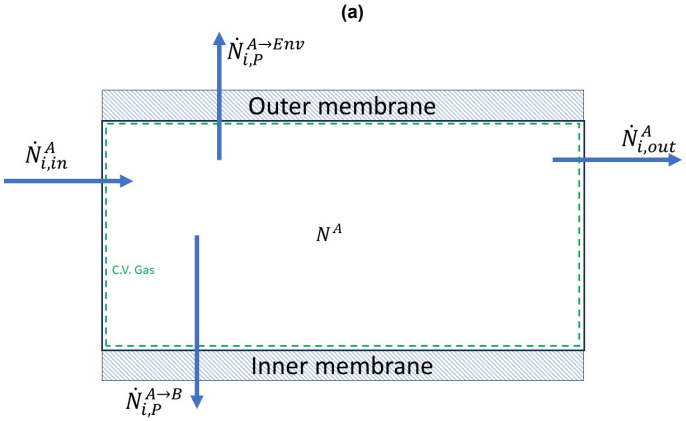

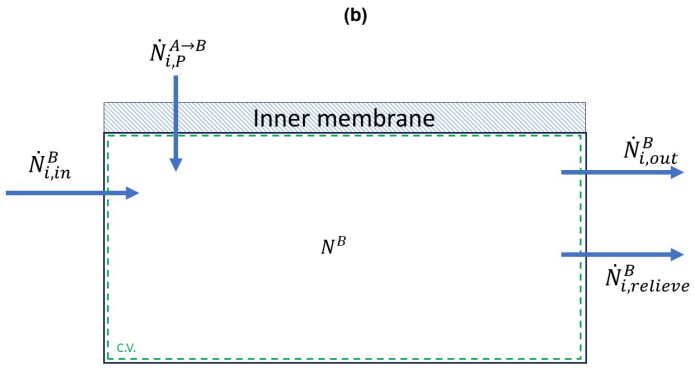

Figure 4.1: (a) Control volume of gas compartment A, the arrows indicate the chosen direction of permeation; (b) Control volume of gas compartment B, the arrows indicate the chosen direction of permeation

along. Therefore, this phenomenon has been neglected. Furthermore, it has been assumed that the liquid fraction is very small compared to the gas fraction. It has been assumed that only liquid droplets are present in the system in the system. One could thus say that the area of contact between the liquid droplets and the gas phase is much larger than the volume of the liquid phase. The temperature of the liquid phase will thus rapidly adapt to the temperature of the gas phase. The temperature of the two phases has been taken as equal. Therefore, the gas and liquid phases are part of the same control volume. The following balances can be set up.

$$\frac{dN_i^{\mathrm{A}}}{dt} = \dot{N}_{i,\mathrm{in}}^{\mathrm{A}} - \dot{N}_{i,\mathrm{out}}^{\mathrm{A}} - \dot{N}_{i,\mathrm{P}}^{\mathrm{A}\to\mathbf{B}} - \dot{N}_{i,\mathrm{P}}^{\mathrm{A}\to\mathrm{Env}} \tag{4.3}$$

$$\frac{dN_i^{\mathrm{B}}}{dt} = \dot{N}_{i,\mathrm{in}}^{\mathrm{B}} - \dot{N}_{i,\mathrm{out}}^{\mathrm{B}} - \dot{N}_{i,\mathrm{relieve}}^{\mathrm{B}} + \dot{N}_{i,\mathrm{P}}^{\mathrm{A}\to\mathbf{B}} \tag{4.4}$$

Here, $\dot{N}$ indicates a mol flow [mol/s]. The in, out, and relief subscripts indicate the inlets through the compressors and the outlets through the valves. Subscript P indicates that the mol flow is due to permeation, while the associated superscripts indicate the permeation direction.

4.1.1. Gas permeation

Due to concentration and pressure gradients over the membranes considered in the system, permeation of the considered molecules is prone to happen. For permeation, N_2, O_2 and H_2 are considered. The H_2O has been left out in the gas and liquid phase. The mole fraction of H_2O in the system is assumed to be very small. Leading to extremely low gradients, and consequently, the permeation flux will also be negligible. The system for permeation will consist of four components: a membrane and three gasses. Fick's law describing conventional mass transfer is incomplete, leading to wrong predictions in multicomponent systems [52]. Maxwell-Stefan diffusion applies to multicomponent systems. It takes into consideration the intermolecular influence of the permeating species. When molecules diffuse at different speeds, friction occurs between the species, altering the resulting diffusion speed. The Maxwell-Stefan equation takes these frictions into account. The theory starts with the momentum balance, which considers the driving forces and the intermolecular friction.

$$F_{i,\mathrm{tot}} = F_i + F_{i,\mathrm{F}} \tag{4.5}$$

Here, $F_{i,\mathrm{tot}}$ is the total force on the molecules [N/mol], F_i is the driving force on the molecules [N/mol], and $F_{i,\mathrm{F}}$ is the friction force on the molecules. The theory then assumes that diffusion occurs in a steady state, meaning the sum of the momentum balance, $F_{i,\mathrm{tot}}$, becomes zero, leading to the following equality. Here, the friction force has already been opened up.

$$F_i = \sum_{j\neq i} \zeta_{i,j} x_j (u_i - u_j) \tag{4.6}$$

Here, $\zeta_{i,j}$ [N s/(mol m)] is the friction coefficient between species i and j, x_j is the mol fraction of species j and u [m/s] is the diffusive species velocity. The driving force is, just as in Fick's law, the negative gradient of the total potential, which can consist of multiple contributions.

$$F_i = -\frac{d\psi_i}{dz} \tag{4.7}$$

The total potential is symbolised by ψ [J/mol] while z [m] is the interphase thickness. To keep things simple, the diffusion is considered one-dimensional, and the flow near interfaces assumes the film model. This means that there only is a potential gradient over the film. Equation 4.6 is simplified to the difference form of the Maxwell-Stefan equation.

$$-\frac{\Delta\psi_i}{\Delta z} = \sum_{j\neq i} \zeta_{i,j}\overline{x}_j(\overline{u}_i - \overline{u}_j) \tag{4.8}$$

Here, the average values, indicated by the overline, over the film thickness, Δz, are used. The Maxwell-Stefan equation can also be rewritten using the species fluxes instead of the species velocities using $J_i = u_i c x_i$.

$$-\frac{\Delta\psi_i}{\Delta z}\overline{x}_i\overline{c} = \sum_{j\neq i} \zeta_{i,j}(\overline{x}_j J_i - \overline{x}_i J_j) \tag{4.9}$$

The flux of the species with respect to the interphase is J [mol/m^{2}s], and $\overline{c}$ [mol/m^3] is the average molar concentration. The above equation is for an isothermal process. Often, in reality, a temperature gradient exists within the diffusional film. Extra thermal diffusion terms should be added to the Maxwell-Stefan equation to account for this gradient. However, these terms are small and will, therefore, be neglected. The driving force remains the potential gradient but is taken at a constant temperature. For the difference form of the Maxwell-Stefan equation, this means that the average temperature of the film is used. The thermal diffusion terms are also present in the energy transfer over the film but are again neglected. The driving force in the Maxwell-Stefan equation is system-dependent and can consist of multiple contributions, such as the activity, electrical, pressure, centrifugal, gravitational, or magnetic forces. Only the activity and pressure forces play a role in the membrane permeation in the considered system. The gravitational forces have been neglected. The activity and pressure forces can be combined into a single force containing the species' partial pressure gradient.

$$\underbrace{-RT\frac{d\ln x_i}{dz}}_{\text{activity force}}\ \underbrace{-V_i\frac{dP}{dz}}_{\text{pressure force}} = -RT\left[\frac{1}{x_i}\frac{dx_i}{dz} + \frac{1}{P}\frac{dP}{dz}\right] = -\frac{RT}{p_i}\frac{dp_i}{dz} \tag{4.10}$$

Here, R is the gas constant [J/(mol K)], T is the temperature [K], x_i is the mol fraction of species i, V_i the volume [m^3] of species i, P the pressure [Pa], p_i the partial pressure [Pa] of species i and z the thickness of the film. The difference form of Equation 4.10 becomes:

$$-\frac{RT}{\overline{p_i}}\frac{\Delta p_i}{\Delta z} \tag{4.11}$$

A membrane is a solid matrix. It is not considered as part of the mixture. Furthermore, it is stagnant, meaning its flux is equal to zero. The difference equation for membrane permeation becomes

$$-\overline{x}_i\overline{c}\frac{RT}{\overline{p_i}}\frac{\Delta p_i}{\Delta z} = \sum_{\substack{j\neq i\\ j\neq M}} \zeta_{i,j}(\overline{x}_j J_i - \overline{x}_i J_j) + \zeta_{i,M} J_i \tag{4.12}$$

Here, the subscript M denotes the membrane. Introducing the Maxwell-Stefan diffusivity, Đ$_{i,j}$ [m^2/s] and the mass transfer coefficient, $k_{i,j}$ [m/s].

$$\text{Đ}_{i,j} = \frac{RT}{\zeta_{i,j}} \qquad k_{i,j} = \frac{\text{Đ}_{i,j}}{\Delta z} \tag{4.13}$$

Equation 4.12 can be rewritten as:

$$-\overline{x}_i\frac{\Delta p_i}{\overline{p}_i} = \sum_{\substack{j\neq i\\ j\neq M}} \frac{\overline{x}_j J_i - \overline{x}_i J_j}{k_{i,j}\overline{c}} + \frac{J_i}{k_{i,M}\overline{c}} \tag{4.14}$$

For a gas mixture consisting of N_2, O_2, and H_2 permeating to a polymer membrane, this gives the following set of equations.

$$\begin{aligned}
-\overline{x}_{\mathsf{N}_2}\frac{\Delta p_{\mathsf{N}_2}}{\overline{p}_{\mathsf{N}_2}} &= \frac{\overline{x}_{\mathsf{O}_2}J_{\mathsf{N}_2}-\overline{x}_{\mathsf{N}_2}J_{\mathsf{O}_2}}{k_{\mathsf{N}_2,\mathsf{O}_2}\overline{c}}+\frac{\overline{x}_{\mathsf{H}_2}J_{\mathsf{N}_2}-\overline{x}_{\mathsf{N}_2}J_{\mathsf{H}_2}}{k_{\mathsf{N}_2,\mathsf{H}_2}\overline{c}}+\frac{J_{\mathsf{N}_2}}{k_{\mathsf{N}_2,M}\overline{c}}\\
-\overline{x}_{\mathsf{O}_2}\frac{\Delta p_{\mathsf{O}_2}}{\overline{p}_{\mathsf{O}_2}} &= \frac{\overline{x}_{\mathsf{N}_2}J_{\mathsf{O}_2}-\overline{x}_{\mathsf{O}_2}J_{\mathsf{N}_2}}{k_{\mathsf{O}_2,\mathsf{N}_2}\overline{c}}+\frac{\overline{x}_{\mathsf{H}_2}J_{\mathsf{O}_2}-\overline{x}_{\mathsf{O}_2}J_{\mathsf{H}_2}}{k_{\mathsf{O}_2,\mathsf{H}_2}\overline{c}}+\frac{J_{\mathsf{O}_2}}{k_{\mathsf{O}_2,M}\overline{c}}\\
-\overline{x}_{\mathsf{H}_2}\frac{\Delta p_{\mathsf{H}_2}}{\overline{p}_{\mathsf{H}_2}} &= \frac{\overline{x}_{\mathsf{N}_2}J_{\mathsf{H}_2}-\overline{x}_{\mathsf{H}_2}J_{\mathsf{N}_2}}{k_{\mathsf{H}_2,\mathsf{N}_2}\overline{c}}+\frac{\overline{x}_{\mathsf{O}_2}J_{\mathsf{H}_2}-\overline{x}_{\mathsf{H}_2}J_{\mathsf{O}_2}}{k_{\mathsf{H}_2,\mathsf{O}_2}\overline{c}}+\frac{J_{\mathsf{H}_2}}{k_{\mathsf{H}_2,M}\overline{c}}
\end{aligned} \tag{4.15}$$

Equation 4.15 is a set of three equations containing three unknowns: the molecule fluxes. This set needs to be solved with different input parameters for the inner and outer membranes. The friction between the permeating molecules is often neglected when considering Maxwell-Stefan diffusion through polymer membranes. The terms have minimal influence on the fluxes [52].

$$\dot{N}_{i,\mathsf{M}}^{\mathsf{inner}} = J_{i,\mathsf{M}}^{\mathsf{inner}} \times A_{\mathsf{M}}^{\mathsf{inner}} \tag{4.16}$$

$$\dot{N}_{i,\mathsf{M}}^{\mathsf{outer}} = J_{i,\mathsf{M}}^{\mathsf{outer}} \times A_{\mathsf{M}}^{\mathsf{outer}} \tag{4.17}$$

The resulting molflows per molecule can be determined using the above equations. Here, A_{M} represents the area [m^2] of the inner or outer membrane.

4.1.1.1. Maxwell-Stefan diffusion coefficients

To solve Equation 4.15 for the fluxes of the components, the Maxwell-Stefan diffusivities Đ must be known. The major problem with multicomponent mass transfer is that these are often unavailable. Most data is reported as Fick diffusivities for binary mixtures [52]. This is the case for polymer permeation, where data is often available for single parents. The available information is not sufficient enough to asses Maxwell-Stefan diffusivities. Therefore, these diffusivities need to be determined differently.

The free volume theory can predict the Maxwell-Stefan diffusivities of multicomponent mixtures [53]. The theory's central idea is that a molecular mixture contains 'holes': openings with a volume of the order of a molecule. A molecule's diffusion requires a large enough hole so that the molecule can move to it. The chance of finding a hole large enough for the molecule is simply the volume of the molecule over the available free volume, the sum of the volumes of all the holes. Furthermore, molecules are considered as hard spheres.

$$\phi = \mathsf{exp}\left[-0.7\frac{V_1^{\$}}{V_f}\right] \tag{4.18}$$

Here, ϕ represents the chance of a molecule finding a 'holes' larger than its volume, $V_1^{\$}$ is the volume [m^3] of the molecule and V_f is the free available volume [m^3].

Let's start with a pure fluid. At low temperatures or high pressures, the fluid will assume a closely packed structure, which contains no free volume. At higher temperatures or lower pressures, the fluid will expand, and free volume will arise. These ideas help predict the *self-diffusivity*, the local rate of diffusional mixing, of the considered fluid. This is done by following a radioactive tracer '$1\bullet$' with properties identical to the fluid '1'. It is assumed that the fluid molecules are arranged on a cubic lattice and spaced out by the distance l [m], which is close to the diameter of the molecule d_1 [m]. After a certain period, the molecules can move up one position. This randomly happens in one of six directions: up, down, left, right, forward, or backward. This happens numerous times per second and causes diffusion. If the movement of the molecule is not impeded, one could conclude that diffusion is proportional to the frequency of the steps and the square of the lattice distance, which can also be written as a product of displacement and velocity.

$$Đ_1 \approx \frac{u_1 d_1}{6} \tag{4.19}$$

Here, $Đ_1$ [m^2/s] is the 'unimpeded' self-diffusivity coefficient, and u_1 is the molecular velocity. It is expected that the molecular velocity is of the order of the thermal velocity of the molecule.

$$u = \sqrt{\frac{3k_bT}{m_1}} \tag{4.20}$$

Where k_B is the Boltzmann constant [J/K], T [K] is the temperature and m_1 the mass of a single molecule. As it is assumed that the fluid has a cubic structure and the molecules are spheres, the volume they actually occupy in the lattice is equal to d_1^3. The mass of a molecule can, therefore, be written as a product of the maximal density of the fluid and the volume it occupies in the fluid.

$$Đ_1 \approx \frac{1}{6}\sqrt{\frac{3k_bT}{\rho_{0,1}d_1}} \tag{4.21}$$

The order of magnitude of the 'unimpeded' diffusivities is around 10^{-8} m^2s^{-1}. This can be combined with the idea that a molecule can only move when there is a free position; this leads to

$$Đ_{1,1\bullet} = Đ_1 \exp\left[-0.7\frac{V_{0,1}}{V_{f1}}\right] \tag{4.22}$$

Here,$Đ_{1,1\bullet}$ [m^2/s] is the self diffusivity, $V_{0,1}$ [m^3] is the minimum volume of fluid 1 and V_{f1} [m^3] is the free volume of fluid 1. The usage of the minimum volume is needed because we are no longer talking about a single molecule but the whole fluid. Furthermore, only one fluid is considered to assess self-diffusivity. The appropriate equation for the effective friction coefficient follows, where the 'unimpeded' friction coefficient ζ_1 can be determined using Equation 4.13.

$$\zeta_{1\bullet,eff} = \zeta_1 \exp\left[\frac{V_{0,1}}{V_{f1}}\right] \tag{4.23}$$

Additional assumptions are needed based on mixing rules to use the theory for a mixture. First, all species in the mixture contribute to the free volume. The following equation can be set up if a ternary mixture is considered.

$$V_f = x_1V_{f1}^* + x_2V_{f2}^* + x_3V_{f3}^* \tag{4.24}$$

The superscript $*$ denotes that the pure component is considered. In this case, the total free volume is thus the sum of the free volumes per pure component. The second rule concerns a component's amount of volume 'seen'. It is assumed that the free volume seen by a component is proportional to its surface fraction, σ. In a ternary mixture considering spherical molecules, this gives:

$$\begin{aligned} S &= x_1{V_1^*}^{\frac{2}{3}} + x_2{V_2^*}^{\frac{2}{3}} + x_3{V_3^*}^{\frac{2}{3}} \\ \sigma_1 &= \frac{x_1{V_1^*}^{\frac{2}{3}}}{S} \quad \sigma_2 = \frac{x_2{V_2^*}^{\frac{2}{3}}}{S} \quad \sigma_3 = \frac{x_3{V_3^*}^{\frac{2}{3}}}{S} \end{aligned} \tag{4.25}$$

The free volumes associated with the different species are then written as:

$$V_{f1} = \frac{\sigma_1}{x_1}V_f \quad V_{f2} = \frac{\sigma_2}{x_2}V_f \quad V_{f3} = \frac{\sigma_3}{x_3}V_f \tag{4.26}$$

The third rule is the usage of the minimal density of the mixture in Equation 4.21 instead of the component density. The minimal density of the mixture is the molar averaged minimal density.

The second assumption is that the mutual coefficient is the geometrical average of the self-friction coefficients.

$$\zeta_{i,j} = \sqrt{\zeta_{i,i\bullet}\zeta_{j,j\bullet}} \tag{4.27}$$

Furthermore, the concentration of the radioactive tracers is very low. Only one molecule is considered. Therefore, the tracers do not influence each other. The effective friction coefficients can be written as

$$\zeta_{i\bullet,eff} = \sum_{j=i}^{N} x_j\zeta_{i\bullet,j} \tag{4.28}$$

A relation for the mutual friction coefficients can be set up by combining Equation 4.27 and Equation 4.28.

$$\zeta_{i,j} = \frac{\zeta_{i\bullet,eff}\zeta_{j\bullet,eff}}{\sum_a^N x_a\zeta_{a\bullet,eff}} \tag{4.29}$$

Although the free volume theory is a very simple theory for fluid mixtures, it can also describe the movement of small permeants through a stagnant polymer membrane. It can be extended to an infinite number of components. The pre-exponential of the components can be estimated using Equation 4.21. It is important to note that its molecular chain repeat element is considered the basic molecular unit for the membrane. For PVC, this is CH_2CHCl. The minimum volume of the considered molecules comes from the assumption that fluids form a cubic matrix of hard spheres. The spheres will take up a volume equal to a cube with a side length equal to the sphere's diameter.

$$V_1^{\$} \approx d_1^3 \tag{4.30}$$

The minimum volume of the polymer membrane is unknown and will be fitted to obtain good results. Krishna et al. [52] recommend starting with an estimated free volume of about 5% of the polymer volume for glassy polymers (10% for rubbery polymers).

The above method describes how to approach the Maxwell-Stefan friction coefficients. It is based on loose arguments, and the inputs need some tweaking to obtain results in accordance with reality. The company has provided the permeability for pure hydrogen through the membrane: 3.2×10^{-15} [mol m /(m^2 Pa s)]. It has been assumed that the permeability was measured at 283.25 K. Let's now consider only the penetration of pure hydrogen through the membrane. Equation 4.15 reduces to:

$$-\overline{x}_{\mathsf{H_2}} \frac{\Delta p_{\mathsf{H_2}}}{\overline{p}_{\mathsf{H_2}}} = \frac{J_{\mathsf{H_2}}}{k_{\mathsf{H_2,M}} \overline{c}} \tag{4.31}$$

The steps above were followed to find the friction coefficient between the hydrogen and the membrane. Equation 4.13 is used to transform the coefficient into a mass transfer coefficient. The two parameters available for variation are the mol fraction of H_2, $x_{\mathsf{H_2}}$ and the free volume fraction of the membrane. The following steps were taken to obtain the membrane's minimal and free volume and concentration of H_2.

First, the amount of mol of chain repeat elements in the pure membrane was determined.

$$n_{\mathsf{PVC}} = \frac{\rho_{\mathsf{PVC}}}{M_{\mathsf{PVC}}} V_{\mathsf{M}} \tag{4.32}$$

Here, n_{PVC} [mol] is the number of mols in the membrane, ρ_{PVC} [kg/m^3] is the density of the chain repeat element, M_{PVC} [kg/mol] is the molar mass of the chain repeat element and V_{M} [m^3] is the volume of the membrane. The mol fraction of the membrane follows from the input fraction of H_2 as only two species are considered. This leads to the amount of mol of H_2 [mol] in the membrane and, subsequently, the concentration in the membrane. The minimal volume of the H_2 is calculated using Equation 4.30 multiplying by the Avogadro constant and the amount of mol of H_2.

$$V_{0,\mathsf{H_2}} = V_1^{\$} N_{\mathsf{A}} n_{\mathsf{H_2}} \tag{4.33}$$

The real volume of the pure H_2,$V^*_{\mathsf{H_2}}$, is determined using the ideal gas law. The free volume volume of H_2, $V^*_{f,\mathsf{H_2}}$, difference between the actual and minimal volume of H_2. The free volume of the polymer, $V^*_{f,\mathsf{PVC}}$, is the free volume fraction of polymer times the volume. The number of mols, the minimal volumes and the molar masses lead to the combined minimal density, the last unknown to solve the system. To translate the determined flux to a permeability coefficient Equation 2.2 is used. The resulting mol fraction of H_2 and minimal volume fraction of the membrane are 0.0000004 and 0.05, respectively. The resulting permeability coefficient is 3.38×10^{-15} mol m /(m^2 Pa s) at a temperature of 283.15 K. The same method was applied for a system considering the polymer membrane, H_2, N_2 and H_2O. The mol fractions of N_2 and O_2 have been taken as 0.00000008 and 0.00000005, respectively.

4.1.2. Condensation

Water traces are present in gas compartment B's hydrogen inlet stream and gas compartment A's air inlet stream. It is initially guessed that the conditions in the gasholder fluctuate between 1-1.5 bar and 265-323 K. At these conditions, phase changes of water are prone to happen in the gas compartments. Nitrogen, oxygen and hydrogen condense at around 130 K, 160 K and 35 K, respectively. The system will never meet these conditions, and therefore, only the condensation of water will be considered. Furthermore, the solubility of all other elements in water will also be neglected. The liquid phase consists of pure water. Water condensation is the process where water vapour becomes liquid. This is

an exothermic process, and it is, therefore, essential to consider with regard to the energy balance. Condensation happens when the gas phase is saturated with water vapour. In other words, the gas phase can not contain any more water. The saturation vapour pressure of water can be determined using the Buck equations [54].

$$P_{\text{sat}} = 611.21 \exp\left[(18.678 - \frac{T}{234.5})(\frac{T}{257.14+T})\right] [Pa] \quad \text{for } T > 0°\text{C} \tag{4.34}$$

$$P_{\text{sat}} = 611.15 \exp\left[(23.036 - \frac{T}{333.7})(\frac{T}{279.82+T})\right] [Pa] \quad \text{for } T \leq 0°C \tag{4.35}$$

Here, P_{sat} represents the saturation vapour pressure [Pa] at temperature T [°C]. With the saturation pressure of water known, condensation can be determined. If the partial pressure of water vapour in the considered compartment is larger than the saturation pressure, the excess water will condense. Inversely, if the partial pressure of water vapour is smaller than the saturation pressure, water will evaporate if present in the liquid phase. Thus, the vapour pressure of water will always converge to the saturation pressure of water to equilibrate the system. To approach the amount of mol water condensing, the following differential equation is assumed to hold

$$\dot{N}_{\text{H}_2\text{O,cond}} = \frac{p_{\text{H2O}} - p_{\text{sat}}}{\tau_{\text{cond}}} \times \frac{N_0}{P_0} \tag{4.36}$$

Here $\dot{N}_{\text{H}_2\text{O,cond}}$ is the mol flow rate [mol/s] of condensing water, p_{H2O} is the partial pressure [Pa] of water in the gas phase, p_{sat} is the saturation vapour pressure [Pa], τ is a time constant [s], N_0 is an initial mol constant equal to one mol and P_0 is an initial pressure constant equal to 101325 Pa. The value of the time constant τ_{cond} determines the condensation rate. It is important to note that this relation assumes that the nucleation of water happens instantly. Furthermore, the solubility of all other elements in liquid H_2O has been neglected, meaning the liquid phase consists of pure H_2O.

4.2. Energy Balance

The energy balance of a control volume indicates the rate of change of the amount of energy present in the control volume at time t. It consists of the net rate of energy transferred by heat, the net rate of energy transferred by thermodynamic work in the system, and the net rate of energy transfer due to mass flow in the control volume. The general formula for the energy rate balance is the following:

$$\frac{dE_{\text{cv}}}{dt} = \dot{Q} - \dot{W}_{\text{cv}} + \sum \dot{m}_{\text{in}}(h_{\text{in}} + \frac{V_{\text{in}}^2}{2} + gz_{\text{in}}) - \sum \dot{m}_{\text{out}}(h_{\text{out}} + \frac{V_{\text{out}}^2}{2} + gz_{\text{out}}) \tag{4.37}$$

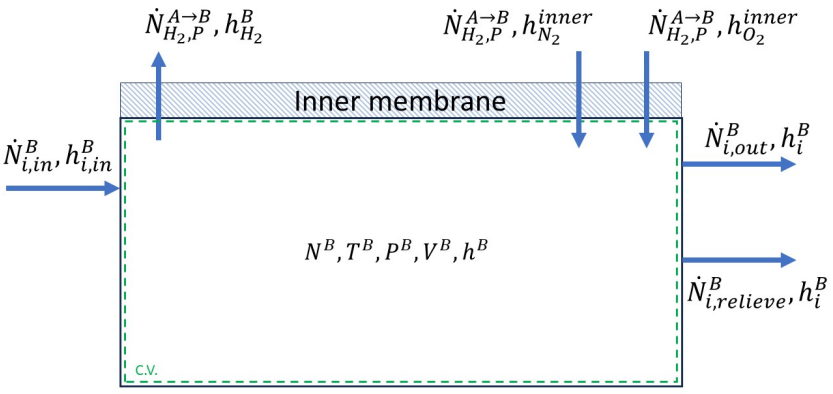

Figure 4.2: Control volume for the example case of compartment B, the direction, origin and destination of permeation are indicated by the arrows

Several control volumes have been defined in the system. The gas compartments form two control volumes. The membranes are treated as separate elements from the gas compartments and are

represented by an additional control volume. This results in a total of four control volumes. In this section, we will derive the energy balance for the control volume in gas compartment B. The control volumes are illustrated in the diagram shown in Figure 4.2. The directions of permeation have been determined beforehand and are indicated by the arrows. Similarly, it was determined beforehand that a part of the water in the control volume would condense. As ideal mixing has been assumed, the flows leaving the control volume have a temperature equal to that of the control volume, meaning their specific enthalpies are also equal. In the energy balance equation, the specific enthalpy is expressed in J/mol instead of J/kg, which means that mol flows are used instead of mass flows. It is assumed that the kinetic and potential energies of mass are negligible. The general energy balance around the control volume becomes

$$\begin{aligned}\frac{dE^{\mathsf{B}}}{dt} = \dot{Q}^{\mathsf{B}} - \dot{W}^{\mathsf{B}} + \sum_{i=1}^{N} \dot{N}^{\mathsf{B}}_{i,\mathsf{in}} h^{\mathsf{B}}_{i,\mathsf{in}} - \sum_{i=1}^{N} \dot{N}^{\mathsf{B}}_{i,\mathsf{out}} h^{\mathsf{B}}_{i,} - \sum_{i=1}^{N} \dot{N}^{\mathsf{B}}_{i,\mathsf{relieve}} h^{\mathsf{B}}_{i} \\ -\dot{N}^{\mathsf{A}\to\mathsf{B}}_{\mathsf{H_2,P}} h^{\mathsf{B}}_{\mathsf{H_2}} + \dot{N}^{\mathsf{A}\to\mathsf{B}}_{\mathsf{N_2,P}} h^{\mathsf{inner}}_{\mathsf{N_2}} + \dot{N}^{\mathsf{A}\to\mathsf{B}}_{\mathsf{O_2,P}} h^{\mathsf{inner}}_{\mathsf{O_2}} - \dot{N}^{\mathsf{B}}_{\mathsf{H_2O,cond}} h^{\mathsf{B}}_{\mathsf{H_2O}} + \left(h^{\mathsf{B}}_{\mathsf{H_2O,G,m}} - h^{\mathsf{B}}_{\mathsf{H_2O,L,m}}\right) \dot{N}^{\mathsf{B}}_{\mathsf{H_2O,cond}}\end{aligned} \tag{4.38}$$

The last term of the equation is necessary to account for the exothermic nature of water condensation. This will add energy to the system. The inverse happens when water evaporates. This term is also known as the latent heat of condensation or the enthalpy of condensation Δh^{cond} [J/ mol]. The conservation of energy over compartment B can also be expressed as:

$$\frac{dE^{\mathsf{B}}}{dt} = N^{\mathsf{B}} \frac{du^{\mathsf{B}}}{dt} + u^{\mathsf{B}} \frac{dN^{\mathsf{B}}}{dt} \tag{4.39}$$

The specific internal energy of compartment B can be described as a function of temperature and the molar volume $u^{\mathsf{B}}(T^{\mathsf{B}},\, V^{\mathsf{B}}_{\mathsf{m}})$.

$$du^{\mathsf{B}} = \frac{\partial u^{\mathsf{B}}}{\partial T^{\mathsf{B}}} dT^{\mathsf{B}} + \frac{\partial u^{\mathsf{B}}}{\partial V^{\mathsf{B}}_{\mathsf{m}}} dV^{\mathsf{B}}_{\mathsf{m}} \tag{4.40}$$

This equation can be simplified using the following thermodynamic relations [55]

$$\frac{\partial u^{\mathsf{B}}}{\partial T^{\mathsf{B}}} = c^{\mathsf{B}}_{\mathsf{v,m}} \tag{4.41}$$

$$\frac{\partial u^{\mathsf{B}}}{\partial V^{\mathsf{B}}_{\mathsf{m}}} = \left[T^{\mathsf{B}} \left(\frac{\partial p^{\mathsf{B}}}{\partial T^{\mathsf{B}}} \right)_{V^{\mathsf{B}}_{\mathsf{m}}} - p^{\mathsf{B}} \right] \tag{4.42}$$

$$u^{\mathsf{B}} = h^{\mathsf{B}} - p^{\mathsf{B}} v^{\mathsf{B}}_{\mathsf{m}} \tag{4.43}$$

Equation 4.42 is equal to 0 for an ideal gas. The small amount of water in the control volume has been neglected. Thus, combining equations 4.39, 4.40, 4.41 and 4.43 leads to

$$\frac{dE^{\mathsf{B}}}{dt} = N^{\mathsf{B}} c^{\mathsf{B}}_{\mathsf{c,v}} \frac{dT^{\mathsf{B}}}{dt} + h^{\mathsf{B}} \frac{dN^{\mathsf{B}}}{dt} - p^{\mathsf{B}} V^{\mathsf{B}}_{\mathsf{m}} \frac{dN^{\mathsf{B}}}{dt} \tag{4.44}$$

The overall energy conservation equation becomes

$$\begin{aligned}N^{\mathsf{B}} c^{\mathsf{B}}_{\mathsf{v,m}} \frac{dT^{\mathsf{B}}}{dt} + h^{\mathsf{B}} \frac{dN^{\mathsf{B}}}{dt} - p^{\mathsf{B}} v^{\mathsf{B}}_{\mathsf{m}} \frac{dN^{\mathsf{B}}}{dt} = \dot{Q}^{\mathsf{B}} - \dot{W}^{\mathsf{B}} + \sum_{i=1}^{N} \dot{N}^{\mathsf{B}}_{i,\mathsf{in}} h^{\mathsf{B}}_{i,\mathsf{in}} - \sum_{i=1}^{N} \dot{N}^{\mathsf{B}}_{i,\mathsf{out}} h^{\mathsf{B}}_{i} \\ - \sum_{i=1}^{N} \dot{N}^{\mathsf{B}}_{i,\mathsf{relieve}} h^{\mathsf{B}}_{i} - \dot{N}^{\mathsf{A}\to\mathsf{B}}_{\mathsf{H_2,P}} h^{\mathsf{B}}_{\mathsf{H_2}} + \dot{N}^{\mathsf{A}\to\mathsf{B}}_{\mathsf{N_2,P}} h^{\mathsf{inner}}_{\mathsf{N_2}} + \dot{N}^{\mathsf{A}\to\mathsf{B}}_{\mathsf{O_2,P}} h^{\mathsf{inner}}_{\mathsf{O_2}} + \Delta h^{\mathsf{cond}} \dot{N}^{\mathsf{B}}_{\mathsf{H_2O,cond}}\end{aligned} \tag{4.45}$$

The second term in the L.H.S. of Equation 4.45, $h^{\mathsf{B}} \frac{dN^{\mathsf{B}}}{dt}$, containing the enthalpy and the net rate of change in moles of compartment B can be opened up using Equation 4.2 and Equation 4.3

$$h^{\mathrm{B}}\frac{dN^{\mathrm{B}}}{dt} = \left(-\dot{N}^{\mathrm{A}\to\mathrm{B}}_{\mathrm{H_2,P}}h^{\mathrm{B}}_{\mathrm{H_2}} + \dot{N}^{\mathrm{A}\to\mathrm{B}}_{\mathrm{N_2,P}}h^{\mathrm{B}}_{\mathrm{N_2}} + \dot{N}^{\mathrm{A}\to\mathrm{B}}_{\mathrm{O_2,P}}h^{\mathrm{B}}_{\mathrm{O_2}} - \dot{N}^{\mathrm{B}}_{\mathrm{H_2O,cond}}h^{\mathrm{B}}_{\mathrm{H_2O}}\right) + \sum_{\mathrm{i}=1}^{\mathrm{N}}\left(\dot{N}^{\mathrm{B}}_{i,\mathrm{in}} - \dot{N}^{\mathrm{B}}_{i,\mathrm{out}} - \dot{N}^{\mathrm{B}}_{i,\mathrm{relieve}}\right)\times h^{\mathrm{B}}_i \tag{4.46}$$

Now, given Equation 4.46, the following equation can be set up

$$N^{\mathrm{B}}c^{\mathrm{B}}_{\mathrm{v,m}}\frac{dT^{\mathrm{B}}}{dt} - p^{\mathrm{B}}v^{\mathrm{B}}_{\mathrm{m}}\frac{dN^{\mathrm{B}}}{dt} + \left(-\dot{N}^{\mathrm{A}\to\mathrm{B}}_{\mathrm{H_2,P}}h^{\mathrm{B}}_{\mathrm{H_2}} + \dot{N}^{\mathrm{A}\to\mathrm{B}}_{\mathrm{N_2,P}}h^{\mathrm{B}}_{\mathrm{N_2}} + \dot{N}^{\mathrm{A}\to\mathrm{B}}_{\mathrm{O_2,P}}h^{\mathrm{B}}_{\mathrm{O_2}} - \dot{N}^{\mathrm{B}}_{\mathrm{H_2O,cond}}h^{\mathrm{B}}_{\mathrm{H_2O}}\right) + + \sum_{\mathrm{i}=1}^{\mathrm{N}}\left(\dot{N}^{\mathrm{B}}_{i,\mathrm{in}} - \dot{N}^{\mathrm{B}}_{i,\mathrm{out}} - \dot{N}^{\mathrm{B}}_{i,\mathrm{relieve}}\right)\times h^{\mathrm{B}}_i = \dot{Q}^{\mathrm{B}} - \dot{W}^{\mathrm{B}} + \sum_{i=1}^{N}\dot{N}^{\mathrm{B}}_{i,\mathrm{in}}h^{\mathrm{B}}_{i,\mathrm{in}} - \sum_{i=1}^{N}\dot{N}^{\mathrm{B}}_{i,\mathrm{out}}h^{\mathrm{B}}_i - \sum_{i=1}^{N}\dot{N}^{\mathrm{B}}_{i,\mathrm{relieve}}h^{\mathrm{B}}_i - \dot{N}^{\mathrm{A}\to\mathrm{B}}_{\mathrm{H_2,P}}h^{\mathrm{B}}_{\mathrm{H_2}} + \dot{N}^{\mathrm{A}\to\mathrm{B}}_{\mathrm{N_2,P}}h^{\mathrm{inner}}_{\mathrm{N_2}} + \dot{N}^{\mathrm{A}\to\mathrm{B}}_{\mathrm{O_2,P}}h^{\mathrm{inner}}_{\mathrm{O_2}} + \Delta h^{\mathrm{cond}}\dot{N}^{\mathrm{B}}_{\mathrm{H_2O,cond}} \tag{4.47}$$

This simplifies to

$$N^{\mathrm{B}}c^{\mathrm{B}}_{\mathrm{v,m}}\frac{dT^{\mathrm{B}}}{dt} - p^{\mathrm{B}}v^{\mathrm{B}}_{\mathrm{m}}\frac{dN^{\mathrm{B}}}{dt} = \dot{Q}^{\mathrm{B}} - \dot{W}^{\mathrm{B}} + \sum_{i=1}^{N}\dot{N}^{\mathrm{B}}_{i,\mathrm{in}}\left(h^{\mathrm{B}}_{i,\mathrm{in}} - h^{\mathrm{B}}_i\right) + \dot{N}^{\mathrm{A}\to\mathrm{B}}_{\mathrm{N_2,P}}\left(h^{\mathrm{inner}}_{\mathrm{N_2}} - h^{\mathrm{B}}_{\mathrm{N_2}}\right) + \dot{N}^{\mathrm{A}\to\mathrm{B}}_{\mathrm{O_2,P}}\left(h^{\mathrm{inner}}_{\mathrm{O_2}} - h^{\mathrm{B}}_{\mathrm{O_2}}\right) + \Delta h^{\mathrm{cond}}\dot{N}^{\mathrm{B}}_{\mathrm{H_2O,cond}} \tag{4.48}$$

Using the following thermodynamic relationship [55]

$$h_2 - h_1 = \int_1^2 c_{\mathrm{p}}dT + \int_1^2\left[v - T\left(\frac{\partial v}{\partial T}\right)_p\right]dp \tag{4.49}$$

For an ideal gas, the last term on the right-hand side equals 0. Hence, Equation 4.48 simplifies to

$$N^{\mathrm{B}}c^{\mathrm{B}}_{\mathrm{v,m}}\frac{dT^{\mathrm{B}}}{dt} - p^{\mathrm{B}}v^{\mathrm{B}}_{\mathrm{m}}\frac{dN^{\mathrm{B}}}{dt} = \dot{Q}^{\mathrm{B}} - \dot{W}^{\mathrm{B}} + (T^{\mathrm{in}} - T^{\mathrm{B}})\times\sum_{\mathrm{i}=1}^{\mathrm{N}}\dot{N}^{\mathrm{B}}_{i,\mathrm{in}}\times c^{\mathrm{B}}_{\mathrm{p,i}} + (T^{\mathrm{inner}} - T^{\mathrm{B}})\times\dot{N}^{\mathrm{A}\to\mathrm{B}}_{\mathrm{N_2,P}}\times c^{\mathrm{B}}_{\mathrm{p,N_2}} + (T^{\mathrm{inner}} - T^{\mathrm{B}})\times\dot{N}^{\mathrm{A}\to\mathrm{B}}_{\mathrm{O_2,P}}\times c^{\mathrm{B}}_{\mathrm{p,O_2}} + \Delta h^{\mathrm{cond}}\dot{N}^{\mathrm{B}}_{\mathrm{H_2O,cond}} \tag{4.50}$$

Equation 4.50 can be rearranged to give the net rate of change of compartment B.

$$\frac{dT^{\mathrm{B}}}{dt} = \frac{1}{N^{\mathrm{B}}c^{\mathrm{B}}_{\mathrm{v,m}}}\left[\dot{Q}^{\mathrm{B}} - \dot{W}^{\mathrm{B}} + p^{\mathrm{B}}v^{\mathrm{B}}_{\mathrm{m}}\frac{dN^{\mathrm{B}}}{dt} + \Delta h^{\mathrm{cond}}\dot{N}^{\mathrm{B}}_{\mathrm{H_2O,cond}} + (T^{\mathrm{in}} - T^{\mathrm{B}})\times\sum_{\mathrm{i}=1}^{\mathrm{N}}\dot{N}^{\mathrm{B}}_{i,\mathrm{in}}\times c^{\mathrm{B}}_{\mathrm{p},i} + (T^{\mathrm{inner}} - T^{\mathrm{B}})\times\dot{N}^{\mathrm{A}\to\mathrm{B}}_{\mathrm{N_2,P}}\times c^{\mathrm{B}}_{\mathrm{p,N_2}} + (T^{\mathrm{inner}} - T^{\mathrm{B}})\times\dot{N}^{\mathrm{A}\to\mathrm{B}}_{\mathrm{O_2,P}}\times c^{\mathrm{B}}_{\mathrm{p,O_2}}\right] \tag{4.51}$$

This is just an illustrative example of how the energy balance depends on system conditions. Instead of condensation, the liquid phase can evaporate. This changes the direction of the condensation flow. The same holds for the molecules' permeation through the membrane; the direction of permeation can be opposite of what has been assumed in this example. The general control volumes are shown in Figure 4.3a and Figure 4.3b. A general formula for the energy balances is complicated. For compartment B, it can be written as

$$\frac{dT^{\mathrm{B}}}{dt} = \frac{1}{N^{\mathrm{B}}c^{\mathrm{B}}_{\mathrm{v,m}}}\left[\dot{Q}^{\mathrm{B}} - \dot{W}^{\mathrm{B}} + p^{\mathrm{B}}v^{\mathrm{B}}_{\mathrm{m}}\frac{dN^{\mathrm{B}}}{dt} + \Delta h^{\mathrm{cond}}\dot{N}^{\mathrm{B}}_{\mathrm{H_2O,cond}} + (T^{\mathrm{in}} - T^{\mathrm{B}})\times\sum_{\mathrm{i}=1}^{\mathrm{N}}\dot{N}^{\mathrm{B}}_{i,\mathrm{in}}\times c^{\mathrm{B}}_{\mathrm{p},i} + \sum_{i=1}^{N}\dot{N}^{\mathrm{A}\to\mathrm{B}}_{i,\mathrm{P}}(h^{\mathrm{A}\to\mathrm{B}}_i - h^{\mathrm{B}}_i)\right] \tag{4.52}$$

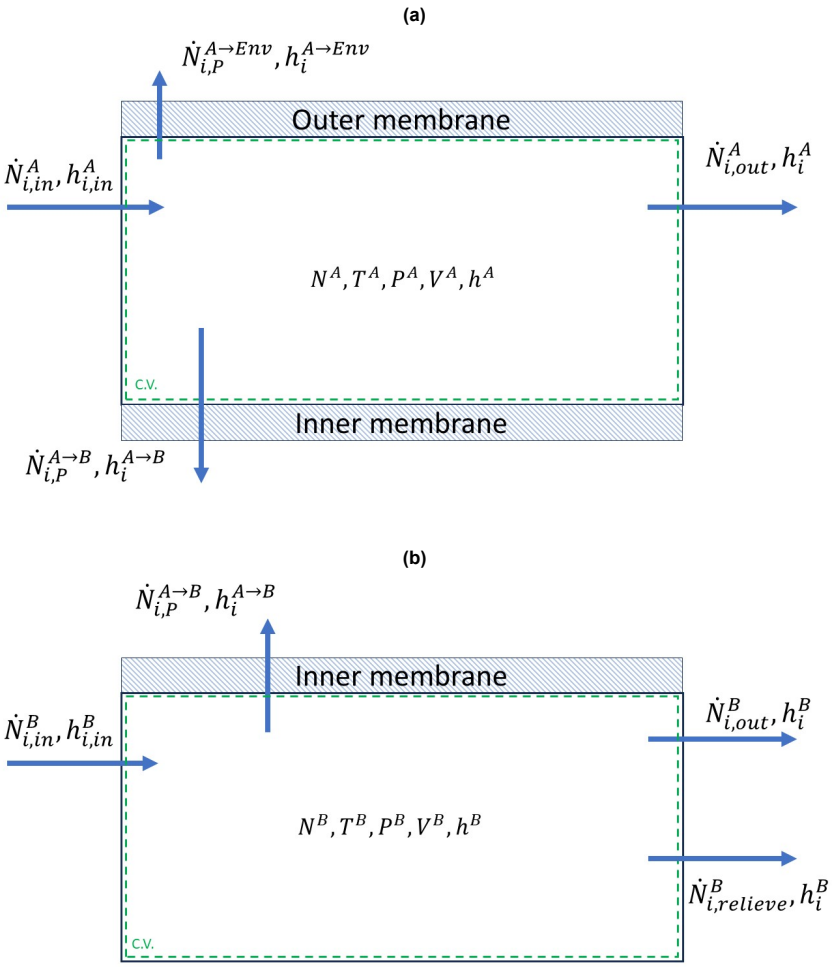

Figure 4.3: (a) Control volume of gas compartment A for the energy balance, the chosen direction, origin and destination of permeation and condensation are indicated by the arrows; (b) Control volume of gas compartment B for the energy balance, the chosen direction, origin and destination of permeation and condensation are indicated by the arrows

Where

$$h_i^{\mathrm{A}\to\mathrm{B}} = \begin{cases} h_i^{\mathrm{inner}}, & \text{for } \dot{N}_{i,\mathrm{P}}^{\mathrm{A}\to\mathrm{B}} > 0 \\ h_i^{\mathrm{B}}, & \text{for } \dot{N}_{i,\mathrm{P}}^{\mathrm{A}\to\mathrm{B}} \leq 0 \end{cases} \tag{4.53}$$

The same can be done for the energy balance of compartment A

$$\begin{aligned} \frac{dT^{\mathrm{A}}}{dt} = \frac{1}{N^{\mathrm{A}} c_{\mathrm{v,m}}^{\mathrm{A}}} \Bigg[& \dot{Q}^{\mathrm{A}} - \dot{W}^{\mathrm{A}} + p^{\mathrm{A}} v_{\mathrm{m}}^{\mathrm{A}} \frac{dN^{\mathrm{A}}}{dt} + \Delta h^{\mathrm{cond}} \dot{N}_{\mathrm{H_2O,cond}}^{\mathrm{A}} + (T^{\mathrm{in}} - T^{\mathrm{A}}) \times \\ & \sum_{\mathrm{i=1}}^{\mathrm{N}} \dot{N}_{i,\mathrm{in}}^{\mathrm{A}} c_{\mathrm{p},i}^{\mathrm{A}} - \sum_{i=1}^{N} \dot{N}_{i,\mathrm{P}}^{\mathrm{A}\to\mathrm{B}} (h_i^{\mathrm{A}\to\mathrm{B}} - h_i^{\mathrm{A}}) - \sum_{i=1}^{N} \dot{N}_{i,\mathrm{P}}^{\mathrm{A}\to\mathrm{Env}} (h_i^{\mathrm{A}\to\mathrm{Env}} - h_i^{\mathrm{A}}) \Bigg] \end{aligned} \tag{4.54}$$

Where

$$h_i^{\mathrm{A}\to\mathrm{B}} = \begin{cases} h_i^{\mathrm{inner}}, & \text{for } \dot{N}_{i,\mathrm{P}}^{\mathrm{A}\to\mathrm{B}} \leq 0 \\ h_i^{\mathrm{A}}, & \text{for } \dot{N}_{i,\mathrm{P}}^{\mathrm{A}\to\mathrm{B}} > 0 \end{cases} \tag{4.55}$$

$$h_i^{\mathrm{A}\to\mathrm{Env}} = \begin{cases} h_i^{\mathrm{outer}}, & \text{for } \dot{N}_{i,\mathrm{P}}^{\mathrm{A}\to\mathrm{Env}} \leq 0 \\ h_i^{\mathrm{A}}, & \text{for } \dot{N}_{i,\mathrm{P}}^{\mathrm{A}\to\mathrm{Env}} > 0 \end{cases} \tag{4.56}$$

The energy balance around the membranes is more straightforward. It is assumed that there is no exchange of matter. Furthermore, the membrane does not perform any thermodynamic work as it does not change in volume. Its thermal expansion has been neglected. Therefore, the right-hand side of Equation 4.38 reduces simply to the net heat transfer rate. Moreover, this also simplifies the left-hand side of the equation, as the internal energy of the membrane is only dependent on the change in temperature of the membrane. Hence, the energy balances are reduced to the following

$$\frac{dT^{\text{inner}}}{dt} = \frac{\dot{Q}^{\text{inner}}}{N^{\text{inner}} \cdot c_{\text{v,m}}^{\text{inner}}} \tag{4.57}$$

$$= \frac{\dot{Q}}{m^{\text{inner}} \cdot c_{\text{v}}^{\text{inner}}} \tag{4.58}$$

$$\frac{dT^{\text{outer}}}{dt} = \frac{\dot{Q}^{\text{outer}}}{N^{\text{outer}} \cdot c_{\text{v,m}}^{\text{outer}}} \tag{4.59}$$

$$= \frac{\dot{Q}}{m^{\text{outer}} \cdot c_{\text{v}}^{\text{outer}}} \tag{4.60}$$

4.2.1. Thermodynamic Work

Thermodynamic work is how a thermodynamic system interacts with its surroundings, exchanging energy through various processes. Pressure-volume work is a specific type of work that is of interest when considering a fluid in a compartment. It occurs when the volume of a fluid changes. The following equation describes it

$$W = \int_1^2 p dV \tag{4.61}$$

The quantity of work a fluid does depends on its initial and final state and the system's path from one point to another. The differential of pressure-volume work is

$$\dot{W} = p\frac{dV}{dt} \tag{4.62}$$

4.3. Net rate of change in pressure in the compartments

It is assumed that the gasses present in the compartments follow the ideal gas law. The net rate of change in pressure depends on the net rate of change in temperature, volume, and the amount of moles in the same compartment.

$$\frac{dP}{dt} = \frac{d\frac{NRT}{V}}{dt} \tag{4.63}$$

This can be expanded to give the following relationship:

$$\frac{dP}{dt} = \frac{RT\frac{dN}{dt} + NR\frac{dT}{dt} - P\frac{dV}{dt}}{V} \tag{4.64}$$

4.4. Net rate of change in volume of the compartments

The volume increase in the compartments is difficult to assess. The floor is assumed to be rigid, a solid assumption, as it is made out of concrete. Therefore, the volume of compartment B can only increase by pushing the inner membrane, its boundary layer. Pushing the inner membrane works against the pressure and gravity force. Here, the gravity force is ignored. Thus, in equilibrium, the pressure force due to the pressure in compartment B is equal to that in compartment A. A system will always move to equilibrium, mechanically and chemically. An increase in pressure in compartment B will thus lead to an increase in the volume of compartment B to reach mechanical equilibrium in the system.

$$\frac{dV_{\text{B}}}{dt} = \frac{P_{\text{B}} - P_{\text{A}}}{\tau_P}\frac{V_0}{P_0} \tag{4.65}$$

The change in volume in compartment B has been approached with Equation 4.65. Here, τ_P is a time constant [s] regulating the speed at which the system moves to equilibrium, V_0 is an initial volume constant, 1 m^3, and P_0 is the same initial pressure constant, 101325 Pa, as in Equation 4.36. In reality,

volume change depends on many factors, more than just pressure. If one looks at the ideal gas law, the simplest equation of state, the volume depends on pressure, temperature and amount of mols. This leads to a similar equation as Equation 4.64. A problem arises when defined like this as the system becomes unsolvable. One would find that the net change in volume equals the net rate of change in the volume of the compartment. A true answer but not solvable. Therefore, the above relation has been set up.

As the outer membrane has been assumed to be rigid, the total volume of the gasholder does not change; see section 3.1. This means the following equation holds for the volume change in compartment A.

$$\frac{dV_{\mathsf{A}}}{dt} = -\frac{dV_{\mathsf{B}}}{dt} \tag{4.66}$$

5

Heat transfer

Heat transfer is the energy exchanged between materials due to a temperature difference, flowing from the hotter material to the colder material. Like thermodynamic work, heat transfer is a path-dependent process function. There are three modes of heat transfer: conduction, convection, and radiation [56–58]. Conduction is the transfer of energy through two objects that are in contact. It also happens in one material if its temperature is not uniform. Fourier's law of conduction describes this method of heat transfer.

$$\dot{Q} = -kA\frac{dT}{dx} \tag{5.1}$$

Here, k [W / (m^2 K)] represents the thermal conductivity, A [m^2] is the contact area, and dT/dx [K] is the temperature gradient in the x direction. Convection is the transfer of energy from one place to another by the movement of fluids. There are two types of convection: natural and forced convection. Natural convection occurs when buoyancy forces cause fluid motion, while forced convection is caused by fluid motion induced by external means. The following primary relationship represents convection.

$$\dot{Q} = h_{\mathsf{c}}A(T - T_{\mathsf{f}}) \tag{5.2}$$

Here, h_{c} [W / (m^2 K)] is the heat transfer coefficient, A [m^2] is the heat transfer area, T [K] is the object temperature and T_{f} [K] is the fluid temperature.

Radiation is the transfer of energy by electromagnetic waves. Unlike conduction and convection, it requires no intervening medium to propagate. All objects above absolute zero emit thermal radiation. The net rate of radiative heat transfer between two objects is a more nuanced and intricate form of heat transfer than other forms. It depends on surface temperatures, surface radiation properties, and the geometry of the configuration.

To determine the net rate of heat transfer for every component in the system, the appropriate set of conductive, convective and radiative heat transfer equations must be set up. This is done component per component.

5.1. Dimensionless numbers of importance in heat transfer

Dimensionless numbers are crucial in analysing fluid behaviour, flow, and transport phenomena. They are used in the thermal modelling of different convective and conductive heat transfer [56–58].

The Nusselt number is the ratio of total heat transfer over conductive heat transfer at the boundary layer of a fluid. It is an essential parameter to determine the heat transfer coefficient h_{c} [W / (m^2 K)].

$$Nu = \frac{h_{\mathsf{c}}L_{\mathsf{c}}}{k} \tag{5.3}$$

The Nusselt number is described with Equation 5.3 where L_{c} [m] is the characteristic length, and k [W/(m K)] is the thermal conductivity of the fluid. Typically, the Nusselt number is expressed as a function of the Rayleigh and the Prandtl number, $Nu = f(Ra, Pr)$, for natural convection and a function of the Reynolds and the Prandtl number, $Nu = f(Re, Pr)$, for forced convection. The Prandtl number is the

ratio of momentum diffusivity over thermal diffusivity—in other words, the kinematic viscosity over the thermal diffusivity.

$$Pr = \frac{\nu}{\alpha} = \frac{c_{\mathsf{p}}\mu}{k} \tag{5.4}$$

In Equation 5.4, ν [m^2/s] is the kinematic viscosity, α [m^2/s] the thermal diffusivity, c_{p} [J/(kg K)] the specific heat capacity at constant pressure, μ [(N s)/ m^3] the dynamic viscosity of the fluid and k [W / (m K)] the thermal conductivity of the fluid.

The Grashof number is the ratio of buoyancy forces to viscous forces acting on a fluid. When studying situations involving natural convection, it often arises as a significant factor.

$$Gr = \frac{\beta g L_{\mathsf{c}}^3 |\Delta T|}{\nu^2} \tag{5.5}$$

Here, β [1/K]is the fluid's volume expansion coefficient. It is approximately equal to $\frac{1}{T_{\mathsf{fluid}}}$ for an ideal gas. g [m /s^2] is the gravitational acceleration due to Earth, ν [m^2/s] is the kinematic viscosity, L_{c} [m] is the characteristic length and ΔT [K] is the temperature difference between the surface and bulk temperatures.

The Rayleigh number of a fluid is dimensionless and is associated with buoyancy-driven flow, also called free convection. It is defined as the product of the Grashof number with the Prandtl number. The value of the Rayleigh number characterises the flow regime: a value in a low range indicates laminar flow, while a value in a higher range indicates turbulent flow. If the value of the Rayleigh number is smaller than a particular critical value, there is no fluid motion. The heat transfer takes place through conduction instead of convection.

$$Ra = Gr \times Pr \tag{5.6}$$

The Reynolds number is primarily used in forced convection correlations. It is the ratio between the inertial and viscous forces and determines the flow regime. At low Reynolds numbers, flows are laminar, while at high Reynolds numbers, flows are turbulent.

$$Re = \frac{\rho u L_{\mathsf{c}}}{\mu} = \frac{u L_{\mathsf{c}}}{\nu} \tag{5.7}$$

In Equation 5.7, ρ [kg/m^3] is the fluid density, u [m/s] the fluid speed, L [m] is the characteristic length, μ [(N s)/ m^3] the dynamic viscosity of the fluid and ν [m^2/s] is the kinematic viscosity of the fluid.

The Richardson number is used in heat transfer by convection to indicate the importance of natural convection relative to forced convection. It is defined as the ratio of the buoyancy term over the flow shear term and can be written in terms of the Grashof and Reynolds number. If $Ri < 0.1$, the buoyancy forces are negligible, and the forced convection dominates. If $Ri > 10$, the buoyancy forces are dominant; thus, forced convection is insignificant. If $0.1 < Ri < 10$, natural and forced convection occur.

$$Ri = \frac{Gr}{Re^2} \tag{5.8}$$

5.2. Radiation between grey surfaces

Thermal radiation is a complex process, and various fluxes are pertinent to its analysis [56–58]. Therefore, some critical fundamentals related to thermal radiation will be addressed here. The emmissive power, E [W/m^2], is the rate at which radiation is emitted from a surface per unit area. It is defined by the Stefan-Boltzmann law as

$$E = \epsilon \sigma T_{\mathsf{surface}}^4 = \epsilon E_b \tag{5.9}$$

Here, σ is a constant equal to 5.6697×10^{-8} [W/(m^{2}K^4)], T is the surface temperature [K] and ϵ is the emissivity, a surface property indicating the ratio of its emissive power to that of a black body. The emissive power of a blackbody is represented as E_b. The surface also receives radiation; the net rate at which radiation is incident upon the surface per unit of the surface area is called irradiation, G [W/m^2]. The surface will reflect part of the irradiation while the rest will be absorbed. In reality, irradiation can also be transmitted, passing through the medium of the irradiation. In the case considered here, all surfaces are assumed to be opaque, meaning none transmit any radiation. As all irradiation must either be absorbed or reflected, the following equality is deduced

$$\rho + \alpha = 1 \tag{5.10}$$

Here, ρ is the fraction of the reflected irradiation and α is the fraction of irradiation absorbed, equal to the emissivity ϵ of a real surface. Now the radiosity, J [W/m^2], can be defined. The radiosity of a surface accounts for all the radiation leaving the surface, including the reflected irradiation.

$$J = E + \rho G \tag{5.11}$$

This makes it possible to define the net radiative flux from a surface, q [W/m^2].

$$q = J - G = E + \rho G - G = \epsilon \sigma T^4 - \alpha G \tag{5.12}$$

Given Equation 5.11 and rearranging Equation 5.12 to substitute for G gives

$$J = E + \rho \left(J - q \right) \tag{5.13}$$

Solving for q and using Equation 5.10 with $\alpha = \epsilon$, the following equation can be determined

$$q = \frac{\epsilon}{1 - \epsilon} (\sigma T^4 - J) \tag{5.14}$$

This leads to net radiant energy leaving a surface

$$\dot{Q} = \frac{\epsilon A}{1 - \epsilon} (\sigma T^4 - J) \tag{5.15}$$

Where A is the surface area [m^2]. The net radiant energy exchanged between two surfaces is defined as

$$\dot{Q}_{12} = A_1 F_{12} (J_1 - J_2) = A_2 F_{21} (J_1 - J_2) \tag{5.16}$$

Here, A [m^2] is the area of the considered surface, and F is the so-called shape or view factor. For example, F_{12} represents the fraction of energy leaving surface one that is intercepted by surface two. The shape factor is a geometrical concept and depends only on the surface's size, shape, and orientation. For the here-considered system, the heat transfer by radiation will be solved using the electrical network analogy, which is particularly useful when dealing with grey surfaces. It starts with rewriting Equation 5.16 into

$$\dot{Q}_{12} = \frac{J_1 - J_2}{\frac{1}{A_1 F_{12}}} \tag{5.17}$$

From here, it is possible to define the space resistance $R_{12} = 1/(A_1 F_{12})$ between two radiosities. Equation 5.15 can be rewritten into

$$\dot{Q} = \frac{E_b - J}{\frac{1 - \epsilon}{\epsilon A}} \tag{5.18}$$

This defines $R = (1 - \epsilon)/\epsilon A$ as the surface resistance between an object's black body emissive power and its radiosity. Now, if we consider the thermal radiation between two enclosed grey surfaces, the following electrical circuit can be drawn

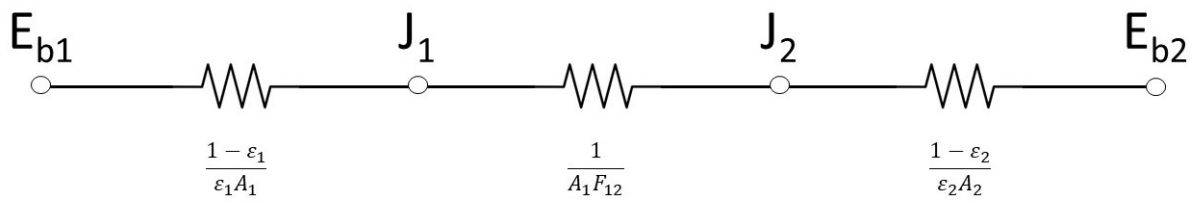

Figure 5.1: Equivalent electrical circuit for radiation exchange in an enclosure of two grey surfaces

The heat transfer from 1 to 2 follows from the addition of the resistances in series.

$$\dot{Q}_{12} = \frac{E_{b1} - E_{b2}}{\frac{1-\epsilon_1}{\epsilon_1 A_1} + \frac{1}{A_1 F_{12}} + \frac{1-\epsilon_2}{\epsilon_2 A_2}} = \frac{\sigma T_1^4 - \sigma T_2^4}{\frac{1-\epsilon_1}{\epsilon_1 A_1} + \frac{1}{A_1 F_{12}} + \frac{1-\epsilon_2}{\epsilon_2 A_2}} \tag{5.19}$$

Therefore, the only unknowns are the emissivity of both surfaces and the shape factor. The emissivity is a material constant. The appropriate electrical network with corresponding shape factors must be determined to resolve the heat transfer by radiation. To facilitate determining the shape factors, the reciprocal rule can be used

$$A_1 F_{12} = A_2 F_{21} \tag{5.20}$$

5.3. Compartment B

Compartment B is the compartment storing the hydrogen gas. It is in direct contact with the inner membrane and the storage floor, which is assumed to be well insulated and, therefore, does not exchange heat with the gas. Furthermore, hydrogen is the main component in the compartment. It is transparent to thermal radiation and neither emits nor absorbs radiation. Hence, only the heat transfer due to convection between the inner membrane and the gas will be considered. The convection is assumed to be natural as the volumetric flow rate of the in- and outlet of compartment B is negligible compared to the compartment's maximum volume. Furthermore, the inner membrane is seen as a horizontal isothermal disc. The amount of heat exchanged depends greatly on whether the disc the discs cools or heat the gas. Due to buoyancy, hot air rises. Thus, if the disc is cooling the gas compartment, it is always in contact with the hot air, leading to a higher temperature difference and, thus, more heat exchange. The inverse is true if the plate is heated. The minimal temperature difference will lead to a small amount of heat transfer. The correlations for natural convection from a uniform horizontal disc are given by Jaffer [59]. Here, the radius of the disc is the characteristic length. For a heated plate facing up or a cooled plate facing down:

$$\overline{Nu}_r = 0.637 \left[(1 - \frac{1}{\sqrt{8}})^{0.5} + (\frac{0.637}{4} Ra^{1/3})^{0.5} \right]^2 \tag{5.21}$$

For a heated plate facing down or a cooled plate facing up:

$$\overline{Nu}_r = \frac{1.363}{4} + \frac{1.363^{(6/5)}}{2^{(7/5)}} \left[\left(\frac{Ra}{(1 + \frac{0.5}{Pr})\sqrt{(1/3)}} \right)^{1.73205081} \right]^{1/5} \tag{5.22}$$

The Rayleigh, Ra, and Prandtl, Pr, numbers can be determined using Equation 5.6, Equation 5.4 and Equation 5.5 as they are only dependent on process conditions and geometrical parameters. Using the found values and Equation 5.3, an average heat transfer coefficient between the gas in compartment B and the inner membrane can be determined. This leads to the following equation.

$$\begin{aligned} \dot{Q}_{\mathsf{B}\to\mathsf{inner}} &= \overline{h}_{\mathsf{B,inner}} \times A^{\mathsf{inner}} \times (T^{\mathsf{B}} - T^{\mathsf{inner}}) \\ &= -\overline{h}_{\mathsf{B,inner}} \times \pi (R^{\mathsf{inner}})^2 \times (T^{\mathsf{B}} - T^{\mathsf{inner}}) \end{aligned} \tag{5.23}$$

The net rate of energy transferred by heat to compartment B is thus

$$\begin{aligned} \dot{Q}^{\mathsf{B}} &= -\dot{Q}_{\mathsf{B}\to\mathsf{inner}} \\ &= \overline{h}_{\mathsf{B,inner}} \times \pi (R^{\mathsf{inner}})^2 \times (T^{\mathsf{B}} - T^{\mathsf{inner}}) \end{aligned} \tag{5.24}$$

5.4. The inner membrane

The inner membrane is in contact with both gasses in compartments A and B. Hence, heat is exchanged by convection between the membrane and the two gases. Furthermore, the membrane was assumed to be uniform in temperature, meaning no conduction inside the membrane occurs.

5.4.1. Convection between the inner membrane and gas compartment A

The heat exchanged with the air compartment depends on the air's flow speed. The convection can either be natural, forced or mixed. To determine the flow speed inside the compartment, the following assumptions have been made based on the work of Avila-Lopez et al. [36] in which the mean air speed was estimated from the volumetric flow rate of the air ($\dot{V}^{\mathsf{A}}$) and the mean cross-sectional area (A_{flow}) of the compartment. First, it was assumed that the compartment could be approached by a cuboid with a squared base of the same area as the inner membrane, see Figure 5.2. The mean height of the

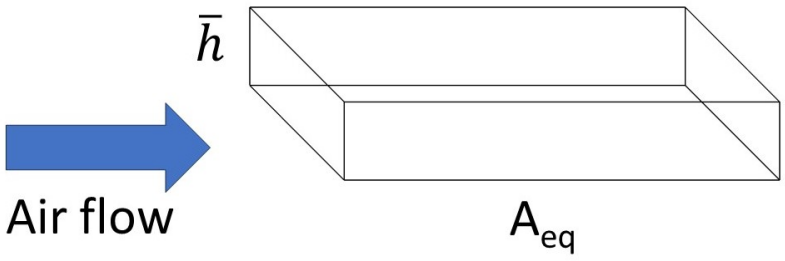

Figure 5.2: Assumed configuration for the determination of the air speed

cuboid is the ratio between the actual volume of the compartment, in this case, V^{a}, and the area of the membrane, which is also the area of the base of the cuboid.

$$\overline{h} = \frac{V^{\mathsf{a}}}{A_{\mathsf{eq}}} \tag{5.25}$$

Thus, using the geometry of the cuboid Figure 5.2, the mean cross-sectional area through which the air flows is equal to

$$A_{\mathsf{flow}} = \overline{h}\sqrt{A_{\mathsf{eq}}} \tag{5.26}$$

The volumetric flow rate of the air can be determined from the mass balance using the ideal gas law. The mol flow through the pressure relief valve of compartment A is assumed to determine the volumetric flow rate through the compartment.

$$\dot{V}^{\mathsf{A}} = \frac{\dot{N}^{\mathsf{A}}_{i,\mathsf{out}} R T^{\mathsf{A}}}{P^{\mathsf{A}}} \tag{5.27}$$

The mean air speed is then determined

$$u^{\mathsf{A}} = \frac{\dot{V}^{\mathsf{A}}}{A_{\mathsf{flow}}} \tag{5.28}$$

Using the geometry parameters and the properties of the air in compartment A, dependent on its composition, the Grashof and Reynolds number can be determined using Equation 5.5 and Equation 5.7. This finally leads to the Richardson number necessary to decide on the convection regime, Equation 5.8.

5.4.1.1. Natural convection

The convection between the inner membrane and the air in compartment A is natural if the Richardson number exceeds 10. In this case, the membrane is assumed to be an isothermal flat plate. Equation 5.21 or Equation 5.22 should be used depending on whether the membrane temperature is superior to the gas temperature.

5.4.1.2. Forced convection

If the Richardson number is smaller than 0.1, the convection between the inner membrane and the air in compartment A is forced. The flow regime is essential when considering forced convection over an isothermal flat plate. A laminar boundary layer forms from the leading edge. This layer transforms into a turbulent boundary layer at Re_{x}. The transition from laminar to turbulent flow significantly influences the heat transfer coefficient.

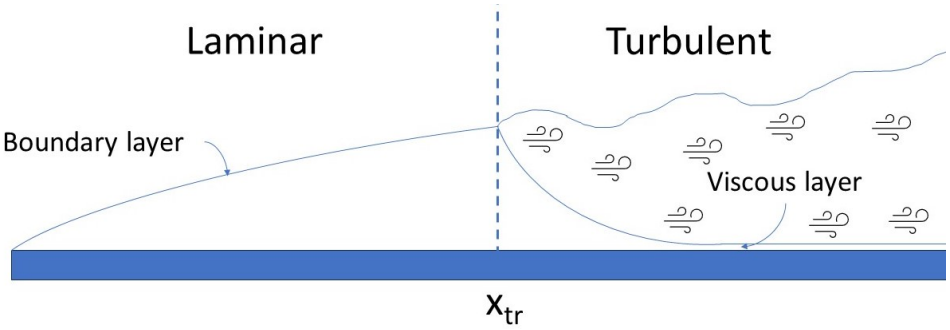

Figure 5.3: Forced flow along a flat plate, showing boundary layer growth and the development of a turbulent boundary layer at distance x_{tr}

To determine the average heat transfer coefficient, it must be evaluated over the laminar and the turbulent part of the flow

$$\overline{h_c} = \frac{1}{L}\left[\int_0^{x_{tr}} h_{c,laminar}dx + \int_{x_{tr}}^{x_L} h_{c,turbulent}dx\right] \tag{5.29}$$

According to Mills [56], this leads to the following correlation for the average Nusselt number. Where the Reynolds number at which transition occurs (Re_{tr}) is equal to 5×10^5.

$$\overline{Nu} = 0.664 Re_{tr}^{\frac{1}{2}} Pr^{\frac{1}{3}} + 0.036 Re_L^{0.8} Pr^{0.43}\left[1 - \left(\frac{Re_{tr}}{Re_L}\right)^{0.8}\right] \; ; \; 0.7 < Pr < 400 \tag{5.30}$$

For flows with $Re < 5 \times 10^5$, the flow is considered laminar, Equation 5.30 reduces to

$$\overline{Nu}_L = 0.664 Re_L^{\frac{1}{2}} Pr^{\frac{1}{3}} \; ; \; Pr > 0.5 \tag{5.31}$$

In both cases, the characteristic length L, necessary in determining the Reynolds number, is taken as half of the plate's diameter, thus the membrane's radius.

5.4.1.3. Mixed convection

Both natural and forced convections happen simultaneously if $0.1 < Ri < 10$. In this case, both processes need to be considered. The direction of the buoyancy force relative to the direction of the flow strongly influences the effect of buoyancy on the heat transferred. In the case considered here, the buoyancy is in a perpendicular (vertical) direction compared to the airflow (horizontal). This means the flow is transverse. Incropera et al. [57] give the following correlation for transverse flow over a horizontal plate.

$$\overline{Nu}^{3.5} = \overline{Nu}_F^{3.5} + \overline{Nu}_N^{3.5} \tag{5.32}$$

Where subscripts F and N represent forced and natural convection.

5.4.2. Radiation towards floor

The floor of the storage is assumed to be well-insulated. Therefore, it does not exchange heat with its environment.

$$\dot{Q}_{inner \to floor} = 0 \tag{5.33}$$

As the gas in compartment B is assumed to be fully transparent to thermal radiation and the two membranes from an enclosure, the radiation scheme between the inner membrane and the floor is represented by Figure 5.1. Therefore, the heat transferred from the inner membrane to the floor through thermal radiation is determined using Equation 5.19. This gives

$$\dot{Q}_{inner \to floor} = \frac{\sigma(T_{inner}^4 - T_{floor}^4)}{\frac{1-\epsilon_{inner}}{\epsilon_{inner} A_{inner}} + \frac{1}{A_{inner} F_{inner \to floor}} + \frac{1-\epsilon_{floor}}{\epsilon_{floor} A_{floor}}} \tag{5.34}$$

The shape factor can be determined using the reciprocal rule, Equation 5.20. The floor is flat and does, therefore, only radiate to the inner membrane ($F_{floor \to inner} = 1$).

$$A_{inner} F_{inner \to floor} = A_{floor} F_{floor \to inner} = A_{floor} \tag{5.35}$$

5.4.3. Radiation towards outer membrane

As the gas in compartment A is assumed to be fully transparent to thermal radiation and the two membranes from an enclosure, the radiation scheme between the inner and outer membrane is represented by Figure 5.1. Therefore, the heat transferred from the inner membrane to the outer membrane through thermal radiation is determined using Equation 5.19. This gives

$$\dot{Q}_{\text{inner}\to\text{outer}} = \frac{\sigma(T^4_{\text{inner}} - T^4_{\text{outer}})}{\frac{1-\epsilon_{\text{inner}}}{\epsilon_{\text{inner}} A_{\text{inner}}} + \frac{1}{A_{\text{inner}} F_{\text{inner}\to\text{outer}}} + \frac{1-\epsilon_{\text{outer}}}{\epsilon_{\text{outer}} A_{\text{outer}}}} \tag{5.36}$$

Due to the geometry of the system, see Figure 2.6, it was assumed that the side of the inner membrane facing the outer membrane is always concave. Therefore, the inner membrane only radiates to the outer membrane and hence $F_{\text{inner}\to\text{outer}} = 1$.

5.4.4. Conclusion heat transfer inner membrane

The net rate of energy transferred by heat to the inner membrane consists of four elements: the heat transferred by convection with the gas in compartments A and B, and the radiative heat transfer with the outer membrane.

The heat transfer by convection from the gas in compartment B is determined by Equation 5.23. In contrast, the heat transfer by convection from the gas in compartment A to the inner membrane depends on the convection type. The steps described above should be followed to determine the flow speed in gas compartment A. From this, the kind of convection and the appropriate Nusselt number follow, leading to the average heat transfer coefficient and, thus, the total energy flow.

$$\dot{Q}_{\text{A}\to\text{inner}} = \overline{h}_{\text{A,inner}} \times A_{\text{inner}} \times (T^{\text{A}} - T^{\text{inner}}) \tag{5.37}$$

The heat transferred by radiation towards the inner membrane from the floor is the inverse of Equation 5.34, and the heat transfer by thermal radiation from the outer to the inner membrane is the inverse of Equation 5.36. Therefore, the total heat transfer towards the inner membrane becomes

$$\dot{Q}^{\text{inner}} = \dot{Q}_{\text{B}\to\text{inner}} + \dot{Q}_{\text{A}\to\text{inner}} - \dot{Q}_{\text{inner}\to\text{outer}} - \dot{Q}_{\text{inner}\to\text{floor}} \tag{5.38}$$

5.5. Compartment A

The heat transfer towards the gas in compartment A is only due to convection, as it is assumed the gas is transparent to radiative heat transfer. The energy flow received by gas compartment A due to convection with the inner membrane is the inverse of the energy flow determined with Equation 5.37.

$$\dot{Q}_{\text{inner}\to\text{A}} = -\dot{Q}_{\text{A}\to\text{inner}} \tag{5.39}$$

A new heat transfer coefficient must be calculated to determine the energy exchanged between gas compartment A and the outer membrane due to convection. This is done using the methodology described in section 5.3. The only difference is the usage of the area of the outer membrane as the area of the squared base of the cuboid. Again, the convection can be natural, forced or mixed depending on the flow speed of the gas. The total energy flow from compartment A to the outer membrane is:

$$\dot{Q}_{\text{A}\to\text{outer}} = \overline{h}_{\text{A,outer}} \times A_{\text{outer}} \times (T^{\text{A}} - T^{\text{outer}}) = -\dot{Q}_{\text{outer}\to\text{A}} \tag{5.40}$$

The total heat flow towards gas compartment A becomes

$$\dot{Q}^{\text{A}} = \dot{Q}_{\text{inner}\to\text{A}} + \dot{Q}_{\text{outer}\to\text{A}} \tag{5.41}$$

5.6. The outer membrane

The heat transfer mechanisms between the outer membrane and the surroundings constitute a highly intricate and multifaceted process. It consists of multiple flows of energy by convection and thermal radiation.

5.6.1. Convection between the outer membrane and gas compartment A

The outer membrane exchanges heat by convection with the gas in compartment A. The total energy flow is calculated using Equation 5.40.

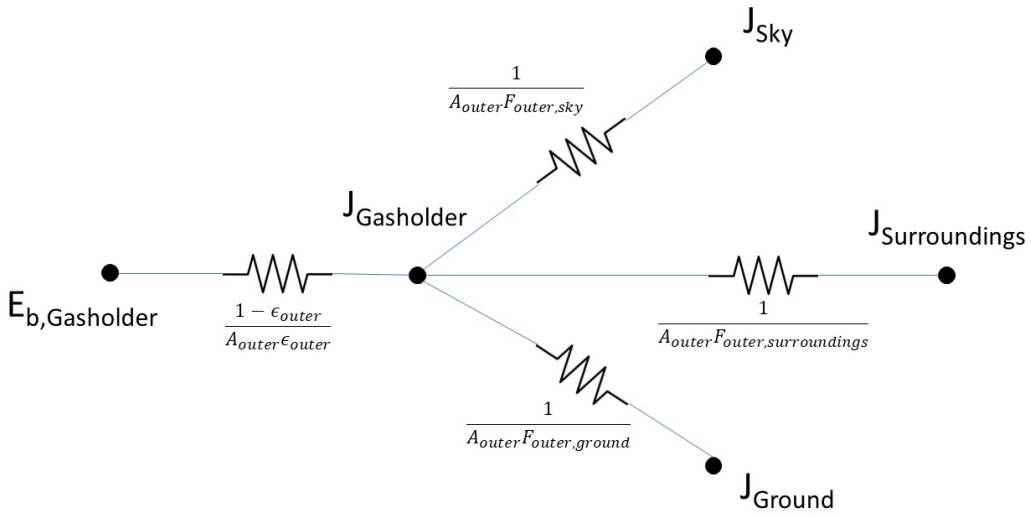

Figure 5.4: Thermal radiation scheme of a gasholder

5.6.2. Convection between the outer membrane and the ambient air

The outer membrane and the air will exchange heat by convection. The type of convection is dependent on the presence of wind. If no wind is present, the convection is assumed to be natural, meaning that $u_{\text{wind}} = 0$. The membrane is then viewed as a flat horizontal plate. If the temperature of the membrane is greater than the ambient air temperature ($T^{\text{outer}} > T^{\text{Env}}$), Equation 5.21 should be used. In the oppsoite case ($T^{\text{outer}} < T^{\text{Env}}$), Equation 5.22 should be used. In both cases, the characteristic length L, necessary in determining the Rayleigh number, is taken as half of the plate's diameter, thus the outer membrane's radius.

When the wind is blowing, meaning $u_{\text{wind}} \neq 0$, the convection is assumed to be forced. The membrane is considered to be a flat horizontal plate. The value of the associated Reynolds number decides if Equation 5.30 or Equation 5.31 should be used.

Determining the average Nusselt number leads to the average heat transfer coefficient and, hence, to the total energy flow from the ambient air to the outer membrane.

$$\dot{Q}_{\text{Env}\rightarrow\text{outer,convection}} = \overline{h}_{\text{Env,outer}} \times A_{\text{outer}} \times (T^{\text{Env}} - T^{\text{outer}}) \tag{5.42}$$

5.6.3. Radiation exchange with inner membrane

The outer membrane exchanges heat through thermal radiation with the inner membrane as the gas in compartment A is transparent. The flow of heat from the inner membrane to the outer membrane is calculated using Equation 5.36.

5.6.4. Long wave radiation exchange with environment

The outer membrane will exchange heat through thermal radiation with its surroundings. The surroundings are divided into three parts: the sky, the ground and the surrounding environment. The surrounding environment contains all objects near the gasholder, such as another gasholder, solar panels, etc. All surroundings are assumed to have the same uniform temperature T_{Env}. Only the radiosities of the components other than the gasholder have been considered for simplicity. Furthermore, the thermal radiation between the components other than the gasholder has been ignored. This leads to the radiation scheme visible in Figure 5.4 and the following relation for the net transfer of thermal radiation.

$$\dot{Q}_{\text{outer}\rightarrow\text{Env,radiation}} = \frac{\sigma\left(T^4_{\text{outer}} - T^4_{\text{sky}}\right)}{\frac{1-\epsilon_{\text{outer}}}{A_{\text{outer}}\epsilon_{\text{outer}}} + \frac{1}{A_{\text{outer}}F_{\text{outer,sky}}}} + \frac{\sigma\left(T^4_{\text{outer}} - T^4_{\text{Env}}\right)}{\frac{1-\epsilon_{\text{outer}}}{A_{\text{outer}}\epsilon_{\text{outer}}} + \frac{1}{A_{\text{outer}}F_{\text{outer,Env}}}} + \frac{\sigma\left(T^4_{\text{outer}} - T^4_{\text{ground}}\right)}{\frac{1-\epsilon_{\text{outer}}}{A_{\text{outer}}\epsilon_{\text{outer}}} + \frac{1}{A_{\text{outer}}F_{\text{outer,ground}}}} \tag{5.43}$$

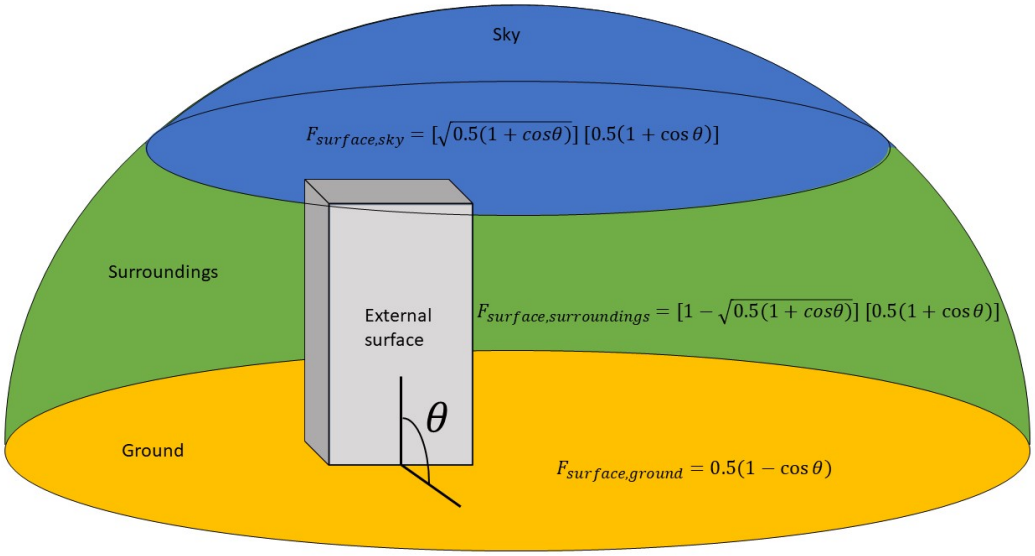

Figure 5.5: Schematic representation of the enclosure and the view factors from an external surface to the sky, surroundings, and ground, reproduced from [36]

To determine the view factors necessary for Equation 5.43, the same method as Avila-Lopez et al. [36] use is followed. They base their findings on the Thermal Analysis Research Program (TARP) manual [60]. TARP has been developed for the thermal analysis of buildings [1]. It states that the view factors of an object towards the ground, surroundings and sky can be approached based on the tilt angle of the external surface θ, see Figure 5.5. The tilt angle is the angle between the Z-axis and the normal to the surface. The TARP manual states that the view factor between a surface and the ground is

$$F_{\text{surface,ground}} = 0.5(1 - \cos\theta) \tag{5.44}$$

This means that the sum of the other view factors, to the surroundings and the sky, is $0.5(1+\cos\theta$. The split factor, $\gamma = \sqrt{0.5(1+\cos\theta)}$, is then introduced, leading to the following equations for remaining view factors.

$$F_{\text{surface,surroundings}} = [1 - \sqrt{0.5(1+\cos\theta)}][0.5(1+\cos\theta)] \tag{5.45}$$

$$F_{\text{surface,sky}} = [\sqrt{0.5(1+\cos\theta)}][0.5(1+\cos\theta)] \tag{5.46}$$

Of course, the gasholder is a hemisphere and only consists of one surface. Due to the curvature of the surface of a hemisphere, it is impossible to determine a tilt angle between the surface and the ground. Hence, the gasholder is taken as a cone of which the radius of the base and the height are equal. This leads to a tilt angle of 135°or $\frac{3}{4}\pi$. The view factors become $F_{\text{outer,ground}} = 0.146$, $F_{\text{outer,Env}} = 0.065$ and $F_{\text{outer,sky}} = 0.789$.

5.6.5. Shortwave solar irradiance absorbed by the outer membrane

The shortwave solar irradiance absorbed by the outer membrane depends on the solar irradiance on the Earth's surface at the location of the gasholder, the absorptivity, the outer membrane area and the view factor between the outer membrane and the sky. The solar irradiation reflected by the ground and the surroundings is ignored.

$$\dot{Q}_{\text{sun}\rightarrow\text{outer}} = G_{\text{surface}}\alpha_{\text{outer}}A_{\text{outer,solar}}F_{\text{surface,sky}} \tag{5.47}$$

Here, I_{surface} is the total solar irradiance on the surface of the outer membrane in [W/m^2], α_{outer} is the fraction of solar irradiation absorbed, A_{outer} is the area of the outer membrane [m^2] and $F_{\text{surface,sky}}$ is the view factor between the cover and the sky, determined with Equation 5.46.

[1] It is still used in the open source software EnergyPlus, see [61]

5.6.6. Conclusion heat transfer outer membrane

The net rate of energy transferred by heat to the outer membrane consists of six elements: the heat transferred by convection with the gas in compartment A, Equation 5.40, the outside air, Equation 5.42 the radiative heat transfer between the outer membrane and the inner membrane, Equation 5.36, the external surroundings, Equation 5.43 and the sun, Equation 5.47.

$$\dot{Q}^{\text{outer}} = \dot{Q}_{\text{A}\rightarrow\text{outer}} + \dot{Q}_{\text{Env}\rightarrow\text{outer,convection}} + \dot{Q}_{\text{Rain}\rightarrow\text{outer}} + \dot{Q}_{\text{inner}\rightarrow\text{outer}} - \dot{Q}_{\text{outer}\rightarrow\text{Env,radiation}} + \dot{Q}_{\text{sun}\rightarrow\text{outer}} \quad (5.48)$$

5.7. Heat transfer model limitations

Although the heat transfer will reasonably estimate real-world heat exchange in the system, a margin of error still exists. Several assumptions have been made in chapter 5. First, the correlations to assess the Nusselt numbers are empirical models for specific cases. The used cases do not always represent the reality of the modelled system. For example, the assumption that the membranes of the gasholder can be represented by flat plates heated up or down could over- or underestimate the total heat exchanged. In reality, the membranes would form a hemispherical shape if gas compartment B were now considered, with the inner membrane being hotter than the gas. Due to buoyancy, the hot gas rises to the top of the compartment. If the inner membrane were flat, it would be in contact with the hottest part of the gas mixture, but due to the hemispherical shape of the membrane, the parts near the base, which are nearly vertical, are in contact with colder parts of the gas increasing the heat transfer. The total heat transferred is thus underestimated. The opposite is true: the transferred heat is overestimated if the gas is warmer than the membrane. The precise use of correlations determined for this use case would give the best results. Furthermore, the radiative heat transfer between the outer member and the environment depends on estimated values for the view factors. The temperature values of the ground and the environment are also unknown. They have been assumed to be equal to the ambient air temperature.

Furthermore, the model considered the storage floor well insulated, meaning it exchanged no heat. In reality, the floor may act as a heat sink, as concrete's heat capacity and density are high. This means that the concrete slab can absorb a lot of energy. It would cool down the system during the summer, while the stored energy would be released during the winter, heating the storage. Considering the concrete floor in the thermal model would flatten the peaks in temperature throughout the year.

Finally, several weather phenomena have been neglected. All forms of precipitation could have a significant influence. Rain would be the most interesting due to its many occurrences at the specified location during the year. Rain or any other form of precipitation introduces an extra heat transfer term for the outer membrane, which can either be conductive or convective depending on whether the matter rests or flows over the cover.

6

Collection and pre-processing of input data

In chapter 4 and chapter 5, it has become clear the system depends on many unknown variables. These variables can be time- and location-dependent, which is the case for the necessary weather data. These variables can also be constants depending on the material type used or the molecules considered. This chapter will cover collecting and pre-processing the unknowns necessary to the model.

6.1. Weather data

The research aims to determine the behaviour of a double membrane gasholder used for hydrogen storage in reaction to weather conditions; finding appropriate weather conditions is essential. The data should represent the range of weather phenomena for the location in question and, at the same time, give annual averages that are consistent with the long-term averages. This type of data is called a typical meteorological year (TMY). A TMY contains hourly data for one year consisting of solar radiation values and meteorological elements. Each month is randomly selected out of at least 12 years. For this project, the TMY has been taken from the Photovoltaic Geographical Information System provided by the European Union [62]. This data can be downloaded directly as an Excel file or by an API in Python using the IOtools package from the PVLIB library [63]. From the returned TMY, the following data has been used:

- The air temperature T_{air} [°C]
- The relative humidity of the air RH [%]
- The global irradiance on the horizontal plane $G(h)$ [W/m^2]
- The bean/direct irradiance on the horizontal plane is always normal to sunrays $Gb(h)$ [W/m^2]
- Diffuse irradiance on the horizontal plane $Gd(h)$ [W/m^2]
- The wind speed at a height of 10 meters WS_{10m} [m/s]
- The surface air pressure P_{air} [Pa]

6.1.1. Effective sky temperature

Data for the effective sky temperature, T_{sky}, used in Equation 5.43, is often unavailable as it is difficult to measure. It is an experimentally determined index. Simple correlations exist approaching the effective sky temperature [64]. In this case, there has been chosen for an empirical model developed by Aubinet [65]. Aubinet based his correlation on meteorological data gathered at Gembloux in Belgium, which is close to Eerbeek, the location of the hydrogen storage, and has similar weather conditions. Furthermore, Aubinet accounted for the cloud coverage in his correlation. The occurrence of clouds is not rare in the Netherlands and has a strong effect on atmospheric radiation. H_2O molecules absorb solar and the Earth's radiation, heating the sky. The model has a correlation coefficient of 0.958.

$$T_{\text{sky}} = 94 + 12.6 \ln P_v - 13K_t + 0.341T_{\text{air}} \tag{6.1}$$

Here, P_v is the partial pressure of water in the air [Pa], K_t is the clearness index, and T_{air} [K] is the temperature of the ambient air. It is defined as the global solar irradiation on the horizontal plane over extraterrestrial solar irradiation on a horizontal plane, E_{a} [W/m^2].

$$K_t = \frac{G(h)}{E_{\text{a}}} \tag{6.2}$$

The extraterrestrial radiation is approached by the following correlation [66]

$$E_{\text{a}} = E_{\text{sc}} \times \left(\frac{R_{\text{av}}}{R}\right)^2 \tag{6.3}$$

E_{sc}, 1367 [W/m^2], is the solar constant. R_{av} [m] is the average distance Earth-Sun distance throughout the year while R [m] is the actual Earth-Sun distance depending on the day of the year. The ratio between the average Earth-Sun distance over the actual distance is approached using:

$$\begin{aligned}\left(\frac{R_{\text{av}}}{R}\right)^2 &= 1.00011 + 0.034221\cos b + \frac{0.00128}{\sin b} + 0.000719\cos 2b + 0.000077\sin 2b \\ b &= 2\pi\frac{DOY}{365}\end{aligned} \tag{6.4}$$

DOY stands for day of the year, indicating the integer from 1 to 365 representing the day of the year.

The partial pressure of water vapour is calculated using the saturation pressure of water in the air, Equation 4.34 and the relative humidity of the air.

$$p_v = Psat * \frac{RH}{100} \tag{6.5}$$

6.1.2. Total solar irradiance on the gasholder

The total solar irradiance on the outer surface of the gasholder, I_{surface} is challenging to determine for a hemisphere. Furthermore, it depends on several factors, including the position of the sun taken from the considered location.

The hourly position of the sun at a specific location can be extracted using the PVLIB package [67]. The command `pvlib.solarposition.get_solarposition` returns a data frame containing the solar azimuth angle [°] and the solar zenith angle [°] for every required timestamp. The solar azimuth angle indicates the horizontal angle from the north, indicated by 0 °. If the sun is positioned precisely in the east, this angle will equal 90 °. The zenith angle is the elevation angle of the sun. It describes the altitude of the sun.

To facilitate the calculation of the total solar irradiance on the gasholder's surface, it has been represented as a pyramid. Its square base is fixed to the ground and covered by the other sides. Therefore, it is never exposed to solar irradiance. The four triangles forming the pyramid's sides are all equal in size. The total area of the triangles is the outer membrane surface area. It has been assumed that the triangles are tilted 45 °, and their tangent vectors point towards the four windrooster directions. In other words, their azimuths are equal to 0 °, 90 °, 180 °, and 270 °, respectively.

Using the `pvlib.irradiance.get_total_irradiance` command, it is then possible to determine the total irradiance falling on each plane. This command requires surface tilt and azimuth angles, the solar zenith and azimuth angles, and the direct normal, global horizontal and diffuse horizontal irradiance. It returns a data frame containing the total in-plane irradiance and its beam, sky diffuse, and ground-reflected components. The total in-plane irradiances on each of the four planes can be added and divided by four. The planes have the same total surface to find the total irradiance falling on the surface of the gasholder.

6.1.3. Corrected windspeed at gasholder height

The wind speed data collected in the TMY are given at a height of 10 meters. This standard measurement needs adjustment to represent the windspeed at the gasholder height. At low altitudes below 60 meters, the wind follows a logarithmic profile. The log-wind profile, an empirical relationship, is commonly used to determine the vertical distribution of the horizontal wind speeds.

$$u_{\text{z}} = u_{10}\log\left[\frac{z/z_0}{10/z_0}\right] \tag{6.6}$$

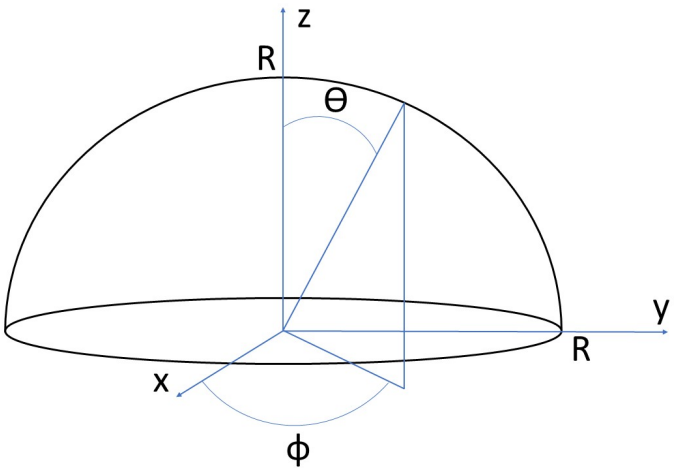

Figure 6.1: Geometry of the hemisphere

Here u_z [m/s] is the wind speed at height z [m], u_{10} is the wind speed at the height of 10 meters, and z_0 is the surface roughness length [m]. It is assumed that the gasholder is positioned in an open area. Therefore, the surface roughness is 0.1 m, representing low crops and occasional large obstacles. The wind speed has been determined at the surface average height of the hemisphere. The average height of the surface of a hemisphere is determined by summing the height of all the points on the hemisphere and dividing by the total number of points, giving the following integral.

$$\overline{z} = \frac{\int\int_S z dA}{\int\int_S dA} \tag{6.7}$$

Polar coordinates were used to solve Equation 6.7. The definition of the axis and the angles can be found in Figure 6.1. The denominator double integral equals the disc's surface area forming the base: πR^2. The height z of the hemisphere's surface equals $\sqrt{R^2 - x^2 - y^2}$.

$$\begin{aligned} \overline{z} &= \frac{1}{A}\int\int_S z dA \\ &= \frac{1}{\pi R^2}\int_0^R \int_0^R \sqrt{R^2 - x^2 - y^2} dx dy \\ &= \frac{1}{\pi R^2}\int_0^{2\pi} \int_0^R \sqrt{R^2 - r^2} r dr d\phi \\ &= \frac{2R}{3} \end{aligned} \tag{6.8}$$

6.2. Hydrogen production

The hydrogen entering compartment B is produced from electricity from a nearby solar farm. The solar farm consists of 2100 panels. It has been assumed that the panels are oriented to the south, their azimuth angle equals 180°, and their tilt angle equals 35°. The total power output per solar panel can be determined using the same solar angles described in subsection 6.1.2 and the same method to determine the total irradiance falling on each solar panel.

$$P_{\text{DC}} = \frac{I_{\text{poa}}}{I_{\text{ref}}} P_{\text{DC0}} \left(1 + \gamma(T_{\text{cell}} - T_{\text{ref}})\right) \tag{6.9}$$

Here, P_{DC} is the total power output of the panel [W], I_{ref} is the reference irradiance equal to 1000 W/m^2, P_{DC0} is the reference power rating [W] of the solar panel at the reference temperature, T_{ref}, 25 °C, γ is the temperature coefficient [%] and T_{cell} [°C] is the cell temperature of the panel. This formula is called by the `pvlib.pvsystem.pvwatts_dc` command. The inputs are the total solar irradiance on the panel, the reference power rating and the cell temperature. GKA182N144 solar panels [68] have been used

in the simulations. The reference power of the panels equals 580W, and their gamma value equals -0.0003%. The panels' temperature is determined using the `pvlib.temperature.faiman` command. The inputs are the total irradiance falling on the panels, the air temperature and the wind speed. To obtain the power output of all the panels, the power output should be multiplied by the number of panels. The panels are directly coupled to the electrolyser. It has been assumed that the losses in the cables are negligible. The electrolyser uses 60 kWh of electricity to produce one kilo of hydrogen. The hydrogen production can thus be determined using the following formula:

$$\dot{N}_{\mathrm{H_2produced}} = \frac{P_{\mathrm{DC}} \times 2100}{60 \times 1000} \frac{M_{\mathrm{H_2}}}{3600} \tag{6.10}$$

Here, $M_{\mathrm{H_2}}$ is the molar mass of hydrogen [kg/mol]. The division by 3600 is necessary to obtain the mol flow of hydrogen produced, $N_{\mathrm{H_2produced}}$ in mol per second. Before entering the system, the hydrogen is cooled to 3°C to remove part of the water present after production. It enters the system with a grade of 2.5. Traces of O_2 and H_2O are present. Their concentration is assumed to be 2000 PPM and 3000 PPM, respectively.

Table 6.1: Table containing the mol fractions of the considered molecules in the hydrogen inlet stream, $\dot{N}_{\mathrm{in}}^{\mathrm{B}}$, of compartment B

Molecule	N_2	O_2	H_2	H_2O gas	H_2O liquid
Mol fraction [-]	0	0.002	0.995	0.007480946284774646	0.003

6.3. Hydrogen demand

The storage's hydrogen outlet is connected to the hydrogen compressor, which works at a constant input debit of 400 Nm^3/h. The ideal gas law and the associated pressure and temperature values for normal conditions can be used to translate this into a mol flow. This results in a mol flow leaving gas compartment B of the storage, $\dot{N}_{\mathrm{out}}^{\mathrm{B}}$ of approximately 2.57 mol per second. The composition of the hydrogen stream leaving compartment B depends on the gas mixture inside the gasholder, assuming that the gases in the compartments are well mixed and that the fluids exiting the storage consist solely of gas. The compression process starts once the storage is fully filled to prevent shutting off the compressor as much as possible. It is stopped once the storage is completely empty. The storage is empty once gas compartment B is at 5% of its maximal value.

6.4. Air inlet and air composition

Compartment A is used to pressurise the storage. The air enters at a constant mol flow. This mol flow, $\dot{N}_{\mathrm{in}}^{\mathrm{A}}$, is assumed to be 3 mol per second. It is essential to take an air inlet superior to the hydrogen outlet; if not, the air in compartment A can not pressurise the system as more gas is leaving the system, leading to a loss in pressure. Its composition is dependent on the weather conditions. The relative humidity of the air, together with the air temperature and pressure, dictates the mol fraction of H_2O in the air.

$$x_{\mathrm{H_2O,air}} = \frac{P_{\mathrm{sat,H_2O,air}}}{P_{\mathrm{air}}} \times \frac{RH_{\mathrm{H_2O,air}}}{100} \tag{6.11}$$

Using the air temperature [°C] and Equation 4.34, the saturation pressure of H_2O in the air, $P_{\mathrm{sat,H_2O,air}}$ [Pa], can be determined. The relative humidity, RH [%], determines the actual partial water pressure in the air. The partial pressure of h_2O in the air divided by the air pressure, P_{air} [Pa] returns the mol fraction of H_2O in the air, $x_{\mathrm{H_2O,air}}$.

On average, there is 0.6 PPM of H_2 in the air [69]. It has been assumed that if the air contains no H_2O, it consists of 784999.4 PPM of N_2 and 215000 PPM of O_2. The presence of H_2O in the air reduces the mol fractions of N_2 and O_2 by the same amount. The mol fraction of H_2 is assumed to remain unchanged.

6.5. User determined variables

The model's initial conditions are user-defined variables. The default initial temperatures are the outside air temperature for gas compartment A and the outer and inner membranes, but these can also be

Table 6.2: Table containing the assumed mol fractions of the considered molecules in the air

Molecule	N_2	O_2	H_2	H_2O gas	H_2O liquid
Mol fraction	0.7849994 - $\frac{x_{H_2O,air}}{2}$	0.215- $\frac{x_{H_2O,air}}{2}$	0.0000006	$x_{H_2O,air}$	0

Table 6.3: Physical constants used in the model

Description	Symbol	Value	Unit
Universal gas constant	R	8.31446261815324	J/(mol·K)
Normal pressure	P_{norm}	101325	Pa
Atmospheric pressure	P_{atm}	101325	Pa
Normal temperature	T_{norm}	273.15	K
Boltzmann constant	k_B	1.380649×10^{-23}	J/K
Avogadro constant	N_A	6.022140857×10^{23}	mol^{-1}
Stefan-Boltzmann constant	σ	5.6697×10^{-8}	$W/(m^2\cdot K^4)$

entered manually. The gas in compartment B is initially considered at 276.15K, the temperature at which the H_2 enters the system. The initial volume of compartment A is a user-defined variable. It is entered as a percentage. The volume of compartment A determines the volume of gas compartment B. The initial compositions are the air composition for gas compartment A and the hydrogen inlet composition for gas compartment B. The number of mols in the compartments is determined using the ideal gas law with the given temperature, pressure and volume. The tool has been built to provide results at any location. It is necessary to provide latitudinal and longitudinal coordinates of the desired storage location. These coordinates will be used to provide the weather data for the location. The user must also provide a starting day and the number of days to simulate.

6.6. Constants

A large number of constants have been gathered. They have been divided into three groups and three tables: Table 6.3, Table 6.4 and Table 6.5.

Table 6.4: Molar Masses and Molecular Diameters

Description	Symbol	Value	Unit
Molar mass of N_2	M_{N2}	28.01340	g/mol
Molar mass of O_2	M_{O2}	31.99880	g/mol
Molar mass of H_2	M_{H2}	2.01568	g/mol
Molar mass of H_2O	M_{H2O}	18.01528	g/mol
Molar mass of PVC chain unit	M_{PVC}	62.5	g/mol
Diameter of N_2 molecule	d_{N2}	364×10^{-12}	m
Diameter of O_2 molecule	d_{O2}	346×10^{-12}	m
Diameter of H_2 molecule	d_{H2}	289×10^{-12}	m
Diameter of PVC molecule	d_{PVC}	0.6×10^{-9}	m

Table 6.5: Properties of Gases at 275 K, all values have extrapolated from the reported in [56]

Description	Symbol	Value	Unit
Heat capacity of H_2 at constant pressure	$c_{p,\mathrm{H_2}}$	30.2654352	J/(mol·K)
Heat capacity of H_2 at constant volume	$c_{v,\mathrm{H_2}}$	21.9509725	J/(mol·K)
Thermal diffusivity of H_2	$\alpha_{\mathrm{H_2}}$	9.55×10^{-5}	m^2/s
Prandtl number of H_2	$Pr_{\mathrm{H_2}}$	0.67	-
Thermal conductivity of H_2	$k_{\mathrm{H_2}}$	0.1895	W/(m·K)
Density of H_2	$\rho_{\mathrm{H_2}}$	0.08927790439324858	kg/m^3
Heat capacity of N_2 at constant pressure	$c_{p,\mathrm{N_2}}$	29.2319829	J/(mol·K)
Heat capacity of N_2 at constant volume	$c_{v,\mathrm{N_2}}$	20.9175202	J/(mol·K)
Thermal diffusivity of N_2	α_{N2}	9.475×10^{-5}	m^2/s
Prandtl number of N_2	$Pr_{\mathrm{N_2}}$	0.69	-
Thermal conductivity of N_2	$k_{\mathrm{N_2}}$	0.02505	W/(m·K)
Density of N_2	$\rho_{\mathrm{N_2}}$	1.2419465013492943	kg/m^3
Heat capacity of O_2 at constant pressure	$c_{p,\mathrm{O_2}}$	29.278902	J/(mol·K)
Heat capacity of O_2 at constant volume	$c_{v,\mathrm{O_2}}$	20.964439	J/(mol·K)
Thermal diffusivity of O_2	$\alpha_{\mathrm{O_2}}$	1.36×10^{-5}	m^2/s
Prandtl number of O_2	$Pr_{\mathrm{O_2}}$	0.69	-
Thermal conductivity of O_2	$k_{\mathrm{O_2}}$	0.0254	W/(m·K)
Density of O_2	$\rho_{\mathrm{O_2}}$	1.4193799128550255	kg/m^3
Heat capacity of H_2O vapor at constant pressure	$c_{p,\mathrm{H_2O}}$	33.328268	J/(mol·K)
Heat capacity of H_2O vapor at constant volume	$c_{v,\mathrm{H_2O}}$	25.0138053	J/(mol·K)
Thermal diffusivity of H_2O vapor	$\alpha_{\mathrm{H_2O}}$	0.0015026788321167868	m^2/s
Prandtl number of H_2O vapor	$Pr_{\mathrm{H_2O}}$	0.8154014598540147	-
Thermal conductivity of H_2O vapor	$k_{\mathrm{H_2O}}$	0.018308029197080293	W/(m·K)
Density of H_2O vapor	$\rho_{\mathrm{H_2O}}$	0.005506649185041584	kg/m^3
Heat capacity of liquid H_2O at constant volume	$c_{v,\mathrm{H_2O},l}$	75.97043576	J/(mol·K)
Thermal diffusivity of liquid H_2O	$\alpha_{\mathrm{H_2O},l}$	1.7×10^{-6}	m^2/s
Prandtl number of liquid H_2O	$Pr_{\mathrm{H_2O},l}$	12.9	-
Thermal conductivity of liquid H_2O	$k_{\mathrm{H_2O},l}$	0.556	W/(m·K)
Latent heat of condensation H_2O	h_{cond}	40660	J/mol

7

Gasholder control

As mentioned, the gasholder is pressurised by filling compartment A with air. This inner membrane is free to move, equilibrating the pressure in both compartments when compartment B, filled with hydrogen, is not at its maximum volume. The pressure in the compartments is controlled using analogue-controlled pressure relief valves. The relief valves are opened when an overpressure is detected. Two proportional-integral-derivative (PID) controllers determine the opening of the valves. The PID controller is a widely used control loop mechanism that uses feedback [70]. It is employed in a variety of applications that require continuously modulated control. The controller continuously calculates an error, $e(t)$, which is the difference between the desired value, the set point, and the current measured value, the process variable. The control signal, u, entirely depends on the error.

$$u = \underbrace{k_p e}_{\text{Proportional term}} + \underbrace{k_i \int_0^t e(\tau)\, d\tau}_{\text{Integral term}} + \underbrace{k_d \frac{de}{dt}}_{\text{Derivative term}} \tag{7.1}$$

Here, u is the current control signal, e is the current error, τ is the variable of integration, and k_p, k_i, and k_d are the proportional, integral and derivative gain, respectively. The proportional gain multiplies the error by a constant. A high proportional gain leads to a fast response to a change in error and system oscillations. If the proportional gain is too high, a system can become unstable. Increasing the proportional gain reduces the steady-state error of the controller but will never eliminate it [70]. The integral term can eliminate the steady-state action. It represents the accumulated offsets corrected over time. For small integral gains, the response slowly creeps towards the reference value. It moves faster to the desired value at a higher gain, but the system becomes more oscillatory. It is often sufficient only to implement a proportional and integral gain in the controller to obtain an adequate response leading to a PI controller. The derivative gain reduces the oscillations and the settling time of a system.

The PID controllers were tuned by brute force. First, the integral and derivative gain were set to zero. The proportional gain was increased until an adequate response was observed. After that, the integral gain was increased. If the results were sufficient, a PI controller was used; otherwise, the derivative gain was increased, leading to a PID controller.

7.1. Actuator delay and boundary conditions

The PID controllers determine the pressure relief valves' desired outlet flow [mols/s]. First, the valves are connected to the outside air; thus, the pressure in the system will always be equal to or higher than the pressure of the valve's outlet. This means there's only one direction in which flow is possible in the valves: exiting the system. When the PID controller determines that the pressure in the compartment is too low, the adequate response of the control system is to shut the valve entirely. This is a critical boundary condition that must be implemented in the system. To do so, it has been chosen to work with a percentage of valve openings. The valves can open between 0% and 100%. To transform the output of the PID controller, a flow in mol per second, the following assumptions have been made:

- The fluid flows, initially, through an infinitely large area; thus, it is assumed its flow speed is approximately 0

- The fluid is incompressible
- The valve can be represented as a small channel with area A [m^2]
- The Bernoulli principle is applicable
- The elevation in the channel is constant

The Bernoulli principle for an incompressible fluid can be written as

$$P + \frac{1}{2}\rho V^2 + \rho g z = \text{constant} \tag{7.2}$$

Here, P [Pa] is the pressure, ρ [kg/m^3] is the density of the fluid, V [m/s] is the speed of the fluid, g [m/s^2] is the acceleration due to gravity and z [m] is the elevation above the reference plane. With the above assumptions, the following equality can be set up:

$$\begin{aligned} P_{\text{c}} &= P_{\text{atm}} + \frac{1}{2}\rho V_{\text{atm}}^2 \\ \Rightarrow V_{\text{atm}} &= \sqrt{\frac{2(P_{\text{c}} - P_{\text{atm}})}{\rho}} \end{aligned} \tag{7.3}$$

Here, P_{c} [Pa] is the pressure inside the gas compartment and P_{atm} [Pa] is the atmospheric pressure. With the determination of the flow speed through the valve, the desired opening area follows

$$A = \dot{N}\frac{v}{V} \tag{7.4}$$

Here, A [m^2] is the desired flow area, $\dot{N}$ [mol/s] is the desired mol flow determined by the PID controller, v [mol/m^3] is the molar volume of the fluid, and V [m/s] is the flow speed of the volume. The desired opening percentage is just the ratio of the desired flow area over the maximum flow area of the valves times 100. This can not exceed 100%. Due to the nature of the code, the time interval is one second; another boundary condition has been added to account for actuator speed. It is unrealistic for a valve to open or close fully within one second. Therefore, it has been assumed that the valve opens and closes in 10 seconds, meaning that the maximum change in opening percentage is $\pm$ 10%.

7.2. Regimes

During the gasholder's operation, several possible control regimes have been defined. Each regime determines the PID controller's set point pressure. Also, the proportional, integral, and derivative gain values change per regime. The first regime defined is empty storage. The storage is defined as empty when the volume of gas compartment B is at 5% or less of its maximum value. The PID controller of the pressure relief valve of compartment A is tasked to keep the pressure in the compartment at 106325 Pa. The pressure relief valve in compartment B is unnecessary as it is not at its maximum loading capacity. Its desired opening is set at 0%. The same parameters are used when the gasholder is in the stand-by regime.

The gasholder enters the stand-by regime when the hydrogen production and demand are equal to zero, and the gasholder is neither full nor empty. This will happen during the nights when the hydrogen compressor is shut off. The pressure is kept low, 106325 Pa, to minimise permeation through the membranes and the duty of the air blower of compartment A. The stand-by regime has two controllers. The previous regime decides which controller is used. The controller's gains are different to ensure adequate reaction to the pressure change. The controller can enter the stand-by regime after the inflation or deflation regime.

In the case where hydrogen is produced, multiple regimes are possible. The first is the inflation regime. During this regime, the hydrogen production entering the system is greater than the hydrogen demand exiting it, while the load in gas compartment B is not at its maximum. The PID controller for the pressure relief valve of compartment A maintains the pressure at 141325 Pa, the maximum allowable pressure of the compartment. The relief valve of compartment B is desired to be closed. The volume of compartment B will continuously increase until it reaches its maximum volume. This means that the storage enters the full storage regime: the hydrogen compressor at the system's exit will be activated, and the storage will deliver hydrogen at a flow rate of 2.57 mol per second. During

the full storage regime, both relief valves are controlled by a PID controller. The desired pressure is 141325 Pa in compartments A and B, respectively. Due to the activation of the compressor leading to hydrogen demand, the gasholder can enter the deflation regime. If the hydrogen demand exceeds the hydrogen production, the total amount of mol in compartment B will decrease, deflating the storage. Only the controller for the pressure relief valve of gas compartment A is active; its set point is 111325 Pa. This slight overpressure ensures that the hydrogen will flow smoothly to the compressor. Once the storage enters the deflation regime, it can not exit until it is completely empty or full again. These conditions have been added to prevent the controller from increasing the pressure after the storage has been fully drained. The storage is mostly drained at the end of the day when the sun is still shining and thus H_2 being produced. There will still be a small amount of hydrogen produced. This is not enough to fully blow up the storage; thus, it can be done at low pressure. This avoids pressure drops and saves compressor energy. More hydrogen can also be produced during the deflation regime than the compressor demand. This will increase the pressure in compartment B. Therefore, going from the deflation regime to the full storage regime is possible. This happens when, during deflation, the gas in compartment B reaches its maximum volume and a pressure greater than 141325 Pa. A last boundary condition has to be added. The hydrogen production can stop just before the storage is completely filled. The pressure in the system is that of the inflation regime. The system will go into the stand-by regime, lowering the pressure to 106325 Pa. Due to the decrease in pressure, the volume of compartment B increases. This could lead to the volume of compartment B reaching its maximum value. In this case, the deflation regime is also started.

8

Results

This chapter will lay out the simulation results. They are divided into different sections: Condensation, section 8.1, Control system section 8.2, Maxwell-Stefan diffusion section 8.3, Heat transfer section 8.4, Purtiy section 8.5, Efficiency section 8.6 and Loaction comparison section 8.7.

8.1. Condensation

Short simulations were run to verify whether the water present in the system was prone to condensation. Water condenses when its partial vapour pressure in the air exceeds its saturation pressure. The saturation pressure of water depends heavily on the temperature of the gas. Furthermore, the amount of water entering gas compartment A depends on the relative humidity, temperature, and pressure of the outside air. It has been chosen to run four different simulations over two days. Every model element has been included: H_2 production and demand, mass and energy balances and heat transfer. This is also defined as normal operation. The simulations were started on the first of January, April, July, and October to account for the various weather conditions during the year. The simulations were first run without adding a condensation term. Only the gas phase was considered.

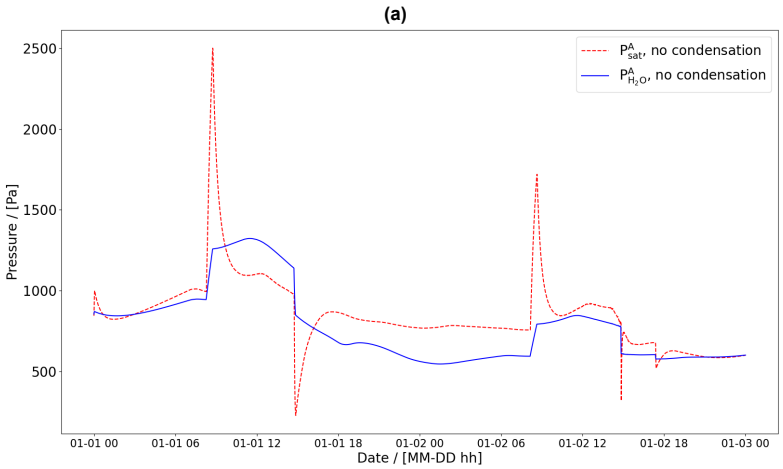

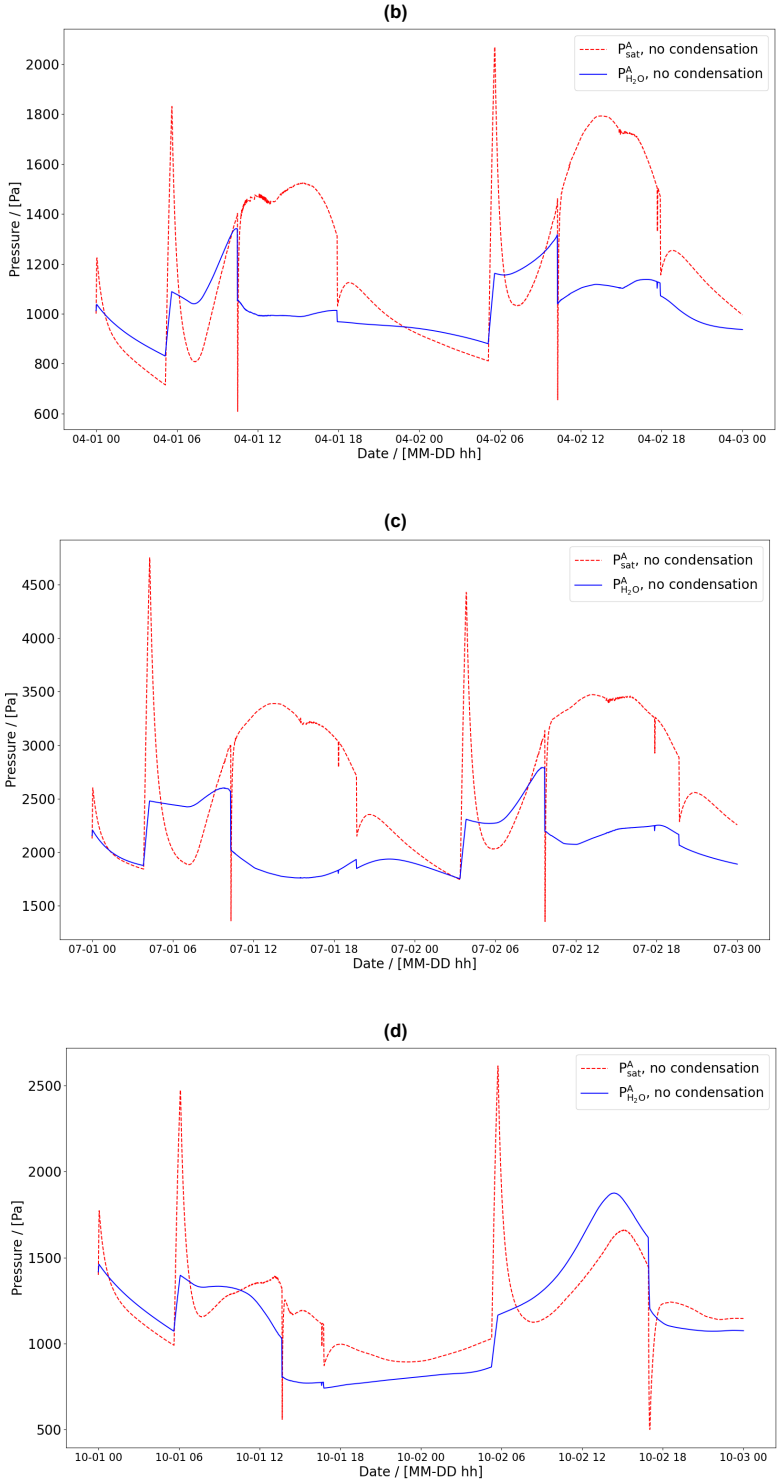

Figure 8.1: Partial and saturation pressures of H_2O in gas compartment A if no condensation were considered. In the regions where the partial pressure of H_2O is higher than the saturation pressure, condensation is expected. All aspects of the model have been considered. Simulations ran for two days in each season of the year. (a) Winter: 01-01 to 01-03 without condensation; (b) Spring: 04-01 to 04-03 without condensation; (c) Summer: 07-01 to 07-03 without condensation; (d) Autumn: 10-01 to 10-03 without condensation

Figure 8.1 shows the results of four short simulations of two days considering no condensation during different seasons. Only the partial and saturation pressure of H_2O in gas compartment A is shown because more water is present in the air than in the hydrogen inlet stream. The hydrogen is

cooled to 3°C before entering the system. The hydrogen stream entering the system consists of 0.3% of water vapour. Condensation is more prone to happen in gas compartment A. All four subfigures show that condensation will occur in the system. The partial pressure of H_2O, indicated by the blue lines, is at some point during the two-day simulations higher than the saturation pressure, shown by the dashed red line. This means that the water present in the system will condense. The condensed water will evaporate again when the partial pressure in the compartment is less than its saturation pressure. A good example is seen in Figure 8.1d between 10-02 06 and 10-02 18. the partial pressure of H_2O in the compartment lays well above the saturation pressure. H_2O will condense. From the above results, it can be concluded that condensation and evaporation will happen in the system. Equation 4.36 was used to consider the phase change of water in the system. The time constant τ_{cond} determines the rate at which the condensation happens.

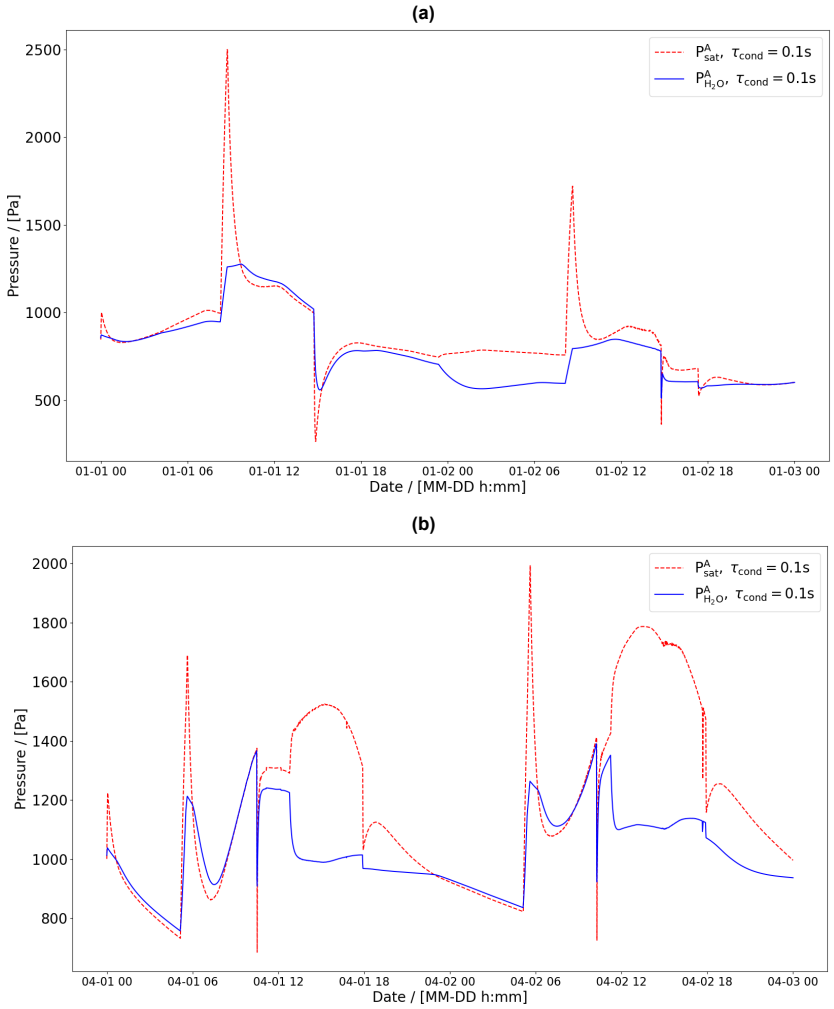

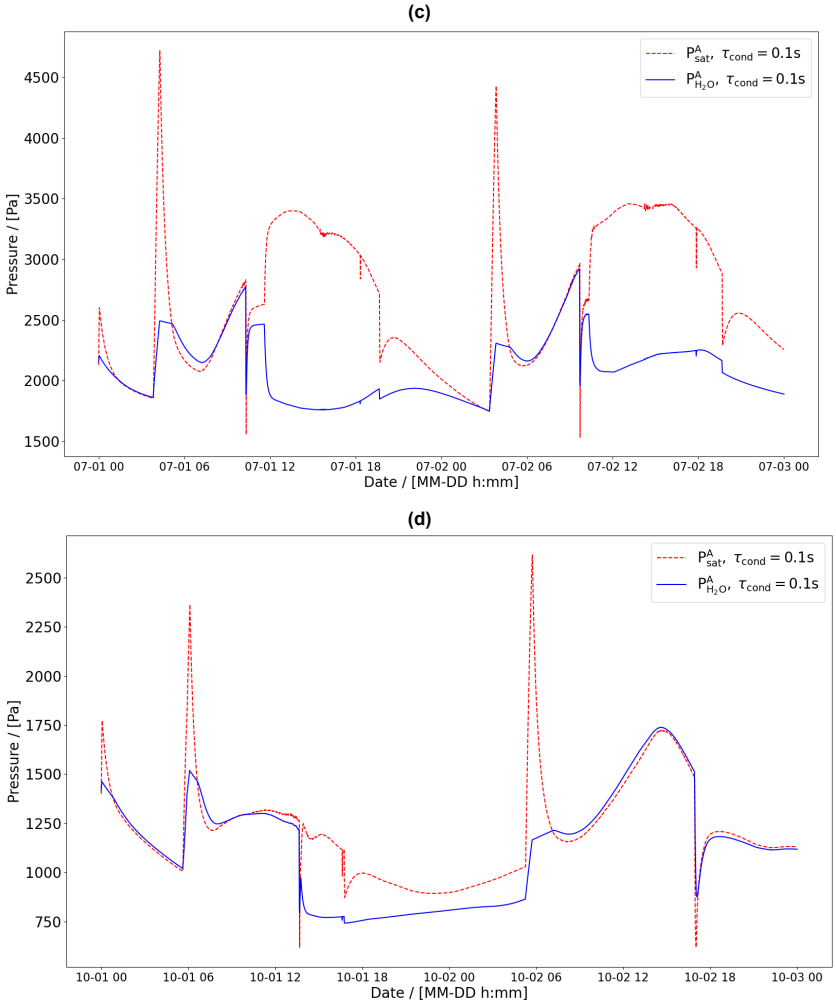

Figure 8.2: Partial and saturation pressures of H_2O in gas compartment A if condensation were considered with $\tau_{cond} = 0.1$s. In the regions where the partial pressure of H_2O is higher than the saturation pressure, condensation is expected. Once water has condensed, it will evaporate if the partial pressure of H_2O in gas form is less than the saturation pressure. All aspects of the model have been considered. Simulations ran for two days in each season of the year. (a) Winter: 01-01 to 01-03 with condensation; (b) Spring: 04-01 to 04-03 with condensation; (c) Summer: 07-01 to 07-03 with condensation; (d) Autumn: 10-01 to 10-03 with condensation

The condensation time constant, τ_{cond}, was set to 0.1 s. The results are shown in Figure 8.2. The system reacts to the new input. Let's again look at the conditions for the two-day simulation that runs in October: Figure 8.1d and Figure 8.2d. It can be seen that the partial pressure of H_2O lies closer to the saturation pressure of the compartment. Water in the system condenses to adjust to the changing conditions. In general, in all the four subfigures of Figure 8.2, it can be seen that the partial pressure of H_2O vapour does not exceed the saturation pressure by a large amount anymore. The small difference is not unrealistic. There is a continuous flow of air through the comportment. It is thus logical that the system is not in equilibrium at every instance. Phase changes in the system contribute to the overall energy balance of the system; see section 4.2. Condensation is exothermic, while evaporation is endothermic.

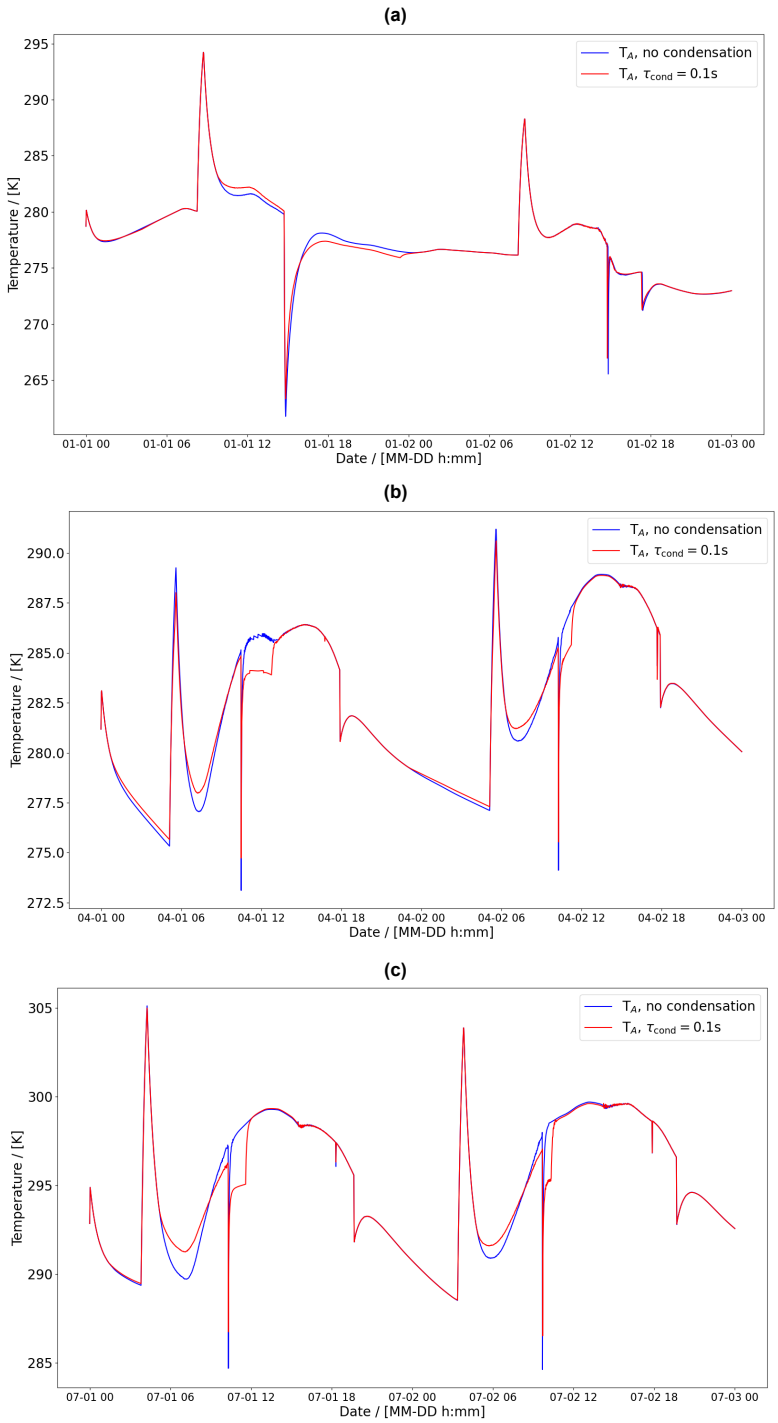
(a)
T_A, no condensation
T_A, $\tau_{cond} = 0.1$s
Temperature / [K]
295
290
285
280
275
270
265
01-01 00
01-01 06
01-01 12
01-01 18
01-02 00
01-02 06
01-02 12
01-02 18
01-03 00
Date / [MM-DD h:mm]
(b)
T_A, no condensation
T_A, $\tau_{cond} = 0.1$s
Temperature / [K]
290.0
287.5
285.0
282.5
280.0
277.5
275.0
272.5
04-01 00
04-01 06
04-01 12
04-01 18
04-02 00
04-02 06
04-02 12
04-02 18
04-03 00
Date / [MM-DD h:mm]
(c)
T_A, no condensation
T_A, $\tau_{cond} = 0.1$s
Temperature / [K]
305
300
295
290
285
07-01 00
07-01 06
07-01 12
07-01 18
07-02 00
07-02 06
07-02 12
07-02 18
07-03 00
Date / [MM-DD h:mm]

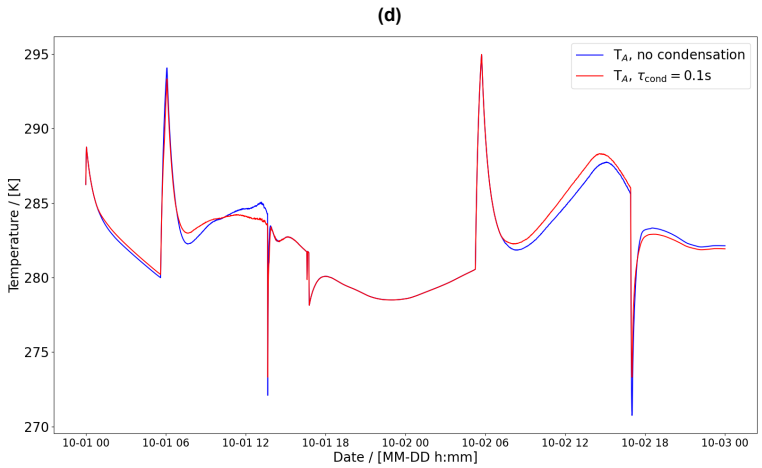

Figure 8.3: Comparisons of the temperature evolutions in gas compartment A with and without condensation. (a) Winter: 01-01 to 01-03 temperature comparison between the experiments with and without condensation; (b) Spring: 04-01 to 04-03 temperature comparison between the experiments with and without condensation; (c) Summer: 07-01 to 07-03 temperature comparison between the experiments with and without condensation; (d) Autumn: 10-01 to 10-03 temperature comparison between the experiments with and without condensation

It is clear from all subfigures in Figure 8.3 that the addition of phase change in the system influences the temperature profile. It seems that condensation restrains the negative peaks in temperature. The system without condensation achieves a lower temperature while cooling than the system considering condensation. This is logical. The saturation pressure of H_2O in the air decreases with decreasing temperature. More water vapour will thus condense when the system cools down. Water condensation is an exothermic process that adds heat to the system. The system will thus cool down less. The water will later evaporate, reducing the temperature of the system. This can, for example, be seen in Figure 8.3b just after the sharp decrease in temperature at around 04-01 12. The water just condensed, slowing the cooling of the system. After the system heats up again, the water has to evaporate again, slowing the heating of the compartment. It can be concluded that the addition of condensation is a necessary feature, although, for each season, the temperature profiles with or without condensation follow a similar trend.

The total amount of condensed water in the system per season is shown in Figure A.1. It can be observed that during the warmer periods of the year, the spring and summer, water condenses, forms a liquid phase and then evaporates again. This is in line with the assumption that the volume of water is very small. However, during the colder seasons, autumn and spring, large amounts of water condense, forming a substantial liquid phase. During normal operation over longer periods than 3 months, the liquid phase would continue to exist between the autumn and the winter. this would lead to an even larger liquid phase of around 240 L in compartment A. The current minimal volume of compartment A is around 30 m^3 or 30000 L. The volume of the liquid phase is still negligible relative to the total volume of the compartment, but the liquid phase cannot be considered droplets anymore. this will ultimately change the energy balance as the liquid phase must be considered a separate phase with its own balances. Furthermore, the mass of water must be supported by the inner membrane, changing the pressure in the compartments. This can be avoided by draining the water once it forms.

8.2. The control system

Short simulations were run to demonstrate the different regimes and verify that the control system works appropriately. The simulations contain all elements of the model. Four cases were studied, one for each season in the year. The simulations were started using the default temperatures and pressures; see section 6.5. The volume of compartment A was set at its maximum. The simulations were run for two days each. The start dates are the first of January, April, August, and October.

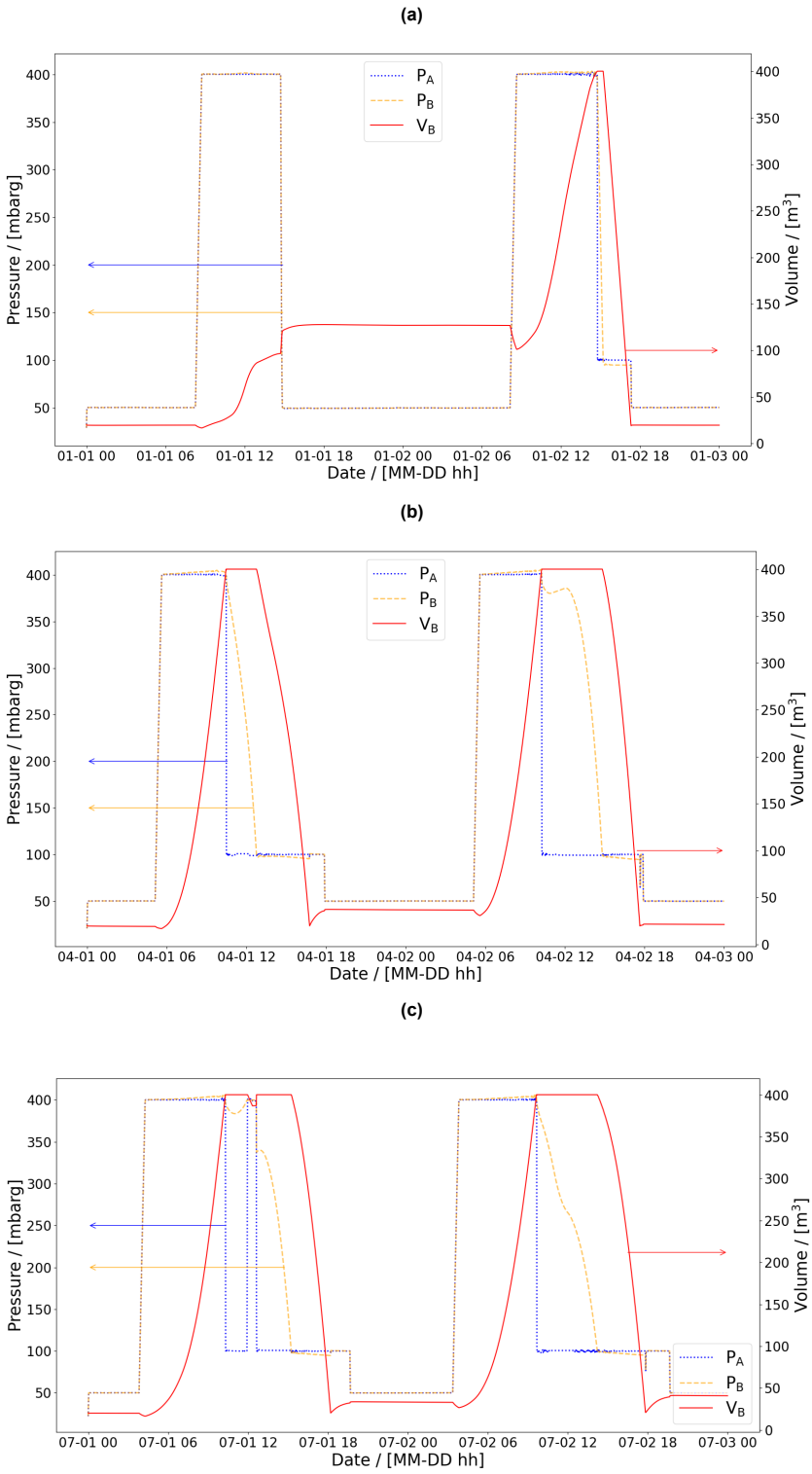

Figure 8.4a represents the characteristic curve of the gasholder during the first two days of the year. It can be observed that the controller directly acts to the empty storage regime and brings the pressure in both compartments to around 5000 Pascal's gauge (Pag) or 50 millibar gauge (mbarg). The pressure is kept constant until around 7 o'clock in the morning. The sudden rise in pressure is due to the electrolyser starting to produce hydrogen. This means the inflation regime has started, and the controller of pressure relief valve A maintains the pressure in compartment A at 400 mbarg. Subsequently, the pressure in comparison B also becomes 400 mbarg. The inner membrane is free to move, and thus, the pressure

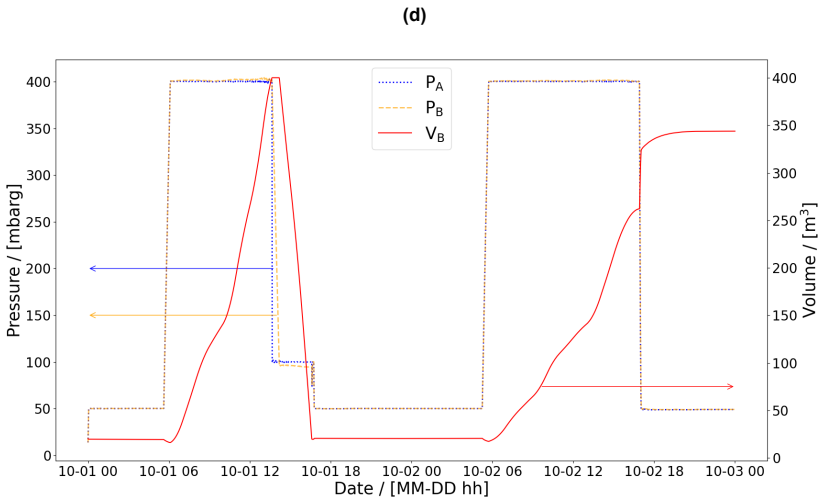

Figure 8.4: Characteristic curve of the gasholder for cycles in the four seasons: the dashed lines represent the pressures in the compartments: blue for the pressure in compartment A and yellow for the pressure in compartment B. The red line represents the volume of compartment B; it should be read on the right axis. Simulations ran for two days; all model elements have been considered. (a) Winter: 01-01 to 01-03; (b) Spring: 04-01 to 04-03; (c) Summer: 07-01 to 07-03; (d) Autumn: 10-01 to 10-03

in both compartments will equilibrate. The small decrease in volume of compartment B, observable at the start of the inflation regime, is because the controller reacts faster than the electrolyser produces H_2. It will try to reach the assigned pressure quickly, closing the air relief valve and increasing the number of mols in the system and the pressure. The pressure in compartment A rises quicker than in compartment B, meaning the volume of compartment B has to shrink to equilibrate the pressures. This is visible in all subfigures of Figure 8.4 when the inflation regime is started. During the inflation regime, the volume of compartment B rises once the desired pressure is reached. At 01-01 14, the production of H_2 stops. The storage has not yet been fully filled. Thus, the compressor station is not yet activated. There's neither demand nor production of H_2, and the system enters the stand-by phase. The pressure drops quickly and then is maintained at 50 mbarg by the system. During the pressure drop, the volume of compartment B increases, which is logical as it decompresses.

After the second inflation regime, in Figure 8.4a, the volume of compartment B reaches its maximum volume, defined as its maximum storage capacity. The compressor station is then turned on, starting the storage drainage. The deflation regime starts. The control system controls the pressure of compartment A to 100 mbarg. The pressure in compartment B also drops quickly due to drainage of the storge. Once both pressures equilibrate, the volume of compartment B shrinks. The controller keeps the storage in the deflation regime until the minimum volume of compartment B is reached. Once the storage is fully drained, there are two possibilities: no more hydrogen is produced, meaning the gasholder enters the stand-by regime, or hydrogen is still being produced, meaning the gasholder stays in the deflation regime. In this case, the storage enters the stand-by regime.

The other option is visible in all other subfigures. Let's take Figure 8.4b. The storage is drained twice in two days. The first time it is drained, the electrolyser still produces hydrogen as the controller keeps the pressure in the compartments at 100 mbarg. Due to system drainage, the pressure in compartment B is lower than in compartment A. Once the storage is empty, the controller has to react to the new conditions. This causes the small spikes to be visible every time the system's drainage is completed while hydrogen is still produced. There's another interesting feature in this graph. In the second cycle, the pressure in compartment B rises after the system's drainage has started. This happens because the production of hydrogen is greater than the demand. The system recognises this but keeps the gasholder in the deflation regime. This is also visible in Figure 8.4c. Only here is so much hydrogen produced that the storage is filled again. The controller enters the full storage regime until there is a greater demand of H_2 than production. Both pressure relief valves are controlled in this regime to maintain the pressure in the compartments 400 mbarg. Valve B is open for about 20 minutes, venting excess hydrogen from the system. The hydrogen production during the system's drainage also explains the time variations observable between the different drainage regimes. Hydrogen is still being produced.

Its quantity varies per day and per time instance. The drainage in the summer takes longer than, for example, in the winter as more hydrogen is produced. The last interesting observation is that the storage is fully filled twice in two days during spring and summer, while in the autumn and winter, this only happens once. This is logical as the production of hydrogen is dependent on the power production of solar panels. The panels produce more during sunny days.

Overall, the exact same phenomena, as described for Figure 8.4a, is visible in all the other sub-figures. The controller stabilises the pressure at the desired values within an appropriate time. The control system reacts accordingly to the system's changing inputs. the values used as gains for the controllers are presented in Table 8.1.

Table 8.1: Proportional, Integral and Derivative gain values of the PID controllers determining the pressure for the different regimes

Regime & valve	Proportional gain	Integral gain	Derivative gain	Regulated pressure [mbarg]
Empty storage valve A	0.5	0.00001	2	50
Stand-by deflation valve A	15	0.0001	2	50
Stand-by inflation valve A	0.5	0.00001	2	50
Inflation valve A	1	0.000001	2	400
Full storage valve A	0.5	0.00001	0.5	400
Full storage valve B	0.5	0.00001	0.5	400
Deflation valve A	1	0.00001	2	100

8.3. Maxwell-Stefan diffusion

To verify the statement made in subsection 4.1.1 concerning the influence of the friction between the different permeating molecules to be negligible, multiple experiments have been run with the complete Maxwell-Stefan (MS) diffusion and the same experiment with the partial Maxwell-Stefan diffusion. It was chosen to compare both methods without considering the in and outlet flows of the system. This means that no hydrogen is entering or leaving the system. The gas in compartment B is at a standstill. Here, the effects of diffusion should be distinctive, as they are the only way gas compartment B's composition changes. Initially, gas compartment A was filled at 50% of its maximum capacity. The starting regime of the gasholder is the stand-by regime.

(a)

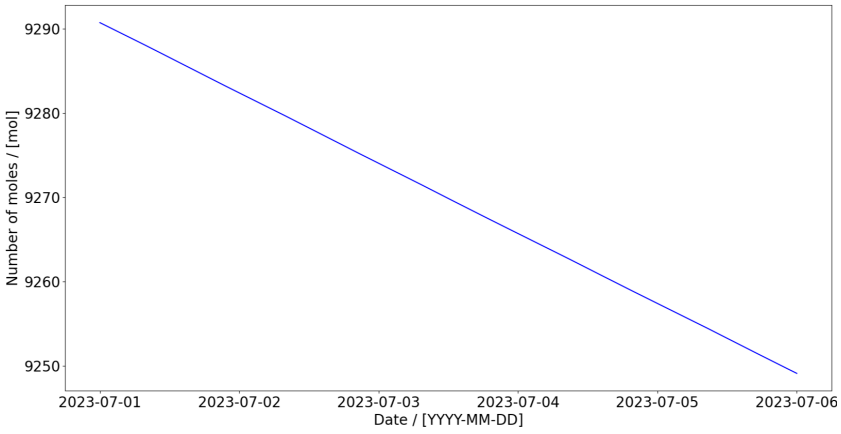

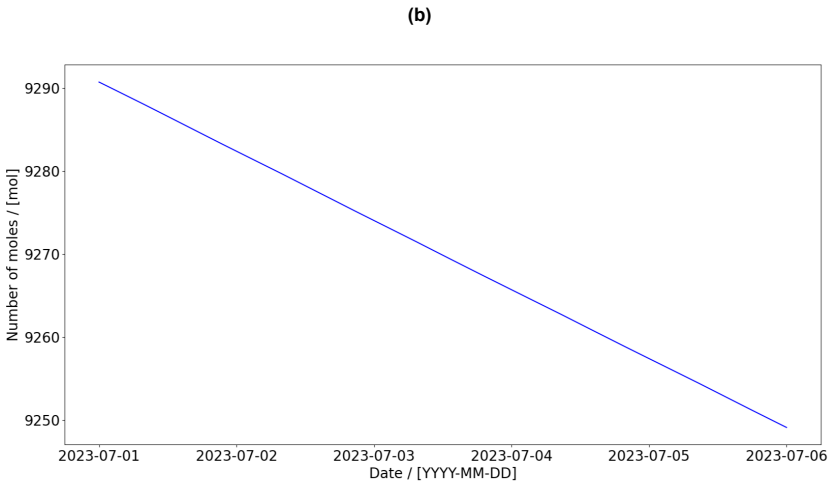

Figure 8.5: Number of mols of H_2 in compartment B. The simulation was run for 5 days. The gas in compartment B was at a standstill. The only way molecules leave or enter the compartment is through the membrane. (a) Maxwell-Stefan diffusion with friction between permeating molecules considered; (b) Maxwell-Stefan diffusion only considering the friction between the permeating species and the membrane

Figure 8.5 shows the evolution of the number of mols of H_2 in gas compartment B for both the experiment considering the full Maxwell-Stefan equation and the experiment considering only the friction between the H_2 and the membrane in the Maxwell-Stefan equation. The difference between the two graphs is not visible to the naked eye. Both graphs start at around 9290 mols of H_2. The amount of mols degrades to around 9250 mols over five days. The difference in the number of mols of N_2 and O_2 is also not visible; see Figure A.2 and Figure A.3 respectively. Therefore, it has been decided to subtract the amount of mol H_2 in gas compartment B for the partial MS diffusion from the amount of mol of H_2 in compartment B for full MS diffusion.

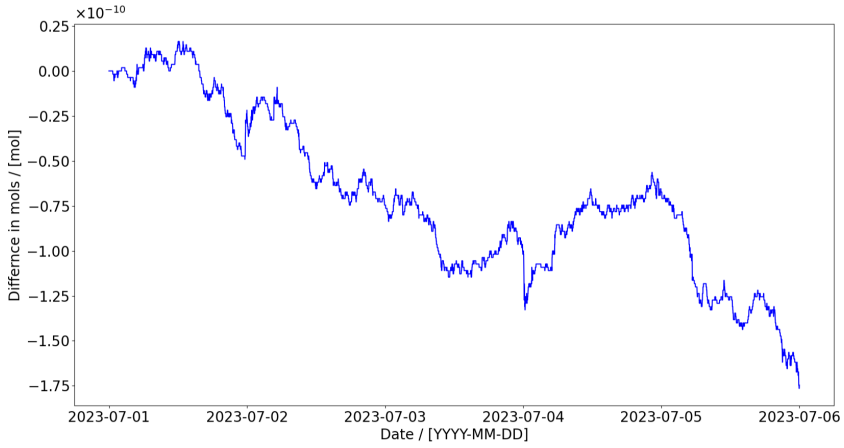

Figure 8.6: Difference in the amount of H_2 in compartment B between a simulation considering all frictions terms of Maxwell-Stefan diffusion and a simulation considering only the friction between the permeating species and the membrane.

Figure 8.6 shows the difference in the number of mols of H_2 in comparison B determined by the model using full and partial MS diffusion. Care is advised when reading the y-axis; the numbers on the axis must be multiplied by 10^{-10}; see the upper left corner. From the graph, two things can be understood: using the partial MS diffusion, only containing the friction term between the membrane and H_2, overestimates the flux through the membrane, and this difference is negligible. A difference of 1.75×10^{-10} mol after five days is insignificant. Around 40 mols of H_2 have already permeated in the same period. The same conclusion can be drawn from the difference difference in the number of

mols of N_2 and O_2 in compartment B; see Figure A.4 and Figure A.5 respectively. In these cases, the difference is positive rather than negative, which is logical as the direction of permeation is inversed. The partial form of the MS diffusion overestimates the amount of mol permeating from compartment A through the inner membrane to compartment B, leading to a higher amount of mol in the compartment. The errors after five days are around 4×10^{-11} and 2×10^{-11} mol for N_2 and O_2 restively. The relative error, the difference divided by the total permeated amount, is of the same order of magnitude for the three considered permeated molecules. The author has no explanation for the apparent linear trend in the error for N_2 and O_2. This trend is not visible in the difference of H_2.

From these tests, it can be concluded that solely considering the friction between the membrane and the permeating molecule is an adequate way to model diffusion. From now on, only partial MS diffusion is considered in the code as it requires less computational power. It runs seven times faster.

The fluxes of the molecules through the membranes can be used to determine the effective Fick permeability per molecule. This value can be compared to the real Fick diffusion provided by the company; see subsubsection 4.1.1.1.

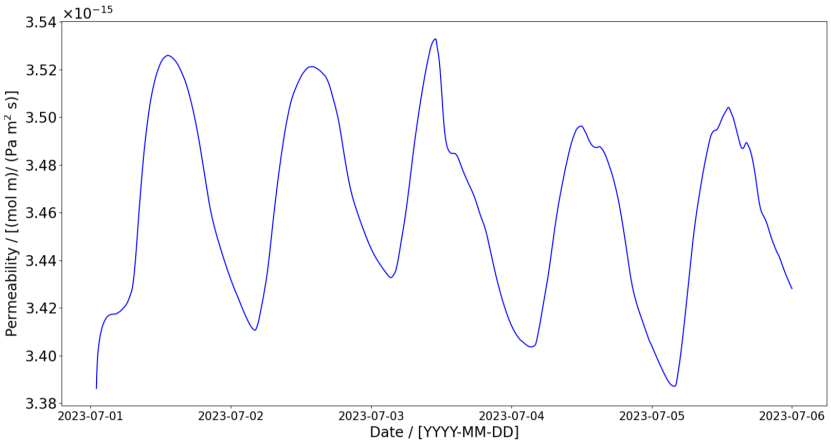

Figure 8.7: Calculated effective permeability for H_2 through the inner membrane for the stand-by case only considering partial MS-diffusion

Figure 8.7 shows the permeability of H_2 through the inner membrane versus time. This permeability is in line with what was expected. The determined permeability of 3.38×10^{-15} [(mol m) / (Pa m^2 s)] in subsubsection 4.1.1.1 is slightly lower than the average permeability read from the graph. This is because it was determined at 283.15 K. In most instances, the inner membrane temperature is slightly higher; see Figure A.6. Diffusion increases with temperature. The permeabilities for N_2 and O_2 are visible in Figure A.7 and Figure A.8, respectively. They are a factor of ten lower than the permeability of H_2.

8.4. Heat transfer

The results of the five-day simulation, which only considers partial MS diffusion described in section 8.3, were used to verify that the tool's heat transfer part behaves appropriately.

Figure 8.8 shows the temperature profiles in the gasholder when the gas in compartment B is at a standstill. It is visible that the gas in compartment B starts at 276.15 K. The other elements start at the ambient air temperature. All temperatures quickly converge to the same value to balance the system. This is logical as the higher the temperature difference between elements, the higher the heat flux between the elements. The quick dip in temperature is the system adjusting its pressure. The controller of relief valve A drops the pressure from 100 mbarg to 60 mbarg. The controller's gains may not be suitable for this type of experiment. A pressure drop is accompanied by a drop in temperature. For compartment A, the pressure drops because more mols exit the system through the relief valve than mols enter the system. This reduces the system's enthalpy more than the decrease in volume (the gas performs negative work), which heats up the system. In compartment B, the expansion of the gas dominates. The total number of mols is nearly constant for a small period of time as the valves are closed and the diffusion of the molecules through the inner membrane is very low.

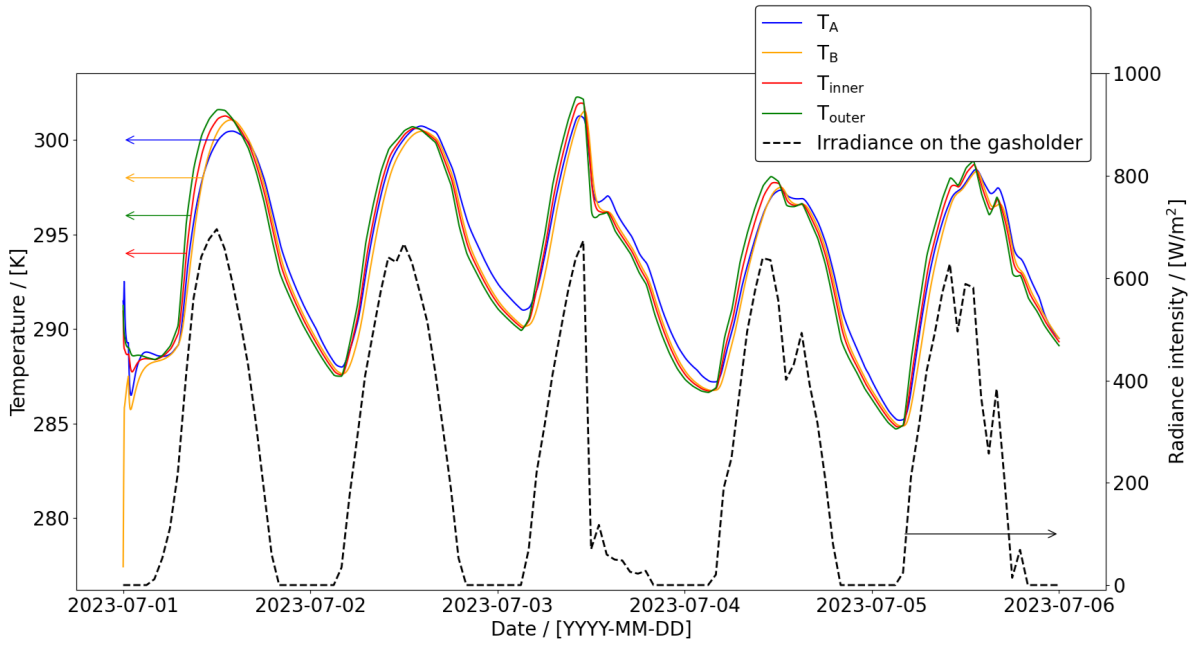

Figure 8.8: Temperature evolution in the compartments when the gasholder is at a standstill, no H_2 is produced or taken from the storage. Compartment A is filled at 50% of its maximum volume.

Once the day starts and irradiance starts to fall on the gasholder, the gasholder starts to heat up. The outer membrane heats the fastest because it is the element of the solder that receives the solar radiation. The gas in compartment A heats up the slowest. This is because the compartment has continuous airflow. Hot air leaves the system while cool air, at ambient temperature, enters the system. This can be seen in Figure A.11. The ambient air temperature is lower than the gas temperature in compartment A. The continuous airflow in the compartment prevents the compartment from heating up any further. With the current constants, it seems that the radiative heat exchange between the membranes is dominant over the convective heat transfer between the gases and the membranes. The inner membrane temperature exceeds the temperature of the gasses in compartments A and B while the gasholder warms up. The gas in compartment B is at a standstill. The only possible heat exchange is through mass transfer, which is nearly negligible due to the low diffusion rates or convective heat transfer with the inner membrane. It continues warming as long as the temperature of the inner membrane is greater than the temperature of the gas in compartment B, which is to be expected. The gasholder starts to cool once the day ends and the night starts. The outer membrane cools the fastest. It loses energy through radiative heat transfer to the environment and the sky. This subsequently means the cooling of the inner membrane and the gas in compartment B. The gas in compartment A is less affected. The ambient temperature of the air dominates the temperature evolution in the compartment due to the continuous airflow; see Figure A.11. The ambient temperature is superior to the gas temperature in compartment B.

Generally, the gasholder's reaction to weather conditions while at a standstill is as expected. The outer membrane is the most affected, which is logical as it is the part of the gasholder in contact with the outside world. The gas in compartment B is at a standstill and thus only exchanges heat with the inner membrane, which is visible in the graph. The ambient air temperature mostly determines the gas temperature in compartment A. There is a continuous airflow in the compartment used to pressurise the gasholder.

Figure 8.9 shows the temperature profile in the gasholder during normal operation. A production and a demand of H_2 have been considered in this case. When compared to Figure 8.8, some major differences are visible. These differences, as shown by the peaks in the gas temperature profiles in compartments A and B, are due to the gasholder regimes and the controller changing the pressures in the compartments. It is interesting to compare the temperature profiles to the characteristic curve of the gasholder, Figure 8.4a. It can be seen that once the sun starts to shine around 01-01 08, the produc-

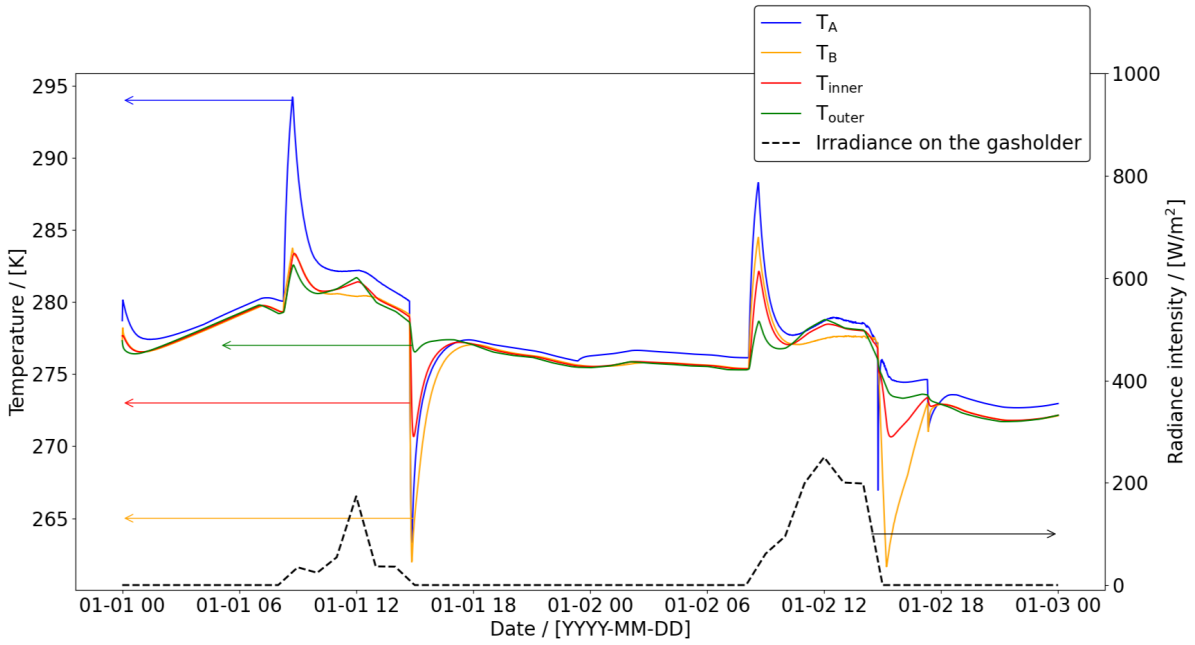

Figure 8.9: Temperature profile of the gasholder during normal operation from 01-01 to 01-03

tion of H_2 starts. The gasholder enters the inflation regime, increasing the pressure in the storage. To increase the pressure in the gasholder, the controller shuts the pressure relief valve of compartment A. This means that the number of mols entering the system is greater than the number of mols leaving the system, increasing the enthalpy and, thus, the compartment's temperature. This explains the peak in the temperature profile of gas compartment A. The heat transfer to other elements, and the continuous airflow through the compartment quickly smoothens the peak. The inverse of this temperature peak is visible once the H_2 production stops. The gasholder enters the stand-by regime, reducing the system's pressure to 50 mbarg. To attain the new pressure, the controller of valve A opens the valve, letting more airflow out of compartment A than in. This reduces the enthalpy and, thus, the temperature of compartment A. Due to heat transfer, the first temperature peak of gas compartment A entrains small peaks in the temperature profiles of the other elements of the model. During the inflation phase, the temperature in compartment B remains rather constant. Although mols are entering the system, increasing its enthalpy, they enter at 276.15 K. The gas also has to perform thermodynamic work by increasing the volume of the compartment, decreasing the energy in the compartment. These terms balance out, and the compartment's temperature remains stable during inflation. Once the hydrogen production is halted, a big decrease in temperature in gas compartment b is also visible. The compartment is at a standstill; thus, heat transfer and thermodynamic work are the only energy exchange. By decreasing the pressure in compartment A, compartment B will expand to balance out the pressure. This is visible in Figure 8.4a. The increase in volume means the gas performs work, decreasing its temperature.

Both the negative peaks in temperature gas compartments A and B cause the temperature of the inner membrane to drop as well due to heat transfer. The outer membrane is less affected as it changes energy with the environment and prevents it from cooling significantly.

At night, the compartments' temperatures pull towards each other and seem to find equilibrium. The outer membrane loses a lot of energy during the night due to radiation from the sky. The temperature of the inner membrane and, thus, also of gas compartment B is dominated by the temperature of the outer membrane during the stand-by regime. The temperature of compartment A is a bit higher than that of the rest of the elements of the gasholder due to the continuous airflow through the compartment.

At the start of the second inflation regime, the temperature profile of compartment A again peaks as the pressure increases. The peak in the temperature profile of gas compartment B is larger than during the start of the first inflation regime. This is because the volume of the compartment decreases more, performing a larger amount of negative work; see Figure 8.4a. Once compartment B is fully filled, the system enters the deflation regime. This induces a decrease in pressure in the system due to the

regulation of valve A. Due to the small volume of compartment A is at its minimum volume, and the system's temperature changes rapidly. It is also rapidly brought up to temperature again. The decrease in temperature of the gas in compartment B is less steep. It continues until the system is fully drained as more mols leave the system than enter the system, reducing the enthalpy of the system. After the system is fully drained, the temperature of compartment B rises again due to the exchange of heat with the inner membrane. A small dip in the temperature of compartment A is visible once the deflation regime ends and the standby regime starts. Control valve A adjusts the system pressure from 100 mbarg to 50 mbarg. Mols leave compartment A, reducing its enthalpy.

Overall, the temperature evolutions in the system make sense. The effects of the different regimes changing the pressures in the system are visible and as expected. The last thing to notice is that the peaks decrease the temperature in the system, causing it to reach temperatures below 273.15 K. At these temperatures, water starts to form ice. This has not been accounted for in the model.

8.5. Purity

8.5.1. Safety limits

Hydrogen is a dangerous gas to store. Its flammability range is vast, as described in subsection 2.1.2. Only 4% or 40000 PPM of oxygen is needed for a combustible hydrogen-oxygen mixture. To verify the safety margins of the storage, different experiments were run to determine the maximum storage time before combustion risks arose. The interesting case is the long-term storage of hydrogen. This happens, for example, when the compressor station is broken. There is no demand for hydrogen out of the system. In this case, the electrolyser will be switched off, leaving the gas in compartment B at a standstill. Diffusion through the membrane will cause the composition of the gas to change. An increase in temperature means an increase in the permeation flux. Therefore, these experiments were conducted during the warmer periods of the year. They were started on the first of July. The original amount of hydrogen in the storage also influences the results, as a low storage volume would mean that less permeation is needed to change the composition of the mixture. The initial conditions of all the experiments were exactly the same. The outside weather conditions determined the compartment's composition, temperatures and pressures. The only variable that changed between the experiments was the initial volume of the compartments

8.5.1.1. Compartment B initially 10% filled

The initial conditions of the first experiment considered compartment B to be filled to 10% of its maximum volume. We are only interested in the composition of gas compartment B as the air in compartment A is constantly blown through by the air inlet. The simulation was run for 62 days.

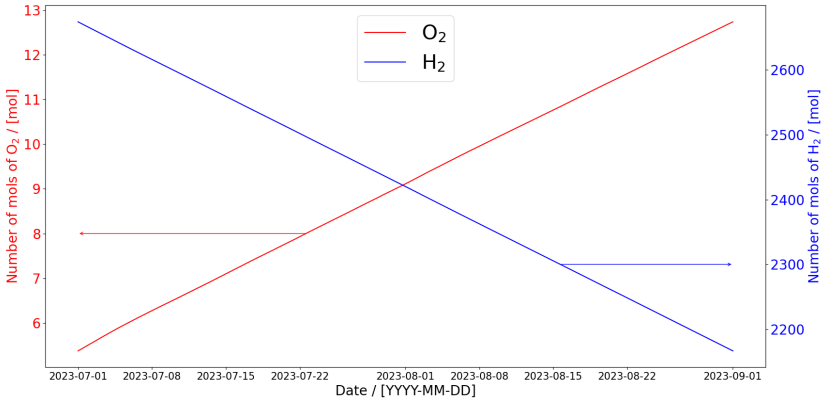

Figure 8.10: Amount of mols of H_2, right axis, and O_2, left, in gas compartment B initially 10% filled axis vs time

Figure 8.10 shows the amount of mols of H_2 and O_2 in gas compartment B. As expected, the amount of H_2 declines due to the permeation through the inner membrane. The inverse happens for O_2. The

number of mols increases due to the permeation of O_2 through the inner membrane from compartment A to B.

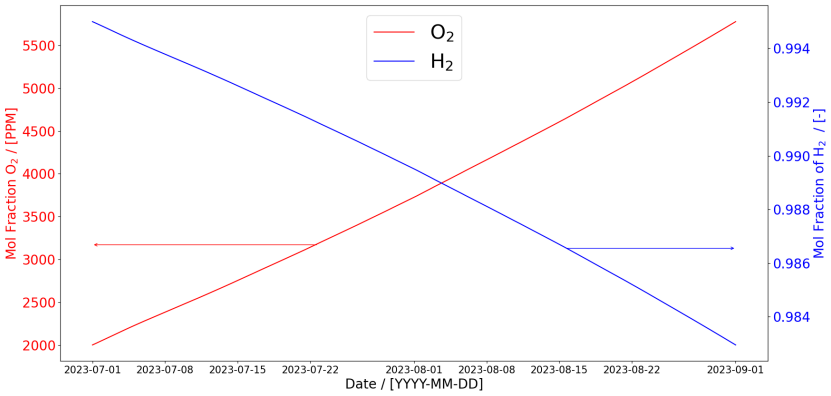

Figure 8.11: Mol fraction of H_2, right axis, and O_2, left axis, in gas compartment B initially 10% filled vs time

Figure 8.11 shows the effect on the mol fractions in the compartment. After 62 days, the concentration of O_2 is around 5500 PPM. This is nowhere near the 40000 PPM needed to form a combustible mixture with H_2. Although the profile for the mol fraction of O_2 in compartment B is not fully linear, a linear fit could approach the number of days after which O_2 represents 40000 PPM of the mixture. In 62 days, the concentration of O_2 has increased by nearly 4000 PPM.

$$x_{O_2} = 2000 + \frac{4000}{62} \times N_{\text{days}} \tag{8.1}$$

Here, x_{O_2} [PPM] is the mol fraction of O_2 in the mixture and N_{days} is the number of days the compartment is at a standstill. If this equation is solved, it would take 589 days before the oxygen concentration reaches 40000 PPM.

8.5.1.2. Compartment B initially 25% filled

Figure 8.12 shows the amount of mols of H_2 and O_2 in gas compartment B. The same amount of mols have permeated as for the case where compartment B is initially filled at 10% instead of 25%; see subsubsection 8.5.1.1.

Due to the larger volume of compartment B, the permeation of O_2 has less influence on the composition of the gas mixture; see Figure 8.13. After 62 days, the concentration of O_2 has reached 3750 PPM, an increase of 1750 PPM from its initial value. Using the same method as Equation 8.1, the gas mixture would take approximately 1346 days to reach a combustible composition. Of course, the mol fraction profile's linear approximation is incorrect. With time, more and more H_2 will permeate, meaning

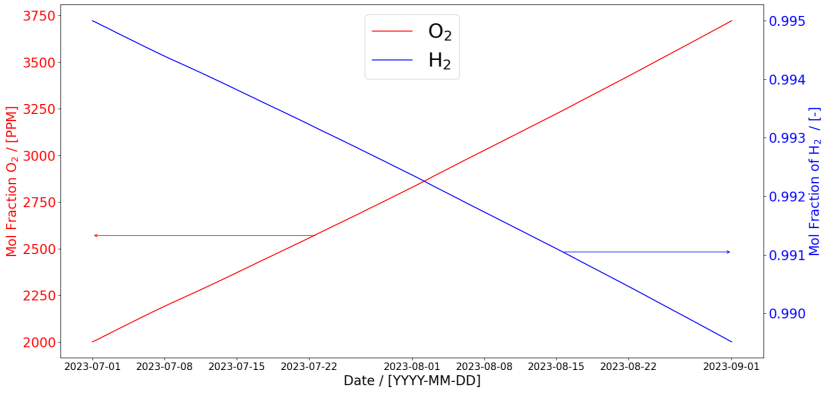

Figure 8.12: Amount of mols of H_2, right axis, and O_2, left, in gas compartment B initially 25% filled axis vs time

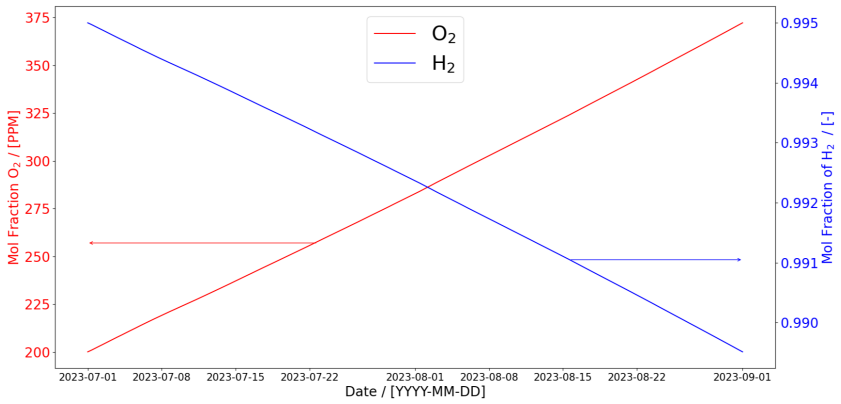

Figure 8.13: Mol fraction of H_2, right axis, and O_2, left axis, in gas compartment B initially 25% filled vs time

the number of mol in gas compartment B shrinks. The concentration difference over the membrane is larger for H_2 than for N_2 and O_2 as the air in compartment A is continuously flushed, meaning there is nearly no hydrogen present in compartment A. This, combined with the fact that H_2 has a higher permeability through the membrane than N_2 and O_2, means its absolute flux is also higher. The shrinking of the number of mols means that the permeation of O_2 has a greater effect. The combustible mixture will thus be reached faster than the suggested timescale here. The linear approach indicates that it will still take a long time.

8.5.2. Product purity requirements

The flow leaving gas compartment B to the electrolyser undergoes a cleaning step before being compressed and delivered to the client. This cleaning step is necessary to remove excess oxygen and water from the product. Thus, nitrogen is the main impurity problem, as it is not removed post-storage. The maximum allowed contamination of N_2 in the final product is 300 PPM; see subsection 2.1.6. If it is assumed that all the excess H_2 and O_2 can be removed and the only impurity is N_2.

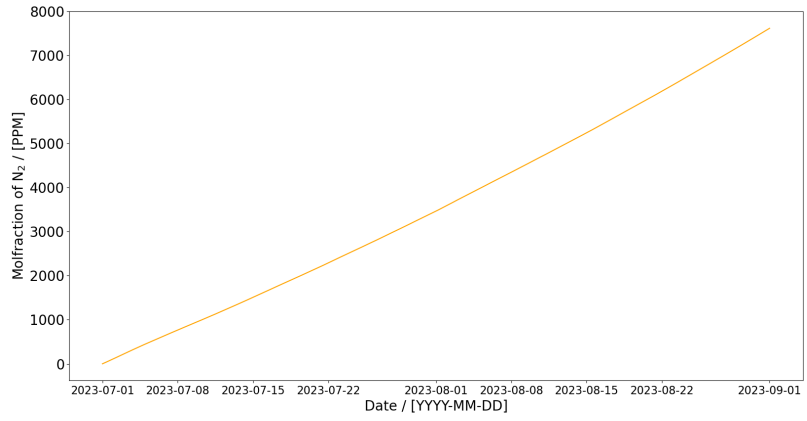

Figure 8.14: Molfraction of N_2 is gas compartment B initially 10% filled vs time

Figure 8.14 and Figure 8.15 represent the molfractions of N_2 in gas compartment B versus time with the compartment being 10% and 25% percent filled. If the threshold of 300 PPM of N_2 is enforced and the other impurities, O_2 and H_2O, are left in the product, it can be observed that after about three days, the gas in compartment B does fulfil the requirements anymore when initially filled at 10% of its volume. It happens exactly on 07-03 at 15:31. When the storage is originally filled at 25%; this takes until 07-06 10:46. This time period is very short compared to the time required for the mixture to be combustible, determined in subsection 8.5.1. This is logical as 300 PPM is substantially less than 40000 PPM.

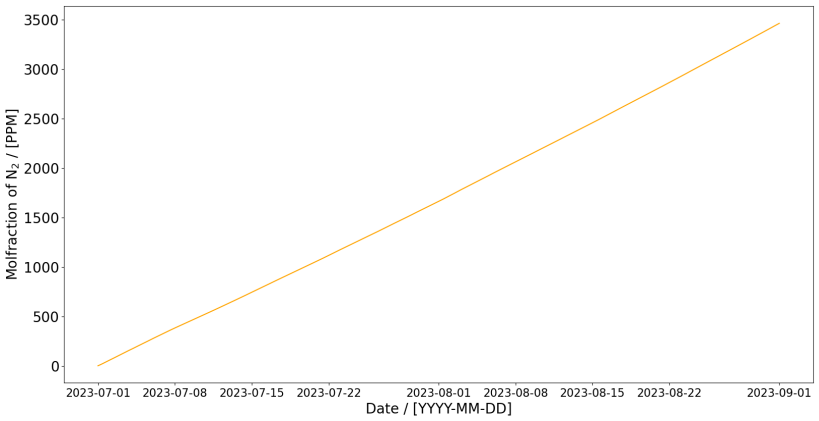

Figure 8.15: Molfraction of N_2 is gas compartment B initially 25% filled vs time

From this, one can conclude that if no downstream N_2 cleaning is available, one should not worry about reaching explosion limits as the product will long before be contaminated with N_2 and, therefore, should be discarded.

(a)

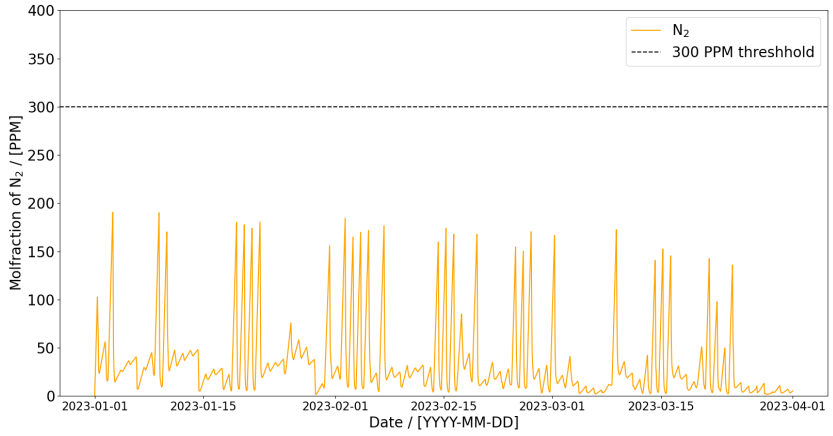

(b)

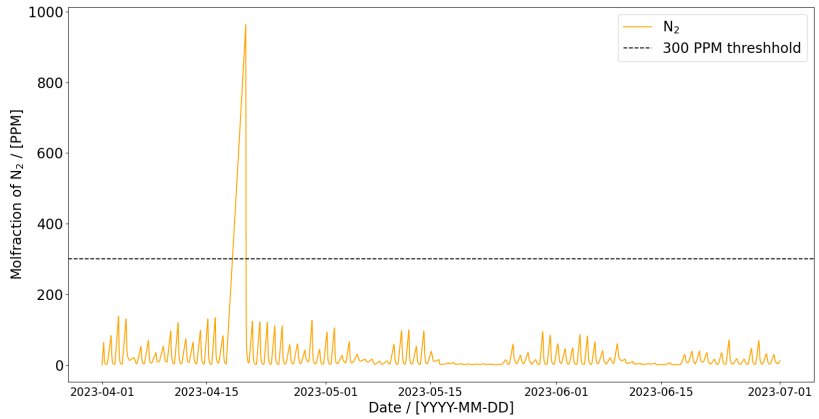

Figure 8.16 shows the profile of the concentration of N_2 in gas compartment B for normal opera-

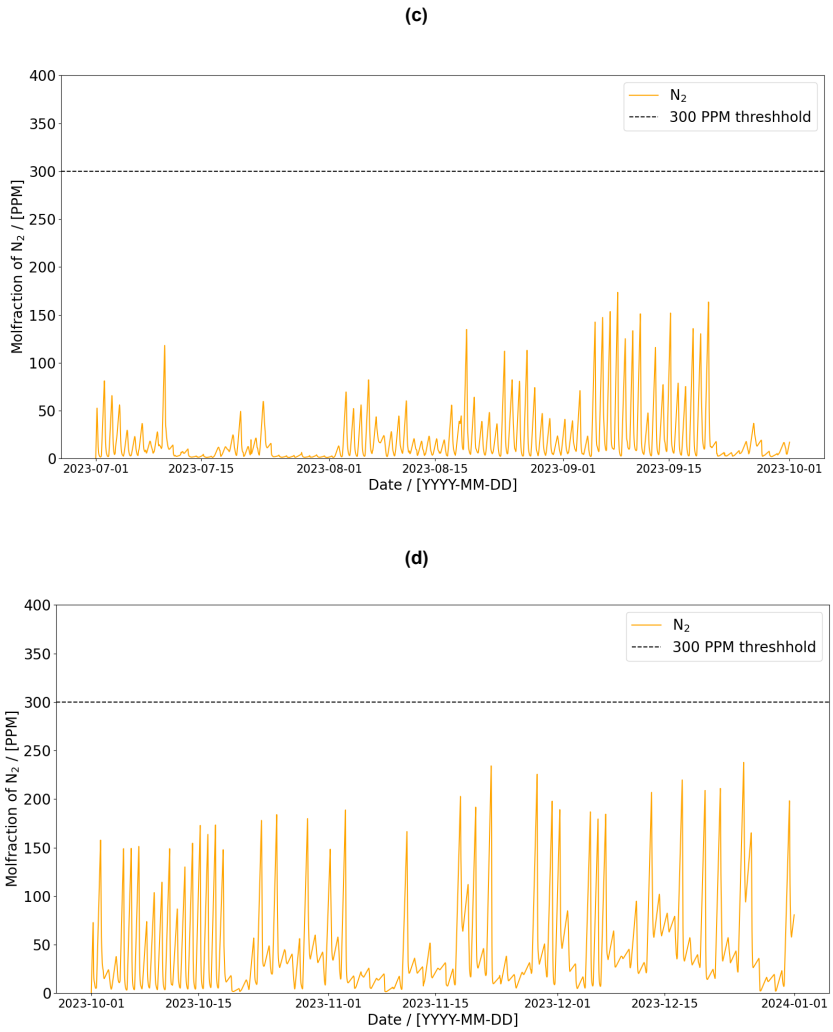

Figure 8.16: Concentration of N_2 in gas compartment B vs time. The simulations represent the normal operation during the four different seasons. Every aspect of the simulation was considered. (a) Winter: 01-01 to 03-31; (b) Spring: 04-01 to 06-30; (c) Summer: 07-01 to 09-30; (d) Autumn: 10-01 to 12-31

tion during the four seasons. A trend can be observed. The concentration of N_2 seems to hit higher values in the year's colder months. This is logical as there are fewer sun hours per day during these colder months, meaning that, generally, less H_2 production. The storage inflation thus takes more time, meaning the N_2 has more time to permeate.

It can be observed that during the normal operation of the gasholder, the concentration of N_2 hits maximally around 200 PPM. This is less than the maximum allowed concentration of 300 PPM. Only in April, Figure 8.16b, the concentration of N_2 surpasses the threshold of 300 PPM. This is because the weather data determined in section 6.1 returns a value of 0 W/m^2 for the global horizontal, direct normal and direct horizontal irradiance from 04-18 to 04-20. Therefore, no H_2 is produced during this time, and the storage is left at a standstill for a long time. This is also visible in Figure A.9 and Figure A.10. The storage should be fully emptied as the product is unusable without downstream cleaning.

8.6. Storage efficiency

Due to the diffusion through the membrane and pressure relief valve B, hydrogen can leave the system. This hydrogen is lost and can not be recuperated. Analysing these losses is interesting. Ultimately, the efficiency of hydrogen storage can be determined.

(a)

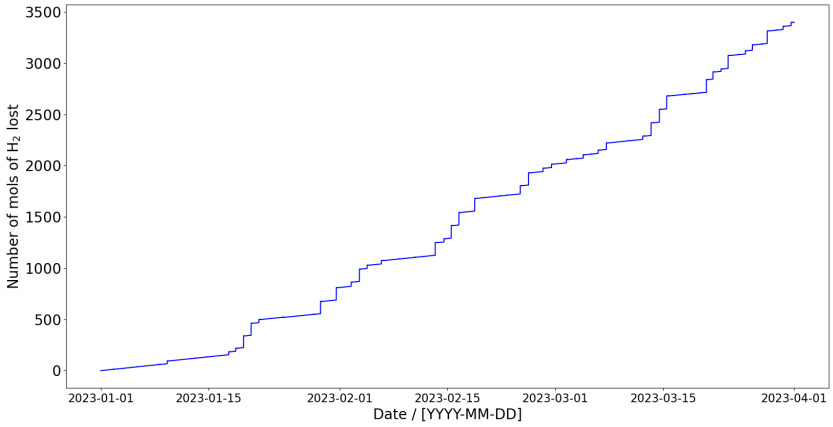

(b)

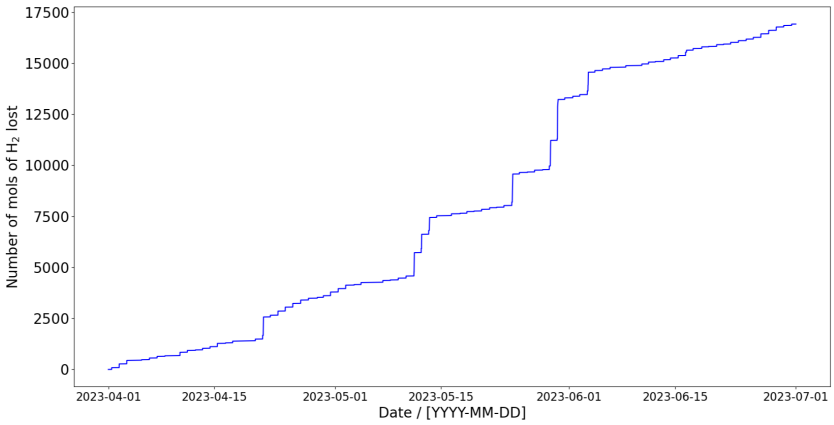

In Figure 8.17, the total number of mols lost per season can be observed. It can be seen that the absolute number of mols of H_2 lost during the colder seasons is less than during the warmer seasons. For example, in the winter, 2500 mols of H_2 will be lost, while in the summer, the number of mols of H_2 lost is 8000. This difference is logical. First of all, the diffusion through the membranes increases with temperature. More mols will thus be lost through permeation during the warmer periods. But this is not the main reason for this difference. During summer, more hydrogen is produced. This means the storage is filled more often, activating the full storage regime, which activates the pressure relief valve in compartment B. This was already visible in Figure 8.4, there was only one drainage cycle during the winter and autumn, while two drainage cycles are observable in the spring and summer. This figure can also explain the large loss of H_2 at the start of the summer. It is observable that the gasholder entered the full storage regime after the deflation started. This means the pressure relief valve for compartment B is active to prevent overpressures in the system. In 20 minutes, the system loses 1000 mol of H_2, a flow of 0.83 mol/s. The steep rises in the H_2 losses are moments when the pressure relief valve of compartment B is opened, venting excess H_2.

The losses don't necessarily mean the storage is less efficient in the summer than in winter. Figure A.12 shows the total amount of mols produced per season during normal operation in Eerbeek. It can be observed that during the summer, twice as much hydrogen is produced compared to in the winter. A logical finding is that solar irradiance is stronger in the summer, producing more power from solar panels. The storage efficiency is defined as the total amount of H_2 produced minus the total amount of hydrogen lost during operation; the result is divided by the total amount of H_2 produced.

All hydrogen lost is emitted into the atmosphere. In subsection 2.1.4, it was determined that the global warming potential of hydrogen is equal to 11.6. This means that emitting one kilo of hydrogen

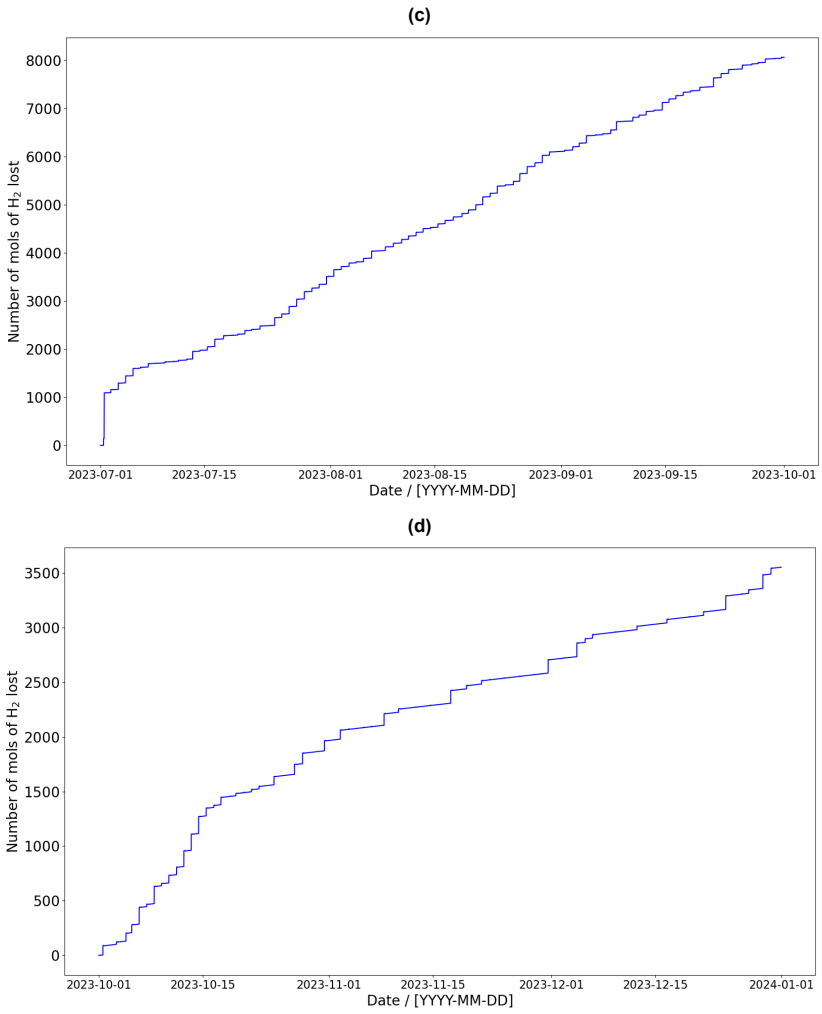

Figure 8.17: Total losses of H_2 in the system during normal operation in Eerbeek during the 4 seasons. (a) winter; (b) spring; (c) summer; (d) autumn

equals emitting 11 kilo of CO_2. Using the molar mass of H_2 and the amount emitted per season, the environmental impact of the storage can be determined. It will be very small, but interestingly, even a process storing green hydrogen has a carbon footprint. This highlights that a fully climate-neutral economy is extremely difficult to create.

Table 8.2: Table containing the absolute values of H_2 lost and produced, the storage efficiency, and the carbon footprint of the storage per season in Eerbeek

Season	**Amount of H_2 lost / [mol]**	**Amount of H_2 produced / [mol$\times 10^6$]**	**Storage efficiency / [%]**	**Equivalent amount of CO_2 emitted / [kg]**
Winter	3400	1.92	99.82	79.5
Spring	16900	4.77	99.65	395
Summer	8075	4.09	99.80	189
Autumn	3553	1.81	99.79	83.1

8.7. Location comparison

As the tool is built to simulate the behaviour of storage at different locations worldwide, it is interesting to compare the results of the simulations for two different locations. Additional simulations have been run. The chosen location is the centre of Spain, with a latitude of 41.22414580285254 and a longitude

of -3.948451093547769. All elements of the simulation have been considered. The default values generated by the weather conditions have been used as initial conditions. The only difference in input between the two simulations is the location data. The results of these simulations will be compared with those run in the previous chapters.

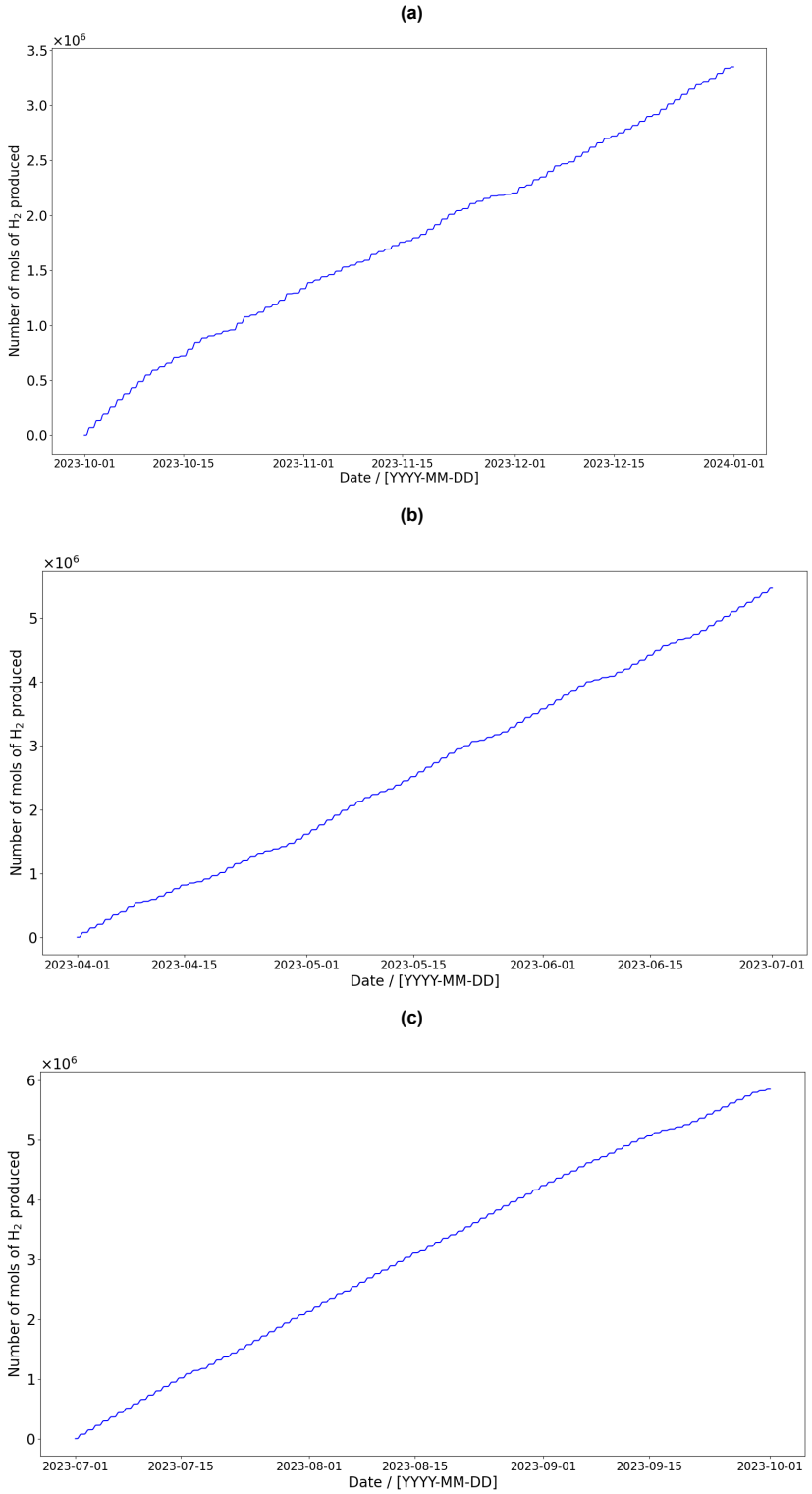

Figure 8.18 shows the total amount of mols produced by the electrolyser during operation in Spain.

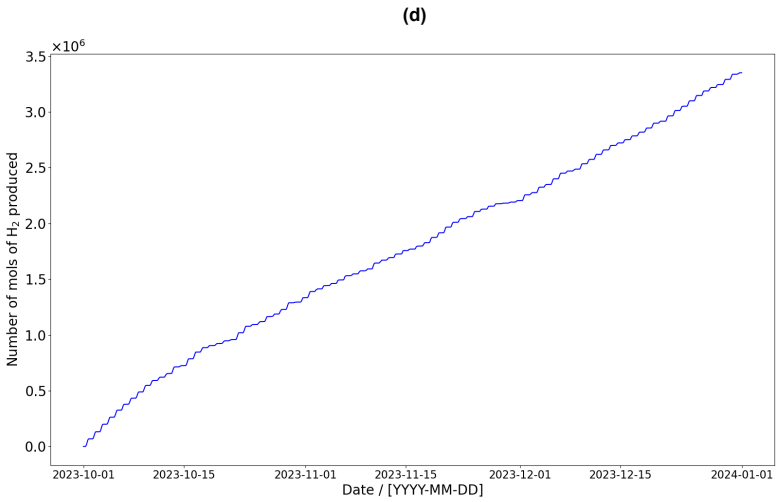

Figure 8.18: Total H_2 produced during normal operation in Spain during the 4 seasons. (a) winter; (b) spring; (c) summer; (d) autumn

In Spain, the amount of produced H_2 is greater than that produced in Eerbeek during every season. This is an expected finding as Spain is known to be a more sunny country than the Netherlands. The hydrogen is produced through a solar-powered electrolyser. The major differences are found during the winter and autumn. The production of H_2 nearly doubles. The exact values have been reported in Table 8.3.

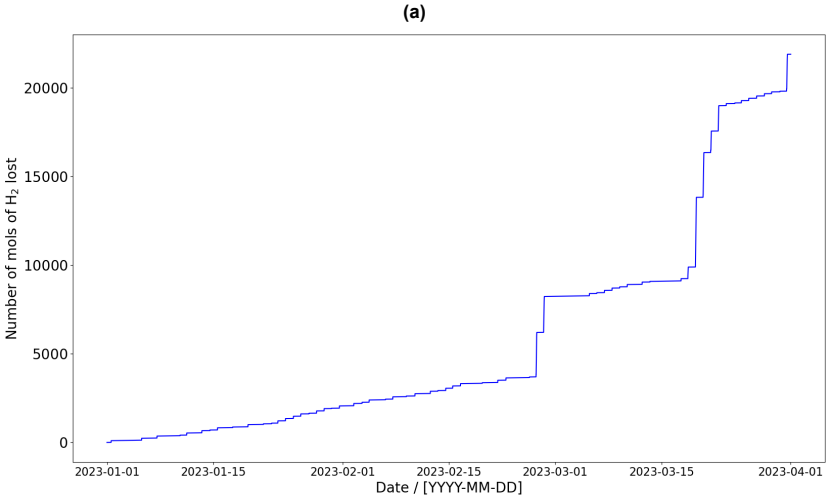

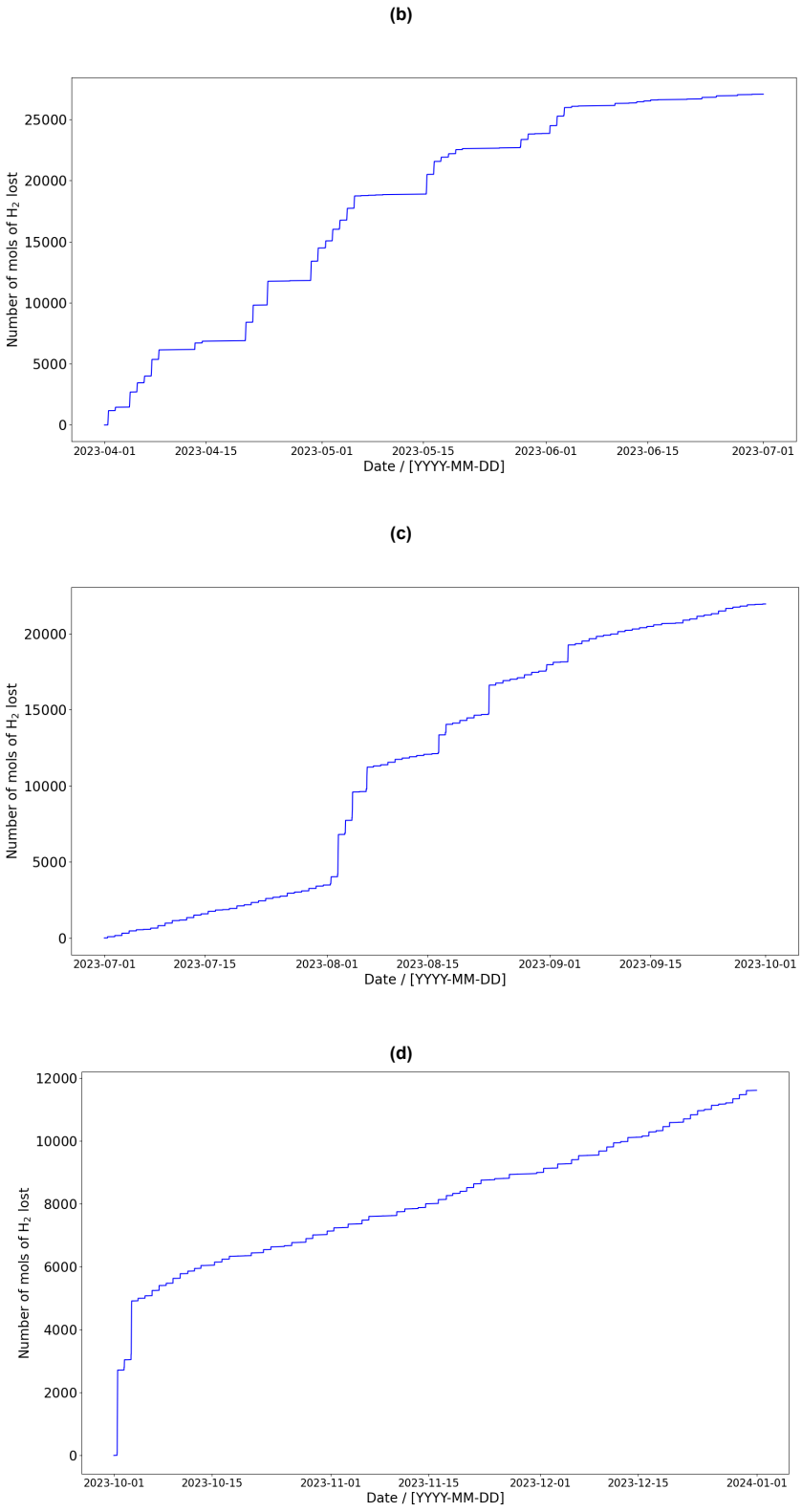

Figure 8.19: Total losses of H_2 in the system during normal operation in Spain during the 4 seasons. (a) winter; (b) spring; (c) summer; (d) autumn

As observed in section 8.6, more production is expected to bring more losses. This is visible in Figure 8.19. The loss is greater per season in Spain as the solar irradiance on the solar panels is greater. This means more hydrogen is produced in the same period of time, leading to greater inlet

flows. Hence, hydrogen production is often greater than the electrolyser demand when the storage drains after being completely filled. Consequently, the storage is sometimes completely filled while the production exceeds the demand. In this case, the pressure relief valve B controller is activated, venting excess H_2. This is visible in Figure 8.4c and discussed in section 8.2. If the system's performance was based on the storage of H_2, only the gasholder is considered, while the rest of the balance of the plant (BoP) is neglected. It could be said that the storage performs better in Eerbeek than in Spain. The storage has higher storage efficiencies in Eerbeek than in Spain during all seasons. This is not a fair conclusion to draw. The main goal of the storage is to serve as a buffer. Long-term storage is not envisioned. The storage is there to minimise the power cycling of the compressor further downstream. Furthermore, the whole idea of the company is to produce H_2 and deliver it to customers. As mentioned above, the production of H_2 is greater in Spain than in Eerbeek. This is also visible in the number of compressor cycles per season at each location; see Figure A.13 and Figure A.14. The results have been summarised in Table 8.3 and Table 8.4. In Spain, the storage is drained more often. This is logical as more hydrogen is produced. This results in a higher number of compressor cycles during the operation. It becomes interesting to compare the number of cycles and the total compressor runtime per location. The combination of these two results leads to an average compressor runtime. The average drainage cycle takes longer in Spain, meaning that more H_2 is ultimately produced for every cycle. If the compressor only degrades per power cycle, this operation is desirable.

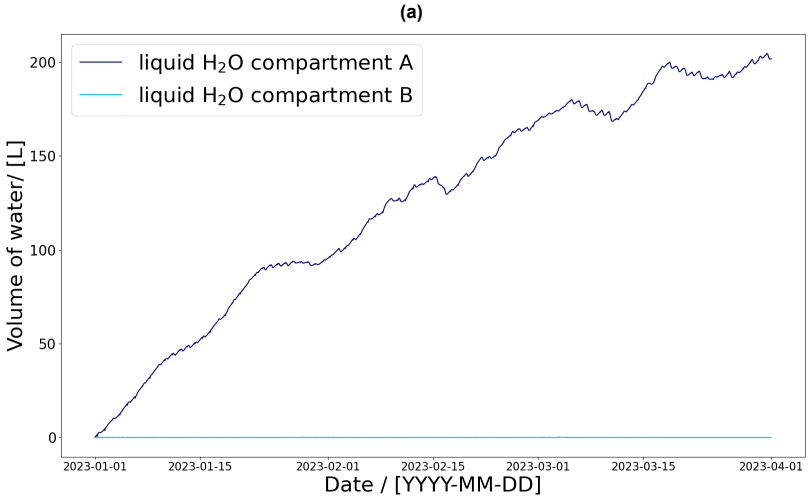

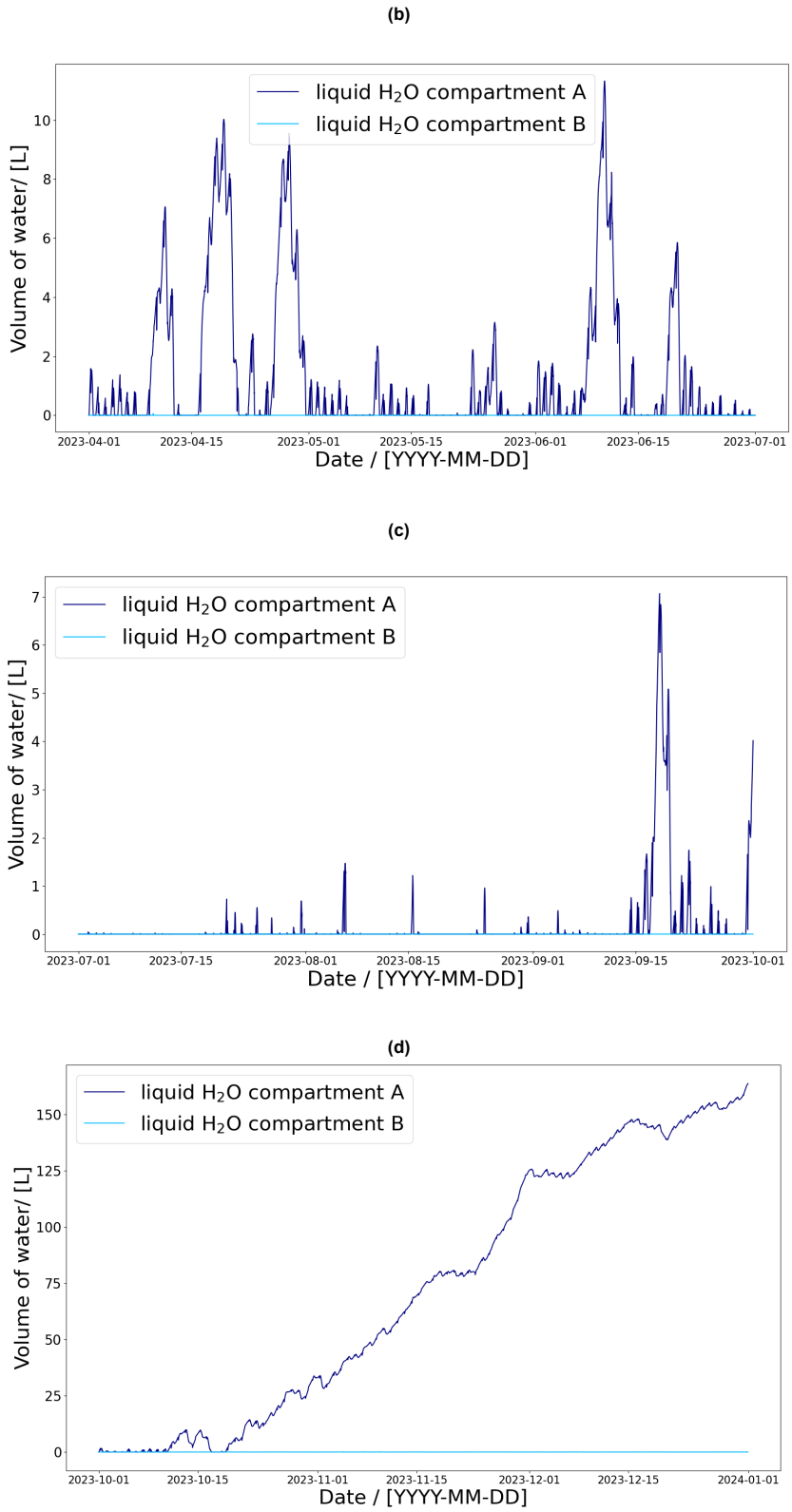

Figure 8.20: Total water forming in the system during normal operation in Spain during the 4 seasons. (a) winter; (b) spring; (c) summer; (d) autumn

At last, the amount of water forming in the system is compared; see Figure A.1 and Figure 8.20. Similar trends can be seen as the ones mentioned in section 8.1. Again, a large volume of liquid H_2O is growing in compartment A. It may seem contradictional to expectations, but a larger volume of

Table 8.3: Table containing the absolute values of H_2 lost and produced, the storage efficiency, the carbon footprint of the storage, the number of drainage cycles of the storage, the total compressor runtime and the average compressor runtime per season in Spain

	Winter	**Spring**	**Summer**	**Autumn**
Amount of H_2 lost [mol]	21900	27100	22000	11600
Amount of H_2 produced [mol $\times 10^6$]	3.17	5.47	5.85	3.55
Storage efficiency [%]	99.31	99.50	99.62	99.67
Equivalent amount of CO_2 emitted [kg]	512	663	514	271
Number of cycles	76	91	92	82
Total compressor run time / [h]	344	593	635	362
Average compressor run time / [h]	4.53	6.52	6.90	4.66

Table 8.4: Table containing the number of drainage cycles of the storage, the total compressor runtime and the average compressor runtime per season in Eerbeek

	Winter	**Spring**	**Summer**	**Autumn**
Number of cycles	59	88	90	56
Total compressor run time / [h]	209	517	516	197
Average compressor run time / [h]	3.54	5.88	5.73	3.51

H_2O condenses in Spain than in the Netherlands. This happens because the fraction of H_2O vapour is greater in Sprain than in Eerbeek. Without the author knowing beforehand, the location chosen is elevated, with an altitude of 957 m. This means the air pressure is lower in Spain than in the Netherlands. At the same temperature, the air in Spain has a larger concentration of H_2O than in Eerbeek. This can be seen in Figure A.18, the average mol fraction of H_2O in the winter in Eerbeek and Spain is 0.0064 and 0.0074, respectively. In the autumn, these are 0.0090 and 0.0096, respectively. This means that H_2O enters the system in Spain, leading to higher partial water pressure and, thus, more condensation.

Overall, running the operation in Spain is more beneficial than in Eerbeek. The main advantage is the increase in production. Although the storage is less efficient in Spain, the compressor runs for a longer period of time per season, meaning more final product is available. Being able to produce more products with the exact same equipment is a considerable advantage. The higher amount of H_2 vented means that the storage also becomes more polluting in Spain than in Eerbeek. This is something to remember as the company supplies clean energy through green hydrogen. XINTC produces a modular electrolyser whose capacity can easily be scaled. To prevent large amounts of vented H_2, an additional boundary condition can be added to the full storage regime. This regime could also activate a controller regulating the electrolyser capacity. Limiting the electrolyser capacity could prevent the inlet flow from being superior to the outlet flow. The pressure in the system could solely rise due to a temperature increase. This minimises the losses of H_2.

9

Conclusion

This work focused on modelling a double membrane gasholder as a hydrogen storage device at atmospheric pressure. The storage serves as a buffer for the intermittent hydrogen production from solar energy. The downstream compressor's power cycling should be limited as much as possible. A control system was designed to accommodate this kind of operation. The system regulates the pressure in the storage: multiple regimes have been defined to ensure efficient operation. The control system ensures that it starts draining the storage once it has reached maximum capacity and stops when it is emptied. Furthermore, the thermodynamic model of Yuki Junior et al. [4] has been elaborated. The condensation of water has been considered. It was shown that the water in the system is prone to condense, which influences the system's energy. The water in the liquid phase will also evaporate in later instances as the temperature in the compartments rises. The permeation of molecules through the membranes in the system has also been regarded. The flux through the membranes was approached using Maxwell-Stefan diffusion. The diffusion of molecules is essential to account for while storing hydrogen. Hydrogen has a wide combustible range.

Furthermore, the purity requirements for hydrogen are stringent. The model showed that one should not have to worry about safety issues. The hydrogen will long before being contaminated with nitrogen. As no downstream cleaning for nitrogen is available, the hydrogen must be discarded before reaching combustion limits. The results for regular operation show that this contamination limit is nearly never reached. Only when there are multiple days of no sun hours does the nitrogen form a purity problem. Incorporating heat transfer in the system meant an accurate estimation of the system conditions was made at every instance. The model showed the influence of weather conditions on the storage. During colder periods, more condensation is expected in the system, and less hydrogen is produced. This means the storage makes fewer cycles, and the molecules have more time to diffuse through the membrane. During the warmer periods of the year, more hydrogen is produced in the same amount of time. This leads to more hydrogen losses due to venting through the pressure relief of compartment B. Storage is less efficient in warmer locations with high solar irradiance. Although storage is less efficient, choosing a location with long hours and high solar irradiance benefits the whole process. This results in a larger amount of final product and is beneficial for the power-cycle efficiency of the compressor.

Overall, the model is capable of predicting the storage behaviour. It can be used to determine the production of hydrogen and the number of cycles. The model also determines the composition of the gas exiting the storage towards the compressor. These will depend on outside weather conditions. Furthermore, the model is fully modular. It can be used at all locations around the world. The user only has to provide the latitude and longitude of the desired location. Also, the model can run for multiple gasholders at the same time. The gasholders can be interconnected or stand-alone.

The results indicate that a gasholder is a suitable storage system to accommodate the dynamic storage of hydrogen. Its storage efficiency is high, at least 98% in the worst case, and the storage responds well to the many drainage cycles. the permeation of molecules through the membranes only forms a problem if the storage is at a standstill for more than two days while completely empty. This happens long before safety becomes an issue.

The model has a flaw: the condensation builds up in compartment A, leading to a large volume of water. This volume is too large for the assumptions to make sense. Therefore, a drain should be added.

The drain would remove the liquid water from the storage. Furthermore, it was also suggested to combine the control system regulating the pressure with the electrolyser controller. This could prevent overpressures in compartment B and, thus, the venting of hydrogen, leading to fewer losses. Although the model presents realistic results, increasing accuracy is still possible. The easiest way to increase the model's accuracy is by measuring the correct permeability constants associated with each membrane. At the moment, they have been approximated by an engineering guess. The company provided the permeability of H_2. Based on these values, the permeability of N_2 and O_2 have been approached using the free volume theory applied to the Maxwell-Stefan diffusion. An experiment mimicking exact process conditions could provide more insights into the permeability ratios of the permeability. At the moment, the permeability of H_2 is a factor ten higher than the permeability of N_2 or O_2. The exact ratio will vary with process conditions (temperature pressure, concentration, etc.), but the experimentally determined ratio could indicate the right order of magnitude. An experiment determining the constants used in the heat transfer part is also a simple way to improve the model. The correct emissivity and solar absorption coefficient could greatly influence the temperature profile in the gasholder. The heat transfer part of the model could also be elaborated, as mentioned in section 5.7.

Ideal mixing has been assumed throughout the model, meaning no concentration gradients exist. The permeation of the gasses through the membranes will also lead to potential concentration gradients in the compartments. The diffusion occurs at the membrane's surface, creating regions of lower concentration at the feed side of the membrane and areas of higher concentration at the permeate side of the membrane. This leads to a lower regional concentration gradient over the membrane, affecting the permeation fluxes of the molecules. A one-phase turbulent CFD simulation could provide an understanding of the mixing in the compartments. If these simulations show that low mixing zones near the membranes exist, a molecular simulation over the membranes of the compartments could give more insights into the extent of this effect.

The model also assumes that no liquid leaves the system through the valves. This assumption is not true. In reality, small droplets of water can be suspended in the air. They may be so small that other forces balance out the gravitational pull. This is the case for mist. If the amount of water suspended in the air is known, a Lagrangian particle tracking could indicate the amount dragged out of liquid water dragged out of the system through the valves.

References

1. Calvin, K. *et al. IPCC, 2023: Climate Change 2023: Synthesis Report. Contribution of Working Groups I, II and III to the Sixth Assessment Report of the Intergovernmental Panel on Climate Change [Core Writing Team, H. Lee and J. Romero (eds.)]. IPCC, Geneva, Switzerland.* en. Tech. rep. Edition: First (Intergovernmental Panel on Climate Change (IPCC), July 2023). https://www.ipcc.ch/report/ar6/syr/ (2024).
2. Rivard, E., Trudeau, M. & Zaghib, K. Hydrogen Storage for Mobility: A Review. en. *Materials* **12.** Number: 12 Publisher: Multidisciplinary Digital Publishing Institute, 1973. ISSN: 1996-1944. https://www.mdpi.com/1996-1944/12/12/1973 (2023) (Jan. 2019).
3. Hassan, I. A., Ramadan, H. S., Saleh, M. A. & Hissel, D. Hydrogen storage technologies for stationary and mobile applications: Review, analysis and perspectives. *Renewable and Sustainable Energy Reviews* **149,** 111311. ISSN: 1364-0321. https://www.sciencedirect.com/science/article/pii/S1364032121005980 (2023) (Oct. 2021).
4. Yuki Junior, G. M., Sochard, S., Dinuccio, E. & Marias, F. in *Computer Aided Chemical Engineering* (eds Kokossis, A. C., Georgiadis, M. C. & Pistikopoulos, E.) 3135–3140 (Elsevier, Jan. 2023). https://www.sciencedirect.com/science/article/pii/B978044315274050500X (2023).
5. TZIMAS, E., FILIOU, C., Peteves, S. & VEYRET, J.-B. *HYDROGEN STORAGE: STATE-OF-THE-ART AND FUTURE PERSPECTIVE* tech. rep. (European commision, Jan. 2003). https://publications.jrc.ec.europa.eu/repository/handle/JRC26493.
6. Züttel, A. Hydrogen storage methods. en. *Naturwissenschaften* **91,** 157–172. ISSN: 1432-1904. https://doi.org/10.1007/s00114-004-0516-x (2023) (Apr. 2004).
7. Ghorbani, B., Zendehboudi, S., Saady, N. M. C. & Dusseault, M. B. Hydrogen storage in North America: Status, prospects, and challenges. en. *Journal of Environmental Chemical Engineering* **11,** 109957. ISSN: 22133437. https://linkinghub.elsevier.com/retrieve/pii/S2213343723006966 (2023) (June 2023).
8. Lemmon, E. W., Bell, I. H., Huber, M. L. & McLinden, M. O. *NIST Standard Reference Database 23: Reference Fluid Thermodynamic and Transport Properties-REFPROP, Version 10.0, National Institute of Standards and Technology* 2018. https://www.nist.gov/srd/refprop.
9. Usman, M. R. Hydrogen storage methods: Review and current status. *Renewable and Sustainable Energy Reviews* **167,** 112743. ISSN: 1364-0321. https://www.sciencedirect.com/science/article/pii/S1364032122006311 (2023) (Oct. 2022).
10. Tang, D. *et al.* State-of-the-art hydrogen generation techniques and storage methods: A critical review. *Journal of Energy Storage* **64,** 107196. ISSN: 2352-152X. https://www.sciencedirect.com/science/article/pii/S2352152X23005935 (2023) (Aug. 2023).
11. Leachman, J. W., Jacobsen, R. T., Penoncello, S. G. & Lemmon, E. W. Fundamental Equations of State for Parahydrogen, Normal Hydrogen, and Orthohydrogen. en. *Journal of Physical and Chemical Reference Data* **38,** 721–748. ISSN: 0047-2689, 1529-7845. https://pubs.aip.org/jpr/article/38/3/721/242953/Fundamental-Equations-of-State-for-Parahydrogen (2023) (Sept. 2009).
12. Charalampidi, A.-M. *Evaluation of thermodynamic models for pure hydrogen and hydrogen-containing binary mixtures* PhD thesis (Norwegian University of Science and Technology, June 2022). https://ntnuopen.ntnu.no/ntnu-xmlui/handle/11250/3027678#:~:text=From%20the%20thermodynamic%20model%20comparison,in%20all%20of%20the%20calculations..
13. Tarhan, C. & Çil, M. A. A study on hydrogen, the clean energy of the future: Hydrogen storage methods. en. *Journal of Energy Storage* **40,** 102676. ISSN: 2352152X. https://linkinghub.elsevier.com/retrieve/pii/S2352152X21004151 (2023) (Aug. 2021).

14. Lubitz, W. & Tumas, W. Hydrogen: An Overview. *Chemical Reviews* **107.** Publisher: American Chemical Society, 3900–3903. ISSN: 0009-2665. https://doi.org/10.1021/cr050200z (2023) (Oct. 2007).
15. Crowl, D. A. & Jo, Y.-D. The hazards and risks of hydrogen. *Journal of Loss Prevention in the Process Industries* **20,** 158–164. ISSN: 0950-4230. https://www.sciencedirect.com/science/article/pii/S0950423007000046 (2023) (Mar. 2007).
16. Liu, X. & Zhang, Q. Influence of initial pressure and temperature on flammability limits of hydrogen–air. en. *International Journal of Hydrogen Energy* **39,** 6774–6782. ISSN: 03603199. https://linkinghub.elsevier.com/retrieve/pii/S0360319914003279 (2023) (Apr. 2014).
17. Bjerketvedt, D., Bakke, J. R. & Van Wingerden, K. Gas explosion handbook. en. *Journal of Hazardous Materials* **52,** 1–150. ISSN: 03043894. https://linkinghub.elsevier.com/retrieve/pii/S0304389497816202 (2024) (Jan. 1997).
18. Astbury, G. & Hawksworth, S. Spontaneous ignition of hydrogen leaks: A review of postulated mechanisms. en. *International Journal of Hydrogen Energy* **32,** 2178–2185. ISSN: 03603199. https://linkinghub.elsevier.com/retrieve/pii/S0360319907002091 (2023) (Sept. 2007).
19. Dwivedi, S. K. & Vishwakarma, M. Hydrogen embrittlement in different materials: A review. *International Journal of Hydrogen Energy* **43,** 21603–21616. ISSN: 0360-3199. https://www.sciencedirect.com/science/article/pii/S0360319918331306 (2023) (Nov. 2018).
20. Yao, J., Tan, Q., Venezuela, J., Atrens, A. & Zhang, M.-X. Recent research progress in hydrogen embrittlement of additively manufactured metals – A review. *Current Opinion in Solid State and Materials Science* **27,** 101106. ISSN: 1359-0286. https://www.sciencedirect.com/science/article/pii/S1359028623000517 (2023) (Oct. 2023).
21. Ocko, I. B. & Hamburg, S. P. Climate consequences of hydrogen emissions. English. *Atmospheric Chemistry and Physics* **22.** Publisher: Copernicus GmbH, 9349–9368. ISSN: 1680-7316. https://acp.copernicus.org/articles/22/9349/2022/ (2023) (July 2022).
22. NASA. *The Aura Mission* en. https://aura.gsfc.nasa.gov/ (2023).
23. Sand, M. *et al.* A multi-model assessment of the Global Warming Potential of hydrogen. en. *Communications Earth & Environment* **4.** Number: 1 Publisher: Nature Publishing Group, 1–12. ISSN: 2662-4435. https://www.nature.com/articles/s43247-023-00857-8 (2023) (June 2023).
24. *Purity, Grades and Concentration* en. https://www.boconline.co.uk/en/contact-and-support/technical-advice/speciality-products-advice/purity-grades-concentration/purity-grades.html (2024).
25. *Hydrogen fuel quality* 2019. https://cdn.standards.iteh.ai/samples/69539/4adc159648da4454a4b39d0b87ac348e/ISO-14687-2019.pdf (2024).
26. Andersson, J. & Grönkvist, S. Large-scale storage of hydrogen. en. *International Journal of Hydrogen Energy* **44,** 11901–11919. ISSN: 03603199. https://linkinghub.elsevier.com/retrieve/pii/S0360319919310195 (2023) (May 2019).
27. Ma, N., Zhao, W., Wang, W., Li, X. & Zhou, H. Large scale of green hydrogen storage: Opportunities and challenges. *International Journal of Hydrogen Energy.* ISSN: 0360-3199. https://www.sciencedirect.com/science/article/pii/S0360319923045883 (2023) (Sept. 2023).
28. Schüth, F. Challenges in hydrogen storage. en. *The European Physical Journal Special Topics* **176,** 155–166. ISSN: 1951-6401. https://doi.org/10.1140/epjst/e2009-01155-x (2023) (Sept. 2009).
29. Kumar Sarmah, M., Pratap Singh, T., Kalita, P. & Dewan, A. Sustainable hydrogen generation and storage – a review. en. *RSC Advances* **13.** Publisher: Royal Society of Chemistry, 25253–25275. https://pubs.rsc.org/en/content/articlelanding/2023/ra/d3ra04148d (2023) (2023).
30. Edwards, P., Kuznetsov, V. & David, W. Hydrogen energy. *Philosophical Transactions of the Royal Society A: Mathematical, Physical and Engineering Sciences* **365.** Publisher: Royal Society, 1043–1056. https://royalsocietypublishing.org/doi/full/10.1098/rsta.2006.1965 (2023) (Feb. 2007).

31. Deng, L., Liu, Y. & Wang, W. *Biogas Technology* en. ISBN: 9789811549397. http://link.springer.com/10.1007/978-981-15-4940-3 (2024) (Springer Singapore, Singapore, 2020).
32. Samer, M. en. in *Biogas* (ed Kumar, S.) (InTech, Mar. 2012). ISBN: 978-953-51-0204-5. http://www.intechopen.com/books/biogas/biogas-plant-constructions (2024).
33. Kube, J. Management of Gas Storages in Biogas Plants. en. *Chemical Engineering & Technology* **41,** 702–710. ISSN: 0930-7516, 1521-4125. https://onlinelibrary.wiley.com/doi/10.1002/ceat.201700395 (2023) (Apr. 2018).
34. Reinelt, T. & Liebetrau, J. Monitoring and Mitigation of Methane Emissions from Pressure Relief Valves of a Biogas Plant. en. *Chemical Engineering & Technology* **43,** 7–18. ISSN: 1521-4125. https://onlinelibrary.wiley.com/doi/abs/10.1002/ceat.201900180 (2024) (2020).
35. Ahmadi, A., Avila, M. & Barna, L. Pathways for the thermally optimal design and practice of anaerobic digestion in large-scale biogas plants: Heat transfer modeling and energy analysis. *Chemical Engineering Research and Design* **197,** 884–907. ISSN: 0263-8762. https://www.sciencedirect.com/science/article/pii/S0263876223005233 (2024) (Sept. 2023).
36. Avila-Lopez, M., Robles-Rodriguez, C., Tiruta-Barna, L. & Ahmadi, A. Toward thermal autarky for large-scale biogas plants: Dynamic energy modeling for energy efficiency in anaerobic digesters with enhanced multimembrane gasholders. *Fuel* **339,** 126978. ISSN: 0016-2361. https://www.sciencedirect.com/science/article/pii/S0016236122038029 (2023) (May 2023).
37. Shindo, R. & Nagai, K. en. in *Encyclopedia of Polymeric Nanomaterials* (eds Kobayashi, S. & Müllen, K.) 1–8 (Springer, Berlin, Heidelberg, 2021). ISBN: 978-3-642-36199-9. https://doi.org/10.1007/978-3-642-36199-9_134-1 (2023).
38. Soni, V., Abildskov, J., Jonsson, G. & Gani, R. A general model for membrane-based separation processes. *Computers & Chemical Engineering. Selected Papers from the 17th European Symposium on Computer Aided Process Engineering held in Bucharest, Romania, May 2007* **33,** 644–659. ISSN: 0098-1354. https://www.sciencedirect.com/science/article/pii/S0098135408001506 (2024) (Mar. 2009).
39. Baker, R. en. in *Membrane Technology and Applications* Section 8, 301–353 (John Wiley & Sons, Ltd, 2004). ISBN: 978-0-470-02039-5. https://onlinelibrary.wiley.com/doi/abs/10.1002/0470020393.ch8 (2023).
40. Surya Murali, R., Sankarshana, T. & Sridhar, S. Air Separation by Polymer-based Membrane Technology. *Separation & Purification Reviews* **42,** 130–186. ISSN: 1542-2119. https://doi.org/10.1080/15422119.2012.686000 (2023) (Jan. 2013).
41. Acharya, N. K., Yadav, P. K. & Vijay, Y. K. Study of temperature dependent gas permeability for polycarbonate membrane. en. *Indian Journal of Pure & Applied Physics* **42,** 179–181 (Jan. 2004).
42. Baker, R. W. *Membrane technology and applications* 3rd ed. en. Medium: electronic resource. ISBN: 978-1-118-35971-6. https://onlinelibrary.wiley.com/doi/book/10.1002/0470020393 (John Wiley & Sons, Chichester, West Sussex ; Hoboken, 2012).
43. Fabiani, C., Bimbi, L., Pizzichini, M. & Santarossa, L. Performance of a hollow fibre membrane unit in oxygen-enriched air production. *Gas Separation & Purification* **10,** 75–79. ISSN: 0950-4214. https://www.sciencedirect.com/science/article/pii/0950421496000126 (2023) (Jan. 1996).
44. Kane, M. *Permeability, Solubility, and Interaction of Hydrogen in Polymers- An Assessment of Materials for Hydrogen Transport* English. Technical Report WSRC-STI-2008-00009 (Savannah River Site (SRS), Aiken, SC (United States), Feb. 2008). https://doi.org/10.2172/927901.
45. Coombe, H. S. & Nieh, S. Polymer membrane air separation performance for portable oxygen enriched combustion applications. en. *Energy Conversion and Management* **48,** 1499–1505. ISSN: 01968904. https://linkinghub.elsevier.com/retrieve/pii/S019689040600358X (2023) (May 2007).
46. Pettersen, T. & Lien, K. A new robust design model for gas separating membrane modules, based on analogy with counter-current heat exchangers. en. *Computers & Chemical Engineering* **18,** 427–439. ISSN: 00981354. https://linkinghub.elsevier.com/retrieve/pii/0098135494880212 (2023) (May 1994).

47. Matteucci, S., Yampolskii, Y., Freeman, B. D. & Pinnau, I. en. in *Materials Science of Membranes for Gas and Vapor Separation* (eds Yampolskii, Y., Pinnau, I. & Freeman, B.) 1st ed., 1–47 (Wiley, June 2006). ISBN: 978-0-470-85345-0. https://onlinelibrary.wiley.com/doi/10.1002/047002903X.ch1 (2024).
48. Giacinti Baschetti, M. & Minelli, M. Test methods for the characterization of gas and vapor permeability in polymers for food packaging application: A review. *Polymer Testing* **89,** 106606. ISSN: 0142-9418. https://www.sciencedirect.com/science/article/pii/S014294182030502X (2024) (Sept. 2020).
49. Hermkens, R. & Jansma, S. *Leak tightness of PVC fittings with hydrogen* tech. rep. (Sept. 2022). https://www.netbeheernederland.nl/publication/rapport-leak-tightness-pvc-fittings-hydrogen.
50. San Marchi, C. *Technical Reference on Hydrogen Compatibility of Materials* tech. rep. (2012). https://h2tools.org/sites/default/files/SAND2012_7321.pdf.
51. Tanaka, K., Kita, H., Okano, M. & Okamoto, K.-i. Permeability and permselectivity of gases in fluorinated and non-fluorinated polyimides. en. *Polymer* **33,** 585–592. ISSN: 00323861. https://linkinghub.elsevier.com/retrieve/pii/003238619290736G (2024) (Jan. 1992).
52. Wesselingh, J. & Krishna, R. *Mass Transfer in Multicomponent Mixtures* ISBN: 9040720711 (Delft University Press, 2000).
53. Wesselingh, J. & Bollen, A. Multicomponent Diffusivities from the Free Volume Theory. en. *Chemical Engineering Research and Design* **75,** 590–602. ISSN: 02638762. https://linkinghub.elsevier.com/retrieve/pii/S0263876297715752 (2024) (Sept. 1997).
54. Buck, A. L. New Equations for Computing Vapor Pressure and Enhancement Factor. *Journal of Applied Meteorology and Climatology* **20.** Place: Boston MA, USA Publisher: American Meteorological Society, 1527–1532. https://journals.ametsoc.org/view/journals/apme/20/12/1520-0450_1981_020_1527_nefcvp_2_0_co_2.xml (1981).
55. Moran, M. J. & Shapiro, H. N. *Fundamentals of Engineering Thermodynamics* 9th. en. ISBN: 978-1-119-39142-5. https://books.google.nl/books/about/Fundamentals_of_Engineering_Thermodynami.html?id=QHJlDwAAQBAJ&redir_esc=y (John Wiley & Sons, Incorporated, New York, 2019).
56. Mills, A. F. *Basic heat and mass transfer* Third edition. en. OCLC: 954592884. ISBN: 978-0-9963053-0-3 (Prentice Hall, San Diego, California, 2015).
57. Incropera, F. P., DeWitt, D. P., Bergman, T. L. & Lavine, A. S. *Principles of heat and mass transfer* 7th edition. en. ISBN: 978-0-470-50197-9 (Wiley, Hoboken, NJ, 2013).
58. *VDI Heat Atlas* en (ed VDI-Gesellschaft Verfahrenstechnik und Chemieingenieurwesen) ISBN: 978-3-540-77876-9. https://link.springer.com/10.1007/978-3-540-77877-6 (2024) (Springer Berlin Heidelberg, Berlin, Heidelberg, 2010).
59. Jaffer, A. Natural Convection Heat Transfer from an Isothermal Plate. *Thermo* **3,** 148–175. ISSN: 2673-7264. https://www.mdpi.com/2673-7264/3/1/10 (2023).
60. Walton, G. N. *Thermal Analysis Research Program reference manual* en. Mar. 1983. https://www.govinfo.gov/content/pkg/GOVPUB-C13-6176908b08a357a0ac91a8ab3db55b97/pdf/GOVPUB-C13-6176908b08a357a0ac91a8ab3db55b97.pdf.
61. US Department of Energy. *Table of Contents: Engineering Reference — EnergyPlus 9.0* 2018. https://bigladdersoftware.com/epx/docs/9-0/engineering-reference/index.html.
62. Joint Research Centre. *Photovoltaic Geographical Information System (PVGIS)* Europa.eu. Jan. 2016. https://re.jrc.ec.europa.eu/pvg_tools/en/#MR.
63. Jensen, A. R. *et al.* pvlib iotools—Open-source Python functions for seamless access to solar irradiance data. *Solar Energy* **266,** 112092. ISSN: 0038-092X. https://www.sciencedirect.com/science/article/pii/S0038092X23007260 (2023).
64. Algarni, S. & Nutter, D. Survey of Sky EffectiveTemperature Models Applicable to Building Envelope Radiant Heat Transfer. en. Publisher: [object Object]. http://rgdoi.net/10.13140/RG.2.1.4212.5526 (2024) (2015).

65. Aubinet, M. Longwave sky radiation parametrizations. en. *Solar Energy* **53,** 147–154. ISSN: 0038092X. https://linkinghub.elsevier.com/retrieve/pii/0038092X94904758 (2024) (Aug. 1994).

66. 2021. https://pvpmc.sandia.gov/modeling-guide/1-weather-design-inputs/irradiance-insolation/extraterrestrial-radiation/.

67. Anderson, K. S. *et al.* pvlib python: 2023 project update. *Journal of Open Source Software* **8,** 5994. https://doi.org/10.21105/joss.05994 (2023).

68. 2014. https://www.enfsolar.com/pv/panel-datasheet/crystalline/62165.

69. Glueckauf, E. & Kitt, G. P. The hydrogen content of atmospheric air at ground level. *Quarterly Journal of the Royal Meteorological Society* **83,** 522–528. https://rmets.onlinelibrary.wiley.com/doi/abs/10.1002/qj.49708335808 (Oct. 1957).

70. Åström, K. J. & Murray, R. M. *Feedback systems: an introduction for scientists and engineers* en. ISBN: 978-0-691-13576-2 (Princeton Univ. Press, Princeton, NJ, 2008).

A

Appendix: Additional graphs

This chapter contains the additional graphs not shown in chapter 8.

(a)

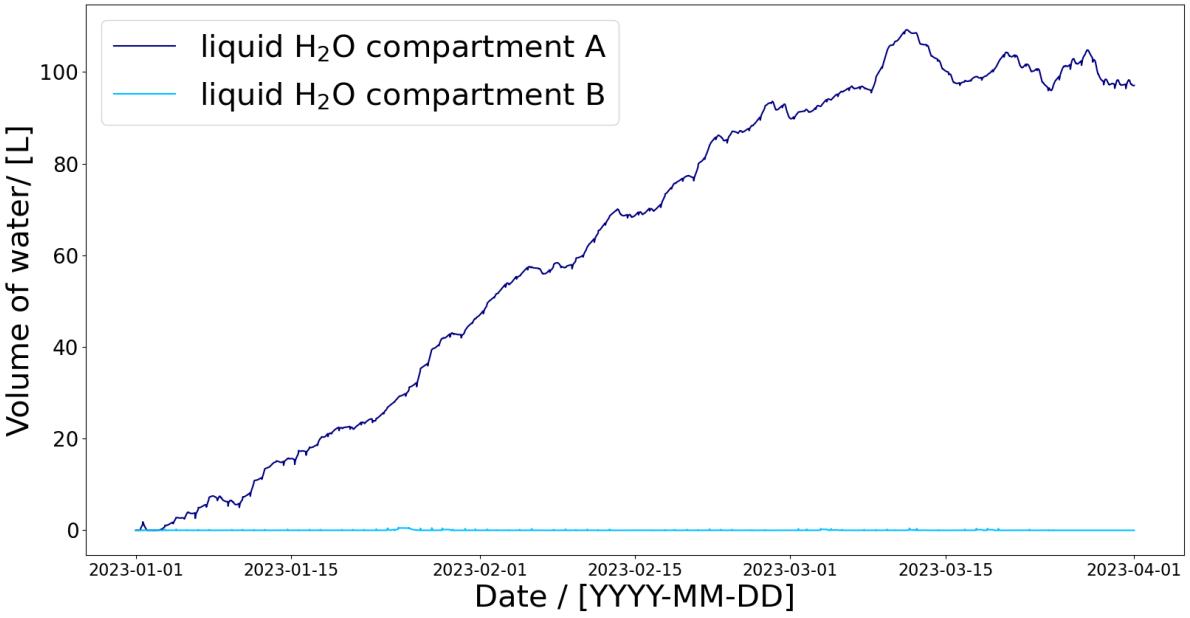
liquid H_2O compartment A
liquid H_2O compartment B
Volume of water/ [L]
0
20
40
60
80
100
2023-01-01
2023-01-15
2023-02-01
2023-02-15
2023-03-01
2023-03-15
2023-04-01
Date / [YYYY-MM-DD]

(b)

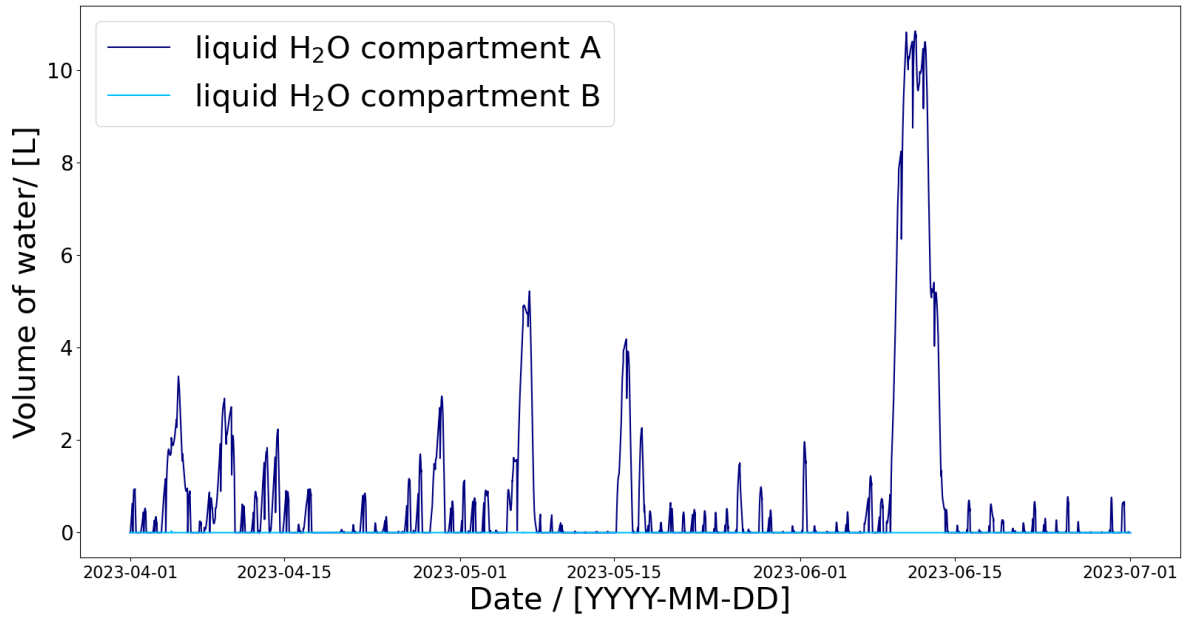
liquid H_2O compartment A
liquid H_2O compartment B
Volume of water/ [L]
0
2
4
6
8
10
2023-04-01
2023-04-15
2023-05-01
2023-05-15
2023-06-01
2023-06-15
2023-07-01
Date / [YYYY-MM-DD]

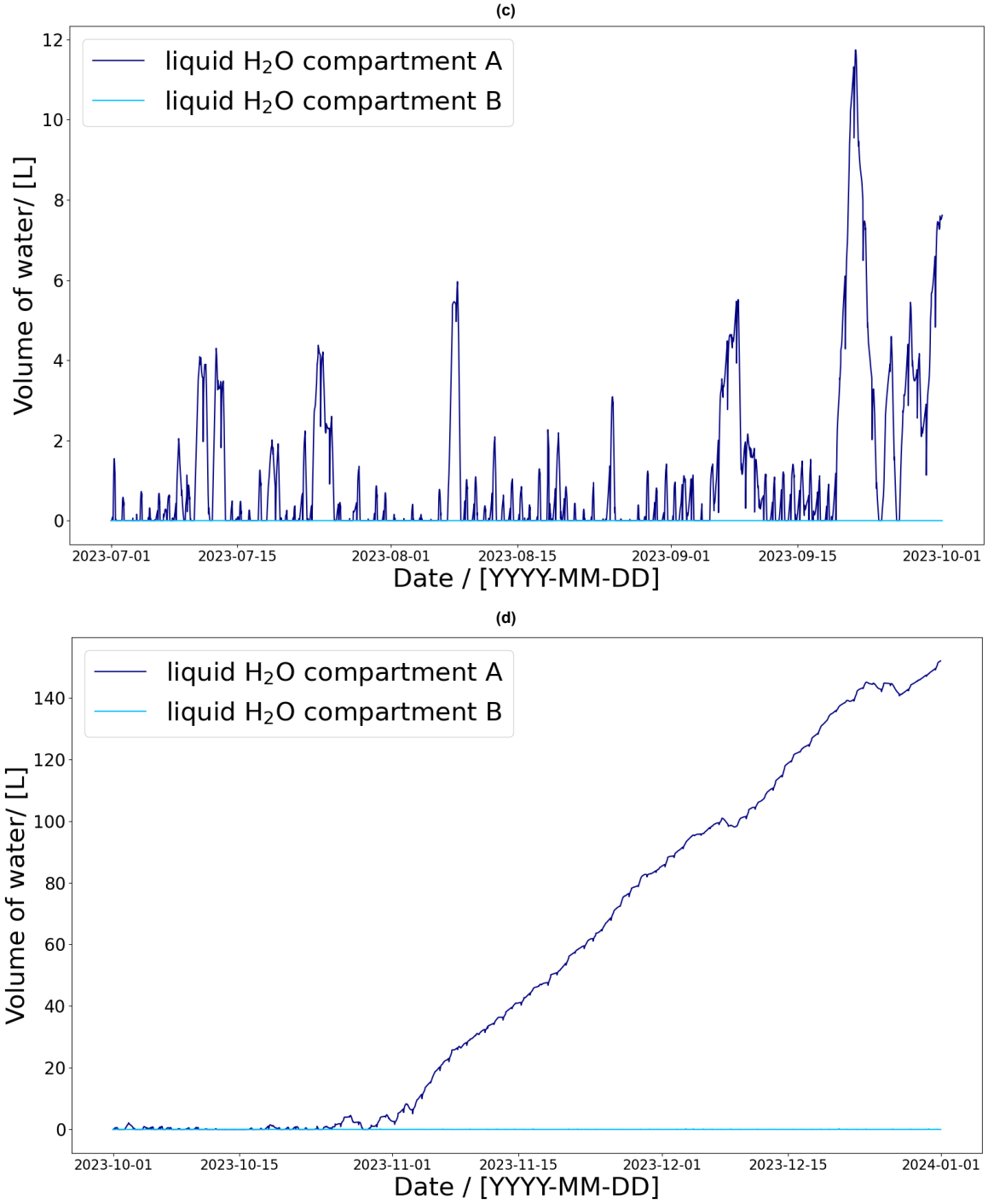

Figure A.1: Volume of the liquid phase in the compartment during normal operation in Eerbeek. It can be observed that a large volume of water forms in compartment A in the autumn and winter. (a) winter; (b) spring; (c) summer; (d) autumn

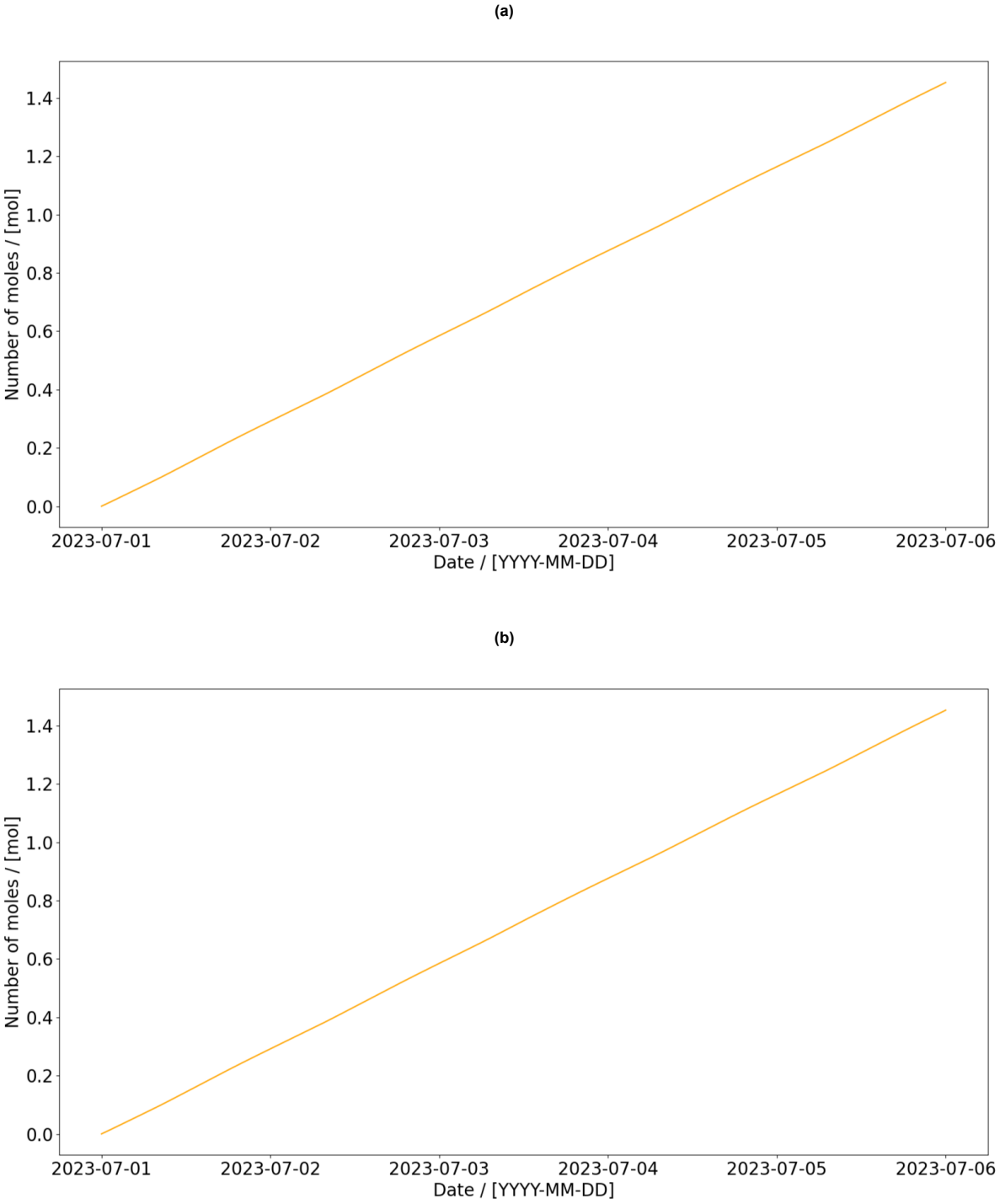

Figure A.2: Number of mols of N_2 in compartment B for the simulation with full Maxwell-Stefan diffusion and partial Maxwell-Stefan diffusion. No difference can be observed with the naked eye. (a) Full Maxwell-Stefan equation; (b) Only the friction between N_2 and the membrane

(a)

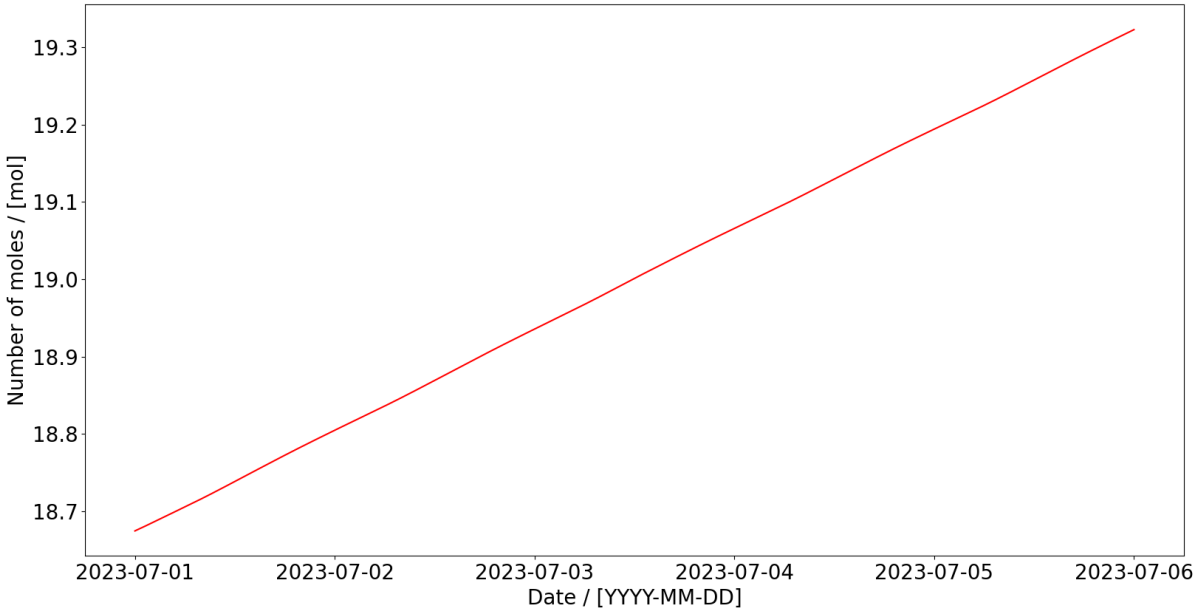

(b)

(c)

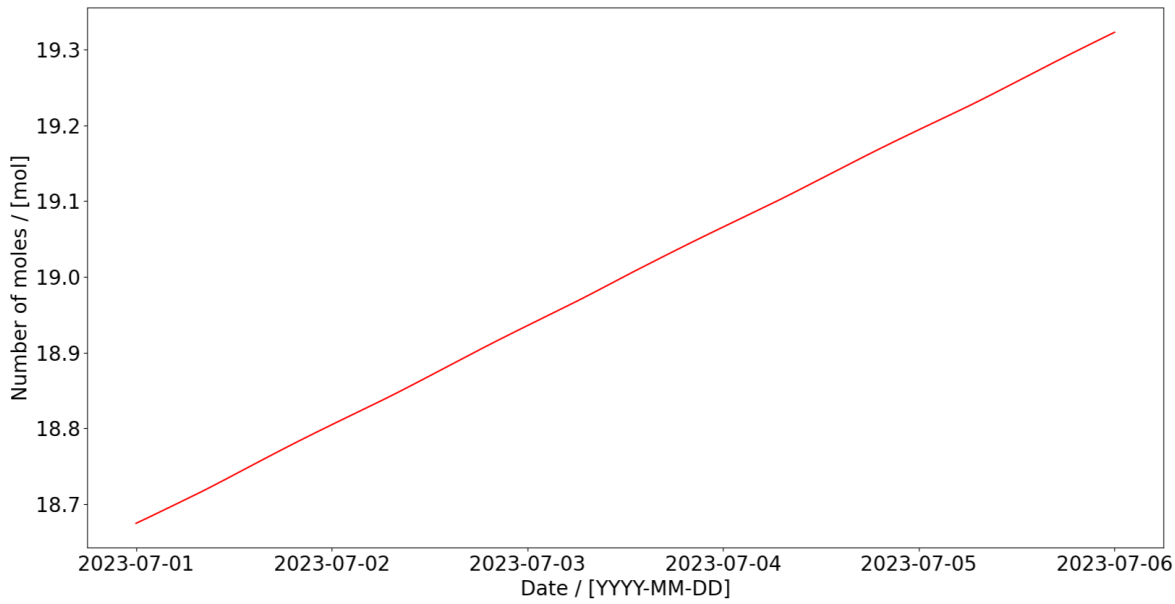

Figure A.3: Number of mols of O_2 in compartment B for the simulation with full Maxwell-Stefan diffusion and partial Maxwell-Stefan diffusion. No difference can be observed with the naked eye. (a) Full Maxwell-Stefan equation; (b) Only the friction between O_2 and the membrane

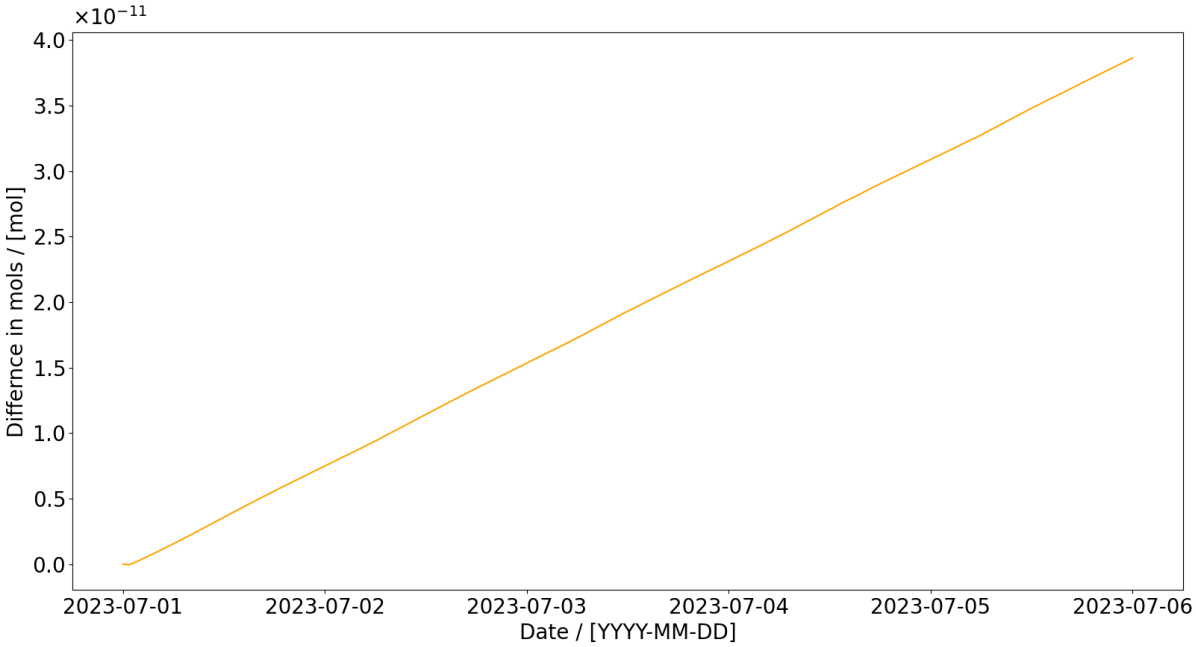

Figure A.4: Difference between the model determined amount of N_2 in compartment B for full and partial MS diffusion

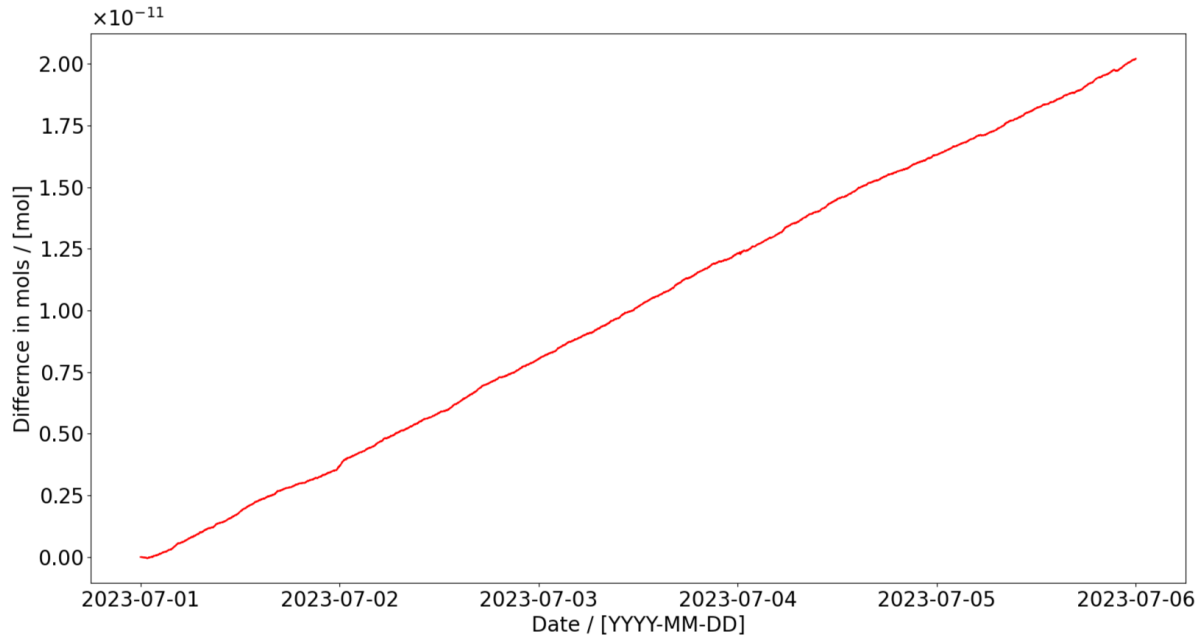

Figure A.5: Difference between the model determined amount of O_2 in compartment B for full and partial MS diffusion

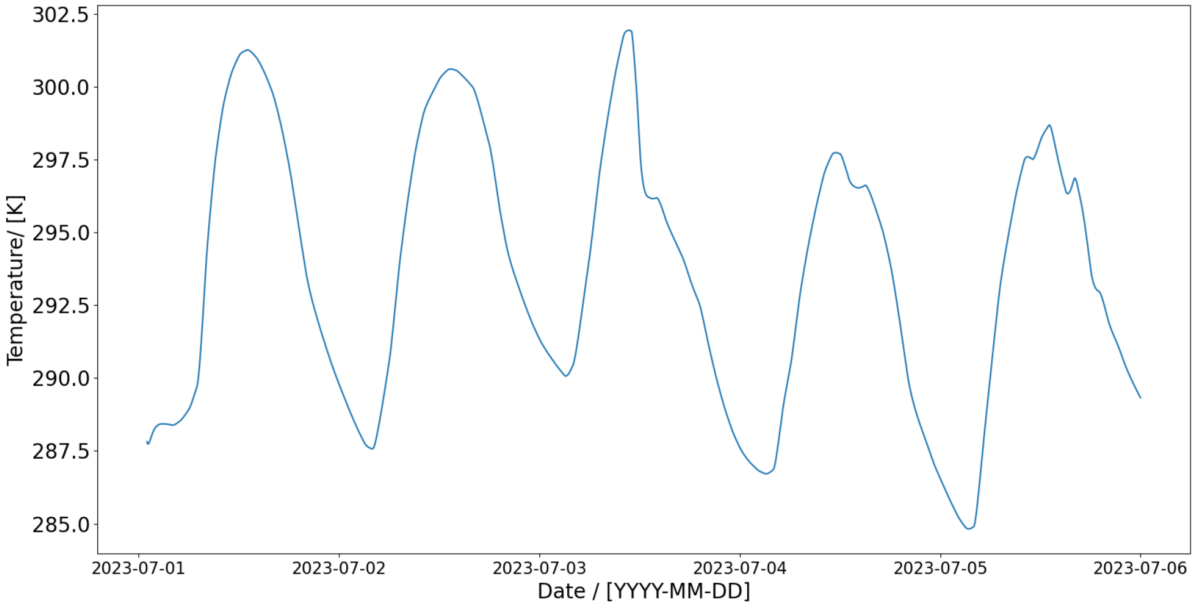

Figure A.6: Temperature of the inner membrane for a period of 5 days started at 07-01. The gas in compartment B is at a standstill; there's no demand or production of H_2. Compartment B was initially filled at 50% of its maximum volume.

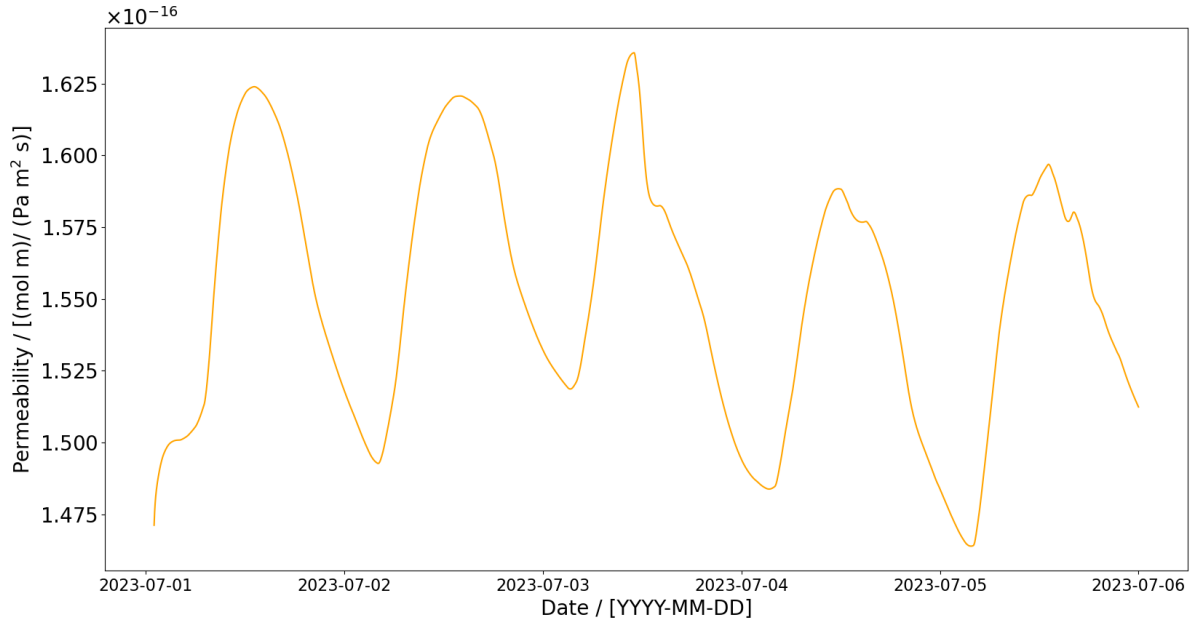

Figure A.7: Permeability of N_2 through the inner membrane for a period of 5 days started at 07-01. The gas in compartment B is at a standstill; there's no demand or production of H_2. Compartment B was initially filled at 50% of its maximum volume.

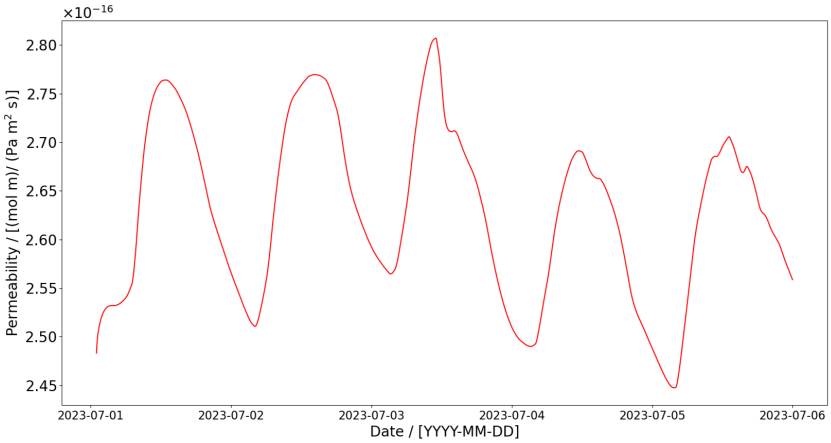

Figure A.8: Permeability of O_2 through the inner membrane for a period of 5 days started at 07-01. The gas in compartment B is at a standstill; there's no demand or production of H_2. Compartment B was initially filled at 50% of its maximum volume.

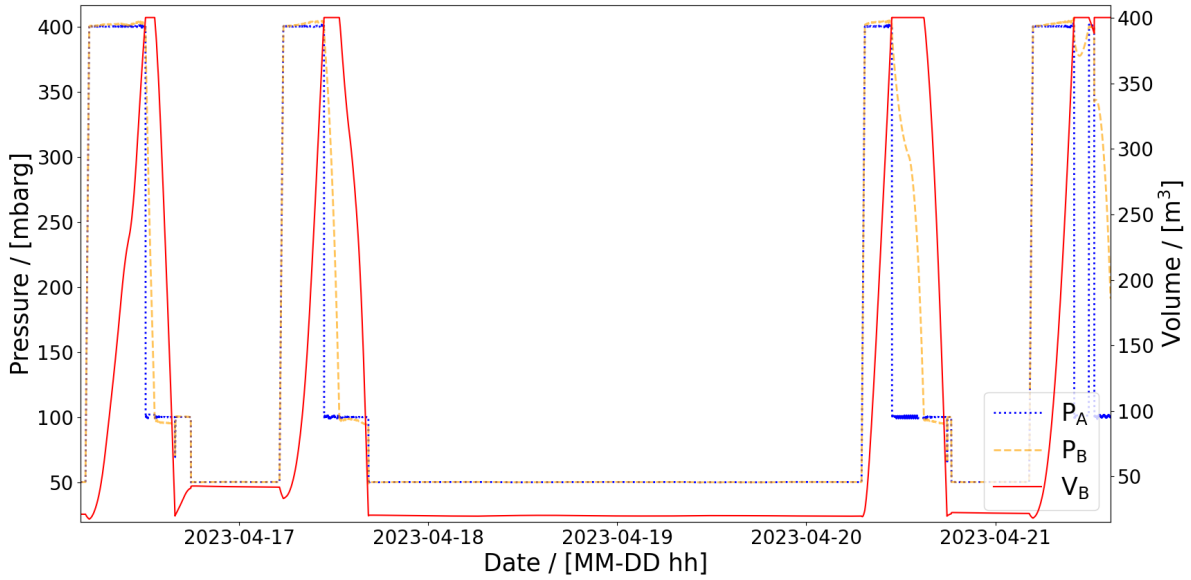

Figure A.9: Characteristic curve of the gasholder during normal operation in spring. It can be observed that the gasholder is empty and remains in standby mode on the 18th and 19th of October as no H_2 is produced.

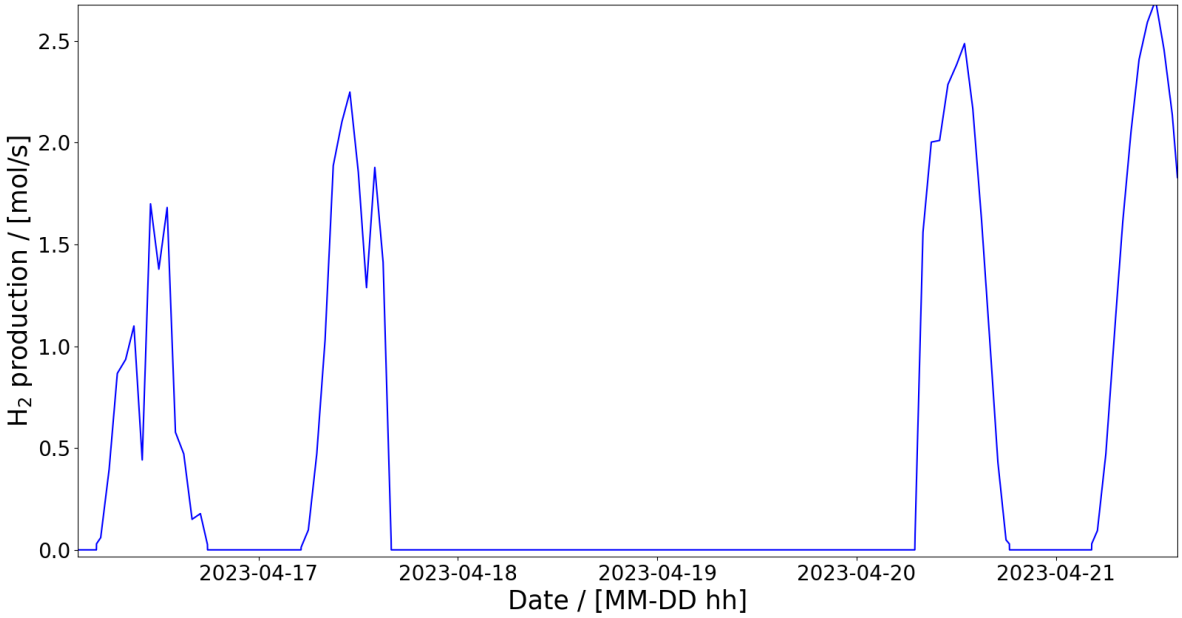

Figure A.10: H_2 production by the electrolyser. It can be observed that no H_2 is produced on the 18th and 19th of October

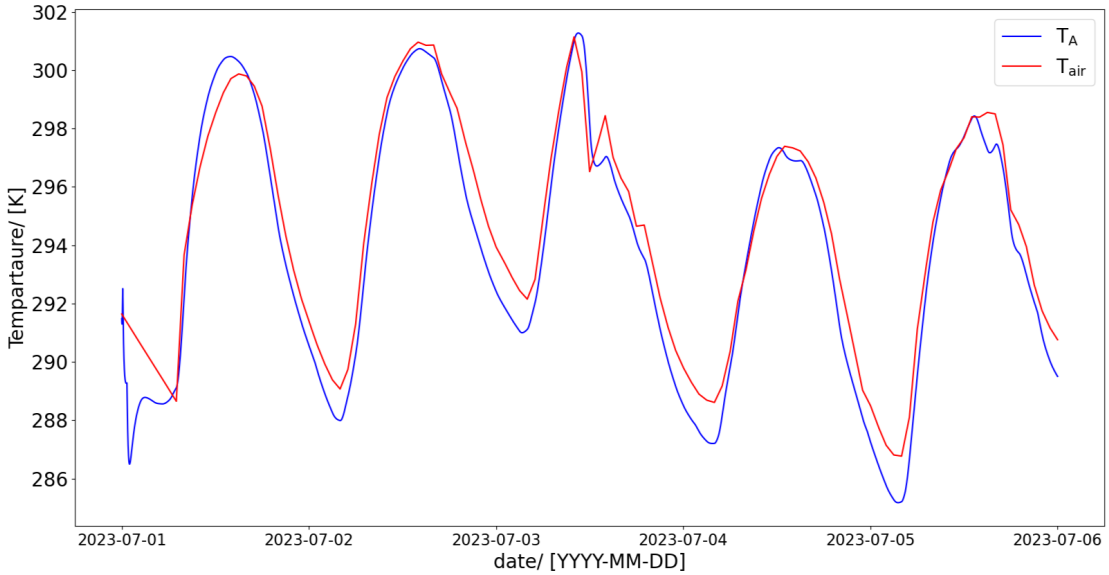

Figure A.11: Ta vs Tair

(a)

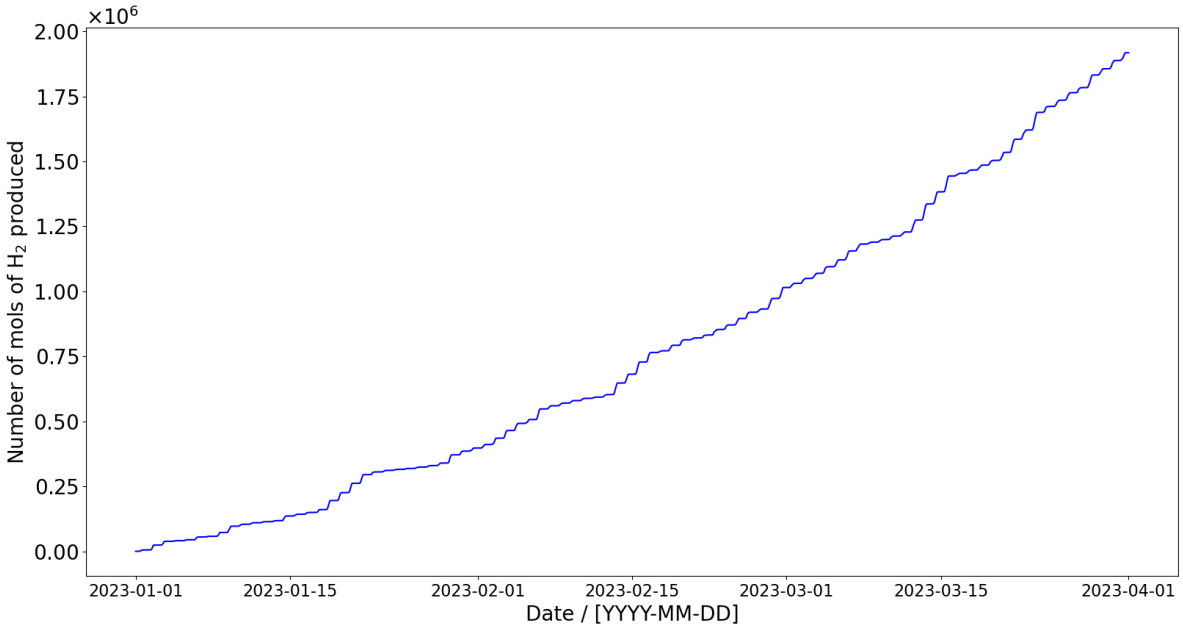
×10^6
2.00
1.75
1.50
1.25
1.00
0.75
0.50
0.25
0.00
Number of mols of H2 produced
2023-01-01
2023-01-15
2023-02-01
2023-02-15
2023-03-01
2023-03-15
2023-04-01
Date / [YYYY-MM-DD]

(b)

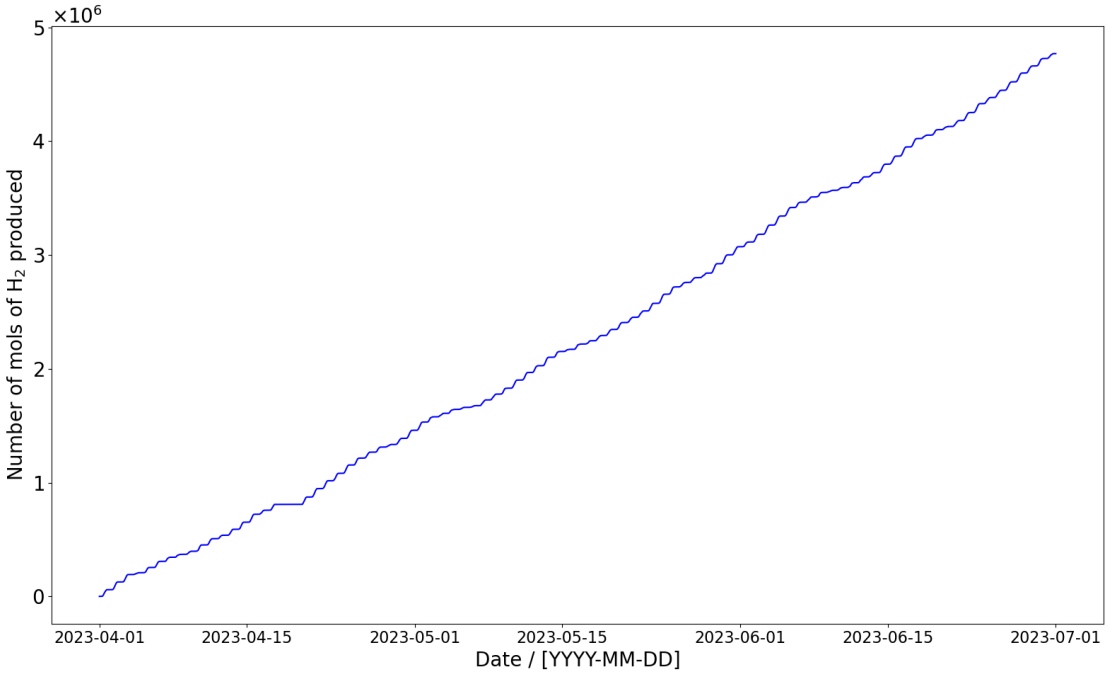
×10^6
5
4
3
2
1
0
Number of mols of H2 produced
2023-04-01
2023-04-15
2023-05-01
2023-05-15
2023-06-01
2023-06-15
2023-07-01
Date / [YYYY-MM-DD]

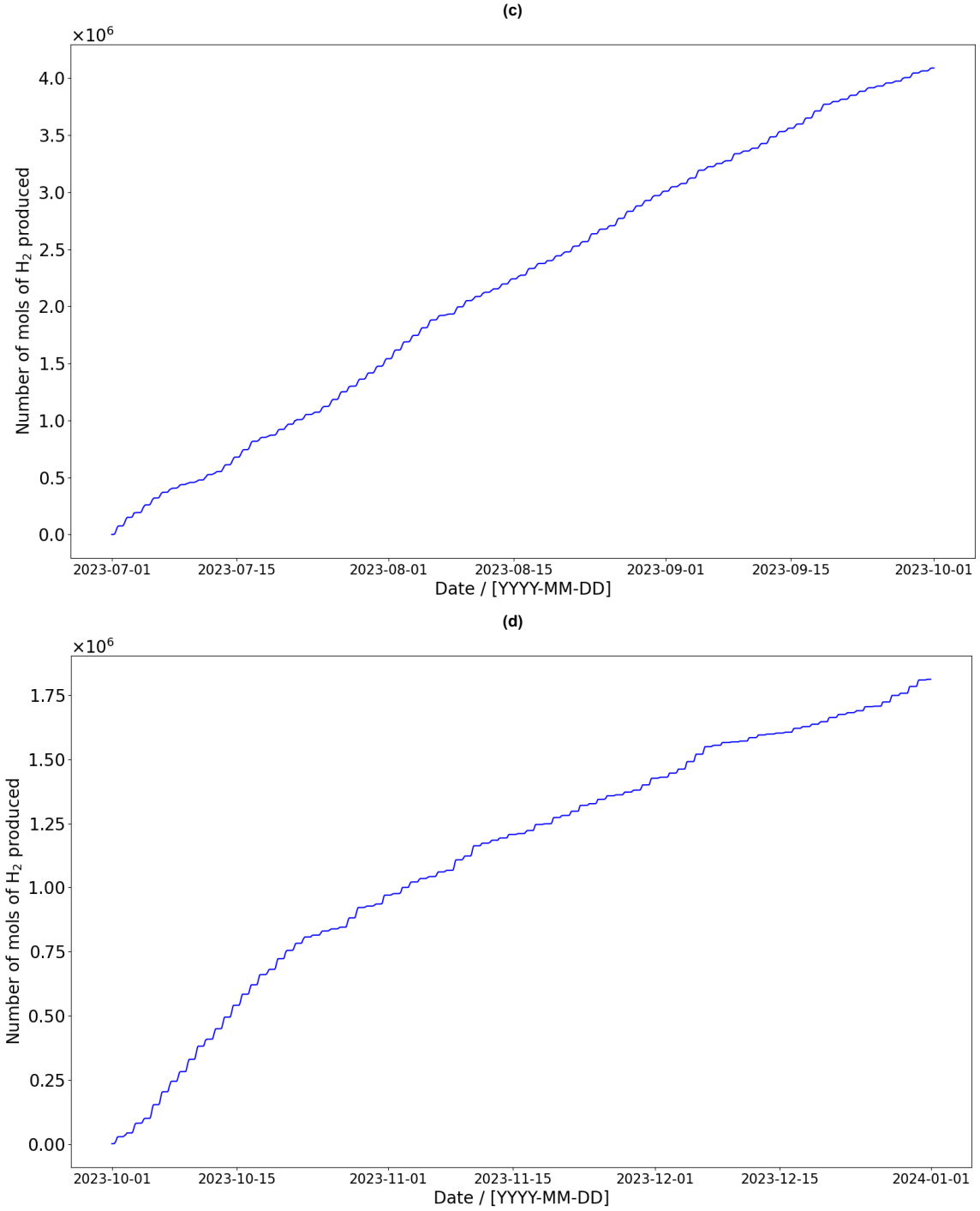

Figure A.12: Total amount of H_2 produced during normal operation in Eerbeek during the 4 seasons. More hydrogen is produced during the sunnier seasons: spring and summer. (a) winter; (b) spring; (c) summer; (d) autumn

(a)

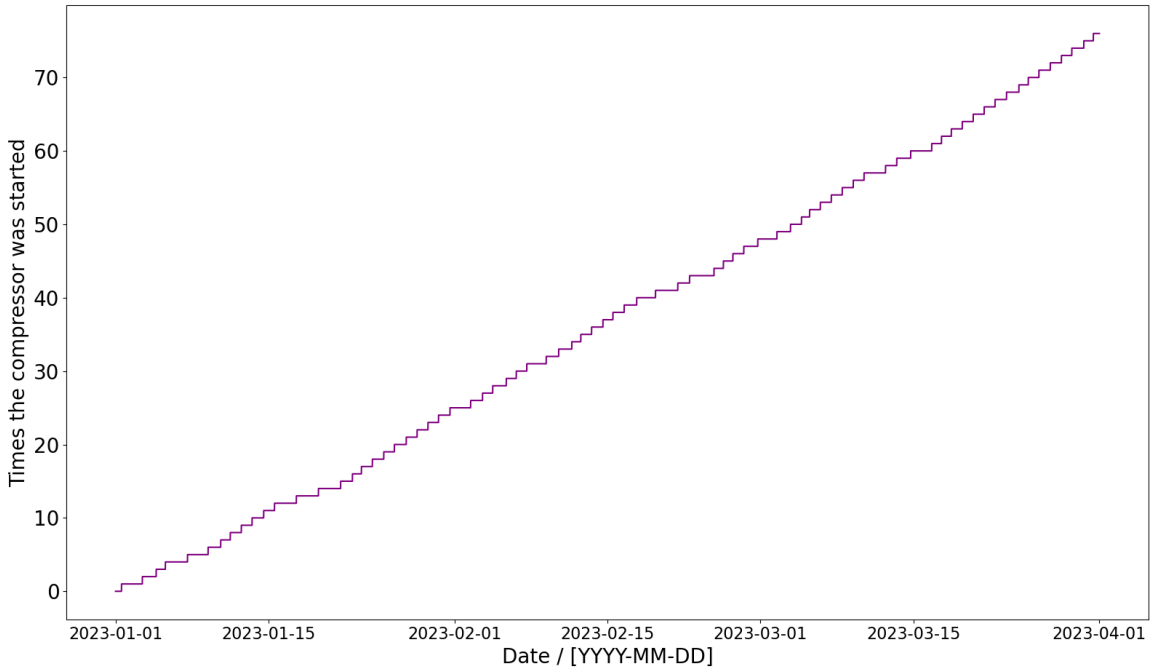
Times the compressor was started
0
10
20
30
40
50
60
70
2023-01-01
2023-01-15
2023-02-01
2023-02-15
2023-03-01
2023-03-15
2023-04-01
Date / [YYYY-MM-DD]

(b)

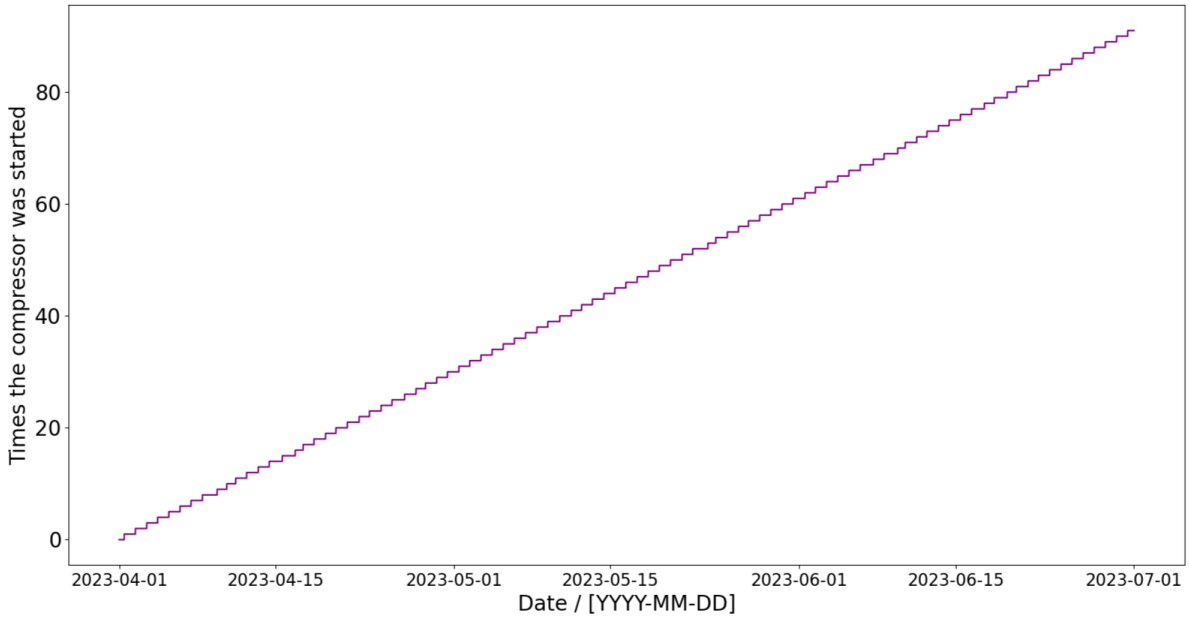
Times the compressor was started
0
20
40
60
80
2023-04-01
2023-04-15
2023-05-01
2023-05-15
2023-06-01
2023-06-15
2023-07-01
Date / [YYYY-MM-DD]

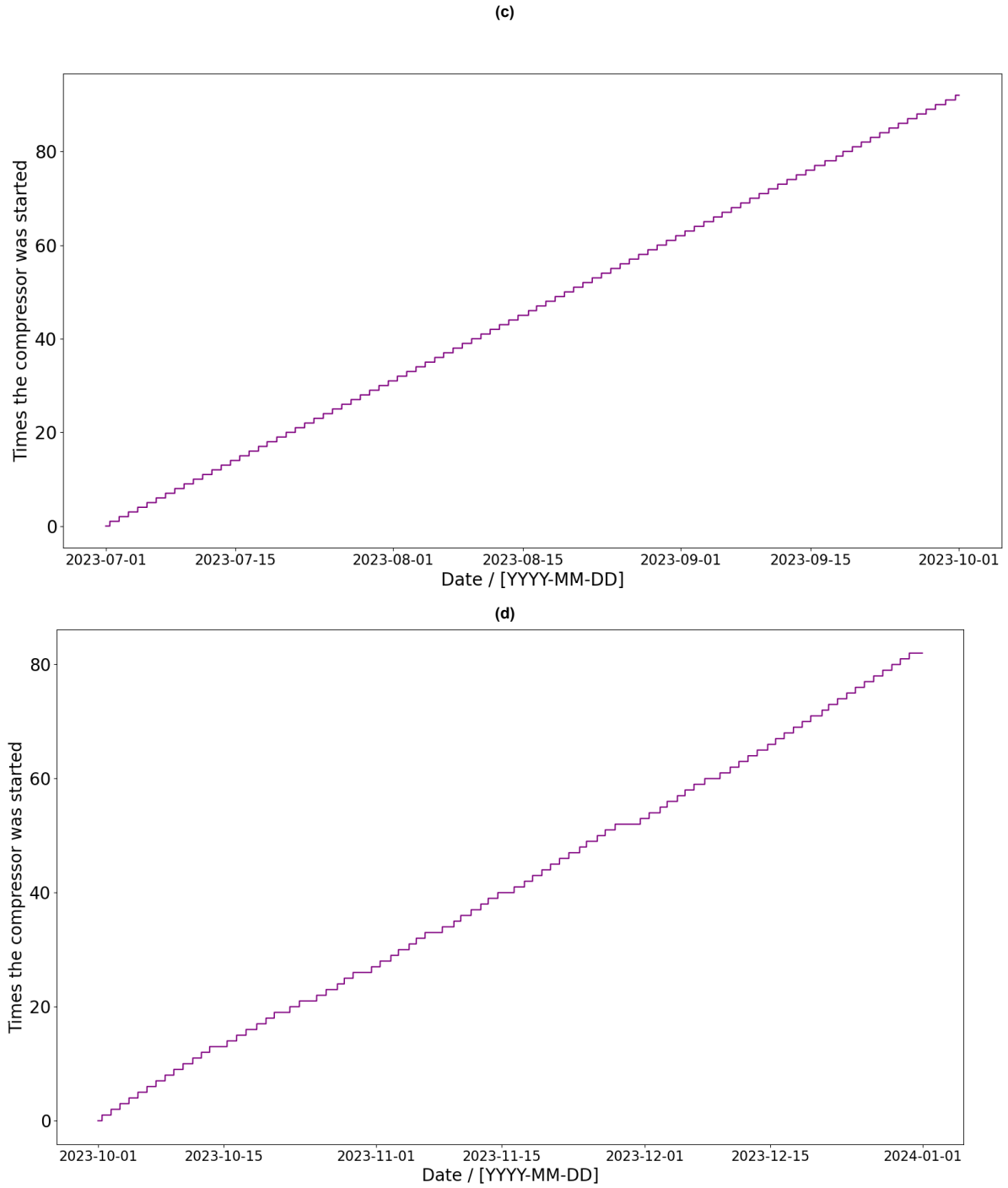

Figure A.13: Total number of storage drainage cycles in Spain during the 4 seasons. The profiles seem linear in the spring and summer as the storage is drained daily. (a) winter; (b) spring; (c) summer; (d) autumn

(a)

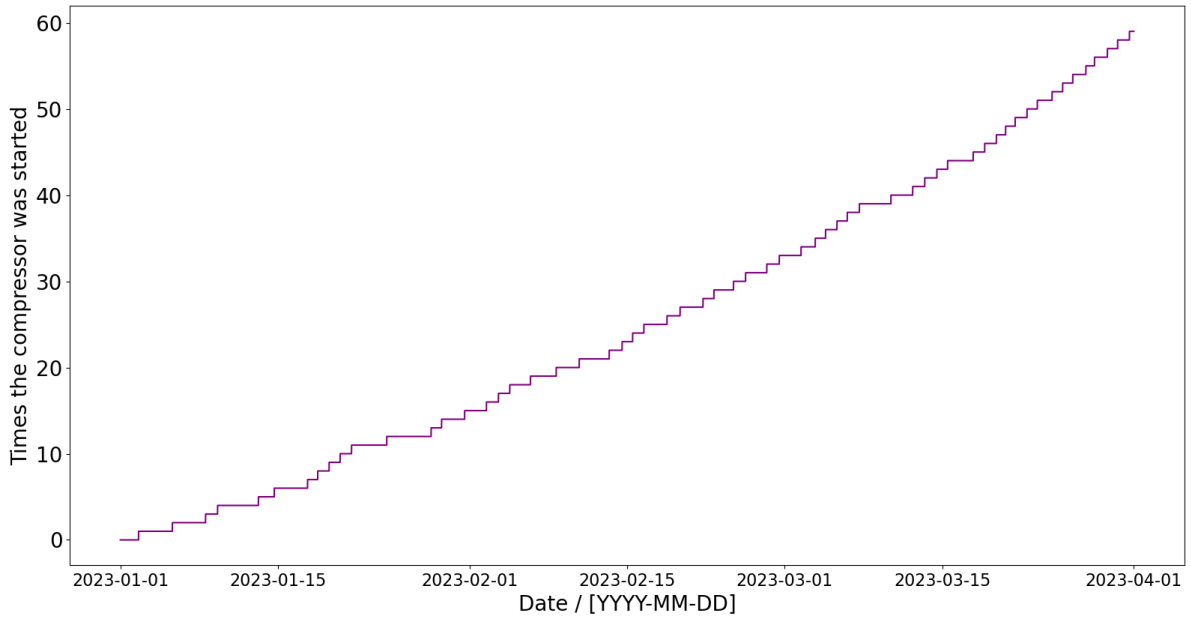
Times the compressor was started
0
10
20
30
40
50
60
2023-01-01
2023-01-15
2023-02-01
2023-02-15
2023-03-01
2023-03-15
2023-04-01
Date / [YYYY-MM-DD]

(b)

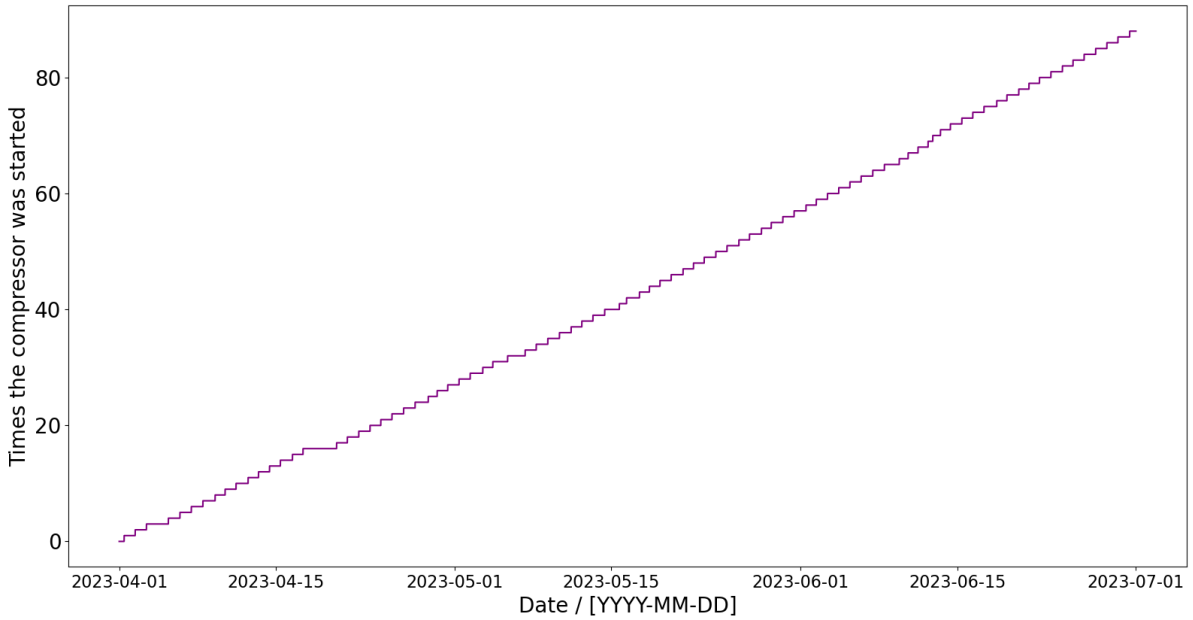
Times the compressor was started
0
20
40
60
80
2023-04-01
2023-04-15
2023-05-01
2023-05-15
2023-06-01
2023-06-15
2023-07-01
Date / [YYYY-MM-DD]

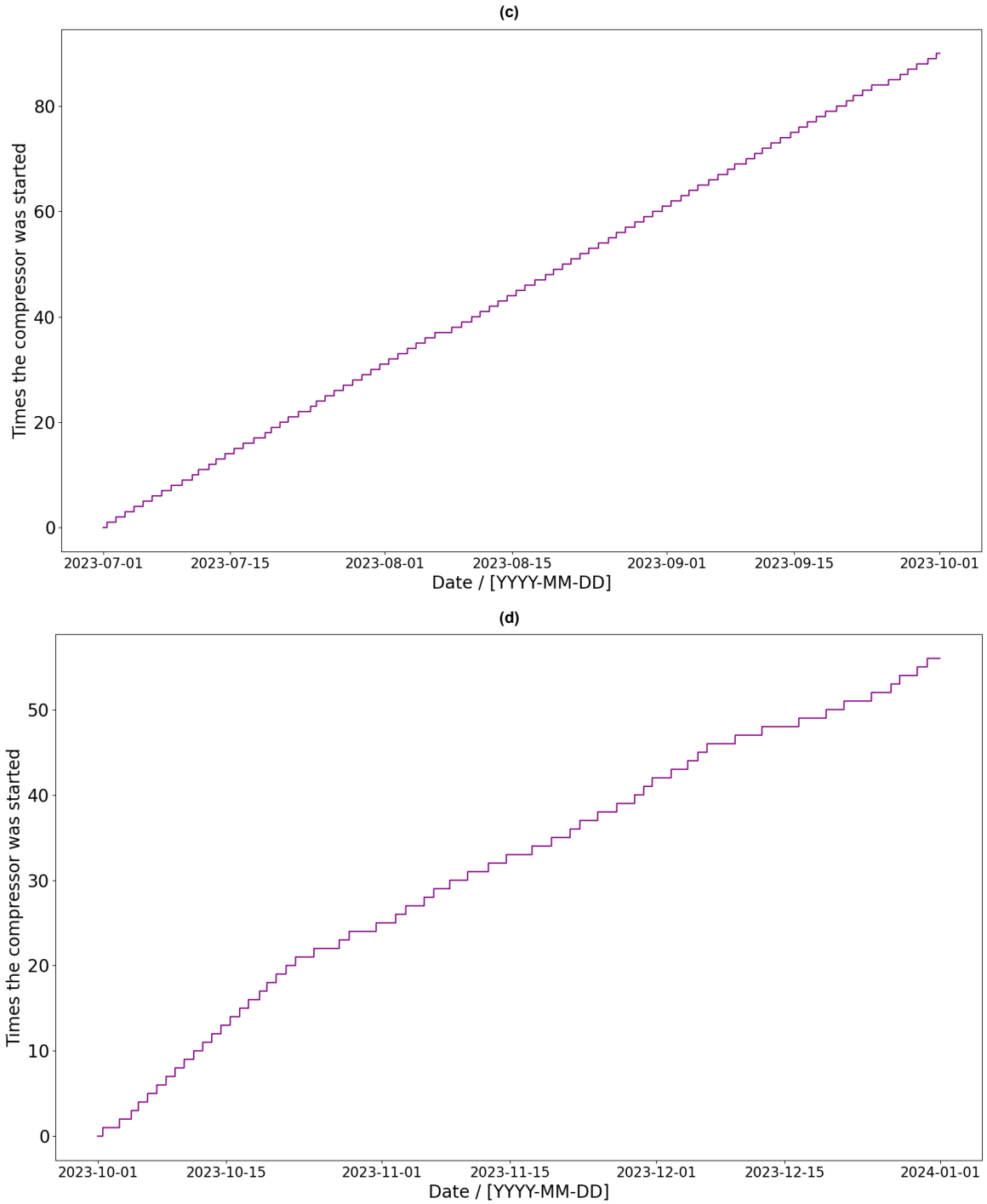

Figure A.14: Total number of storage drainage cycles in Eerbeek during the 4 seasons. The horizontal part of the profiles indicates that the storage was not drained on that particular day. In other words, it has not been filled out completely. (a) winter; (b) spring; (c) summer; (d) autumn

(a)

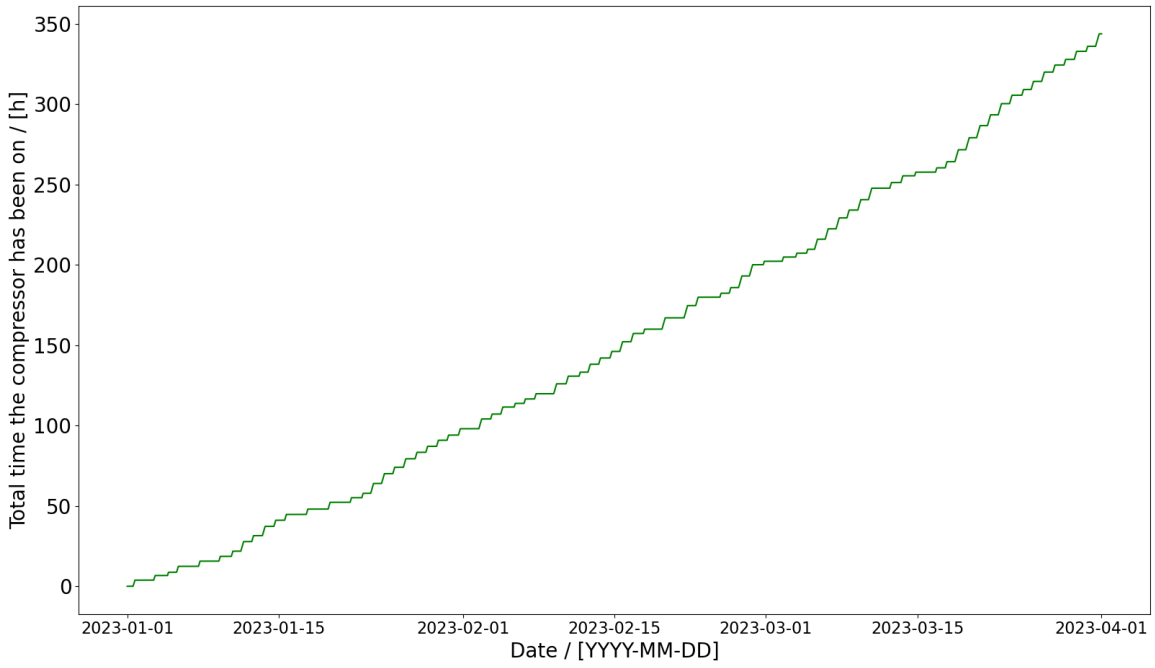
Total time the compressor has been on / [h]
0
50
100
150
200
250
300
350
2023-01-01
2023-01-15
2023-02-01
2023-02-15
2023-03-01
2023-03-15
2023-04-01
Date / [YYYY-MM-DD]

(b)

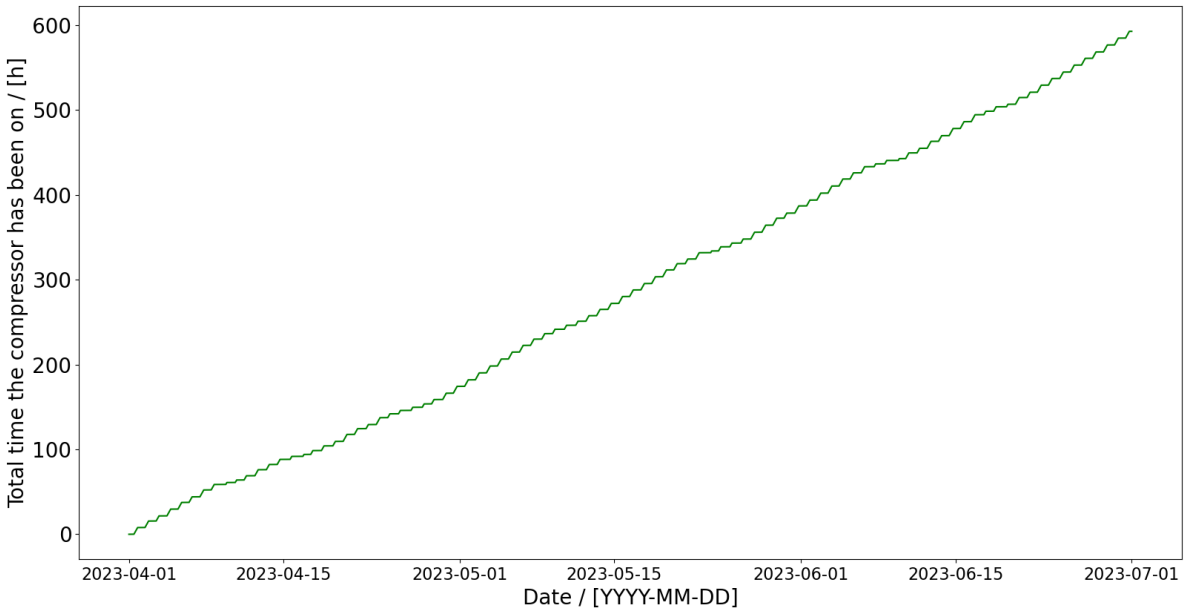
Total time the compressor has been on / [h]
0
100
200
300
400
500
600
2023-04-01
2023-04-15
2023-05-01
2023-05-15
2023-06-01
2023-06-15
2023-07-01
Date / [YYYY-MM-DD]

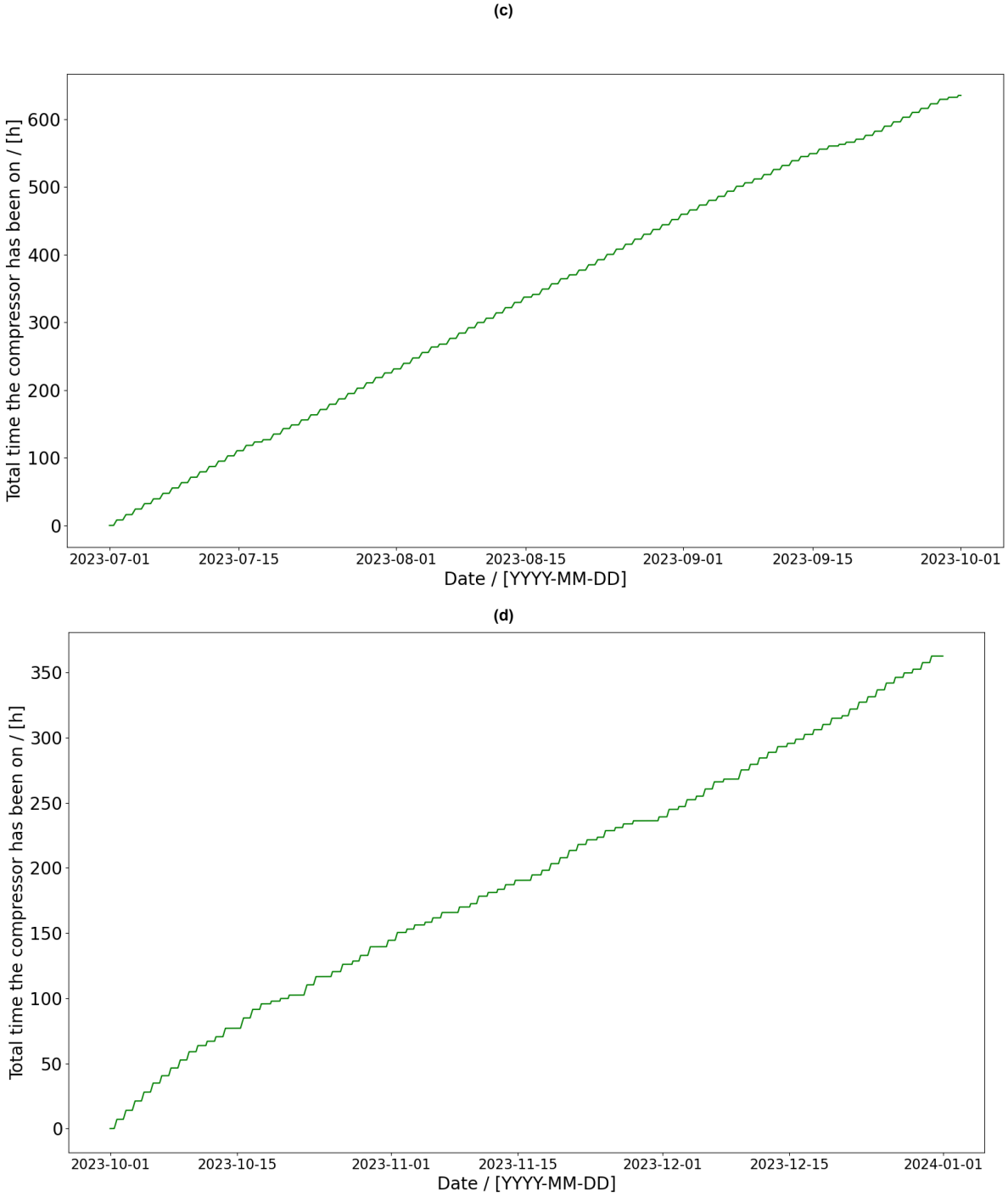

Figure A.15: Total time the compressor ran in hours in Spain during the 4 seasons. (a) winter; (b) spring; (c) summer; (d) autumn

(a)

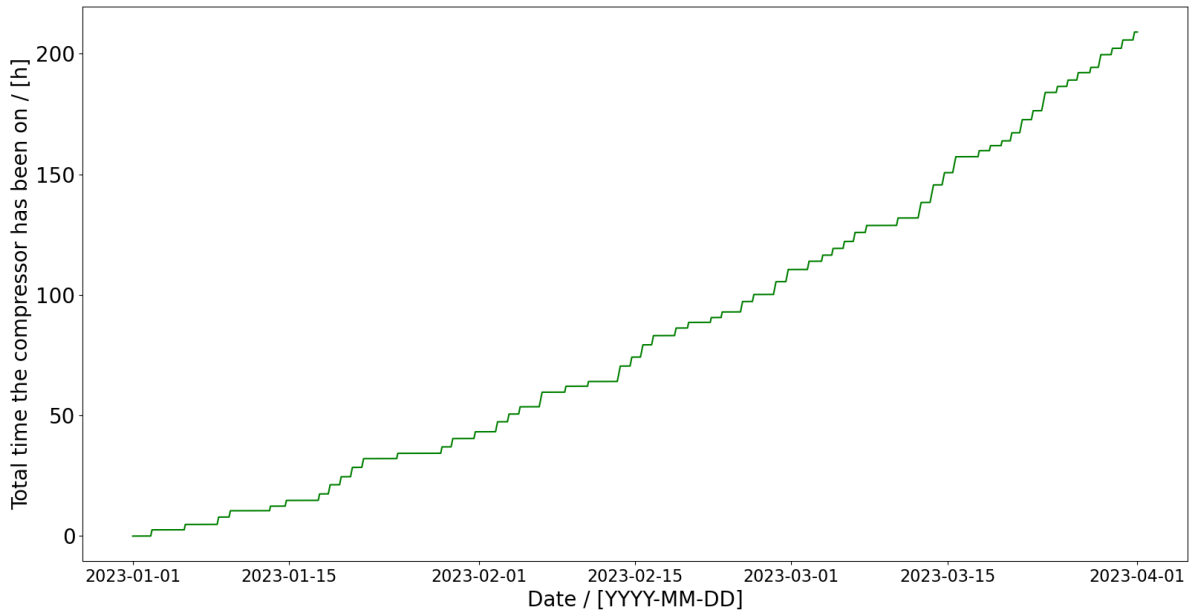
Total time the compressor has been on / [h]
0
50
100
150
200
2023-01-01
2023-01-15
2023-02-01
2023-02-15
2023-03-01
2023-03-15
2023-04-01
Date / [YYYY-MM-DD]

(b)

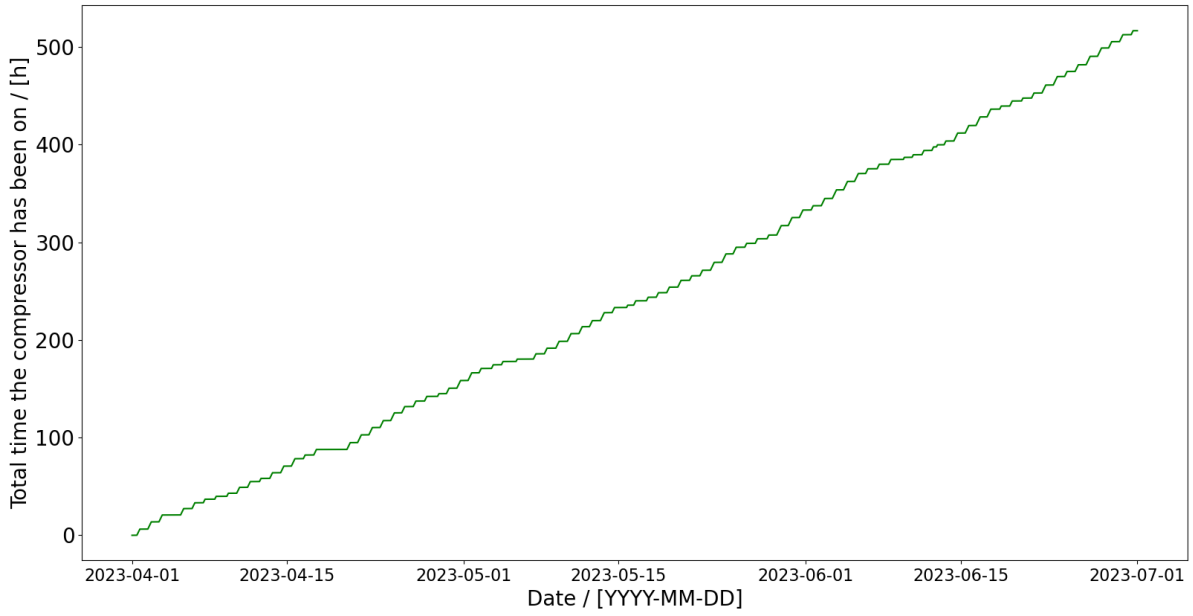
Total time the compressor has been on / [h]
0
100
200
300
400
500
2023-04-01
2023-04-15
2023-05-01
2023-05-15
2023-06-01
2023-06-15
2023-07-01
Date / [YYYY-MM-DD]

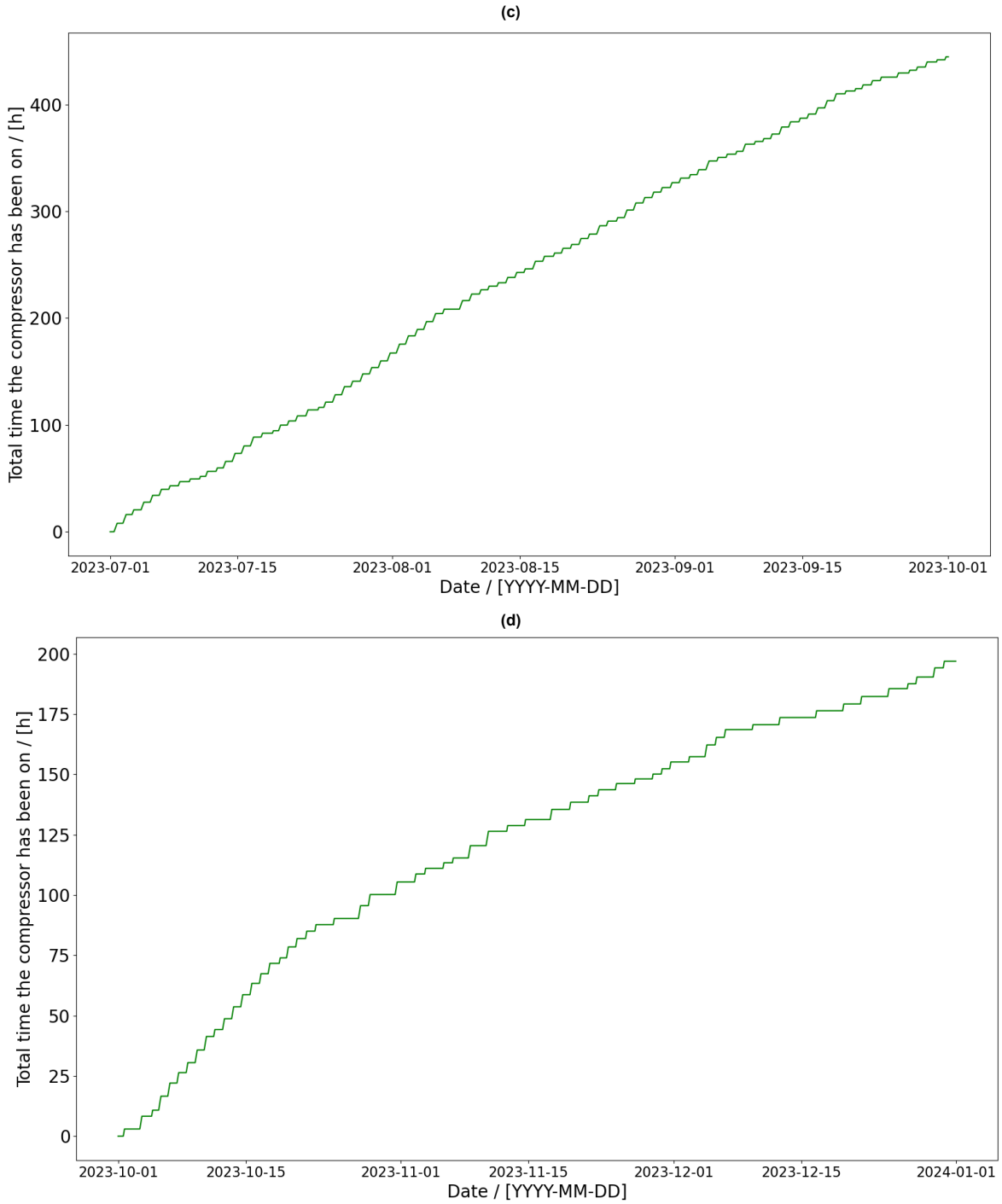

Figure A.16: Total time the compressor ran in hours in Eerbeek during the 4 seasons. (a) winter; (b) spring; (c) summer; (d) autumn

(a)

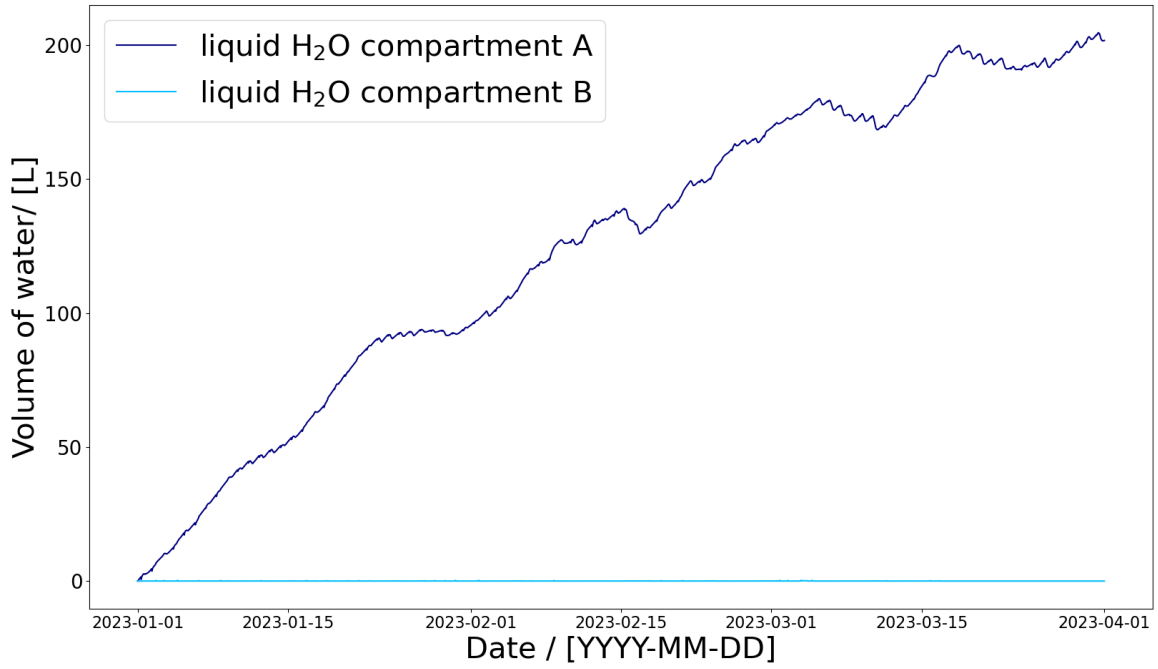
liquid H_2O compartment A
liquid H_2O compartment B
Volume of water/ [L]
200
150
100
50
0
2023-01-01
2023-01-15
2023-02-01
2023-02-15
2023-03-01
2023-03-15
2023-04-01
Date / [YYYY-MM-DD]

(b)

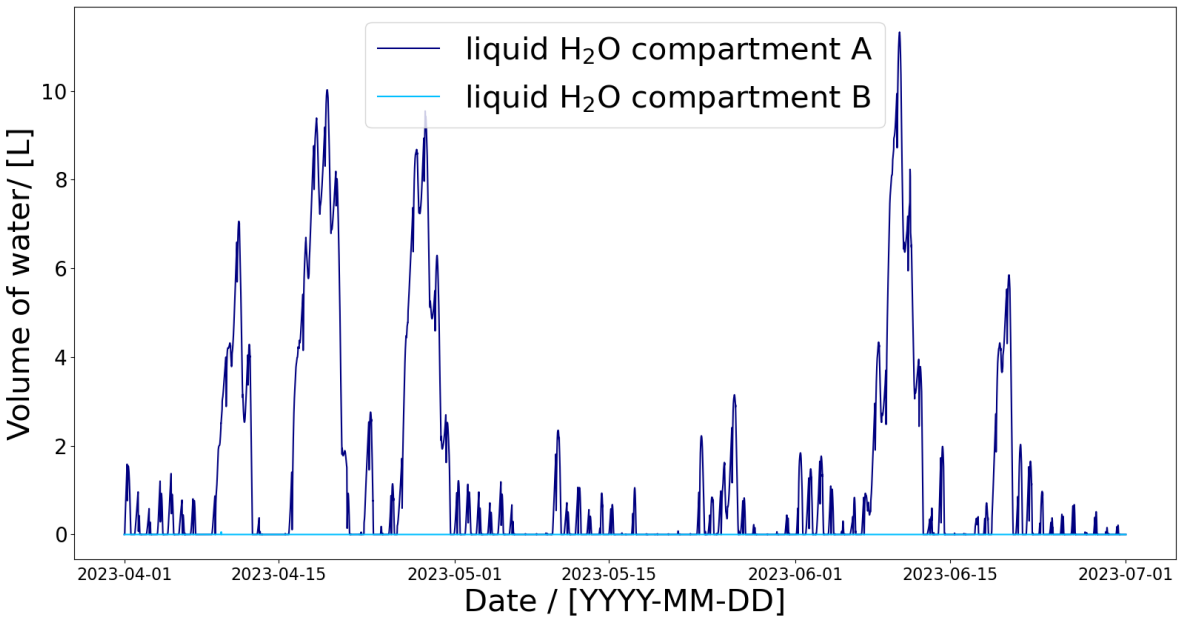
liquid H_2O compartment A
liquid H_2O compartment B
Volume of water/ [L]
10
8
6
4
2
0
2023-04-01
2023-04-15
2023-05-01
2023-05-15
2023-06-01
2023-06-15
2023-07-01
Date / [YYYY-MM-DD]

(c)

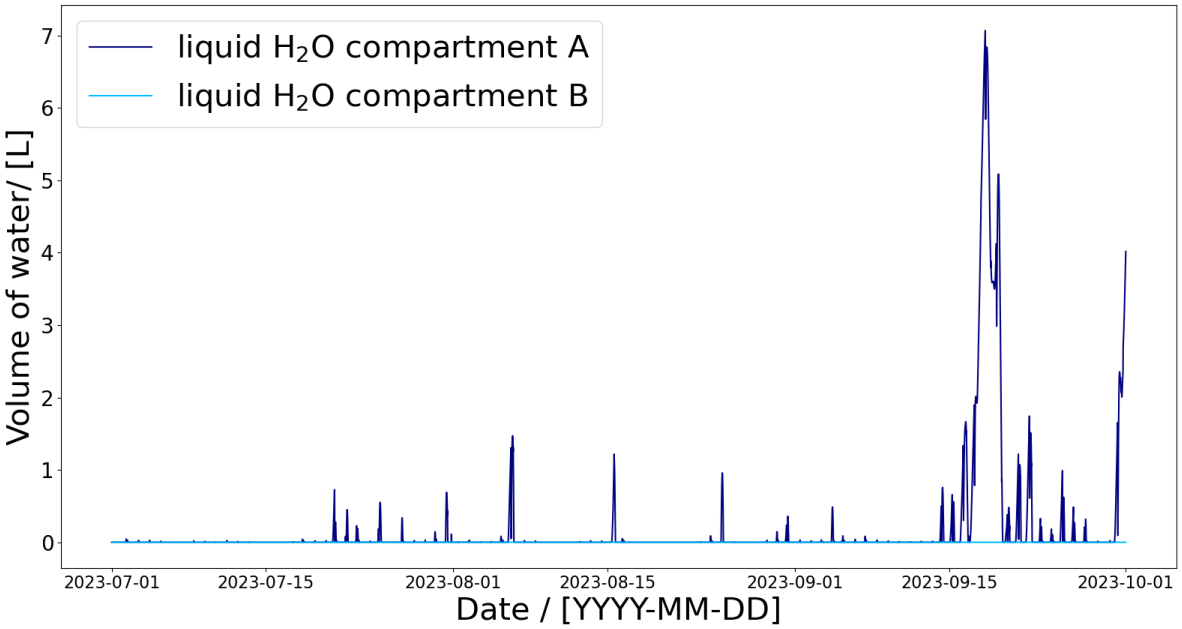

(d)

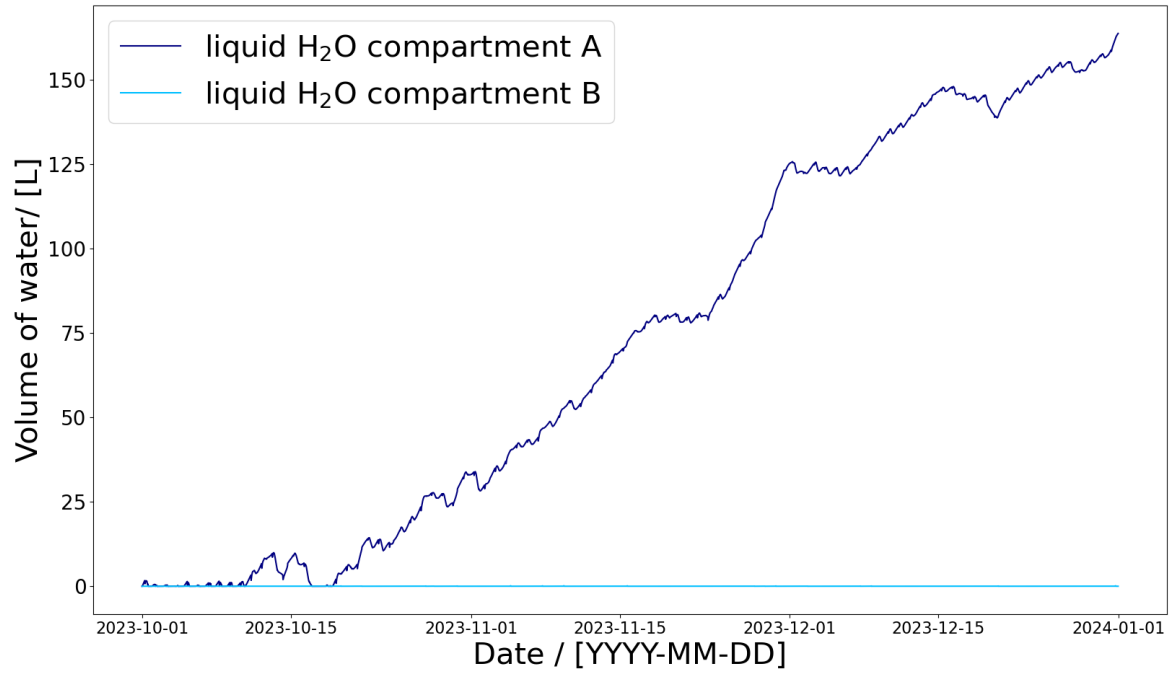

Figure A.17: Total volume of water to expect in the system in Spain during the 4 seasons. (a) winter; (b) spring; (c) summer; (d) autumn

(a)

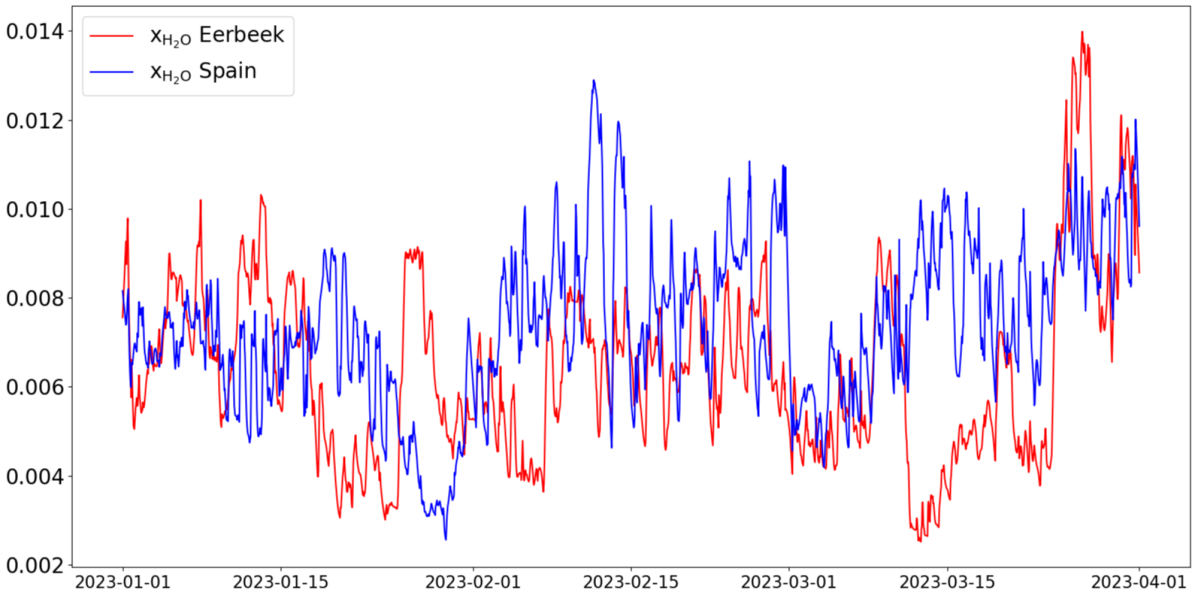

(b)

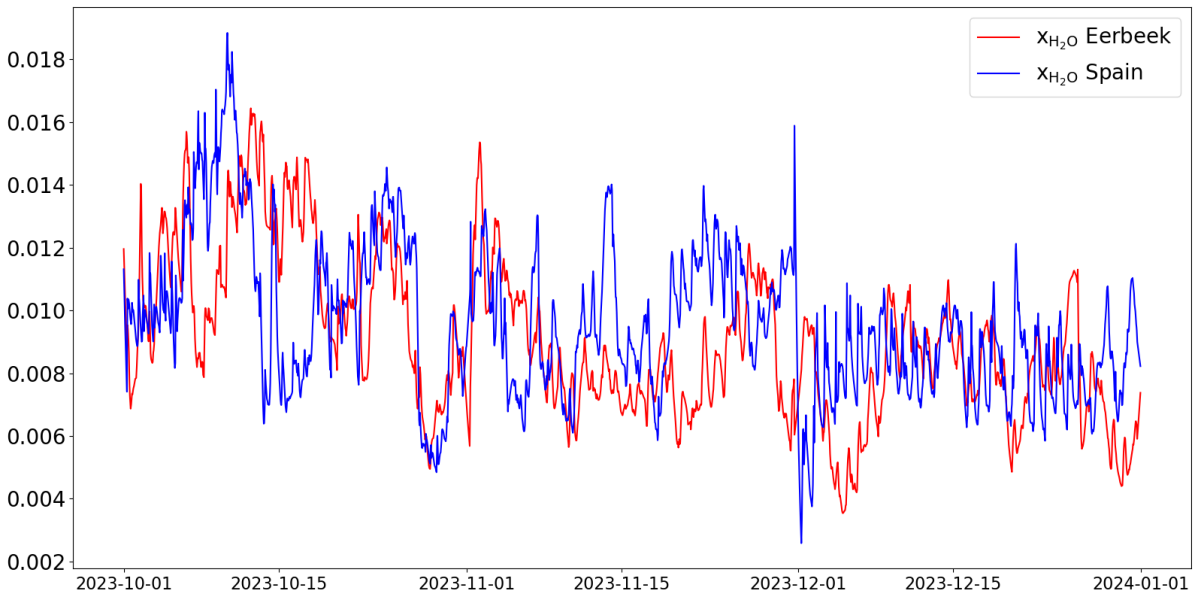

Figure A.18: Mol fraction of H_2O in the outside air in Spain and Eerbeek. (a) winter; (b) autumn

B

Research paper

Introduction

Hydrogen is usually stored at high pressure or in the liquefied form due to its low energy density [5, 9]. The main goal for these types of storage is the long-term storage of as much hydrogen as possible. The main disadvantage of this storage type is that hydrogen compression or liquefaction requires a lot of energy [3, 9]. They may not be suited for every end. If it is desired to store small amounts of hydrogen for short periods of time, another form of storage is needed. Storing the hydrogen in a double membrane gasholder may be more suited. A double membrane gasholder is a storage form often found in biogas plants. It is used above the digester headspace to store the produced biogas by anaerobic digestion. The gas is stored just above atmospheric pressure; thus, no heavy compression is needed.

A double-membrane gasholder consists of two polymeric membranes that delimit two gas compartments. The upper compartment is filled with air, and the gas is stored in the lower compartment. The air compartment is continuously pressurised using a blower. It is used to pressurise the whole storage. The blower injects air at a constant mol flow into the system. Therefore, pressure relief valves are needed to avoid over and underpressures. The valves open or close to control the mol flow leaving the system.

While the transient operation of a double membrane gasholder has been approached by Yuki Junior et al. [4], it has not been applied to hydrogen storage but to biogas storage. This work will focus on modelling the dynamic behaviour of a double membrane gasholder serving as short-term hydrogen storage. The storage serves as a buffer for the intermittent hydrogen production through solar panels. In the here considered use case, it is connected to a compressor requiring a constant debit for operation. The storage's main goal is to avoid this compressor's power cycling. The storage is, therefore, fully blown up before the drainage starts. this leads to the longest compressor run time per cycle.

The model will include aspects not yet considered in prior research, such as condensation, permeation through the membranes and the thermodynamic expansion work of the compartments. The exchange of energy through heat transfer between the elements of the gasholder will be based on the works of Avila-Lopez et al. [36] and Ahmadi et al. [35]. The model developed will predict operation depending on external weather locations, enabling comparison determining ideal storage location.

Model description

The gasholder was separated into different elements. For each element, mass and heat balances were set up. The storage was divided into two gas compartments and membranes; see Figure B.1. The compartments were considered to be spherical to facilitate volume and area calculations. In reality, they are ellipsoidal. The gases in the compartments were assumed to be mixed ideally, leading to a 0-D approach. The compartments have been defined as compartment A, the air-pressurised compartment, and compartment B, the compartment storing the hydrogen. The molecules considered are the basic constituents of air, N_2 and O_2 together with H_2) and H_2. Condensation is prone to happen in the gas compartments, leading to a liquid phase. It has been assumed that only small amounts of liquid form in the gasholder, it is present as droplets, and, thus, that the contact area between the liquid and the gas phase is far greater than the volume of the liquid phase. This leads to a large exchange of energy between the two phases. Due to the large exchange of energy and the small volume of liquid, one could assume the liquid phase to have the same temperature as the gas phase. Furthermore, due to the assumption that the liquid phase is small, it has not been considered part of the system when deriving the heat transfer equations; the gas phase exchanges heat with the membranes.

Operating around atmospheric pressure, the storage will be placed outside without any external heating or cooling source. Therefore, no extreme temperatures or pressures are expected. At these conditions, only H_2O will condense. The solubility of other elements in h_2O has been neglected, and thus, the liquid phase consists of pure H_2O. It is difficult to assess the condensation rate of H_2O; therefore, it has been approached using the following equation.

$$\dot{N}_{\mathrm{H_2O,cond}} = \frac{p_{\mathrm{H2O}} - p_{\mathrm{sat}}}{\tau_{\mathrm{cond}}} \times \frac{N_0}{P_0} \qquad \text{(B.1)}$$

Here $\dot{N}_{\mathrm{H_2O,cond}}$ is the mol flow rate [mol/s] of condensing water, p_{H2O} is the partial pressure [Pa] of water in the gas phase, p_{sat} is the saturation vapour pressure [Pa], τ is a time constant [s], N_0 is an initial mol constant equal to one mol and P_0 is an initial pressure constant equal to 101325 Pa. The value of the time constant τ_{cond} determines the condensation rate. It is important to note that this relation assumes that the nucleation of water happens instantly. The saturation pressure of water vapour has been determined using the empirical Arden Buck equation [54].

Multiple molecules have been considered in this work: N_2 O_2, H_2O and H_2. All molecules but H_2O

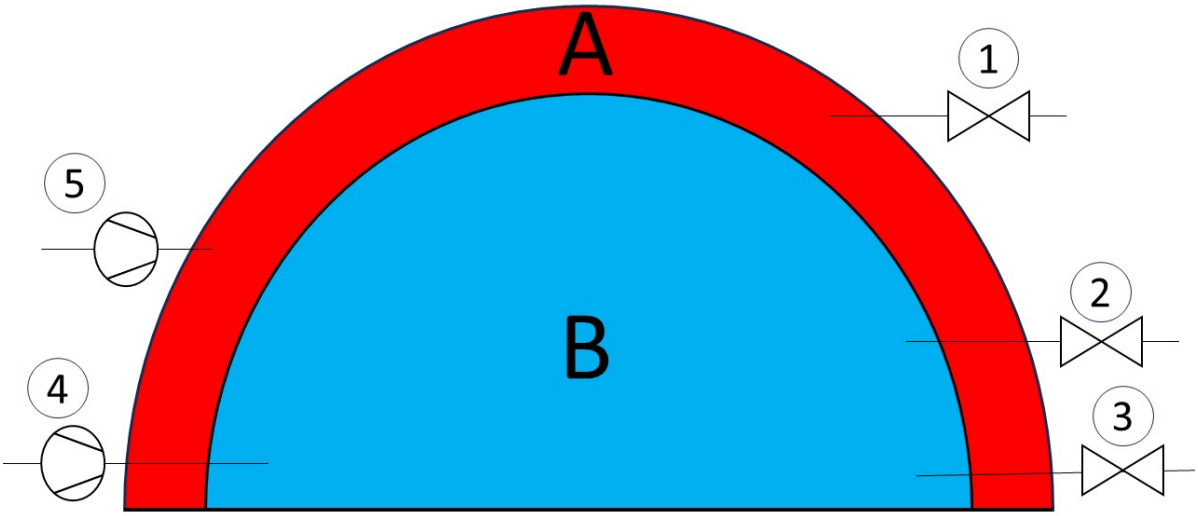

Figure B.1: Simplification of the double membrane gasholder. 1- Air relief valve 2- Hydrogen relief valve 3- Hydrogen outlet valve 4- Hydrogen compressor 5- Air compressor A- Air compartment B- Hydrogen compartment

have been considered for permeation. Fick's law of diffusion is lacking when describing the diffusion of a multicomponent mixture. Therefore, Maxwell-Stefan diffusion was applied to the model [52]. Maxwell-Stefan diffusion considers the intermolecular friction between the permeating species through the membrane.

$$F_i = \sum_{j \neq i} \zeta_{i,j} x_j (u_i - u_j) \tag{B.2}$$

Here, $\zeta_{i,j}$ [N s/(mol m)] is the friction coefficient between species i and j, x_j is the mol fraction of species j and u [m/s] is the diffusive species velocity. The driving force is, just as in Fick's law, the negative gradient of the total potential, which can consist of multiple contributions. In the case considered here, the driving force is due to a concentration and pressure gradient. The Maxwell-Stefan coefficients have been approached using the free volume theory [53]. First, only the peremeation of pure H_2 was considered. The Fickian permeability of H_2 through the polymer membrane was taken as 2.3×10^{-15} [(mol m)/(Pa s m^2]. Based on these results, the free volume fraction of the polymer and the concentration of H_2 have been estimated. These results were then extended to a multicomponent system by including the concentration of N_2 and O_2 in the membrane. When considering multicomponent diffusion through a membrane, the intermolecular friction between the permeating species is often neglected, as its influence on the total flux through the membrane is negligible [52, 53].

As seen in Figure B.1, compartment A has one inlet flow and one outlet flow and is in contact with two membranes. Its mass balance becomes:

$$\frac{dN_i^{\mathsf{A}}}{dt} = \dot{N}_{i,\mathsf{in}}^{\mathsf{A}} - \dot{N}_{i,\mathsf{out}}^{\mathsf{A}} - \dot{N}_{i,\mathsf{P}}^{\mathsf{A}\rightarrow\mathbf{B}} - \dot{N}_{i,\mathsf{P}}^{\mathsf{A}\rightarrow\mathsf{Env}} \tag{B.3}$$

Here, $\frac{dN_i^{\mathsf{A}}}{dt}$ [mol/s] is the net rate of change in the amount of mol of component i in the compartment, $\dot{N}_{i,\mathsf{in}}^{\mathsf{A}}$ [mol/s] is the mol flow of component i entering the compartment after compression, $\dot{N}_{i,\mathsf{out}}^{\mathsf{A}}$ [mol/s] is the mol flow of component i leaving the compartment through the relief valve, $\dot{N}_{i,\mathsf{P}}^{\mathsf{A}\rightarrow\mathbf{B}}$ [mol/s] is the mol flow of component i leaving the compartment due to permeation to compartment B through the inner membrane and $\dot{N}_{i,\mathsf{P}}^{\mathsf{A}\rightarrow\mathsf{Env}}$ [mol/s] is the mol flow of component i leaving the compartment to the environment through the outer membrane.

Compartment B has one inlet flow and two outlet flows, one through the pressure relief valve and one to the hydrogen compressor. Molecules diffuse through the inner membrane.

$$\frac{dN_i^{\mathsf{B}}}{dt} = \dot{N}_{i,\mathsf{in}}^{\mathsf{B}} - \dot{N}_{i,\mathsf{out}}^{\mathsf{B}} - \dot{N}_{i,\mathsf{relieve}}^{\mathsf{B}} + \dot{N}_{i,\mathsf{P}}^{\mathsf{A}\rightarrow\mathbf{B}} \tag{B.4}$$

Here, $\frac{dN_i^{\mathsf{B}}}{dt}$ [mol/s] is the net rate of change in the amount of mol of component i in the compartment, $\dot{N}_{i,\mathsf{in}}^{\mathsf{B}}$ [mol/s] is the mol flow of component i entering the compartment after compression, $\dot{N}_{i,\mathsf{out}}^{\mathsf{B}}$

[mol/s] is the mol flow leaving the compartment to the compressor, $\dot{N}^{\mathsf{B}}_{i,\text{relieve}}$ [mol/s] is the mol flow of component i leaving the compartment through the relief valve, and $\dot{N}^{\mathsf{A}\to\mathbf{B}}_{i,\mathsf{P}}$ [mol/s] is the mol flow of component i entering the compartment through diffusion through the inner membrane.

It is important to note that a permeation direction through the membranes is defined; all flows exit compartment A. This means that when the resulting molflow of permeation is negative, the considered molecule enters compartment A instead of exiting it.

The resulting net change in the amount of mol per molecule per compartment can be added to give the resulting net rate of change of the total mol amount.

$$\frac{dN^{\mathsf{A}}}{dt} = \sum_{i=1}^{\mathsf{N}} \frac{dN^{\mathsf{A}}_i}{dt} \tag{B.5}$$

$$\frac{dN^{\mathsf{B}}}{dt} = \sum_{i=1}^{\mathsf{N}} \frac{dN^{\mathsf{B}}_i}{dt} \tag{B.6}$$

It has been assumed that molecules' permeation through the membrane is instantaneous. They don't have to migrate through the membrane, and the membranes' mass balances are simply zero as they don't exchange any matter.

The energy balances of the gas in the compartments become:

$$\frac{dT^{\mathsf{A}}}{dt} = \frac{1}{N^{\mathsf{A}} c^{\mathsf{A}}_{\mathsf{v,m}}} \Bigg[\dot{Q}^{\mathsf{A}} - \dot{W}^{\mathsf{A}} + p^{\mathsf{A}} v^{\mathsf{A}}_{\mathsf{m}} \frac{dN^{\mathsf{A}}}{dt} + \Delta h^{\text{cond}} \dot{N}^{\mathsf{A}}_{\mathsf{H_2O,cond}} + (T^{\text{in}} - T^{\mathsf{A}}) \times \sum_{\mathsf{i}=1}^{\mathsf{N}} \dot{N}^{\mathsf{A}}_{i,\text{in}} c^{\mathsf{A}}_{\mathsf{p},i} - \sum_{i=1}^{N} \dot{N}^{\mathsf{A}\to\mathsf{B}}_{i,\mathsf{P}} (h^{\mathsf{A}\to\mathsf{B}}_i - h^{\mathsf{A}}_i) - \sum_{i=1}^{N} \dot{N}^{\mathsf{A}\to\mathsf{Env}}_{i,\mathsf{P}} (h^{\mathsf{A}\to\mathsf{Env}}_i - h^{\mathsf{A}}_i) \Bigg] \tag{B.7}$$

Where

$$h^{\mathsf{A}\to\mathsf{B}}_i = \begin{cases} h^{\text{inner}}_i, & \text{for } \dot{N}^{\mathsf{A}\to\mathsf{B}}_{i,\mathsf{P}} \le 0 \\ h^{\mathsf{A}}_i, & \text{for } \dot{N}^{\mathsf{A}\to\mathsf{B}}_{i,\mathsf{P}} > 0 \end{cases} \tag{B.8}$$

$$h^{\mathsf{A}\to\mathsf{Env}}_i = \begin{cases} h^{\text{outer}}_i, & \text{for } \dot{N}^{\mathsf{A}\to\mathsf{Env}}_{i,\mathsf{P}} \le 0 \\ h^{\mathsf{A}}_i, & \text{for } \dot{N}^{\mathsf{A}\to\mathsf{Env}}_{i,\mathsf{P}} > 0 \end{cases} \tag{B.9}$$

and

$$\frac{dT^{\mathsf{B}}}{dt} = \frac{1}{N^{\mathsf{B}} c^{\mathsf{B}}_{\mathsf{v,m}}} \Bigg[\dot{Q}^{\mathsf{B}} - \dot{W}^{\mathsf{B}} + p^{\mathsf{B}} v^{\mathsf{B}}_{\mathsf{m}} \frac{dN^{\mathsf{B}}}{dt} + \Delta h^{\text{cond}} \dot{N}^{\mathsf{B}}_{\mathsf{H_2O,cond}} + (T^{\text{in}} - T^{\mathsf{B}}) \times \sum_{\mathsf{i}=1}^{\mathsf{N}} \dot{N}^{\mathsf{B}}_{i,\text{in}} \times c^{\mathsf{B}}_{\mathsf{p},i} + \sum_{i=1}^{N} \dot{N}^{\mathsf{A}\to\mathsf{B}}_{i,\mathsf{P}} (h^{\mathsf{A}\to\mathsf{B}}_i - h^{\mathsf{B}}_i) \Bigg] \tag{B.10}$$

Where

$$h^{\mathsf{A}\to\mathsf{B}}_i = \begin{cases} h^{\text{inner}}_i, & \text{for } \dot{N}^{\mathsf{A}\to\mathsf{B}}_{i,\mathsf{P}} > 0 \\ h^{\mathsf{B}}_i, & \text{for } \dot{N}^{\mathsf{A}\to\mathsf{B}}_{i,\mathsf{P}} \le 0 \end{cases} \tag{B.11}$$

The superscripts A and B designate the considered compartment, and the subscript i stands for the considered molecule. $\frac{dT}{dt}$ [K/s] is the net rate of change in temperature in the compartment, N [mol] is the total amount of mol in the compartment, $c_{\mathsf{v,m}}$ [J/(K mol)] is the specific heat capacity at constant volume of the gas, $\dot{Q}$ [W] is the amount of energy exchanged through heat transfer, $\dot{W}$ [W] is the amount of energy exchanged through thermodynamic work, p [Pa] is the pressure in the compartment, v_{m} [m^3/mol] is the molar volume of the gas in the compartment, Δh^{cond} [J/mol] is the latent heat of condensation, T [K] is the temperature, c_{p} [J/(K mol)] is the specific heat capacity at constant pressure and h [J/mol] is the enthalpy. It can be observed that for the permeating flows through the membranes, the enthalpy is dependent on whether the flow is exiting or entering the compartment.

The energy balances around the membranes are more straightforward as they don't exchange mass or perform thermodynamic work.

$$\frac{dT^{\text{inner}}}{dt} = \frac{\dot{Q}^{\text{inner}}}{N^{\text{inner}} \cdot c^{\text{inner}}_{\mathsf{v,m}}} \tag{B.12}$$

$$= \frac{\dot{Q}}{m^{\text{inner}} \cdot c^{\text{inner}}_{\mathsf{v}}} \tag{B.13}$$

$$\frac{dT^{\text{outer}}}{dt} = \frac{\dot{Q}^{\text{outer}}}{N^{\text{outer}} \cdot c^{\text{outer}}_{\mathsf{v,m}}} \tag{B.14}$$

$$= \frac{\dot{Q}}{m^{\text{outer}} \cdot c^{\text{outer}}_{\mathsf{v}}} \tag{B.15}$$

Heat Transfer

It has been assumed that the storage floor is well insulated and the gas is invisible to thermal radiation. Therefore, the gas in compartment B only exchanges heat with the inner membrane. It has been assumed that this happens through natural

convection.

$$\dot{Q}_{\mathrm{B}\rightarrow\mathrm{inner}} = \overline{h}_{\mathrm{B,inner}} \times A^{\mathrm{inner}} \times (T^{\mathrm{B}} - T^{\mathrm{inner}}) \quad \text{(B.16)}$$

Here, $\dot{Q}_{\mathrm{B}\rightarrow\mathrm{inner}}$ [W] is the energy exchanged through heat from the gas in compartment B to the inner membrane, $\overline{h}_{\mathrm{B,inner}}$ [W/(m K)] is the heat transfer coefficient between the gas and the membrane, A^{inner} [m^2] is the surface area of the inner membrane and T [K] is the temperature of the inner membrane and the gas in compartment B. The heat transfer coefficient can be determined from the Nusselt number. The Nusselt number is determined using the empirical correlation determined by Jaffer [59] for natural convection on an isothermal circular plate. The correlation depends on whether the plate is hotter or colder than the gas.

The gas in compartment A is constantly blown through. The convection between the gas and the inner or outer membrane can thus be either natural, forced, or both, depending on the flow speed of the gas. The gas flow speed in the compartment has been determined by the analogy described by Avila-Lopez et al. [36]. It assumes that the compartment can be approached by a cuboid with a squared base of the same area as the considered membrane. The height of the cuboid follows from the volume of the compartment, which is set equal to the volume of the cuboid. Then, the cross-sectional area of the cuboid is determined. An estimated flow speed is determined by dividing the volumetric flow rate leaving the compartment by the cross-sectional area of the cuboid. This method determines a different flow speed for the inner and outer membranes as their areas differ. The Richardson (Ri) number can be determined using the flow speeds, gas characteristics, and geometry parameters. Its value determines the convection regime. When the value of the Richardson number is smaller than 0.1, the convection is forced. The Nusselt number is dependent on the Reynolds number. The correlation provided by Mills [56] for forced convection over an isothermal horizontal plate is used. If the Richardson number exceeds 10, the convection regime is natural. Jaffer's equations [59] are used. Both natural and forced convection happen simultaneously if $0.1 < Ri < 10$. In this case, the equation for mixed transverse flow over a horizontal plate by Incorpera et al. [57] is used.

Finally, the outer membrane exchanges heat through convection with the outer air. When the wind speed is not equal to zero, the convection is assumed to be forced. Otherwise, it is considered to be natural. The same correlations as above have been used.

The two membranes exchange heat through radiation with each other. The membranes are considered to be grey surfaces. Furthermore, it has been assumed that the inner membrane is always convex at the side in contact with compartment A. A convex object does not 'see' itself. The view factor from the inner membrane to the outer membrane is one.

$$\dot{Q}_{\mathrm{inner}\rightarrow\mathrm{floor}} = \frac{\sigma(T^4_{\mathrm{inner}} - T^4_{\mathrm{floor}})}{\frac{1-\epsilon_{\mathrm{inner}}}{\epsilon_{\mathrm{inner}} A_{\mathrm{inner}}} + \frac{1}{A_{\mathrm{inner}} F_{\mathrm{inner}\rightarrow\mathrm{floor}}} + \frac{1-\epsilon_{\mathrm{floor}}}{\epsilon_{\mathrm{floor}} A_{\mathrm{floor}}}} \quad \text{(B.17)}$$

Here, $\dot{Q}_{\mathrm{inner}\rightarrow\mathrm{floor}}$ [W] is the heat exchanged through radiation from the inner to the outer membrane, σ [W/(m^2 ^{4})] is the Stefan-Boltzmann constant, T [K] is the temperature, ϵ is the emissivity and A [m^2] is the area.

The outer membrane also exchanges heat through radiation with the environment, both long-wave radiation from the surroundings and short-wave radiation from the sun. The surroundings are assumed to consist of the ground, environment, and sky. The environment contains all objects near the gasholder. Only the radiosities of the components other than the gasholder have been considered for simplicity. Also, the thermal radiation between the components has been ignored. The view factors have been determined using the same method as Avila-Lopez [36] and are based on the Thermal Analysis Research Program [60]. It states that the view factors of an object towards the ground, surroundings and sky can be approached based on the tilt angle of the external surface. The short-wave radiation from the sun received by the outer membrane depends on its surface, its solar absorptivity, the total solar irradiation on the outer membrane and its view factor to the sky. The heat transfer model does not include any form of precipitation.

Collection and pre-processing of input data

Weather data is essential to the model as the system's behaviour depends on it. The Photovoltaic Geographical Information System provides (PVGIS) the weather used [64]. Some additional modifications have to be made to obtain the necessary data. First, the effective sky temperature is determined using an empirical model developed by Aubinet [65]. In the model, the sky temperature depends on the partial pressure of water in the air, the clearness index and the air temperature. The clearness index is defined as the global solar radiation on the horizontal plane over the extraterrestrial solar irradiation on a horizontal plane. The

extraterrestrial radiation is a function of Earth-Sun distance depending on the time of the year [66].

The weather data provided by PVGIS returns a mean wind speed at an elevation of 10 m. This has been corrected to the average height of the gasholder using the log-wind profile with a surface roughness of 0.1 m.

To determine the total irradiance on the gasholder, the gasholder has been approached as a pyramid consisting of four triangular surfaces of equal area titled 45°and oriented towards the four cardinal points. The PVLIB python library provides a command, `pvlib.irradiance.get_total_irradiance`, which uses the irradiation data provided by PVGIS and the solar position, and the plane orientation to return the total irradiation on the plane [67]. As the area of the triangles is equal, the total in-plane irradiance of the four planes can be added, and the total divided by four to obtain the irradiance falling on the gasholder.

The irradiation on the solar panels has been determined using the same Python command as above. In this study, 2100 panels oriented toward the south and tilted 35°have been considered. The reference power of the panels is 580 W, and their gamma value equals -0.0003%. Using the `pvlib.pvsystem.pvwatts_dc` and the above information, the total power output of the panels can determined. Combining this with an electrolyser consuming 60 kWh per kilo of hydrogen produced, the mol flow of produced hydrogen can be determined. The produced hydrogen is assumed to have some impurities, all in the gas phase: 2000 PPM of O_2 and 3000 PPM H_2O.

The air inlet composition is assumed to contain 0.6 PPM of hydrogen [69]. The composition of the other components depends on the air's water content. Water in the air reduces the mol fractions of N_2 and O_2 by an equal amount. Their base mol fractions are 0.7849994 and 0.215, respectively.

Gasholder control

Two PID controllers control the pressure relief valves used in the model. The controllers can change the opening of the valves $\pm$ 10% per timestep. The flow through the valves is determined through the Bernoulli equation, assuming the fluid is incompressible. The PID controllers react to an error, the difference between the actual pressure in the compartment and the desired setpoint value.

During the gasholder's operation, several possible control regimes have been defined. Each regime determines the PID controller's set point pressure. Also, the proportional, integral, and derivative gain values change per regime. The first regime defined is empty storage. The storage is defined as empty when the volume of gas compartment B is at 5% or less of its maximum value. The PID controller of the pressure relief valve of compartment A is tasked to keep the pressure in the compartment at 106325 Pa. The pressure relief valve in compartment B is unnecessary as it is not at its maximum loading capacity. Its desired opening is set at 0%. The same parameters are used when the gasholder is in the stand-by regime.

The gasholder enters the stand-by regime when the hydrogen production and demand are equal to zero, and the gasholder is neither full nor empty. This will happen during the nights when the hydrogen compressor is shut off. The pressure is kept low, 106325 Pa, to minimise permeation through the membranes and the duty of the air blower of compartment A. The stand-by regime has two controllers. The previous regime decides which controller is used. The controller's gains are different to ensure adequate reaction to the pressure change. The controller can enter the stand-by regime after the inflation or deflation regime.

In the case where hydrogen is produced, multiple regimes are possible. The first is the inflation regime. During this regime, the hydrogen production entering the system is greater than the hydrogen demand exiting it, while the load in gas compartment B is not at its maximum. The PID controller for the pressure relief valve of compartment A maintains the pressure at 141325 Pa, the maximum allowable pressure of the compartment. The relief valve of compartment B is desired to be closed. The volume of compartment B will continuously increase until it reaches its maximum volume. This means that the storage enters the full storage regime: the hydrogen compressor at the system's exit will be activated, and the storage will deliver hydrogen at a flow rate of 2.57 mol per second. During the full storage regime, both relief valves are controlled by a PID controller. The desired pressure is 141325 Pa in compartments A and B, respectively. Due to the activation of the compressor leading to hydrogen demand, the gasholder can enter the deflation regime. If the hydrogen demand exceeds the hydrogen production, the total amount of mol in compartment B will decrease, deflating the storage. Only the controller for the pressure relief valve of gas compartment A is active; its set point is 111325 Pa. This slight overpressure ensures that the hydrogen will flow smoothly to the compressor. Once the storage enters the deflation regime, it can not exit until it is completely empty or full again. These conditions have been added to prevent the controller from increasing the

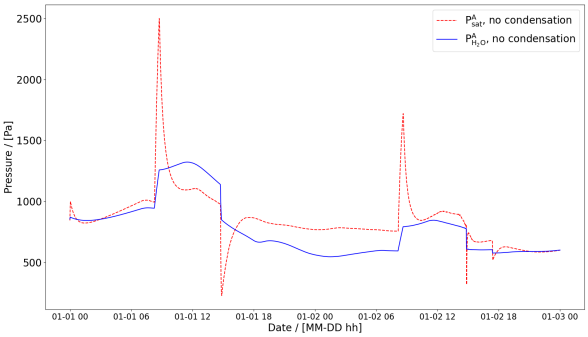

Figure B.2: Partial and saturation pressures of H_2O in gas compartment A if no condensation were considered. In the regions where the partial pressure of H_2O is higher than the saturation pressure, condensation is expected. All aspects of the model but condensation have been considered

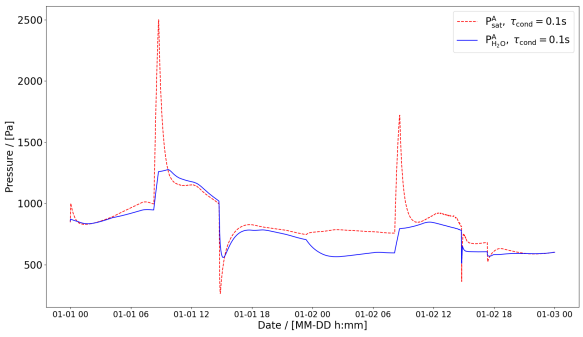

Figure B.3: Partial and saturation pressures of H_2O in gas compartment A if condensation were considered with τ_{cond}=0.1 s. In the regions where the partial pressure of H_2O is higher than the saturation pressure, condensation is expected. All aspects of the model have been considered

pressure after the storage has been fully drained. The storage is mostly drained when the sun is still shining at the end of the day, thus producing H_2. There will still be a small amount of hydrogen produced. This is not enough to fully blow up the storage; thus, it can be done at low pressure. This avoids pressure drops and saves compressor energy. More hydrogen can also be produced during deflation than flow, leaving the storage due to the compressor demand. This will increase the pressure in compartment B. Therefore, going from the deflation regime to the full storage regime is possible. This happens when, during deflation, the gas in compartment B reaches its maximum volume and a pressure greater than 141325 Pa. A last boundary condition has to be added. The hydrogen production can stop just before the storage is completely filled. The pressure in the system is that of the inflation regime. The system will go into the stand-by regime, lowering the pressure to 106325 Pa. Due to the decrease in pressure, the volume of compartment B increases. This could lead to the volume of compartment B reaching its maximum value. In this case, the deflation regime is also started.

Results

First, it was proven that condensation is a necessary phenomenon to consider. To do so, simulations were run without considering phase change. The saturation pressure of water vapour in compartment A was plotted versus the calculated partial pressure in compartment A.

Form Figure B.2, it is clear that condensation is a necessary addition to the model. Water vapour will condense once its partial pressure in the gas exceeds its saturation pressure. This is the case between 0.1-01-01 10 and 01-01 14. During this period, a liquid phase will form in the compartment, which in later instances will evaporate again if the partial pressure of water is lower than the saturation pressure. The condensation of water vapour will heat the system as it is an exotherm process; the evaporation of water will cool down the system.

From Figure B.3, it is clear that adding the condensation term changed the system's behaviour. In the same period, between 0.1-01-01 10 and 01-01 14, the partial pressure of water vapour lays just above the saturation pressure of water vapour. this is due to the vapour condensing. The evaporation of the liquid phase is also visible just after that period. The partial pressure of water vapour in the air lies just below the saturation pressure due to evaporation. The chosen value of τ_{cond} gives a realistic model performance. Logically, the lines do not exactly fall upon each other as the air in the compartment is continuously blown through, and condensation nor evaporation happens instantly.

To prove that intermolecular friction between the permeating species was negligible when considering Maxwell-Stefan diffusion. Two simulations were run where the gasholder was only partially filled; the hydrogen compartment was filled at 50% of its maximum capacity. One simulation contained the full Maxwell-Stefan equation, and the other simulation only considered the friction between the membrane and the permeating species. It has been chosen to compare the mol amount of H_2 over time. H_2 is the smallest permeating molecule considered; therefore, it will have the highest permeation rate. Furthermore, the concentration gradient of H_2 is the highest as compartment B contains nearly pure H_2 while compartment A contains nearly none. The storage was held in the standby phase. No in or outlet was considered for compartment B. The only way H_2 molecules leave the system is through the membrane.

Figure B.4 shows the difference in the mol amount

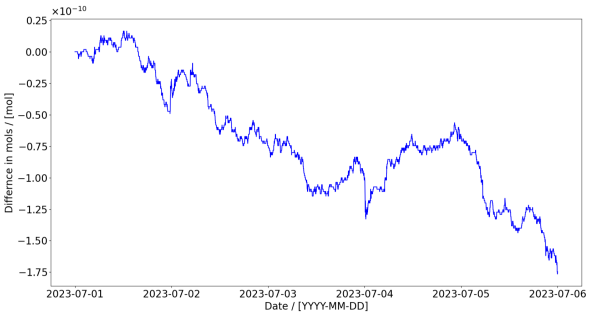

Figure B.4: Difference in the amount of H_2 in compartment B between a simulation considering all friction terms of Maxwell-Stefan diffusion and a simulation only considering the friction between the permeating species and the membrane.

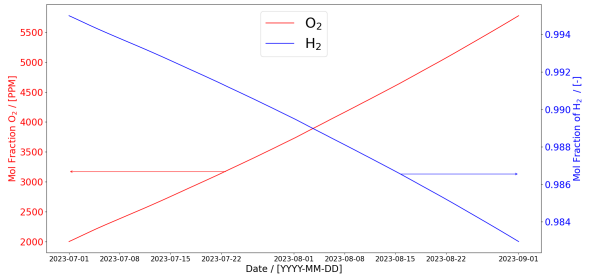

Figure B.5: Mol fraction of H_2, right axis, and concentration of O_2, left axis, in gas compartment B initially 10% filled versus time. The gas in the compartment is at a standstill, meaning molecules only leave or enter the control volume through the membrane.

between the two runs. After five days, the difference is around -1.75$\times 10^{-10}$ mol. The total amount of mol of H_2 permeated in that time is around 40. The difference is thus negligible compared to the total amount. From this, it can be concluded that this assumption holds. Only the friction between the membrane and the permeating species is considered in this model.

Now that the permeation through the membrane is proven to work as expected, the purity of the gas in storage can be assessed. O_2 will diffuse from compartment a to compartment b through the inner membrane. Mixing H_2 with O_2 is dangerous due to the mixture's large combustion range. Only 4% of oxygen is needed to form an explosive mixture [16, 17]; this is equal to 40000 PPM. The standby case has been simulated again, but his time gas compartment B was only filled at 10% of its maximum value.

Figure B.5 shows the evolution of the mol fractions of H_2 and O_2 in the system. The mol fraction of H_2 decreases while the concentration of O_2 increases. This is logical due to the direction of the diffusion through the membrane. After 62 days, the concentration of O_2 is around 5500 PPM. this

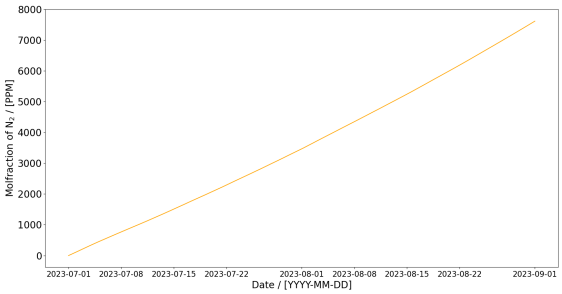

Figure B.6: Concentration of N_2 in gas compartment B initially 10% filled versus time. The gas in the compartment is at a standstill, meaning molecules only leave or enter the control volume through the membrane.

is nowhere near the 40000 PPM needed to form a combustible mixture. Although the profile for the mol fraction of O2 in compartment B is not fully linear, a linear fit could approach the number of days after which O_2 represents 40000 PPM of the mixture. In 62 days, the concentration of O2 has increased by nearly 4000 PPM. This linear fit indicates that it would take 589 days before the oxygen concentration reaches 40000 PPM. The linear approach is not completely true to reality, but it indicates that it will take a long time before safety or purity issues arise.

If now, for the same run, the concentration of N_2 is of interest, Figure B.6, a different story is visible. The maximum allowed contamination of N_2 in the final product is 300 PPM [25] if distribution to fuel cells is wished. This concentration is reached after three days. From this, one can conclude that if no downstream N2 cleaning is available, one should not worry about reaching explosion limits as the product will long before be contaminated with N2 and, therefore, should be discarded. It has been assumed that both O_2 and H_2O downstream postprocessing are available and that their concentration does not raise any purity concerns. The 300 PPM limit is never exceeded during normal operation if H_2 is produced every other day.

The developed model can also compare storage behaviour at different locations. It has been chosen to run four simulations per period of three months representing the different seasons of the year at a location in Spain, Cabezuela, and Eerbeek, Netherlands. The results are visible in Table B.1.

The first thing to note is that the amount of H_2 produced is greater during every season in Spain. This is an expected result. Spain is known to be a sunnier country than the Netherlands. As electricity generated by solar panels produces the hydrogen, the amount of sun is directly linked to the amount of hydrogen produced. The losses also in-

Table B.1: Table containing the major results for all seasons during normal operation in Cabezuela, Spain and Eerbeek, the Netherlands

	Winter	**Spring**	**Summer**	**Autumn**
Cabezuela, Spain				
Amount of H_2 lost [mol]	21900	27100	22000	11600
Amount of H_2 produced [mol $\times 10^6$]	3.17	5.47	5.85	3.55
Storage efficiency [%]	99.31	99.50	99.62	99.67
Equivalent amount of CO_2 emitted [kg]	512	663	514	271
Number of cycles	76	91	92	82
Total compressor run time / [h]	344	593	635	362
Average compressor run time / [h]	4.53	6.52	6.90	4.66
Eerbeek, the Netherlands				
Amount of H_2 lost [mol]	3400	16900	8075	3553
Amount of H_2 produced [mol $\times 10^6$]	1.92	4.77	4.09	1.81
Storage efficiency [%]	99.82	99.65	99.80	99.79
Equivalent amount of CO_2 emitted [kg]	79.5	395	189	83.1
Number of cycles	59	88	90	56
Total compressor run time / [h]	209	517	516	197
Average compressor run time / [h]	3.54	5.88	5.73	3.51

crease in Spain. The loss is greater per season in Spain as the solar irradiance on the solar panels is greater. In the same amount of time, more hydrogen is produced. Thus, hydrogen production is more likely to exceed the hydrogen demand at the start of the drainage cycle. The major losses come from overpressures in compartment B. These can only happen when the storage is fully filled. During an overpressure, the PID controller controls the relief valve of compartment B. It will vent out excess hydrogen to reduce the pressure in the compartment. It is thus logical that more losses occur when more hydrogen is produced. The losses don't increase linearly. This is visible through the lower storage efficiency in Spain. The storage efficiency is defined as the total amount of hydrogen produced minus the hydrogen lost and the total over the total amount of hydrogen produced. Looking solely at storage performance, one could say that storage works better in Spain than in the Netherlands, but this is not a fair conclusion. The main goal of the storage is to minimise the power cycling of the downstream compressor. The results show that the average compressor run time per cycle is substantially higher in Spain than in the Netherlands. This would mean a more efficient use of the compressor over its lifetime. The production of hydrogen is also desired as it is the final product. Producing more products with the same equipment is a distinct advantage. Production in Spain would, therefore, be favoured.

Conclusion

This work focused on modelling a double membrane gasholder as a hydrogen storage device at atmospheric pressure. The storage serves as a buffer for the intermittent hydrogen production from solar energy. The downstream compressor's power cycling should be limited as much as possible. A control system was designed to accommodate this kind of operation. The system regulates the pressure in the storage: multiple regimes have been defined to ensure efficient operation. The control system ensures that it starts draining the storage once it has reached maximum capacity and stops when it is emptied. Furthermore, the thermodynamic model of Yuki Junior et al. [4] has been elaborated. The condensation of water has been considered. It was shown that the water in the system is prone to condense, which influences the system's energy. The water in the liquid phase will also evaporate in later instances as the temperature in the compartments rises. The permeation of molecules through the membranes in the system has also been regarded. The flux through the membranes was approached using Maxwell-Stefan diffusion. The diffusion of molecules is essential to account for while storing hydrogen. Hydrogen has a wide combustible range.

Furthermore, the purity requirements for hydrogen are stringent. The model showed that one should not have to worry about safety issues. The hydrogen will long before being contaminated with nitrogen. As no downstream cleaning for nitrogen is available, the hydrogen must be discarded be-

fore reaching combustion limits. The results for regular operation show that this contamination limit is nearly never reached. Only when there are multiple days of no sun hours does the nitrogen form a purity problem. Overall, the model is capable of predicting the storage behaviour. It can be used to determine the production of hydrogen and the number of cycles. The model also determines the composition of the gas exiting the storage towards the compressor. These will depend on outside weather conditions. Furthermore, the model is fully modular. It can be used at all locations around the world. The user only has to provide the latitude and longitude of the desired location. Storage behaviour and performance per location can be compared.

One of the major next steps for this work is to validate the model by comparing it with experimental results. As it is, it remains unvalidated. Furthermore, extending the control system to regulate hydrogen production from the electrolyser could be beneficial. By switching off part of the electrolyser, hydrogen production can be decreased when overpressures are present in the system, thus reducing the total amount of hydrogen lost through venting by the pressure relief valve. At last, an extension of the model is needed as temperatures below zero Celcius have been returned. This means that the water in the system will form ice. This either needs to be considered or avoided by heating the compartment.